NONDESTRUCTIVE EVALUATION TECHNIQUES FOR FATIGUE AND DAMAGE DETECTION

By

Bharath Basti Shenoy

A DISSERTATION

Submitted to
Michigan State University
in partial fulfillment of the requirements
for the degree of

Electrical and Computer Engineering—Doctor of Philosophy

2024

ABSTRACT

The first part of this doctoral thesis explores the application of Magnetic Barkhausen Noise and Non-Linear Eddy Current techniques for the early-stage detection of fatigue in ferromagnetic materials, with a specific focus on Martensitic Stainless-steel samples. Due to its exceptional mechanical properties at elevated temperatures, stainless steel finds extensive use in various applications. However, material fatigue poses a significant challenge in steel structures, leading to potential catastrophic damage and substantial economic consequences. While conventional nondestructive evaluation techniques excel at detecting macro defects, they often fall short in identifying material degradation at the microstructure level, particularly arising from fatigue.

The Magnetic Barkhausen Noise technique involves capturing signals generated by the movement of domain walls after applying a time-varying magnetic field. Different fatigue stages yield unique Magnetic Barkhausen Noise signatures, facilitating effective classification. In the Non-Linear Eddy Current technique, a robust external magnetic field induces non-linear behavior in the material's magnetization characteristic. The harmonics extracted from the Non-Linear Eddy Current signal provide insights into the material's microstructure, aiding in the classification of samples at various fatigue stages. The research work systematically investigates the feasibility of Magnetic Barkhausen Noise and Non-Linear Eddy Current techniques by employing customized sensor assemblies to capture and analyze signals in both time and frequency domains. Extracted features are further processed using k-medoids clustering algorithm, and Genetic algorithm for robust classification into distinct fatigue stages. The comparative performance of the two magnetic non-destructive evaluation techniques is thoroughly examined.

The research findings indicate that both Magnetic Barkhausen Noise and Non-Linear Eddy Current techniques present promising capabilities for detecting early-stage fatigue in Martensitic Stainless-steel samples and contributes to advancing the fatigue detection in ferromagnetic structures using magnetic non-destructive evaluation techniques.

In the second part of this doctoral thesis, the focus is on addressing critical challenges of monitoring the structural health of engineering structures, which are susceptible to damage from both stress and

environmental factors. Traditional ultrasonic nondestructive evaluation techniques typically involve contact-based procedures that necessitate the use of a couplant. However, this thesis explores the use of Electromagnetic Acoustic Transducers, which offer a compelling non-contact alternative. Electromagnetic Acoustic Transducers utilize the Lorentz force, acting on induced currents, to excite elastic waves in a sample, eliminating the need for direct contact. The drawback of conventional Electromagnetic Acoustic Transducers being limited to conductive or ferromagnetic samples is addressed through the introduction of a novel Electromagnetic Acoustic Transducer, specifically designed for non-conductive samples.

This novel Electromagnetic Acoustic Transducer presents two distinct configurations: (a) Direct excitation and (b) Non-contact induced excitation, both utilizing the Lorentz force transduction mechanism. A thorough investigation into the metal patch geometry employed in both configurations is detailed, providing valuable design insights. The numerical model of these Electromagnetic Acoustic Transducer configurations is developed using COMSOL, and simulation results robustly affirm the feasibility of the proposed approach. By successfully extending the applicability of Electromagnetic Acoustic Transducers to non-conductive samples and introducing the innovative embedded Electromagnetic Acoustic Transducer, this research significantly contributes to advancing the field of structural health monitoring and presents a viable nondestructive evaluation approach for the effective detection of damage in engineering structures.

ACKNOWLEDGEMENTS

I would like to express my heartfelt gratitude to my parents, wife and family. Their unwavering support has been the cornerstone of my journey, and without them, this thesis would not have been possible.

I am deeply grateful to my major advisor, Professor Lalita Udpa, for her unwavering guidance, support, and mentorship throughout my doctoral journey. Her expertise, encouragement, and constructive feedback have been invaluable in shaping this research and my academic growth. I also extend my sincere appreciation to Professor Sunil Chakrapani for his mentorship, assistance in understanding acoustics, and for instilling confidence in my capabilities. Their collective wisdom has significantly enriched my doctoral experience.

I also extend my sincere appreciation to Professor Satish Udpa for providing me with the opportunity to join the NDEL family and for his insightful contributions to my academic and research development. His words of encouragement were instrumental in propelling the advancement of my research.

I would like to express my gratitude to Professor Yiming Deng, who was like a supportive co-advisor throughout this journey. Collaborating with him was a valuable and enriching experience. I extend my gratitude to the members of the NDEL research group for fostering an intellectually and stimulating research environment. Our mutual support has been instrumental throughout the years, and I look forward to sustaining these friendships in the years ahead. I extend my thanks to Zebadiah Miles, a PhD student at Michigan State University, for his collaboration and valuable contributions to the experimental aspects of the research work on electromagnetic acoustic transducers.

Lastly, my sincere thanks to all my friends in Michigan for their encouragement and support, making this academic pursuit a memorable and fulfilling experience. My time in East Lansing was made truly enjoyable by their incredible camaraderie.

TABLE OF CONTENTS

LIST OF TABLES vii

LIST OF FIGURES viii

CHAPTER 1 INTRODUCTION TO FATIGUE 1
1.1 Material fatigue 1
1.2 Microstructural phenomenon in steel 4
1.3 Existing NDE methods 7

CHAPTER 2 PHYSICAL PRINCIPLES OF MBN AND NLEC 10
2.1 Magnetic Barkhausen Noise Technique 10
2.2 NLEC Technique 13

CHAPTER 3 RESEARCH PROBLEM 18
3.1 Research problem representation 18
3.2 Sample database 18

CHAPTER 4 RESULTS AND DISCUSSION 20
4.1 Results and discussion on MBN 20
4.2 Results and discussion on NLEC 28

CHAPTER 5 CONCLUSIONS AND FUTURE WORK 36

CHAPTER 6 INTRODUCTION TO EMAT 38
6.1 Literature review 39
6.2 Transduction mechanisms in EMAT 41
6.3 Typical EMAT designs in Literature 42

CHAPTER 7 LORENTZ FORCE EMAT 46
7.1 Theory 46
7.2 Numerical model in COMSOL 47
7.3 Novel EMAT configurations for non-conductive samples 51

CHAPTER 8 DIRECT EXCITATION 53
8.1 EMAT model in COMSOL 53
8.2 Effect of input current on Lorentz force and displacement in sample 65
8.3 Effect of Aluminum strip geometry on displacement in sample 67
8.4 Impact of skin effect in Aluminum strip on displacement in sample 78
8.5 Experimental validation 79

CHAPTER 9 NON-CONTACT INDUCED EXCITATION: EMBEDDED EMAT . . . 84
9.1 EMAT model in COMSOL 84
9.2 Effect of Aluminum strip geometry on displacement in sample 93
9.3 Effect of line source on acoustic modes in sample 97
9.4 Effect of plastic cover height on displacement in sample 101

9.5 A Comparative Analysis: Gaussian vs. Uniform Distribution of Lorentz force in space . . . 103
9.6 Experimental validation . . . 109

CHAPTER 10 DAMAGE DETECTION IN SAMPLE . . . 114
10.1 Vertical slot defect . . . 114
10.2 Horizontal crack defect . . . 118
10.3 A-scans on sample back-wall . . . 121

CHAPTER 11 CONCLUSIONS AND FUTURE WORK . . . 125

BIBLIOGRAPHY . . . 127

LIST OF TABLES

Table 2.1 MBN system details 12

Table 2.2 NLEC experimental parameters 17

Table 3.1 EPRI MSS sample database 19

Table 4.1 Fatigue thresholds obtained on applying KCA and GA on MBN features 25

Table 4.2 Comparison of other MBN feature combinations 26

Table 4.3 Sample database with fatigue classification 27

Table 4.4 NLEC signal features 31

Table 4.5 Fatigue thresholds obtained on applying KCA and GA on NLEC features 33

Table 4.6 Sample database with fatigue classification 35

Table 8.1 Model parameters for Direct excitation EMAT 55

Table 8.2 Time at which modes peak in Hilbert magnitude plot for Direct Excitation EMAT model 63

Table 8.3 Mode velocities for Direct excitation EMAT model 63

Table 9.1 Model parameters for Induced excitation EMAT model 86

Table 9.2 Time at which modes peak in Hilbert magnitude plot for Induced Excitation EMAT 89

Table 9.3 Mode velocities for Induced Excitation EMAT 90

Table 10.1 Model parameters with defect dimensions 121

LIST OF FIGURES

Figure 1.1 Stages of fatigue failure 2

Figure 1.2 SN curve 3

Figure 1.3 Domains with magnetic moments in steel 6

Figure 2.1 Magnetic flux density changes due to Barkhausen effect 11

Figure 2.2 Time domain MBN signal 11

Figure 2.3 Block diagram of MBN experimental set-up 12

Figure 2.4 Eddy Current in material with and without surface defect 13

Figure 2.5 B-H curve with linear and non-linear eddy current response plots 14

Figure 2.6 Block diagram of NLEC experimental set-up 16

Figure 2.7 NLEC sensor mounted on the EPRI sample 16

Figure 3.1 Overview of the research problem 18

Figure 3.2 Snapshot of a MSS sample provided by EPRI 19

Figure 4.1 Schematic of EPRI stainless-steel sample showing scanning point locations . . . 20

Figure 4.2 Gaussian fitting of MBN signal showing time domain features 21

Figure 4.3 Frequency spectrum of MBN signal showing frequency domain features 22

Figure 4.4 Flowchart of the algorithm used to classify MSS samples based on RUL 23

Figure 4.5 Clustering of MSS samples into fatigue categories 24

Figure 4.6 Classification results based on ground-truth 26

Figure 4.7 Schematic of EPRI sample showing scanning points 29

Figure 4.8 Time domain NLEC signal obtained from NLEC sensor 29

Figure 4.9 Frequency spectrum of the time domain NLEC signal 30

Figure 4.10 Flowchart of the algorithm used to classify MSS samples based on RUL 32

Figure 4.11 Clustering of MSS samples into fatigue categories 33

Figure 4.12 Classification results based on ground-truth NLEC 34

Figure 6.1 Schematic representation of an EMAT 40

Figure 6.2 Lorentz force representation on a metal plate 40

Figure 6.3 Schematic diagram of a Bulk-wave EMAT 43

Figure 6.4 Schematic diagram of a Meander line EMAT 44

Figure 6.5 Schematic diagram of a PPM EMAT 45

Figure 8.1 Direct Excitation model for an EMAT in COMSOL 54

Figure 8.2 Zoomed version of the EMAT model shown in Figure 8.1 54

Figure 8.3 Representation of input current provided to the Aluminum strip 55

Figure 8.4 Input current density provided to Aluminum strip 56

Figure 8.5 z-component of current density at measurement point in Aluminum strip 57

Figure 8.6 y-component of Lorentz force at measurement point in Aluminum strip 58

Figure 8.7 Surface plot of z-component of current density in Aluminum strip at 5 µs 58

Figure 8.8 Surface plot of y-component of Lorentz force in Aluminum strip at 5 µs 59

Figure 8.9 Surface plot of x-component of Lorentz force in Aluminum strip at 5 µs 59

Figure 8.10 Arrow surface plot of y-component of Lorentz force (N/m^3) in Aluminum strip at 5 µs 60

Figure 8.11 Zoomed version of Figure 8.10 60

Figure 8.12 Arrow surface plot of x-component of Lorentz force (N/m^3) in Aluminum strip at 5 µs 61

Figure 8.13 A-scan of displacement at measurement point on plastic back-wall 61

Figure 8.14 Hilbert magnitude of A-scan signal showed in Figure 8.13 62

Figure 8.15 Surface plot of full-field displacement in plastic at 12 µs 64

Figure 8.16 Surface plot of y-component of displacement in plastic at 12 µs 64

Figure 8.17 Surface plot of x-component of displacement in plastic at 12 µs 65

Figure 8.18 Comparison of Lorentz force at measurement point in Aluminum strip for varying coil current magnitudes 66

Figure 8.19 Comparison of A-scans of displacement at measurement point on plastic back-wall for varying coil current magnitudes 66

Figure 8.20 A-scan of displacement for Aluminum strip width = 5mm 67

Figure 8.21 Comparison of displacement A-scans for varying Aluminum strip widths 68

Figure 8.22 Surface plot of full-field displacement in plastic at 12 µs for Aluminum strip width = 5mm 69

Figure 8.23 Surface plot of y-component of displacement in plastic at 12 µs for Aluminum strip width = 5mm 70

Figure 8.24 Surface plot of x-component of displacement in plastic at 12 µs for Aluminum strip width = 5mm 70

Figure 8.25 Surface plot of z-component of current density in Aluminum strip for strip width = 5mm 71

Figure 8.26 Surface plot of y-component of Lorentz force in Aluminum strip at 5 µs for strip width = 5mm 71

Figure 8.27 Surface plot of x-component of Lorentz force in Aluminum strip at 5 µs for strip width = 5mm 72

Figure 8.28 Arrow surface plot of y-component of Lorentz force in Aluminum strip at 5 µs for strip width = 5mm 72

Figure 8.29 Arrow surface plot of x-component of Lorentz force in Aluminum strip at 5 µs for strip width = 5mm 73

Figure 8.30 A-scan of displacement at measurement point on plastic back-wall for Aluminum strip height = 0.1mm 74

Figure 8.31 Comparison of displacement A-scans for varying Aluminum strip heights 74

Figure 8.32 Surface plot of full-field displacement in plastic at 12 µs for Aluminum strip height = 0.1mm 75

Figure 8.33 Surface plot of y-component of displacement in plastic at 12 µs for Aluminum strip height = 0.1mm 75

Figure 8.34 Surface plot of x-component of displacement in plastic at 12 µs for Aluminum strip height = 0.1mm 76

Figure 8.35 Surface plot of z-component of current density in Aluminum strip for strip height = 0.1mm 76

Figure 8.36 Arrow surface plot of y-component of Lorentz force in Aluminum strip at 5µs for strip height = 0.1mm 77

Figure 8.37 Arrow surface plot of x-component of Lorentz force in Aluminum strip at 5µs for strip height = 0.1mm 77

Figure 8.38 Comparison of Hilbert magnitude peaks of A-scans of displacement in plastic, for mode 1, and for different aluminum strip heights 78

Figure 8.39 Experimental set-up for Direct Excitation EMAT 79

Figure 8.40 Aluminum strip geometry used for experiments 80

Figure 8.41 A-scan of displacement at measurement point on plastic back-wall - Simulation result for Aluminum strip B 81

Figure 8.42 A-scan of displacement at measurement point on plastic back-wall - Experimental result for Aluminum strip B 81

Figure 8.43 A-scan of displacement at measurement point on plastic back-wall - Simulation result for Aluminum strip C 82

Figure 8.44 A-scan of displacement at measurement point on plastic back-wall - Experimental result for Aluminum strip C 82

Figure 9.1 Induced Excitation model for an EMAT in COMSOL 85

Figure 9.2 Zoomed version of Figure 9.1 85

Figure 9.3 Arrow surface plot of y-component of Lorentz force in Copper patch at 5µs . . . 87

Figure 9.4 Arrow surface plot of x-component of Lorentz force in Copper patch at 5µs . . . 87

Figure 9.5 A-scan of displacement at measurement point on plastic back-wall for Induced excitation EMAT 88

Figure 9.6 Hilbert magnitude of A-scan signal showed in Figure 9.5 88

Figure 9.7 Surface plot of full-field displacement in plastic at 12 µs for Induced excitation EMAT 90

Figure 9.8 Surface plot of y-component of displacement in plastic at 12 µs for Induced excitation EMAT 90

Figure 9.9 Surface plot of x-component of displacement in plastic at 12 µs for Induced excitation EMAT 91

Figure 9.10 Comparison of A-scans of displacement at measurement point on plastic back-wall for varying coil current magnitudes (Induced Excitation EMAT) . . . 91

Figure 9.11 Comparison of A-scans of displacement at measurement point on plastic back-wall for direct excitation and induced excitation EMAT's 92

Figure 9.12 A-scan of displacement at measurement point on plastic back-wall for Aluminum strip width = 5mm 94

Figure 9.13 Comparison of A-scans of displacement at measurement point on plastic back wall for varying Aluminum strip widths (Induced Excitation EMAT) 94

Figure 9.14 A-scan of displacement at measurement point on plastic back-wall for 0.1mm Aluminum strip height (Induced Excitation EMAT) 95

Figure 9.15 Comparison of A-scans of displacement at measurement point on plastic back wall for varying Aluminum strip heights (Induced Excitation EMAT) 96

Figure 9.16 Induced excitation EMAT model with point source (in 2D) - No aluminum . . . 97

Figure 9.17 Arrow surface plot of x-component of Lorentz force in Copper patch at 5 µs for Induced Excitation EMAT model shown in Figure 9.16 98

Figure 9.18 Arrow surface plot of y-component of Lorentz force in Copper patch at 5 µs for Induced Excitation EMAT model shown in Figure 9.16 98

Figure 9.19 A-scan of displacement at measurement point on plastic back-wall for Induced Excitation EMAT model shown in Figure 9.16 99

Figure 9.20 Quantitative comparison of Induced Excitation EMAT's 99

Figure 9.21 Surface plot of full-field displacement in plastic at 12 µs for EMAT model shown in Figure 9.16 100

Figure 9.22 Surface plot of y-component of displacement in plastic at 12 µs for EMAT model shown in Figure 9.16 100

Figure 9.23 Surface plot of x-component of displacement in plastic at 12 µs for EMAT model shown in Figure 9.16 101

Figure 9.24 Comparison of displacement A-scans at measurement point on plastic back-wall for varying plastic cover heights (Induced Excitation EMAT) 102

Figure 9.25 Comparison of displacement A-scans at measurement point on plastic back-wall for varying aluminum strip placements (Induced Excitation EMAT) 103

Figure 9.26 Representation of input current provided to Aluminum strip 104

Figure 9.27 Arrow surface plot of x-component of Lorentz force (Case 1) in Copper patch at 5 µs 104

Figure 9.28 Arrow surface plot of y-component of Lorentz force (Case 1) in Copper patch at 5 µs 105

Figure 9.29 Arrow surface plot of x-component of Lorentz force (Case 2) in Copper patch at 5 µs 105

Figure 9.30 Arrow surface plot of y-component of Lorentz force (Case 2) in Copper patch at 5 µs 106

Figure 9.31 Displacement A-scans (Mode 1) at measurement point on plastic back-wall . . . 106

Figure 9.32 Surface plot of full-field displacement in plastic at 12 µs - Case 1 107

Figure 9.33 Surface plot of y-component of displacement in plastic at 12 µs - Case 1 107

Figure 9.34 Surface plot of x-component of displacement in plastic at 12 µs - Case 1 108

Figure 9.35 Surface plot of full-field displacement in plastic at 12 µs - Case 2 108

Figure 9.36 Surface plot of y-component of displacement in plastic at 12 µs - Case 2 109

Figure 9.37 Surface plot of x-component of displacement in plastic at 12 µs - Case 2 109

Figure 9.38 Experimental set-up for Induced Excitation EMAT 110

Figure 9.39 A-scan of displacement at measurement point on plastic back-wall - Simulation result for Aluminum strip B (Induced Excitation EMAT) 111

Figure 9.40 A-scan of displacement at measurement point on plastic back-wall - Experimental result for Aluminum strip B (Induced Excitation EMAT) 111

Figure 9.41 A-scan of displacement at measurement point on plastic back-wall - Simulation result for Aluminum strip C (Induced Excitation EMAT) 112

Figure 9.42 A-scan of displacement at measurement point on plastic back-wall - Experimental result for Aluminum strip C (Induced Excitation EMAT) 113

Figure 10.1 Embedded EMAT model with defect in COMSOL 114

Figure 10.2 Defect geometry representation 115

Figure 10.3 A-scan of displacement at measurement point on plastic back wall (No defect and With vertical slot defect) 115

Figure 10.4 Surface plot of full-field displacement in plastic at 12 µs - No defect 116

Figure 10.5 Surface plot of full-field displacement in plastic at 12 μs - With defect 116

Figure 10.6 A-scan of displacement at measurement point on plastic back-wall for varying defect widths (Defect height = 4mm) 117

Figure 10.7 A-scan of displacement at measurement point on plastic back-wall for varying defect heights (Defect width = 1mm) 117

Figure 10.8 A-scans of displacement at measurement point on plastic back-wall (No defect and with Horizontal crack defect) 118

Figure 10.9 Surface plot of full-field displacement in plastic at 12 μs - No defect 119

Figure 10.10 Surface plot of full-field displacement in plastic at 12 μs - With defect 119

Figure 10.11 A-scans of displacement at measurement point on plastic back-wall for varying defect widths (Defect height = 1mm) 120

Figure 10.12 A-scans of displacement at measurement point on plastic back-wall for varying defect heights (Defect width = 4mm) 120

Figure 10.13 A-scan results for a Horizontal crack defect 122

Figure 10.14 A-scan results for a Vertical slot defect 123

CHAPTER 1

INTRODUCTION TO FATIGUE

Stainless-steel is used in many applications because of its excellent mechanical properties at elevated temperatures. Martensitic grade stainless-steel is used to manufacture steam turbine blades in power plants because of its mechanical strength, corrosion resistance and durability. Failure of turbine blades can result in equipment damage contributing to expensive plant failures and safety concerns. One of the primary factors which leads to degradation of the material and structural failure is plastic deformation [1], caused by material fatigue.

1.1 Material fatigue

Material fatigue is defined as a process of progressive localized plastic deformation occurring in a material subjected to cyclic stresses and strains. At high stress concentration locations in the material, the progression of fatigue may culminate in cracks or complete fracture after enough number of loading cycles [2]. Typically, material fatigue investigation in metals was predominantly on monitoring of crack growth [3], because this is the stage that precedes ultimate failure. Fatigue cracking is considered to be one of the most important damage mechanisms of structural components. Hence, it is important to evaluate the material fatigue level prior to the initiation of macro defects in order to ensure the viability of these components.

1.1.1 Stages of fatigue

There are three stages of fatigue failure: Initiation, propagation, and final rupture [4] as shown in Figure 1.1.

Initiation: Irreversible changes in the material which is caused by repetitive shear stress applied on it is the most important factor leading to fatigue crack initiation. Large number of loading applications on the material leads to cumulative damage, in terms of micro-changes. In this fatigue stage, dislocations (i.e., crystallographic defects) play a major part.

Propagation: In this stage, the micro-cracks formed during the crack initiation stage join together and propagate in the direction perpendicular to the tensile stress. The growth of one or few of the

Figure 1.1 Stages of fatigue failure

larger cracks tend to dominate over the others and develop macro cracks. If cyclic loading is still continued, the dominant crack keeps growing in size to the point where it reaches a critical size. This is the point where the material can no longer support the load, i.e., fracture toughness of the material is exceeded by the stress intensity factor. At this point, the crack tends to propagate rapidly.

Final rupture: The cross-sectional area of the material reduces with the propagation of fatigue cracks. When the fatigue crack exceeds a particular size, the material is weakened and results in a final rupture with additional loading cycles.

1.1.2 Fatigue life and SN-curve

The fatigue life of a component can be defined as the number of loading cycles needed to initiate a fatigue crack and propagate it to the critical size. There are two regimes of fatigue, i.e., low cycle and high cycle fatigue.

Low cycle fatigue is a regime of fatigue which is caused by large plastic strains with low number of loading cycles before the occurrence of failure. Loading causes the development of high stress, i.e., greater than the yield strength of the material. This leads to larger plastic deformation and shorter fatigue life. In contrast, high cycle fatigue is a regime which is caused by small elastic strains with higher number of loading cycles before the occurrence of failure. The stress level when compared to low cycle fatigue is much lower, i.e., lower than the material's yield strength. Also, the macroscopic plastic deformation is much smaller when compared to the low cycle fatigue regime. Fatigue life for any given material is found from the SN curve for that material.

A SN-Curve is a plot of magnitude of cyclic stress versus the number of loading cycles to failure for a given material. A sample SN curve is shown in Figure 1.2. SN curves are determined in the laboratory where test specimens are subjected to loading cycles of constant amplitudes until

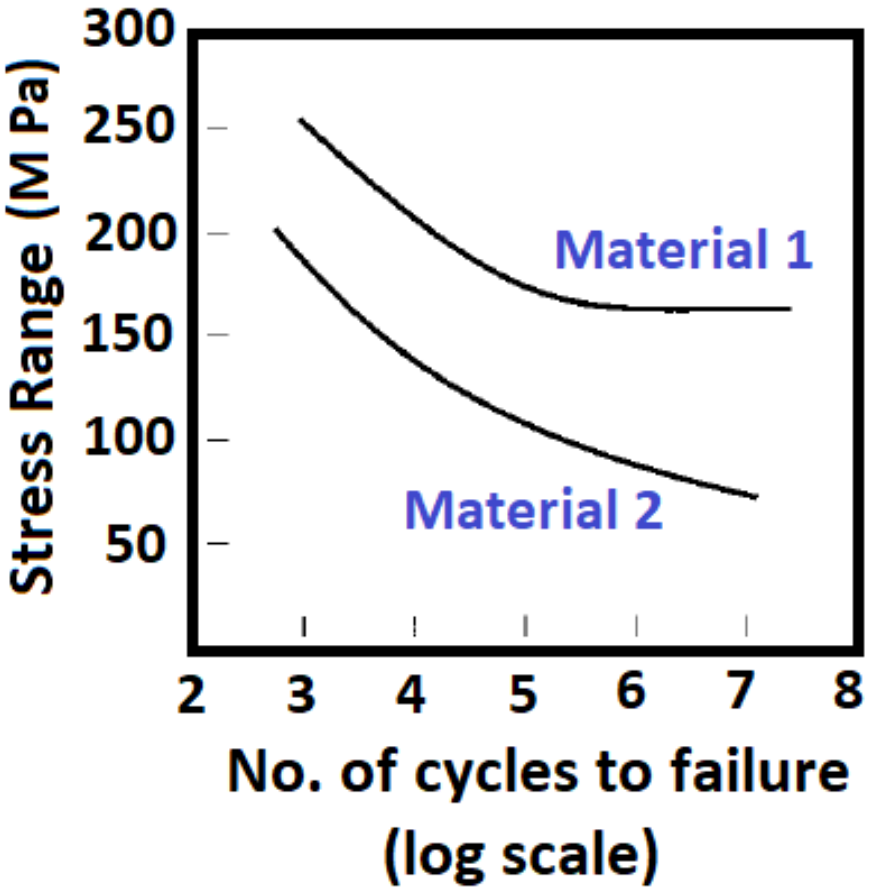

Figure 1.2 SN curve

failure [5]. This technique was used before the microstructural understanding of fatigue process and was based on empirical means. By keeping a safety margin of stress, the fatigue life of the component/material can be easily found using SN curve for that component/material. The major problem with this approach is the statistical variability. That is, we need to consider many specimens of the material tested at different loading levels to define the SN curve with statistical confidence. Hence a technique which can detect the level of fatigue in real-time is greatly beneficial.

1.1.3 Crack growth rate

Predicting crack growth rate during the process of cyclic loading on the material is important, so that the material can be replaced before the crack reaches it's critical size. Paris Law is a mathematical relation which relates the crack growth rate to the stress intensity factor [3].

Experimental evidence shows that the growth rate of the crack has a correlation with cyclic

variation in the stress intensity factor and is given by Paris Law expressed in (1.1),

$$\frac{da}{dN} = A\,\Delta K^{\mathrm{m}} \tag{1.1}$$

Here $\frac{da}{dN}$ is the fatigue crack growth rate per cycle, $\Delta K = K_{\max} - K_{\min}$ is the stress intensity factor range during the cycle, A and m are material parameters that depend on the material, temperature, stress ratio, environment and frequency. Hence, at the material scale, once a fatigue crack is initiated, we can approximately calculate the number of loading cycles before which it reaches the critical size. This gives us an estimate of the remaining fatigue life of the material. However, if the macro defect/crack has not been developed, we cannot apply this approach and there is a need for an alternative solution.

1.2 Microstructural phenomenon in steel

One plausible alternative to tackle the above problem is to look into changes in the material properties, as the material is fatigued. This is where nondestructive evaluation (NDE) can play a major role because it can be used to evaluate the properties of a material, component, or system [6]. The high sensitivity and broad capability of NDE techniques will be an added advantage in determining the severity of material property changes caused by fatigue. The material under consideration in this research work is martensitic grade stainless-steel, which is a ferromagnetic material. A brief review on the phase transformation in steel, magnetization and effect of stress on the magnetic properties of steel is discussed next.

1.2.1 Phase transformation in steel

Pure iron is extremely soft and cannot be used in structural applications. However, when a small percentage of alloying element is added to it, the resulting mixture is a solid solution or a compound. Carbon is a very unique alloying element in iron. The reason is that, addition of carbon in iron produces steel which opens a diversity regarding the microstructure and mechanical properties in an economic way. In iron-carbon solid solution, the carbon atom usually occupies the interstitial site (the gap between the iron atoms in the crystal structure).

Phase is defined as a macroscopic homogeneous body of matter. A solid consists of a periodic

array of atoms which is called a crystal structure. Steel is composed of small crystalline particles which are called grains and each grain has a periodic arrangement of atoms, i.e., the crystal structure. If all grains have the same crystal structure and the only difference between them is their orientation, then we regard it as a single-phase material. This means that dissimilar periodic array of atoms change the micostructure and make a different phase. Hence, there can be several phases with different crystal structures in steel like ferrite, austenite and martensite. The austenite phase is non-magnetic in nature, whereas the martensite is magnetic.

Stainless steels are commonly divided into five groups, depending on the specific amounts of alloying elements, which control the microstructure of the alloy. They are austenitic (face centered cubic crystalline structure), ferritic (body centered cubic crystalline structure), martensitic (body centered tetragonal crystalline structure), duplex (contains approximately equal amounts of ferritic and austenitic phases) and precipitation hardening (contains austenitic or martensitic phases in aged condition). In face centered cubic crystalline structure, atoms are located at each of the corners and the centers of all the cubic faces. But in a body centered crystalline structure, one atom is located in the center of the unit cell in addition to the corner atoms. Each group of stainless steel has its own advantage and is used as per the requirement of a particular application.

Martensitic steel is a type of stainless steel that is known for its strength, corrosion resistance, and durability. These qualities make martensitic steel a good choice for a variety of applications such as fabrication of turbine parts, mechanical valves etc. When the austenite is cooled at a critical rate (typically faster than 86 degrees F per second), the crystal structure gets distorted and strained to form a body-centered tetragonal (BCT) crystalline structure, forming a hard microstructure phase called martensite. Martensitic stainless steels, such as types 403, 410, 410NiMo and 420, are similar in composition to the ferrite group, but contain a balance of Carbon and Nickel vs. Chromium and Molybdenum.

1.2.2 Magnetic Domains and Magnetization

Steel is composed of small crystalline particles which are called grains and each grain has a periodic arrangement of atoms. Each atom has a magnetic moment and thus contributes to the

overall magnetization (**M**) of steel. **M** is defined as the magnetic moment per unit volume of steel and is given as,

$$M = \frac{\sum m}{V} \tag{1.2}$$

where m refers to the individual magnetic moment of an atom and V refers to the total volume of steel. The value of **M** is constant and does not depend on the material's size.

The magnetic moments inside each grain are aligned in the same direction and together represent a magnetic domain. Hence the magnetic domain is a region within the steel (or any magnetic material) in which the magnetization is in a uniform direction. The direction of magnetic moments may differ from one magnetic domain to the other and are usually random in nature. This results in a net zero magnetization without the application of an external magnetic field. When an external magnetic field is applied, the direction of domain magnetic moment aligns in the magnetic field direction, resulting in a non-zero net magnetization of steel. Figure 1.3 shows the domains (including direction of magnetic moments) with and without application of an external magnetic field. Red arrow indicates the direction of external magnetic field.

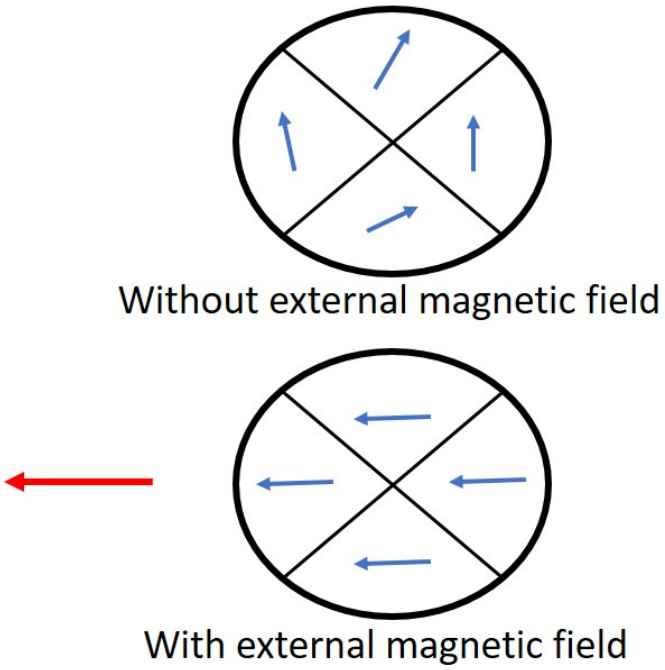

Figure 1.3 Domains with magnetic moments in steel

1.2.3 Effect of stress on magnetic properties of steel

When a ferromagnetic material like martensitic stainless-steel (MSS) is exposed to a magnetic field, its dimension tends to change. The effect responsible for change in dimension is known as magnetostriction.

The fractional change in length, also referred as magnetically induced strain is given by λ expressed in (1.3),

$$\lambda = \frac{\Delta l}{l} \tag{1.3}$$

Here Δl is the change in length due to magnetostriction and l is the original length of MSS material. Saturation magnetostriction (denoted as λ_s) is the value of λ measured at magnetic saturation. λ_s is typically very small and is of the order 10^{-5} in magnetic materials [7]. The magnetically induced strain depends on extent of magnetization in the material and hence on the applied magnetic field intensity $H(A/m)$.

Even though the magnetostrictive strain is very small in magnetic materials, the application of mechanical stress can change the domain structure. This can have a significant effect on the magnetic material properties like permeability and remanence. The effect of mechanical stress on the magnetization behavior of magnetic materials is referred to as magneto-mechanical effect.

In perspective of the research work, fatigue happens because of application of stress on the material and stress in-turn alters the magnetic material properties. Hence it can be concluded that, fatigue ultimately changes the magnetic properties of MSS materials and magnetic NDE techniques will be most-suitable for this application. The following section details and summarizes the existing NDE techniques for fatigue detection.

1.3 Existing NDE methods

Existing NDE methods for fatigue detection include optical [8, 9], acoustic [10, 11], magnetic [12, 13] and thermal [10, 14] and have been applied in metals as well as composites [15–18]. Typically, fatigue affects the electrical impedance and further alters the magnetic properties of materials due to changes in microstructure [19, 20]. Electrical and magnetic NDT methods are

sensitive to the corresponding characteristics and play a major role in detecting fatigue at an early stage, i.e., before the macro crack initiates.

In this area, Magnetic Barkhausen Noise (MBN) has shown promise in fatigue detection and evaluation in carbon steel [21], ferrite steel [22] and martensitic stainless steel [23]. The Barkhausen effect consists of discontinuous changes in magnetic flux density, known as Barkhausen jumps [24]. MBN is a promising electromagnetic nondestructive technique used to characterize ferromagnetic materials and is sensitive to changes in the material microstructure [21]. The MBN signal features is proved to have a linear relationship with the carbon content of steel [21]. MBN technique has also been used particularly in classification of martensitic steel based on fatigue [23]. Principal component analysis (PCA) and probabilistic neural network (PNN) classifies the martensitic stainless-steel samples based on the percentage of remaining fatigue life with 79% classification accuracy [23].

Since the material under consideration is ferromagnetic, a magnetic NDE technique which takes into account local changes in the hysteresis in relation to fatigue is relevant in this scenario. In this regard, the non-linear eddy current (NLEC) technique (i.e., a magnetic NDE technique) was applied on steel to characterize automotive bearing assemblies with challenging geometries and has shown a classification accuracy of approximately 95.7% [25].

Some of the other NDE methods used for material characterization are Magneto-Acoustic Emission (MAE), the 3MA (Micromagnetic Multiparameter Microstructure and Stress Analysis) [26] and Ultrasonic techniques (UT) [27]. A considerable amount of research has been carried out regarding material aging at Fraunhofer Institute – IZFP [27]. The MAE technique is sensitive to the environmental noise and has a low signal to noise ratio. But, MAE signal only responds to domains that are at an angle to the applied stress [21].

This research work investigates the feasibility of magnetic NDE techniques, MBN and NLEC for garnering information related to the fatigue condition in martensitic grade stainless-steel components. The NLEC technique excites the non-linear modes in the sample and measures the amplitude of harmonics. The ratio of harmonic amplitudes provides interesting information related to fatigue

in the steel sample under test. The MBN technique measures the discontinuous changes in magnetic flux density. The features obtained from these measurements provide interesting information related to fatigue in the steel sample under test. The following chapter describes more information on the physical principles for both MBN and NLEC techniques.

Some parts of this doctoral thesis are adapted from [28] ("Fatigue Detection and Estimation in Martensitic Stainless-Steel Using Magnetic Nondestructive Evaluation Technique" by B. B. Shenoy, Z. Li, L. Udpa, S. Udpa,Y. Deng, and T. Seuaciuc-Osorio, Quantitative Nondestructive Evaluation, vol. 85529, p. V001T14A001, American Society of Mechanical Engineers 2021, https://doi.org/10.1115/QNDE2021-74657. Copyright © 2021 by ASME) and [29] ("Magnetic Barkhausen Noise Technique for Fatigue Detection and Classification in Martensitic Stainless-Steel" by B. Basti Shenoy, Z. Li, L. Udpa, S. Udpa, Y. Deng, and T. Seuaciuc-Osorio, Journal of Nondestructive Evaluation, Diagnostics and Prognostics of Engineering Systems, vol. 5, no. 4, p. 041010, 2022, https://doi.org/10.1115/1.4055992. Copyright © 2022 by ASME).

CHAPTER 2

PHYSICAL PRINCIPLES OF MBN AND NLEC

This chapter describes the physical principles of MBN and NLEC techniques in detail and also provides information regarding the experimental set-up used for both techniques.

2.1 Magnetic Barkhausen Noise Technique

Magnetic Barkhausen Noise (MBN) is a NDE technique, which is sensitive to the changes in material microstructure and stress state of the material. This technique has been widely used to investigate ferromagnetic materials [30–33], due to the link between MBN signal and the material's mechanical properties.

The Barkhausen effect consists of discontinuous changes in magnetic flux density, known as Barkhausen jumps [24], as shown in Figure 2.1. These are caused by sudden irreversible motion of magnetic domain walls, when they break away from pinning sites due to changes in the applied external magnetic field [34]. This results in a noise, which is known as the Magnetic Barkhausen Noise (MBN) and it is correlated to the material microstructure as discussed in [21, 35]. Figure 2.2. shows a typical MBN time domain signal obtained from the experimental set-up discussed in the next section.

In a crystalline material such as martensitic stainless-steel, whenever stress is applied, a dislocation travels through the lattice [28]. The movement of dislocations results in plastic deformation of the material. Thus, the material is fatigued. This elongates the grain size, which is a microstructure feature of the material. Changes in grain size will result in changes in the material properties, such as conductivity and permeability. Hence, features obtained from the MBN signal contains information which allows the separation of samples having different levels of fatigue.

2.1.1 MBN system details

The block diagram of the experimental set-up is shown in Figure 2.3. The function generator is used to provide the sinusoidal excitation voltage, which is then amplified using the power amplifier. The output of power amplifier is connected to the MBN sensor. The MBN sensor consists

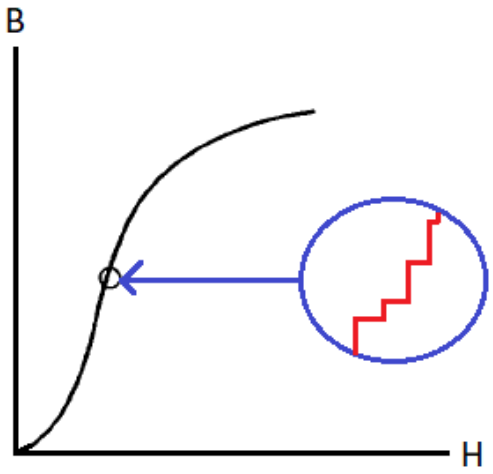

Figure 2.1 Magnetic flux density changes due to Barkhausen effect

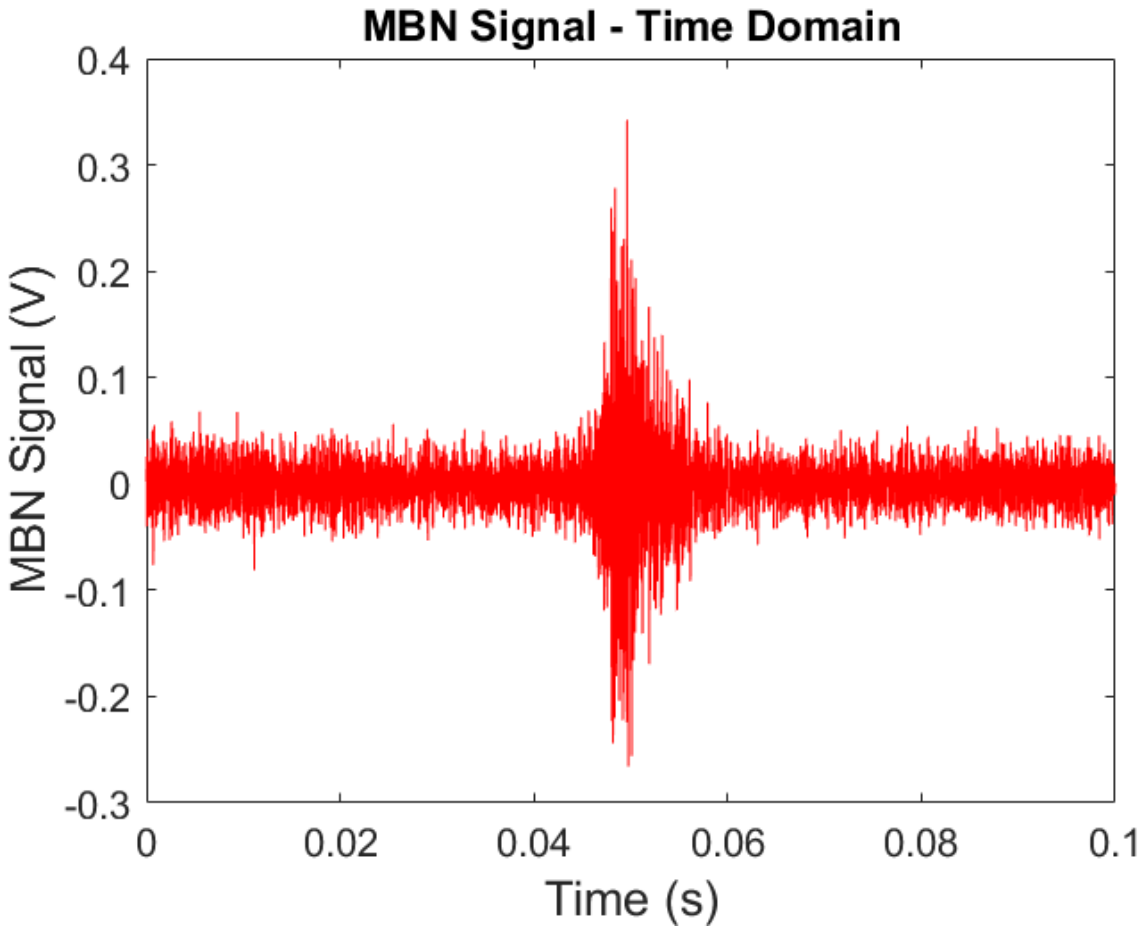

Figure 2.2 Time domain MBN signal

of a U-shaped magnetic core, an excitation coil (which generates the AC magnetic field) and a volumetric pick-up coil (which picks up the generated MBN signal from the stainless-steel sample).

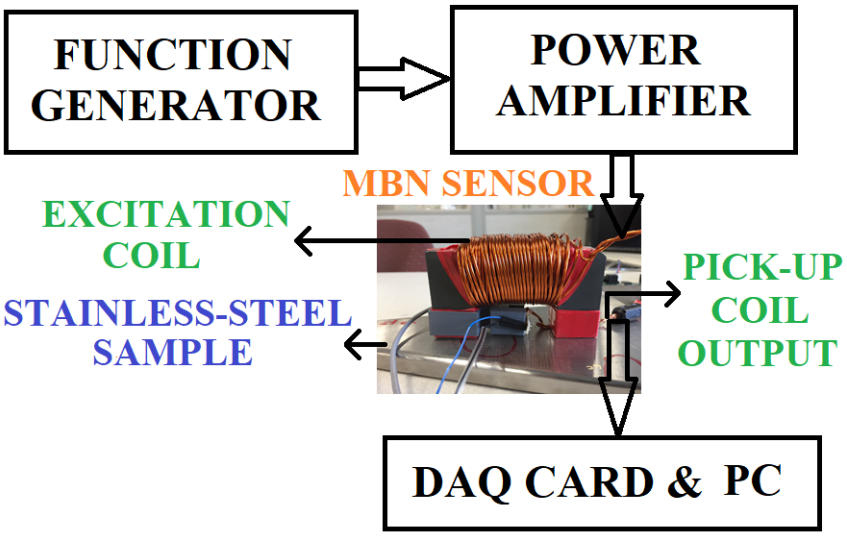

Figure 2.3 Block diagram of MBN experimental set-up

Table 2.1 MBN system details

Function generator output voltage	Sinusoidal signal 4 V (peak to peak)
Frequency of function generator output (Hz)	5
Power amplifier gain (V/V)	10
Excitation coil turns	80
Pick-up coil turns	400
Sampling rate (samples per second)	200,000

The pick-up coil is housed in a holder attached to the magnetic core. DAQ Card and PC are used to acquire and then process the generated MBN signal from the stainless-steel sample. The system details are outlined in Table 2.1.

2.2 NLEC Technique

This section provides a basic introduction to the physical principles of linear and non-linear eddy current techniques.

2.2.1 Conventional ECT

Eddy current testing (ECT) is widely used in NDT of metal components, due to its non-contact operation, rapid inspection capability and sensitivity to defect detection [36].

Conventional (linear) ECT uses electromagnetic induction to detect and characterize surface and sub-surface defects in conductive materials [37]. Here, the eddy current probe is excited using time harmonic excitation. The time harmonic magnetic field induces eddy currents in the sample. In the presence of a defect (i.e., a surface crack), the induced currents are redistributed, as shown in Figure 2.4., resulting in a change in the eddy currents which alters the induced magnetic field and hence the impedance of the probe coil. Hence, by monitoring the impedance changes in the coil, we can detect defects in the material of interest. ECT works only on non-ferromagnetic conducting materials and the operation is largely linear. Ferromagnetic materials can be inspected using the non-linear operation of the ECT technique.

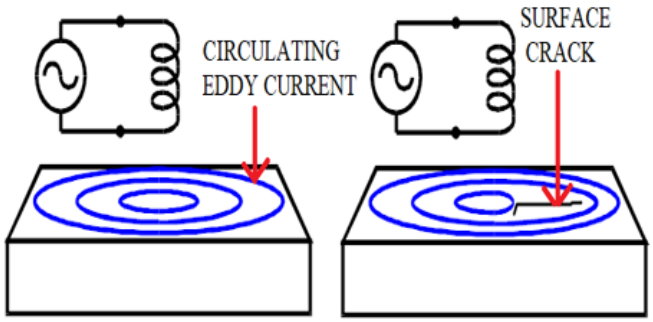

Figure 2.4 Eddy Current in material with and without surface defect

2.2.2 Non-linear eddy current technique

In non-linear eddy current (NLEC) technique, a strong periodic excitation magnetic field is applied forcing the material to operate in the non-linear region of its magnetization characteristic, as shown in Figure 2.5. This results in response signals that contain higher order harmonic frequencies.

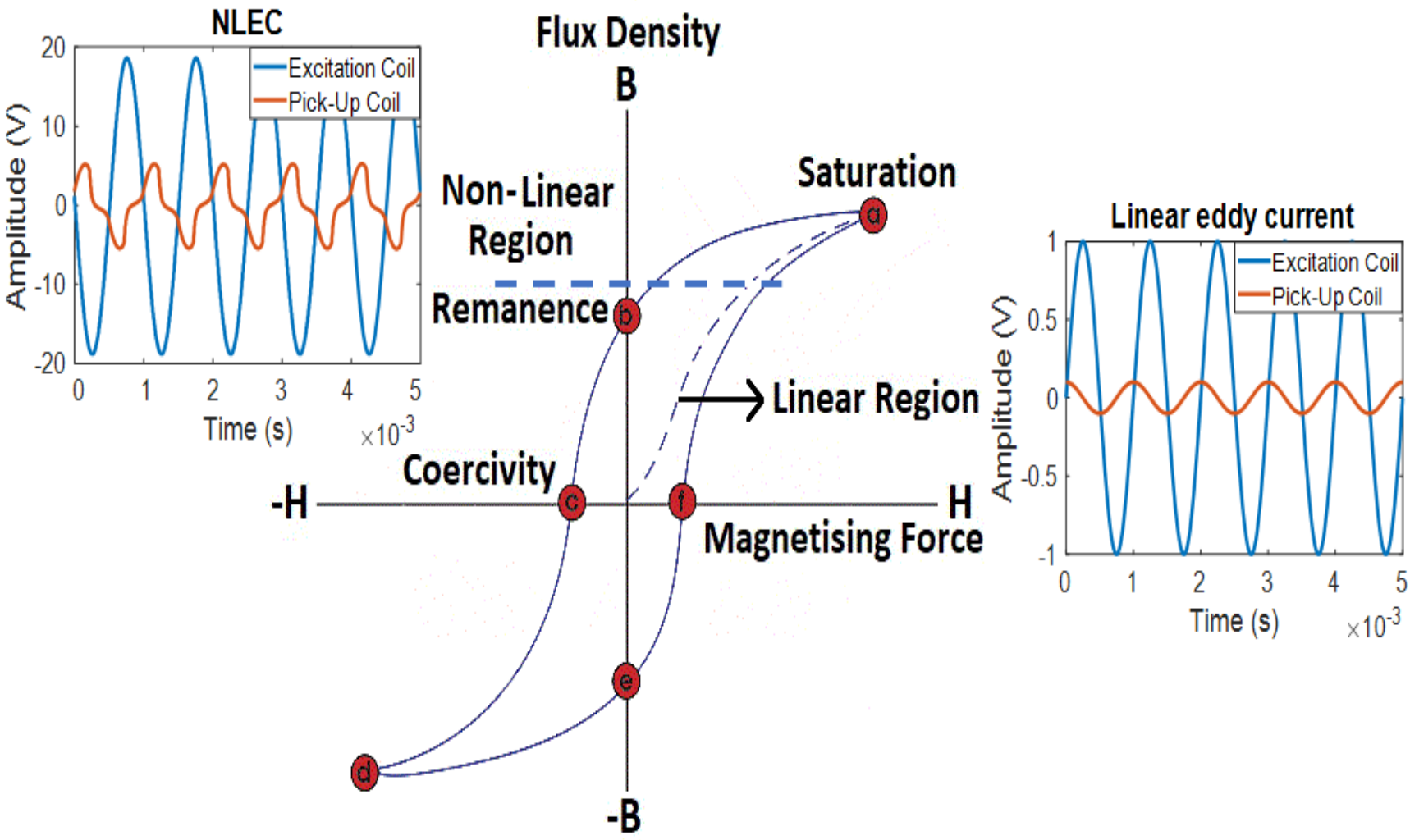

Figure 2.5 B-H curve with linear and non-linear eddy current response plots

Typical excitation and response signals for linear eddy current and NLEC techniques are also shown in Figure 2.5. It can be observed that the linear eddy current output response (the waveform in orange) is sinusoidal and of the same frequency as that of the excitation current, but with a different amplitude and phase.

On the other hand, NLEC output response has higher order harmonic frequencies when compared to the excitation signal. The non-linear eddy current technique was successfully applied to evaluate the case hardening profile of automotive bearing assemblies, in nondestructive evaluation laboratory (NDEL) at Michigan State University [25]. Bruchwald. O et al. [38] designed a customized high temperature resistant eddy current sensor at Institut für Werkstoffkunde (IW), Leibniz University Hannover and studied the higher order harmonics to quantify the material transformation and microstructure evolution in steel. Also, L. V. Fricke et al. performed a higher order harmonic analysis on the eddy current signal to differentiate between the microstructural constituents formed in steel [39].

In a crystalline material (like the Martensitic stainless-steel (MSS)), when stress is applied, a dislocation travels through the lattice. The movement of dislocations result in plastic deformation of the material. This elongates the grain and increases its size, which is a microstructure feature of the material. Changes in grain size will result in changes in the material properties, such as conductivity and permeability. Hence features of the NLEC response signals contain information that allows us to separate the MSS samples at different levels of fatigue.

2.2.3 NLEC system details

Figure 2.6. shows the block diagram of NLEC experimental set-up along with schematic of connections of the NLEC sensor [40]. The function generator is used to generate a low frequency sinusoidal signal which is further amplified using a power amplifier and given to the NLEC sensor. The NLEC sensor consists of a measurement probe (MP) and a reference probe (RP), as shown in Figure 2.6. Each probe consists of one excitation coil and one pick-up coil. The two excitation coils (E1 and E2) are connected in series and the two pick-up coils (P1 and P2) are connected in a differential configuration. In each of the probes (MP or RP), the excitation coil is wound

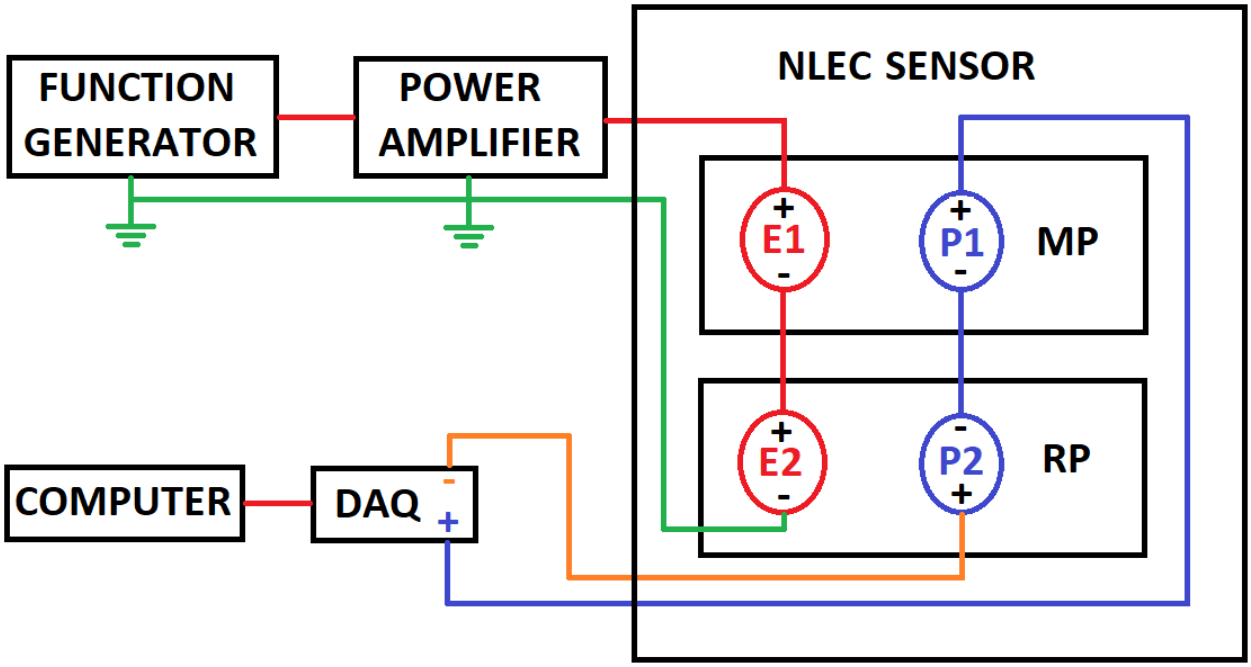

Figure 2.6 Block diagram of NLEC experimental set-up

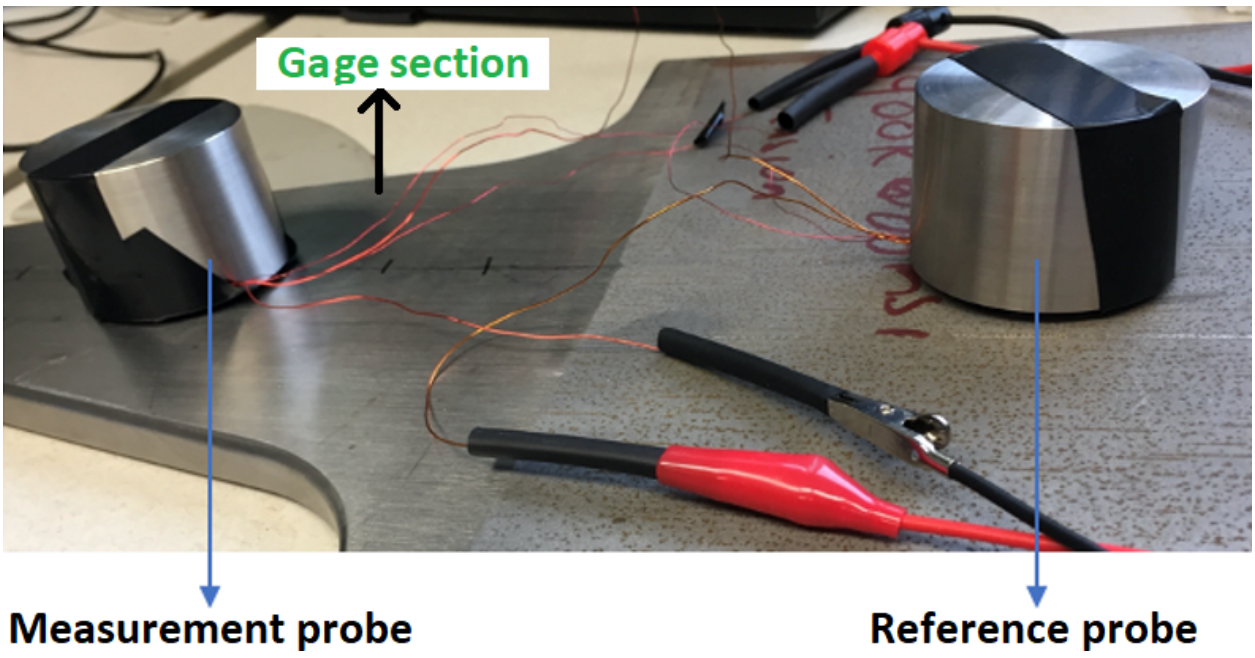

Figure 2.7 NLEC sensor mounted on the EPRI sample

around the pick-up coil with the help of a 3-D printed bobbin and a custom designed metal pot core. The pick-up coils collect the NLEC signal from MSS sample under test and gives it to the data acquisition (DAQ) set-up, i.e., using the NI DAC board and then to the computer for further data processing. The measurement probe is placed on the gage section of the MSS sample and

the reference probe is placed as shown in Figure 2.7. The experimental parameters are outlined in Table 2.2. American wire gauge is abbreviated as AWG.

Table 2.2 NLEC experimental parameters

Function generator output	Sinusoidal signal of 14 V (peak-peak) at 17 Hz
Power amplifier gain	10
Excitation coil turns & AWG	600 & 32 AWG
Pick-up coil turns & AWG	1200 & 26 AWG
Sampling rate (samples per second)	10,000

CHAPTER 3

RESEARCH PROBLEM

3.1 Research problem representation

Overview of the research problem is summarized in Figure 3.1. In the funded research project, martensitic stainless-steel samples (un-cracked) with different loading cycles were first provided by Electric Power Research Institute (EPRI). NDE measurements were then performed. The number

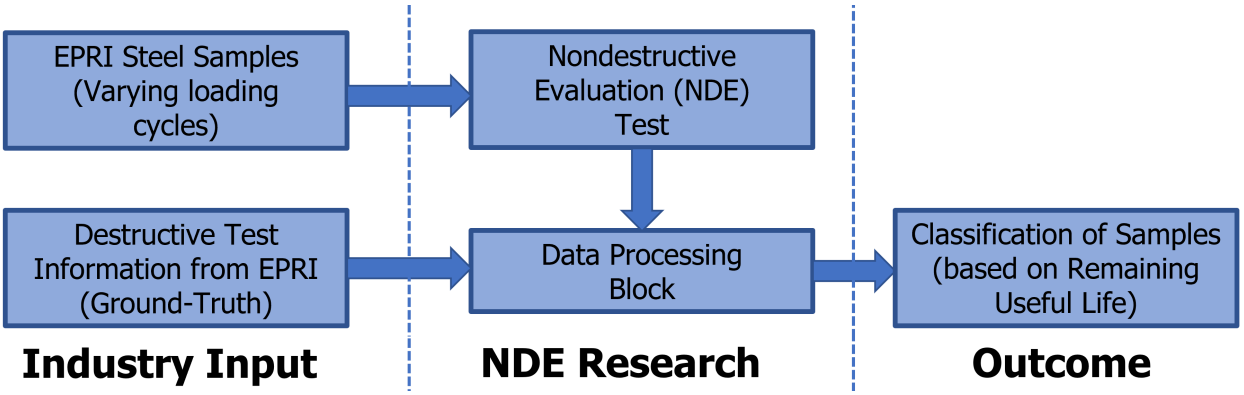

Figure 3.1 Overview of the research problem

of loading cycles were known at the time of NDE measurements. Following this, the samples were loaded further till they developed a crack. The data on additional loading cycles to failure was then provided by EPRI. Details regarding the stainless-steel samples is given in this chapter. Goal of the research work is to classify the stainless-steel samples (having different levels of fatigue) into broad fatigue categories, i.e., low fatigue, mid fatigue, and high fatigue. The contribution of the research work is mainly in developing techniques to classify the samples based on levels of fatigue. The following section describes the database of martensitic stainless-steel samples.

3.2 Sample database

The geometry of a typical martensitic stainless-steel (MSS) sample is shown in Figure 3.2. A set of 16 samples were stressed by applying varying number of loading cycles (0, 150K, 300K, 450K, 600K, 750K, and 900K) and sent to MSU for data collection. These samples were then sent back to EPRI for destructively estimating the remaining useful life, by subjecting them to additional loading cycles till failure or cracking.

Table 3.1 presents two columns for each sample showing number of loading cycles at NDE test and additional cycles to failure which is a measure of remaining useful life (RUL).

RUL of a sample is calculated as,

$$RUL = Loading\ cycles\ at\ failure - Loading\ cycles\ at\ NDE\ test \tag{3.1}$$

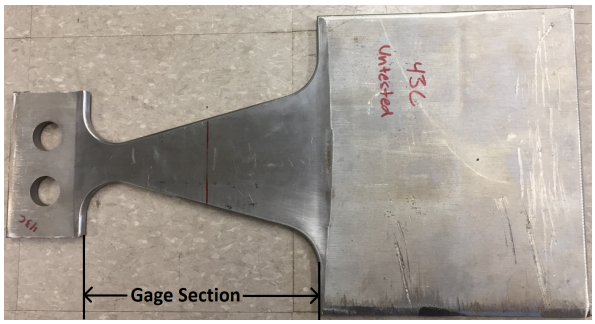

Figure 3.2 Snapshot of a MSS sample provided by EPRI

Table 3.1 EPRI MSS sample database

MSS sample ID	Loading cycles (at NDE Test)	Additional cycles to failure
41C	0	2,889,703
44C	0	1,318,034
30C	450,000	1,103,303
43C	0	690,512
42C	900,000	603,724
7C	150,000	551,901
37C	900,000	514,878
9C	300,000	493,803
19C	450,000	464,392
46C	450,000	447,380
8C	150,000	352,928
35C	150,000	309,868
32C	450,000	306,142
27C	750,000	297,627
21C	600,000	200,007
10C	300,000	127,204

CHAPTER 4

RESULTS AND DISCUSSION

This chapter provides a detailed discussion on the results of both MBN and NLEC techniques.

4.1 Results and discussion on MBN

This section describes the data collection and feature extraction procedure for MBN technique along with a detailed discussion on results.

4.1.1 Data collection and feature extraction

The MBN time-domain data is collected at 19 (18 scanning and 1 reference) points on the EPRI stainless-steel sample, the schematic of which along with the dimensions are shown in Figure 4.1. The MBN sensor is placed on the sample in such a way that, the center of the pick-up coil (which is volumetric) is placed on a particular scanning point (say 1, which is shown in Figure 4.1). The MBN data (voltage signal) is recorded using LabView and then a similar procedure is carried out for the remaining 17 scanning points. The 18 scanning points are chosen on the gage section of the sample (fatigued region) and the reference point is chosen at the center of non-fatigued region. The pick-up coil captures the localized effect of fatigue at a particular scanning point.

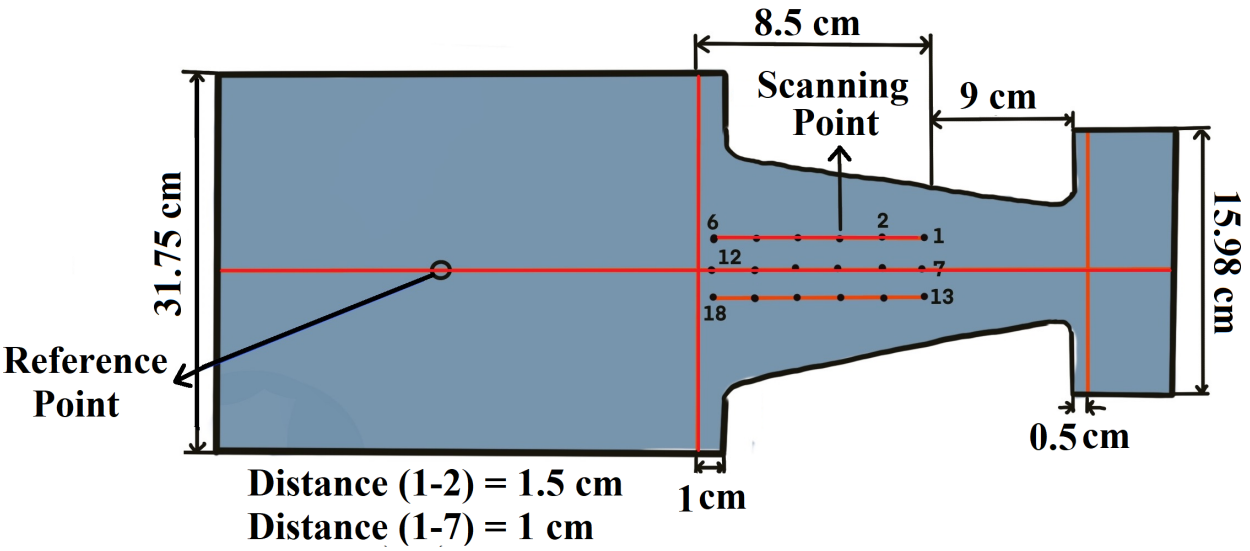

Figure 4.1 Schematic of EPRI stainless-steel sample showing scanning point locations

The MBN data obtained at each scanning point (1 to 18) provides useful information related to the change in permeability due to stress (loading) applied on the sample, which is linked to

the microstructure and fatigue condition of the sample. Many scanning points are chosen and the extracted features are averaged to obtain a better representation for a particular sample, in-terms of fatigue. The goal of the research work (as previously mentioned) is to classify the 16 samples (in Table 3.1) into broad fatigue categories, i.e., low fatigue, mid fatigue, and high fatigue based on MBN signal features and RUL.

The upper profile of the MBN signal shown in Figure 4.2. is fitted by using a mixture of two Gaussian distributions. This provides a way to obtain the time domain MBN signal features shown in Figure 4.2. The time domain features such as MBN signal peak (MP), Full width at half maximum (FWHM) and Difference between peaks of Gaussian fitted curve 1 and 2 (DBP) are related to the microstructure of the material [23].

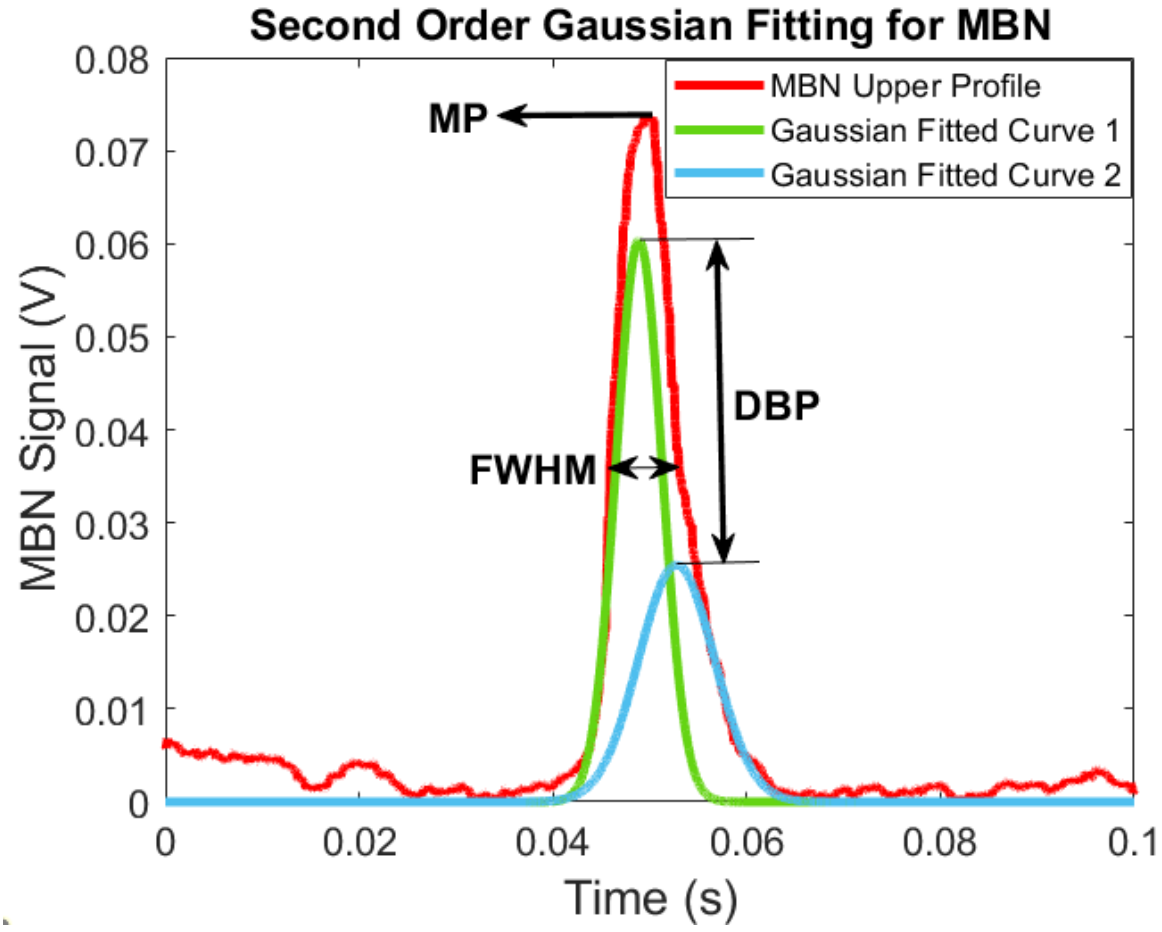

Figure 4.2 Gaussian fitting of MBN signal showing time domain features

The frequency spectrum of the MBN signal provides two more features, i.e., Maximum fre-

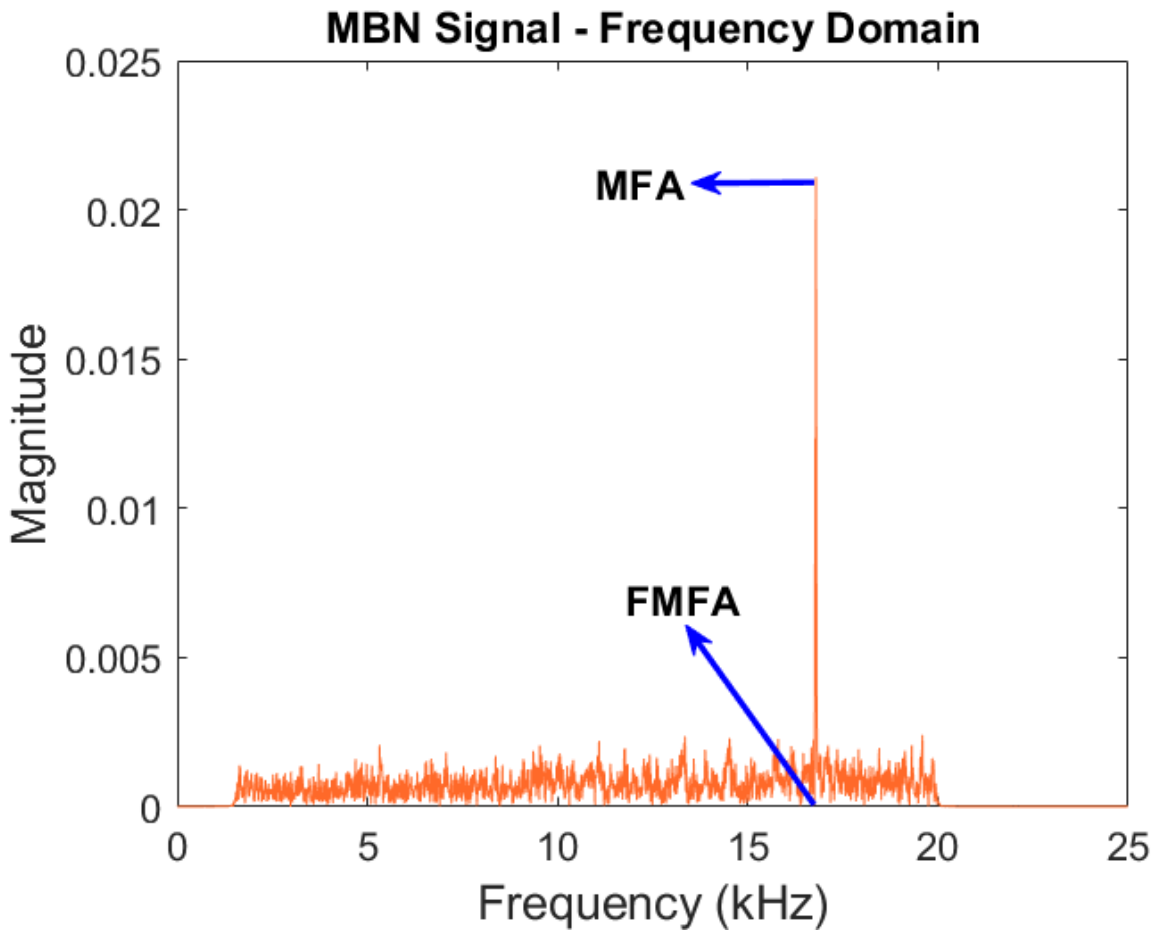

Figure 4.3 Frequency spectrum of MBN signal showing frequency domain features

quency spectrum amplitude (MFA) and Frequency for maximum frequency spectrum amplitude (FMFA) as shown in Figure 4.3. Another MBN signal feature, i.e., MBN signal energy is related to grain boundary misorientation angle that influences the arrangement of magnetic domains along the boundary [34]. Each feature shows a variation across the entire EPRI sample database.

The normalized feature (NR) for each sample is given as,

$$NR_{jk} = \frac{\sum_{i=1}^{18} A_{ijk}}{18 * R_{jk}} \tag{4.1}$$

where i refers to a particular scan position, ranges from 1 to 18.

j refers to the sample number, ranges from 1 to 16.

k refers to the corresponding feature, ranges from 1 to 6.

A_{ijk} refers to the feature value at a particular scanning point.

R_{jk} is the feature value at reference point for a particular sample.

NR will be used as a representation for each sample while applying the KCA and GA on the MBN features.

4.1.2 Results

The flowchart of the approach used to classify the martensitic stainless-steel (MSS) samples (provided by EPRI) into broad fatigue categories is given in Figure 4.4. Features MP, FWHM,

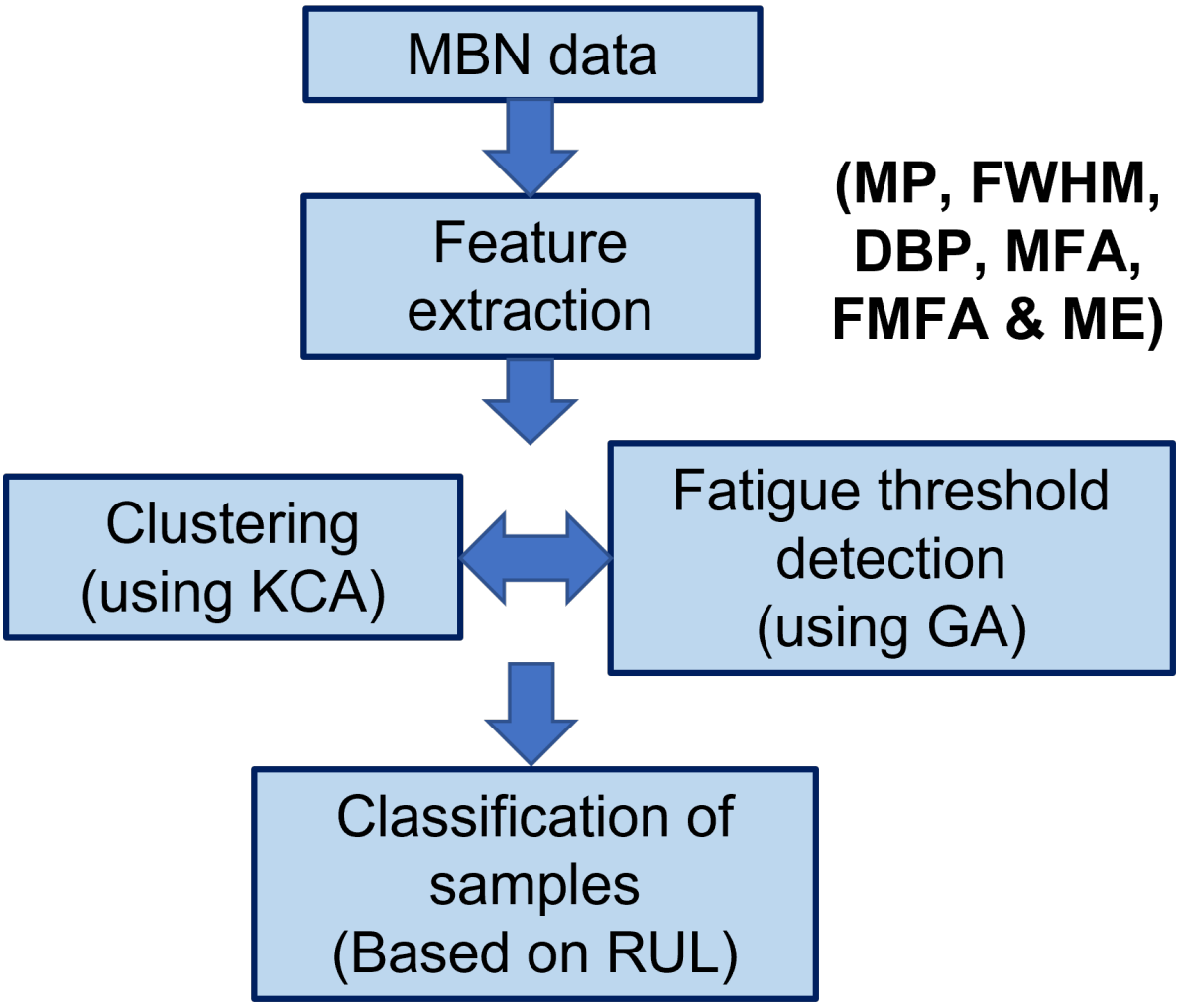

Figure 4.4 Flowchart of the algorithm used to classify MSS samples based on RUL

DBP, MFA, FMFA and ME are extracted from the MBN time domain data. They are utilized to obtain the fifteen combinations (e.g., MP vs FWHM, MFA vs FMFA etc.) in the 2D feature space and then fed as inputs to K-medoids clustering algorithm (KCA) and Genetic algorithm (GA) blocks. The idea here is to investigate the signal features which are most-sensitive to the material's fatigue state. KCA helps to cluster the samples and GA helps to obtain fatigue thresholds with

optimum system performance. The combined output of KCA and GA is the sample classification based on remaining useful life (RUL).

The system performance (SP) proposed to evaluate the sample classification accuracy is quantitatively expressed as,

$$System\ Performance = \frac{C}{T} \tag{4.2}$$

where, C is the number of correctly classified samples and T is the total number of samples.

The feature combination which leads to optimum system performance (i.e., highest number of correctly classified samples) is obtained as FWHM vs DBP and the clustering results are shown in Figure 4.5.

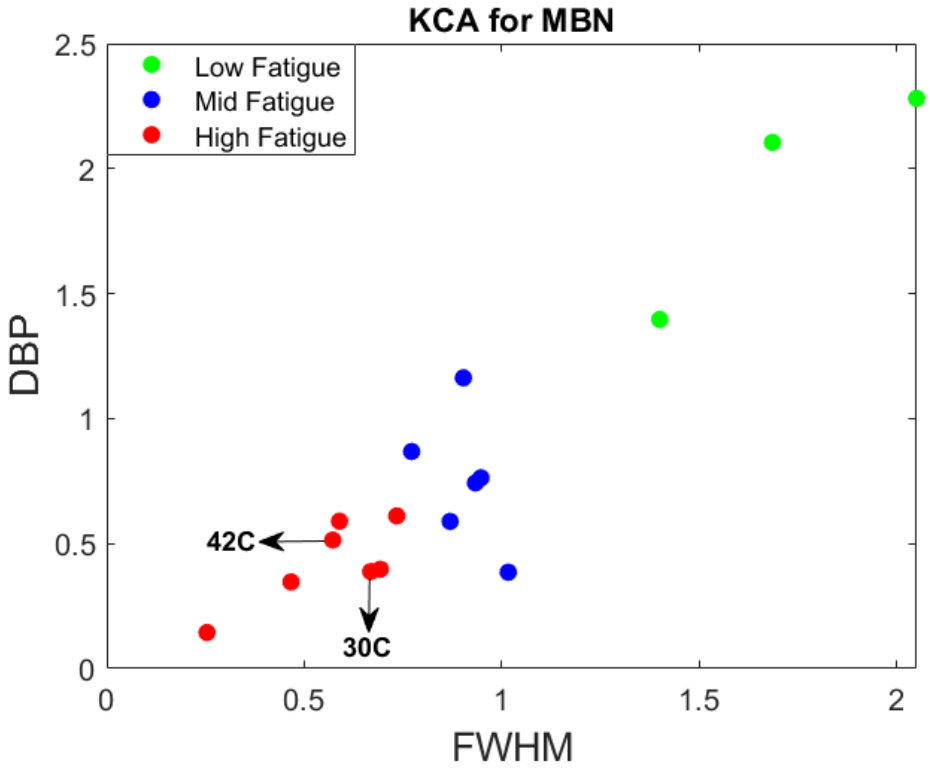

Figure 4.5 Clustering of MSS samples into fatigue categories

The Barkhausen effect is caused by sudden irreversible motion of magnetic domain walls, when they break away from pinning sites due to changes in the applied external magnetic field [34]. FWHM is a common qualifier that changes significantly with distribution of the phase boundary domain wall pinning strength [41]. Also, the DBP extracted from among the gaussian fitting curves

varies linearly with the carbon content on various types of mild steels and is linked with the material microstructure [21]. For comparison, few other feature combinations and their system performance are given in table 4.2. The fatigue thresholds for these combinations are same as obtained in Table 4.1.

The green, blue, and red dots (Figure 4.5.) are the representations for all MSS samples which are categorized as low fatigue, mid fatigue, and high fatigue respectively. After applying KCA and GA on the MBN features, the obtained thresholds for the broad fatigue categories are given in Table 4.1.

Table 4.1 Fatigue thresholds obtained on applying KCA and GA on MBN features

Fatigue category	**Fatigue threshold (based on RUL)**
Low fatigue	≥ 690 K
Mid fatigue	> 310 K to < 690 K
High fatigue	≤ 310 K

Hence, samples having a RUL lesser than or equal to 310 K are classified as high fatigue, between 310 K to 690 K as mid fatigue and above or equal to 690 K as low fatigue.

The classification results based on ground-truth (i.e., after applying the fatigue thresholds in table 4.1 to categorize the samples in table 3.1) is shown in Figure 4.6. Comparing Figure 4.5., and Figure 4.6., it can be observed that there is one mid fatigue sample (42C) which is misclassified as high fatigue and one low fatigue sample (30C) which is also misclassified as high fatigue. The KCA and GA classified fourteen samples (all high fatigue samples, six mid fatigue samples and three low fatigue samples) in different stages of fatigue (i.e., having different RUL) correctly. The system performance is calculated as 87.5% using (4.2).

Discussion on low fatigue threshold selection:

The KCA and GA were applied to MBN features to determine the fatigue thresholds. As discussed earlier, KCA helps to cluster the samples and GA helps to obtain fatigue thresholds with

optimum system performance (i.e., obtain maximum number of correct classifications). Table 4.3 shows the sample database with ground-truth and fatigue classification results.

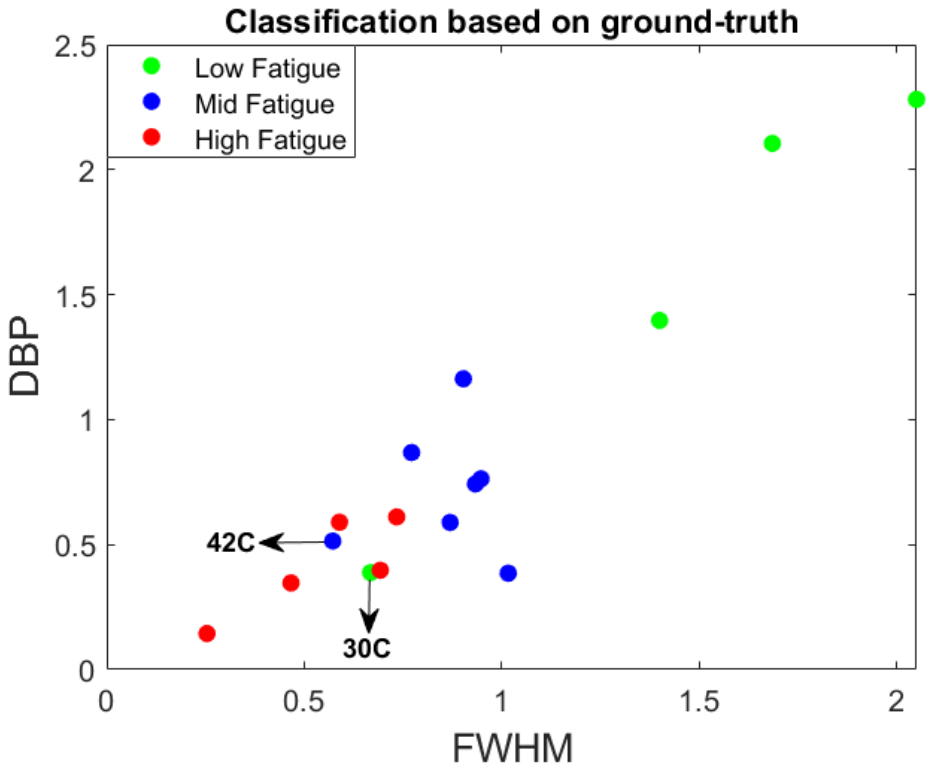

Figure 4.6 Classification results based on ground-truth

Table 4.2 Comparison of other MBN feature combinations

Feature Combination	**System Performance**
FWHM vs DBP	87.50
FWHM vs MFA	81.25
FWHM vs ME	81.25
DBP vs ME	75.00

RUL greater than a fatigue threshold of 690,511 (additional loading cycles to failure) for low fatigue category would result in maximum number of correct classifications as observed from

Table 4.3 Sample database with fatigue classification

Sample ID	**RUL**	**Ground-truth**	**Classification Results**
41C	2,889,703	Low fatigue	Low fatigue
44C	1,318,034	Low fatigue	Low fatigue
30C	1,103,303	Low fatigue	**High fatigue**
43C	690,512	Low fatigue	Low fatigue
42C	603,724	Mid fatigue	**High fatigue**
7C	551,901	Mid fatigue	Mid fatigue
37C	514,878	Mid fatigue	Mid fatigue
9C	493,803	Mid fatigue	Mid fatigue
19C	464,392	Mid fatigue	Mid fatigue
46C	447,380	Mid fatigue	Mid fatigue
8C	352,928	Mid fatigue	Mid fatigue
35C	309,868	High fatigue	High fatigue
32C	306,142	High fatigue	High fatigue
27C	297,627	High fatigue	High fatigue
21C	200,007	High fatigue	High fatigue
10C	127,204	High fatigue	High fatigue

table 4.3. The nearest thousand (floor) which satisfies the above criterion, is used while determining the fatigue threshold value (after obtaining fatigue thresholds using KCA and GA).

Alternatively, since 42C is misclassified, RUL greater than 551,902 for low fatigue threshold would also provide a system performance of 87.5%. This would result in a low fatigue threshold of RUL greater than 552,000. The maximum of 552,000 and 690,000 is chosen as the final low fatigue threshold.

In addition to the above discussion, if we observe table 4.3, there is a lack of data (additional cycles to failure) in the range of 690,000 to 1 million RUL. If there were additional samples in the range, it would be possible to obtain more accurate fatigue thresholds.

In this research work, feasibility of the approach based on available data is presented. Hence, the same approach when applied to a larger data set (i.e., a greater number of samples with varying additional cycles to failure) can provide more accurate fatigue thresholds and classifications.

4.2 Results and discussion on NLEC

This section describes the data collection and feature extraction procedure for NLEC technique along with a detailed discussion on results.

4.2.1 Data collection and feature extraction

NLEC signal is collected at three different positions, on the gage section of the sample (S1-S3 shown in Figure 4.7.). R denotes the position for reference probe at all times during the data collection stage. The measurement probe is moved from S1 to S3 to collect the NLEC signals. The measured NLEC signal (from the NLEC sensor) is given to LabView and MATLAB for further processing. Typical NLEC response signals, obtained from the NLEC sensor, in time domain is shown in Figure 4.8. The waveform in blue is the input signal (function generator output), which is then amplified and given to the excitation coils. The typical NLEC signal (orange), i.e., obtained from differentially connected pick-up coils is shown in Figure 4.8.

The NLEC waveform is an odd signal having a half-wave symmetry. Hence it contains odd harmonic components and zero even harmonic components. The frequency spectrum of the obtained NLEC signal is shown in Figure 4.9. The odd harmonic peaks, i.e., the first, third, fifth

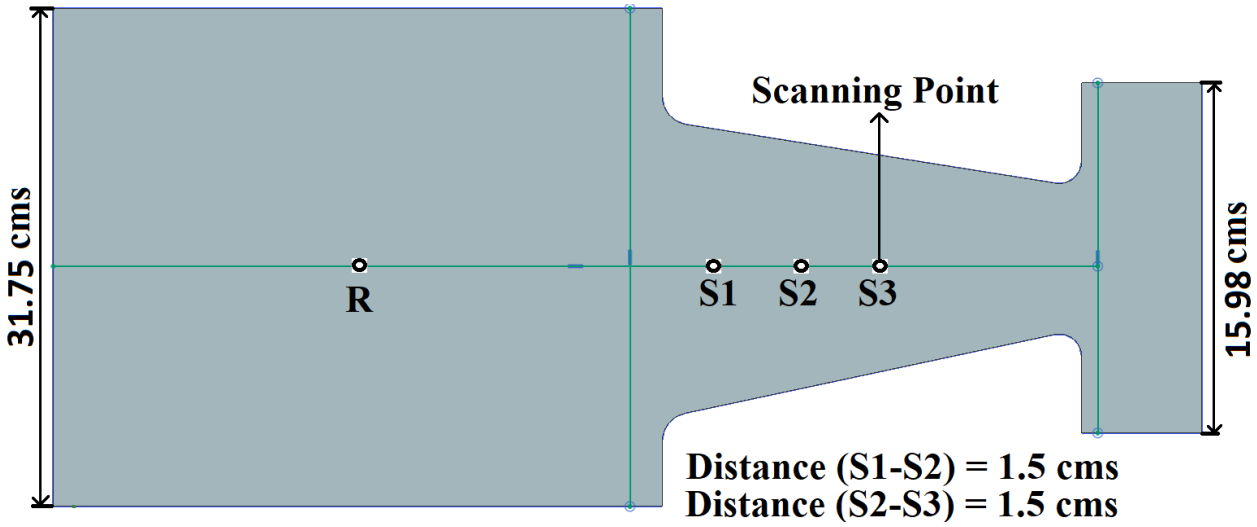

Figure 4.7 Schematic of EPRI sample showing scanning points

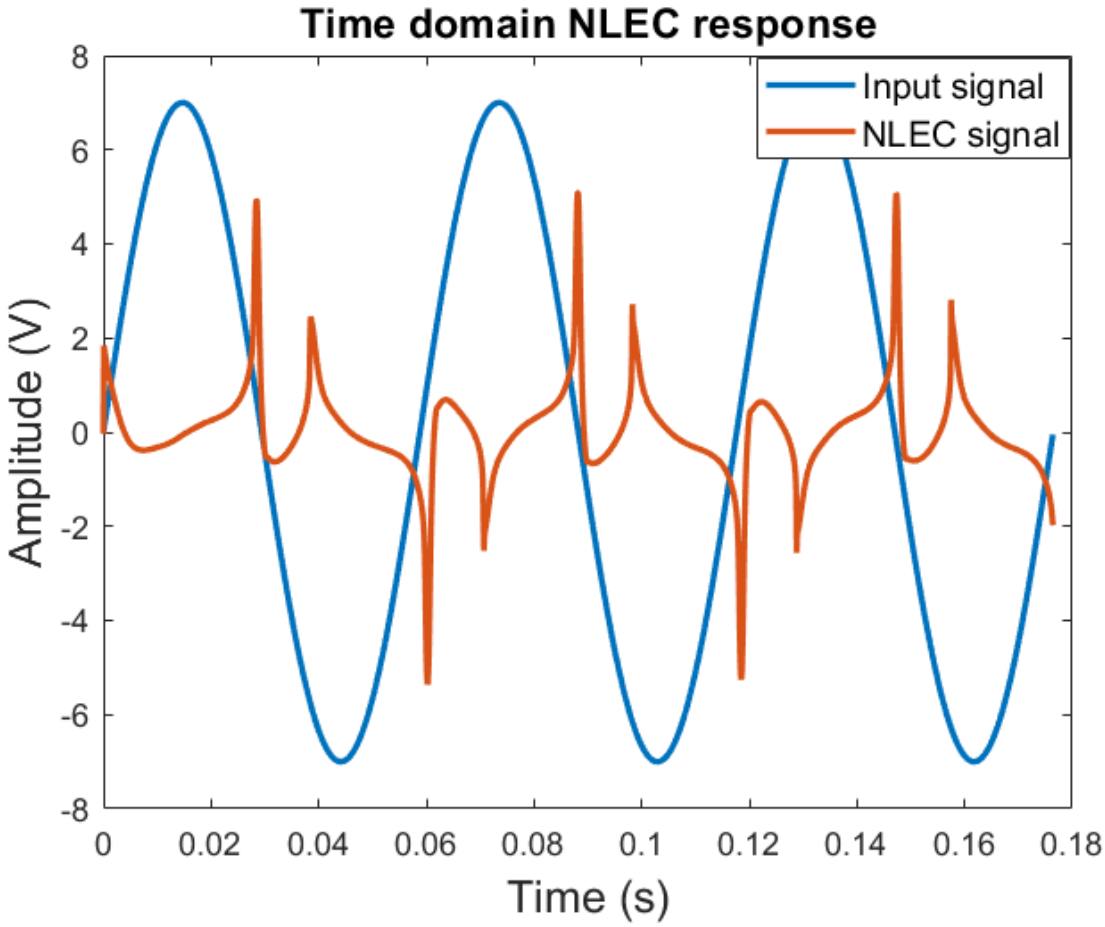

Figure 4.8 Time domain NLEC signal obtained from NLEC sensor

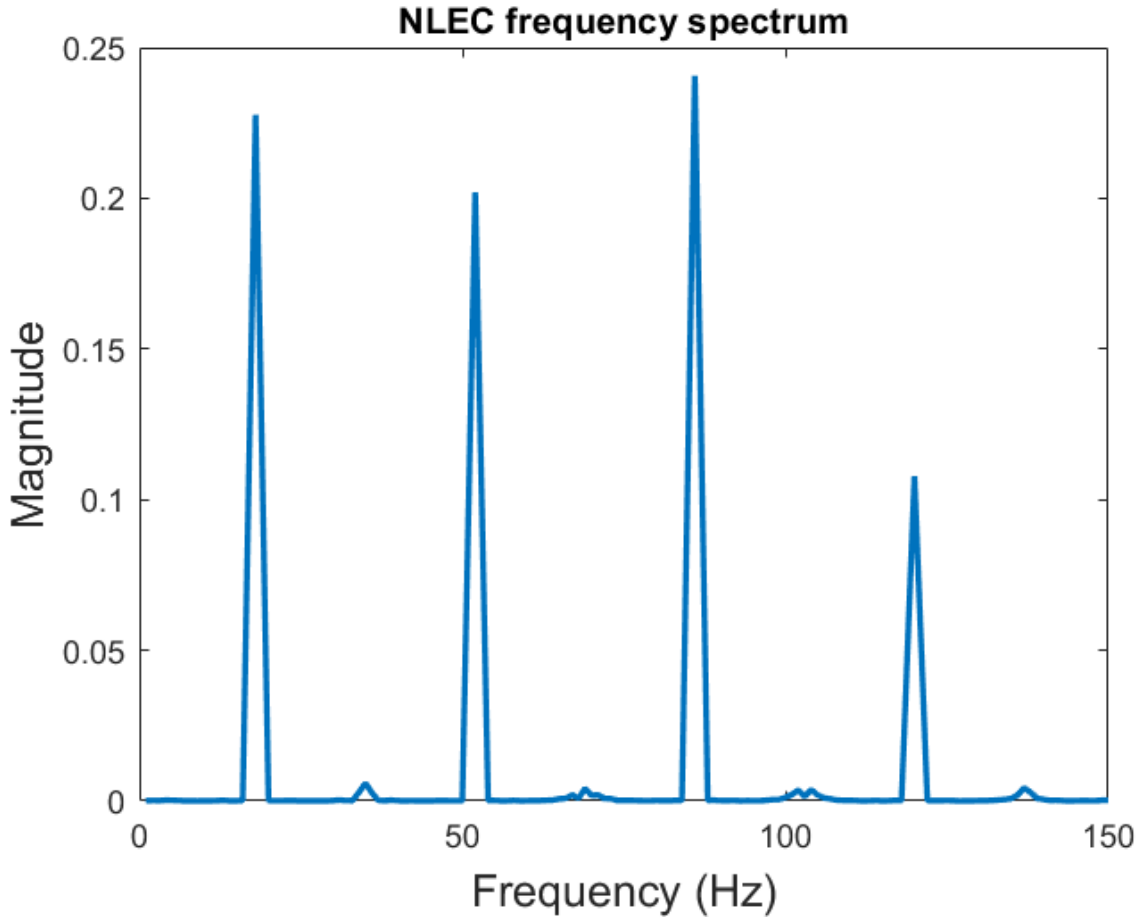

Figure 4.9 Frequency spectrum of the time domain NLEC signal

and seventh odd harmonic peaks can be observed at 17 Hz (fundamental frequency), 51 Hz, 85 Hz and 119 Hz respectively. It can also be observed that, odd harmonic peaks show significantly higher amplitudes and variations, when compared to even harmonic peaks. Features computed from the harmonics are listed in Table 4.4.

The normalized feature value for each sample is obtained by averaging the feature values extracted from each of the three probe positions and is represented as,

$$NR_{ijk} = \frac{\sum_{i=1}^{3} D_{ijk}}{3} \tag{4.3}$$

where i refers to a particular scan position, ranges from 1 to 3.

j refers to the sample number, ranges from 1 to 16.

k refers to the corresponding feature, ranges from 1 to 6.

D_{ijk} refers to the feature value at a particular scanning point.

Table 4.4 NLEC signal features

Feature Set 1 (Odd harmonic peaks)	**Feature Set 2 (Odd harmonic peak ratios)**
First harmonic peak	Third harmonic peak / Fifth harmonic peak
Third harmonic peak	
Fifth harmonic peak	Fifth harmonic peak / Seventh harmonic peak
Seventh harmonic peak	

4.2.2 Results

The flowchart of the algorithm used to classify MSS samples, based on the remaining useful life of the sample, is given in Figure 4.10. NLEC data in time domain is analyzed in frequency domain to extract features, i.e., the odd harmonic peaks (1, 3, 5 & 7, i.e., the first, third, fifth and seventh odd harmonic peaks). Odd harmonic peaks are then used to obtain the possible combinations ($1^{st}/3^{rd}$, $1^{st}/5^{th}$, $1^{st}/7^{st}$, $3^{rd}/5^{th}$, $3^{rd}/7^{th}$ and $5^{th}/7^{th}$) of odd harmonic peak ratios. The odd harmonic peak ratios obtained are then analyzed in the two dimensional feature space using K-medoids clustering algorithm (KCA) [42] and genetic algorithm (GA) [43] to cluster the samples into broad fatigue categories. The six odd harmonic peak ratios are combined, two at a time (i.e., 2D feature space), to obtain fifteen combinations and clustering is done on each of them. KCA and GA then together help to classify the samples into fatigue categories with optimum system performance.

From the physical principles of NLEC operation, the values of the odd harmonics in the received signal are related to local changes in the hysteresis and incremental permeability of the test sample, which in turn relate to fatigue state of the material and associated microstructural changes. The ratios of odd harmonic peaks consider the rate of change of the harmonics, which are sensitive to small changes in the hysteresis curves at different fatigue levels. A six-dimensional clustering in 6D feature space was tried, but the results were not as encouraging as the one obtained using 2D feature space.

The feature combination which leads to optimum system performance (i.e., highest number of

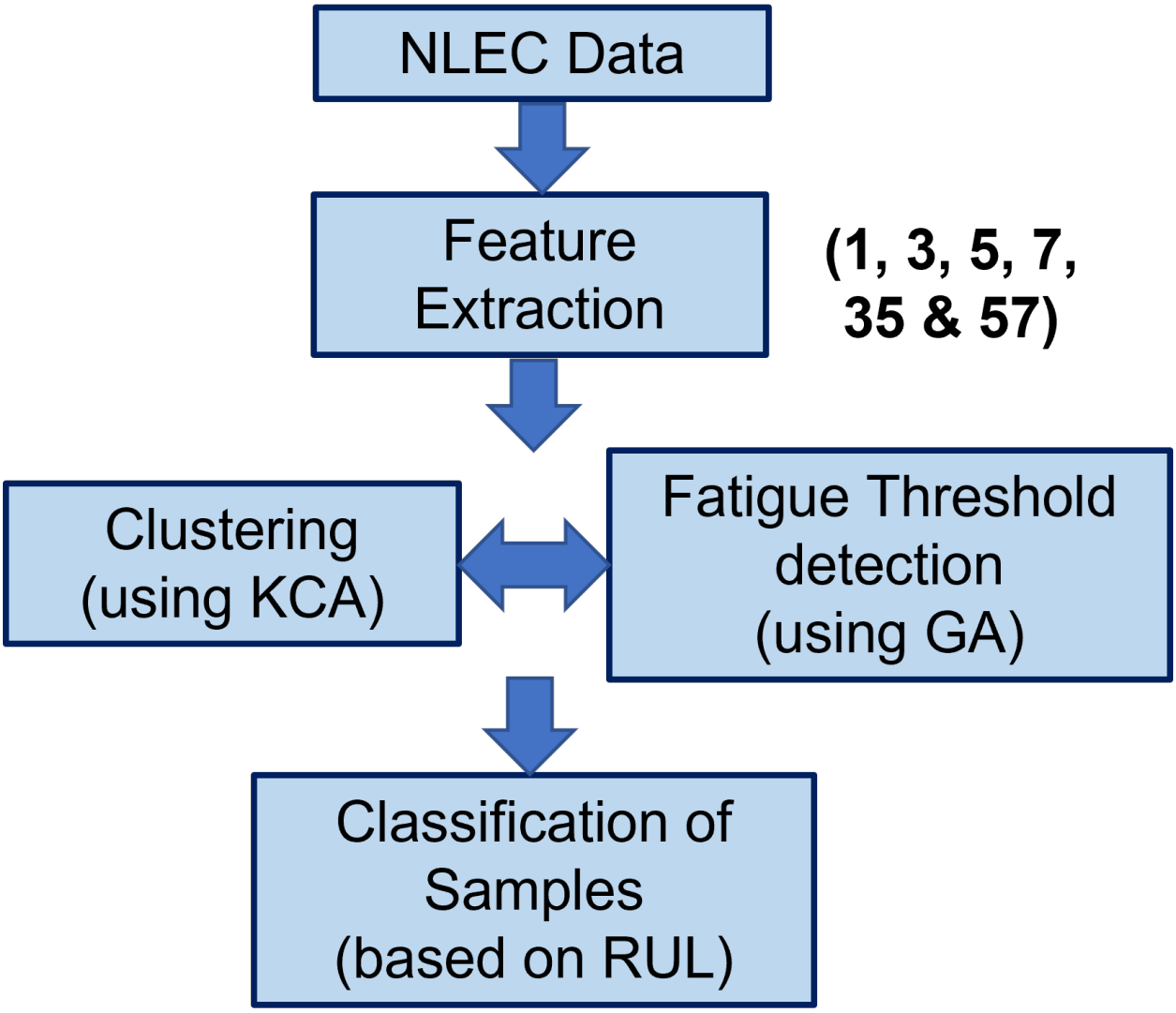

Figure 4.10 Flowchart of the algorithm used to classify MSS samples based on RUL

correctly classified samples) are the odd harmonic peak ratios 35 & 57, i.e., 3rd/5rd and 5th/7th odd harmonic peak ratios.

The system performance to evaluate the sample classification accuracy is quantitatively expressed as,

$$System\ Performance = \frac{C}{T} \tag{4.4}$$

where C is the number of correctly classified samples and T is the total number of samples.

After applying KCA and GA on the frequency domain NLEC features (35 and 57), the thresholds in the feature space for the broad fatigue categories obtained are given in Table 4.5. Hence, samples

Table 4.5 Fatigue thresholds obtained on applying KCA and GA on NLEC features

Fatigue category	**Fatigue threshold (based on RUL)**
Low fatigue	≥ 1.2 M
Mid fatigue	> 310 K to < 1.2 M
High fatigue	≤ 310 K

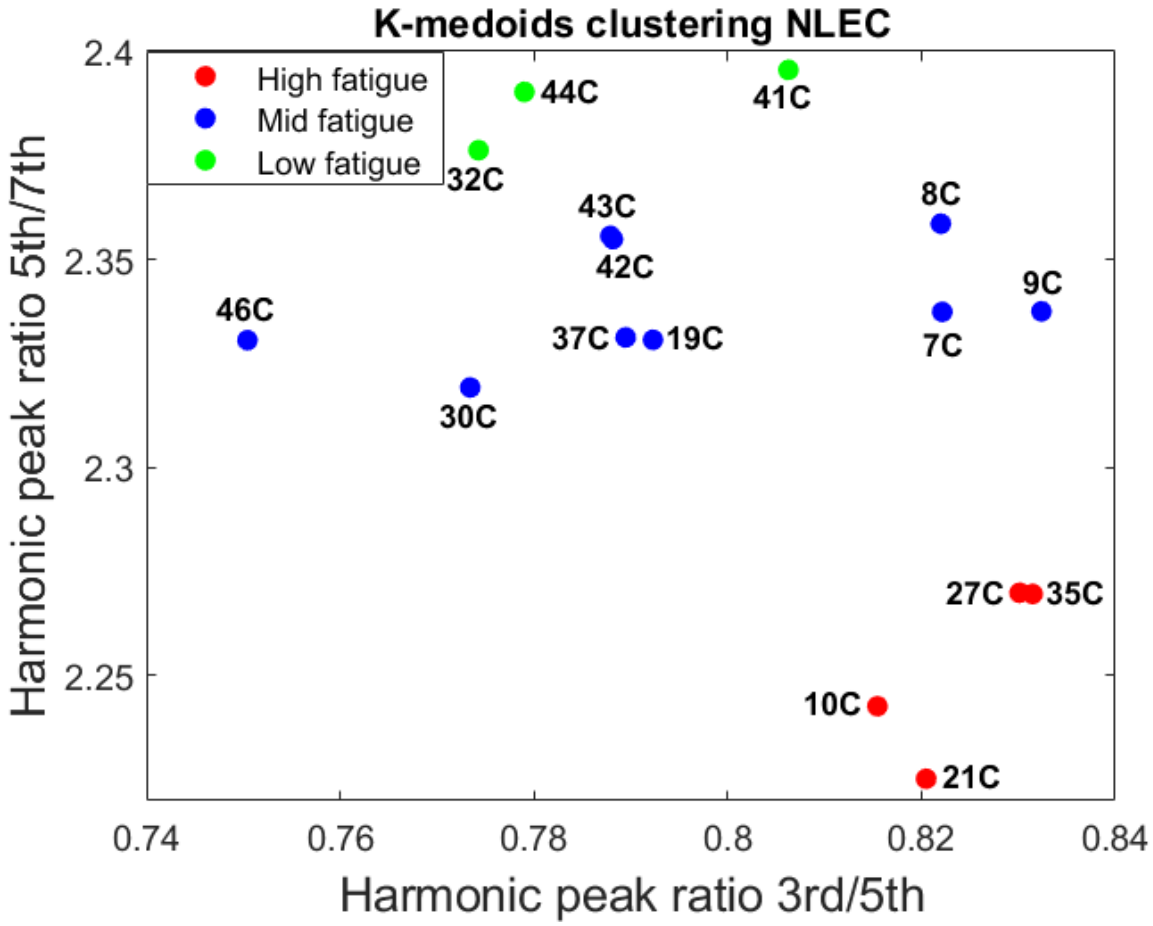

Figure 4.11 Clustering of MSS samples into fatigue categories

having a RUL lesser than or equal to 310 K are classified as high fatigue, between 310 K to 1.2 M as mid fatigue and above or equal to 1.2 M as low fatigue.

The clustering and classification results, after applying KCA and GA on NLEC signal features

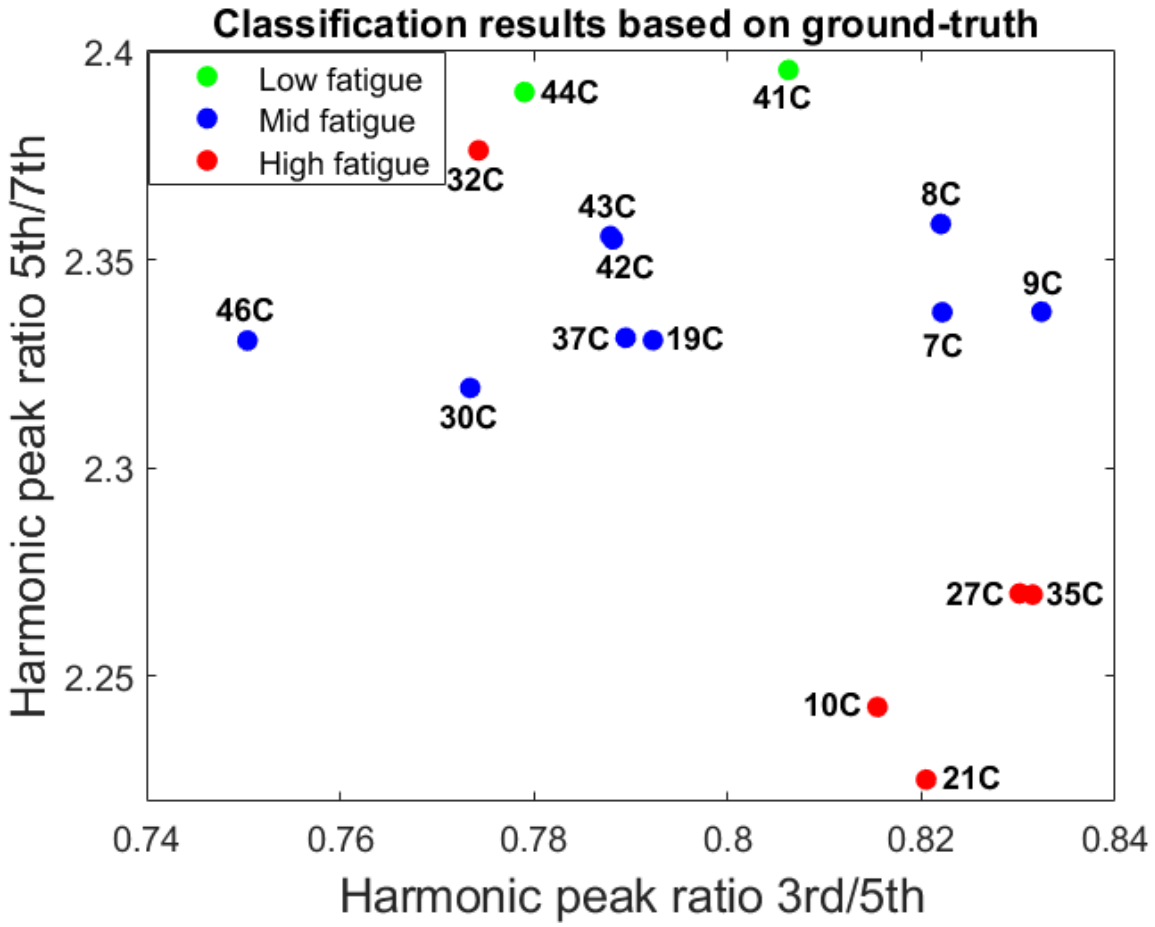

Figure 4.12 Classification results based on ground-truth NLEC

are shown in Figure 4.11. The green, blue, and red dots are the representations for all samples which are categorized as low fatigue, mid fatigue, and high fatigue respectively. Figure 4.12. shows the classification results based on the ground-truth data.

Comparing Figure 4.11., Figure 4.12., and RUL data in Table 3.1, it is observed that, there is one high fatigue sample (32C) which is misclassified as low fatigue. Table 4.6 shows the sample database with ground-truth and fatigue classification results.

The system performance for EPRI MSS sample database shown in Table 4.6 is calculated as 93.75%. The approach should be tested more extensively with additional samples data.

Table 4.6 Sample database with fatigue classification

Sample ID	**RUL**	**Ground-truth**	**Classification Results**
41C	2,889,703	Low fatigue	Low fatigue
44C	1,318,034	Low fatigue	Low fatigue
30C	1,103,303	Mid fatigue	Mid fatigue
43C	690,512	Mid fatigue	Mid fatigue
42C	603,724	Mid fatigue	Mid fatigue
7C	551,901	Mid fatigue	Mid fatigue
37C	514,878	Mid fatigue	Mid fatigue
9C	493,803	Mid fatigue	Mid fatigue
19C	464,392	Mid fatigue	Mid fatigue
46C	447,380	Mid fatigue	Mid fatigue
8C	352,928	Mid fatigue	Mid fatigue
35C	309,868	High fatigue	High fatigue
32C	306,142	High fatigue	**Low fatigue**
27C	297,627	High fatigue	High fatigue
21C	200,007	High fatigue	High fatigue
10C	127,204	High fatigue	High fatigue

CHAPTER 5

CONCLUSIONS AND FUTURE WORK

Both magnetic NDE techniques show promise in classifying the martensitic stainless-steel samples into broad fatigue categories. The conclusions for both techniques are presented in this section.

Non-linear eddy current technique is developed and investigated to check the feasibility of detecting fatigue damage in martensitic grade stainless-steel materials. Odd harmonic peaks and their ratios are identified as non-linear eddy current signal features. A methodology is proposed to classify the stainless-steel samples based on the remaining useful life. K-medoids clustering algorithm and genetic algorithm are applied on the non-linear eddy current signal features, which are computed from the harmonics obtained from the frequency domain representation of the acquired non-linear eddy current data. Results, based on the available data set, indicate that the martensitic grade stainless-steel samples in different stages of fatigue can be classified into broad categories of low, mid and high levels of fatigue based on the remaining useful life with a system performance of 93.75%.

Magnetic Barkhausen Noise technique is developed and investigated to estimate the fatigue damage in martensitic grade stainless-steel samples. Time and frequency domain features of the magnetic Barkhausen noise signal, along with K-medoids clustering algorithm and genetic algorithm are used to classify the samples into broad fatigue categories. The results, based on the available data set, indicate that the martensitic stainless-steel samples having different levels of fatigue damage can be classified into broad fatigue categories, i.e., low fatigue, mid fatigue and high fatigue based on the remaining useful life of the sample. The system performance is obtained as 87.5%.

The lower fatigue threshold obtained for MBN technique is different when compared to NLEC technique. The reason for this is that, there is a lack of data (additional cycles to failure) in the range of 690,000 to 1 million loading cycles. If there were additional samples in the range, it would be possible to obtain more accurate fatigue thresholds and an agreement between the fatigue thresholds for MBN and NLEC techniques will be possible. In this research work, feasibility of

the approach based on the available data set is presented. Hence, the same approach when applied to a larger data set (i.e., a greater number of samples with varying additional cycles to failure) can provide more accurate fatigue thresholds and classifications.

As part of the future work, imaging of the micro-structure (for samples with different loading cycles) can be performed to investigate the changes in grain size, which is a microstructure property of the material. This will give an idea about the correlation of NLEC and MBN signal features with changes in material micro-structure due to fatigue.

CHAPTER 6

INTRODUCTION TO EMAT

Engineering structures are prone to damages from stress and environmental factors. This is a well-known problem in manufacturing industries. Over time, these damages progressively worsen, eventually resulting in the fracturing of vital systems and imposing significant economic losses. Regular inspections are crucial in ensuring the integrity of these structures. One effective way of monitoring the structural health of mechanical structures is by monitoring the properties of the materials used in their construction. Nondestructive evaluation (NDE) techniques are particularly useful in this regard. These techniques rely on changes in material properties to detect potential issues and can be used to identify defects without causing further damage. By utilizing NDE, manufacturing industries can identify problems early on and take corrective action to prevent further damage or fracturing. This can help prevent significant economic losses and ensure the longevity of structures, by retiring only the severely damaged parts. NDE is therefore an invaluable tool for reporting the structural health of mechanical structures and is a critical aspect of modern manufacturing practices.

To detect defect locations in engineering structures, ultrasonic and eddy current NDE inspection techniques are commonly used. Eddy current technique is a simple and effective NDE technique that can be easily applied on structures, but it only works on conductive materials [44]. Another drawback with this technique is that, it can primarily identify only surface and sub-surface defects. When detecting defects inside the material, ultrasonic techniques (typically piezoelectric transducer-based) are commonly used [45]. However, this method is contact-based and requires a couplant [46] to facilitate the transmission of ultrasonic energy from transducer into the sample under test. Impurities or curvature on the material surface can cause problems and require additional effort to set up this NDE technique. In order to address these issues, the Electromagnetic Acoustic Transducer (EMAT) technique has been proposed in this research work. EMAT's have found practical applications and are very effective in evaluation of damage using NDE [47]. With its non-contact, non-destructive testing capabilities, EMAT technology has the potential to revolutionize

quality control in industries [48] that rely on welded structures (such as construction, petroleum, aerospace, and automotive industries).

6.1 Literature review

EMAT is a non-contact ultrasonic NDE technique that can generate elastic waves without a couplant [49]. This makes it a convenient and efficient method for detecting defects. This technique does not require surface preparation [50], which significantly reduces the inspection time. These unique features make EMAT's suitable for a variety of applications, including:

1. Material Characterization: EMAT's can be used to determine the elastic and magnetic properties of materials, which is useful for research and development in fields such as materials science, metallurgy, and magnetic materials.

2. Process Monitoring: EMAT's are used for NDT in industries such as automotive, and power generation to inspect defects, cracks, and corrosion in materials like metals, composites, and ceramics. Also, EMAT's are used to monitor the quality of industrial processes, such as welding, casting, and rolling, by detecting defects or changes in the material properties.

In general terms, EMATs are devices composed of a coil designed to induce dynamic electromagnetic fields at the surface of a conductive material, accompanied by a magnet or a series of magnets to provide a DC biasing magnetic field, as depicted in Figure 6.1. This contrasts with a typical piezoelectric device, as illustrated in the figure, which necessitates a couplant for coupling with the sample surface.

The interaction between induced eddy currents and the static magnetic field leads to the generation of elastic waves within the conductive sample. The ability to generate distinct wave modes is dependent upon the coil's geometry and the arrangement of the magnets. The magnitude of the eddy current depends on several factors, such as magnitude of the coil current, distance between the coil and the sample (known as lift-off), and frequency of the coil current. The interaction between the static magnetic field and eddy current generates a force on the sample surface, known as the Lorentz force. The Lorentz force represents the coupling between electromagnetic and acoustic

domains, and is illustrated in Figure 6.2. Here F refers to the Lorentz force, B_S is the static magnetic flux density and I is the coil current. The generated elastic waves then penetrate into the sample and carries information about the defects present inside.

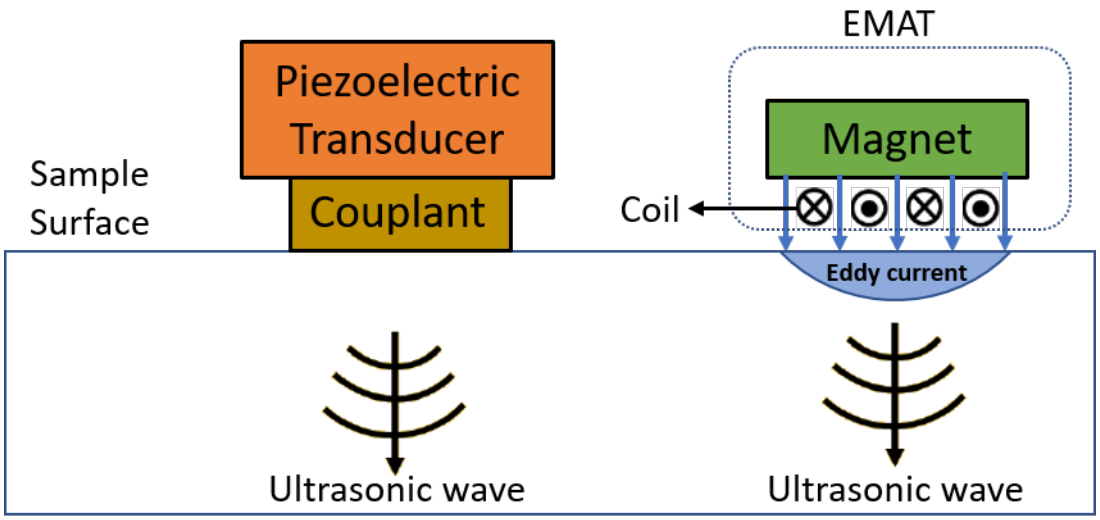

Figure 6.1 Schematic representation of an EMAT

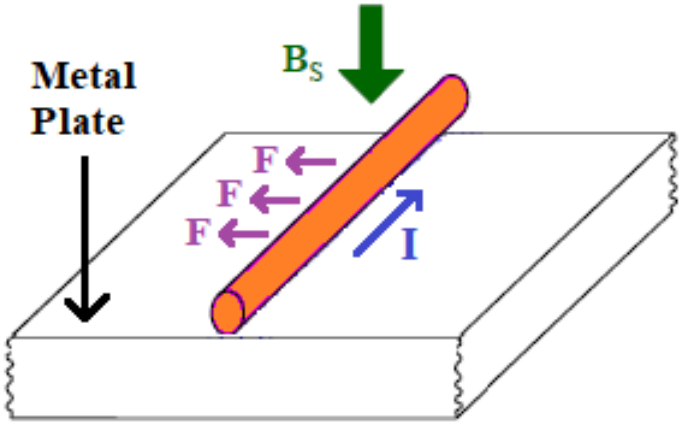

Figure 6.2 Lorentz force representation on a metal plate

While conventional EMAT techniques are used for generating elastic waves in conductive and ferromagnetic materials [51], non-conductive structures pose a challenge. This is because the dynamic magnetic field generated by the EMAT coil cannot induce eddy currents in non-conductive structures. This thesis explores and proposes methods to inspect non-conductive samples using EMAT's, which is the major and interesting contribution of this research work on EMAT's.

6.2 Transduction mechanisms in EMAT

Transduction mechanism refers to the process by which a device or system converts one form of energy or signal into another form that can be used for a specific purpose. In simpler terms, it is how a device turns one type of input into another type of output. Understanding the transduction mechanism is crucial in designing and optimizing the performance of many devices and systems, including sensors, actuators, and communication systems.

There are two transduction mechanisms in a EMAT [52]. They are:

1. Lorentz force transduction mechanism, which works on conductive and ferromagnetic materials.

2. Magnetostriction transduction mechanism, which works only on ferromagnetic materials.

The Lorentz force transduction mechanism used in EMAT's convert electromagnetic waves into elastic waves. When an alternating current is passed through the EMAT coil, eddy currents are induced in the sample under test. The interaction between the static magnetic field and eddy current generates a force on the sample surface, known as the Lorentz force.

The Lorentz force represents the coupling between electromagnetic and acoustic domains, and is given by the equation:

$$F = J \times B \tag{6.1}$$

where F is the force vector, J is the current density vector, and B is the magnetic flux density vector.

The frequency of elastic waves is determined by the frequency of the alternating current provided to the EMAT coil. The amplitude of elastic waves depends on the strength of Lorentz force and the properties of the sample (such as conductivity, density etc.) being tested. To detect the generated elastic wave, an EMAT receiver should be used. As the elastic wave propagates through a conducting sample, the atoms in the lattice move normal to the direction of wave propagation [53]. The interaction between the particle displacement and static magnetic field (generated by permanent

magnet) induces eddy currents at the sample surface (region of skin-depth), which are then detected by the EMAT coil.

The Lorentz force transduction mechanism in EMAT's is a powerful and versatile technique for generating elastic waves in conductive and ferromagnetic materials, and it has a wide range of applications in non-destructive testing and material characterization.

Magnetostriction is a transduction mechanism used in EMAT's for generating elastic waves in ferromagnetic samples. It is based on the principle that when a ferromagnetic sample is subjected to a magnetic field, it undergoes a change in shape or size. This change in shape or size is called magnetostriction. Magnetostriction takes place as a result of the tendency of ferromagnetic domains to align in the direction of an external magnetic field, causing a net mechanical strain [54]. If the magnetic field has a time-varying component, this strain can be harnessed to generate elastic waves [55].

In a EMAT using magnetostriction as the transduction mechanism, a dynamic magnetic field is generated by the EMAT coil carrying alternating current, which interacts with the ferromagnetic sample being tested. This dynamic magnetic field, along with the bias static magnetic field (generated by the permanent magnet) causes the material to undergo a change in shape or size, which generates elastic waves that propagate through the sample. The amplitude of elastic waves generated by magnetostriction is dependent upon the magnetostriction coefficient, elastic constants of the ferromagnetic sample, and the strength of the applied magnetic field. Frequency of the generated elastic wave is determined by frequency of the alternating current provided to the EMAT coil. Further, to detect the generated elastic waves, an EMAT receiver can be used.

6.3 Typical EMAT designs in Literature

The typical EMAT design available in literature are discussed in this section.

6.3.1 Bulk-wave EMAT

The bulk-wave EMAT shown in Figure 6.3 is capable of generating both longitudinal waves (direction of wave propagation is parallel to the direction of particle displacement) and shear waves (direction of wave propagation is perpendicular to direction of particle displacement). The

unidirectional coil elements are positioned under a static magnetic field generated by the permanent magnet. The magnetic field is oriented normally to the surface beneath the coil elements and tangentially at the center of the coil elements [53]. The dynamic magnetic fields generated by the coil elements induces eddy currents on the sample surface. The resulting force (Lorentz force) is parallel to the sample surface. Hence the direction of particle particle displacement is parallel to the sample surface and is perpendicular to the direction of wave propagation as shown in Figure 6.3. This configuration is termed as a shear wave EMAT [53].

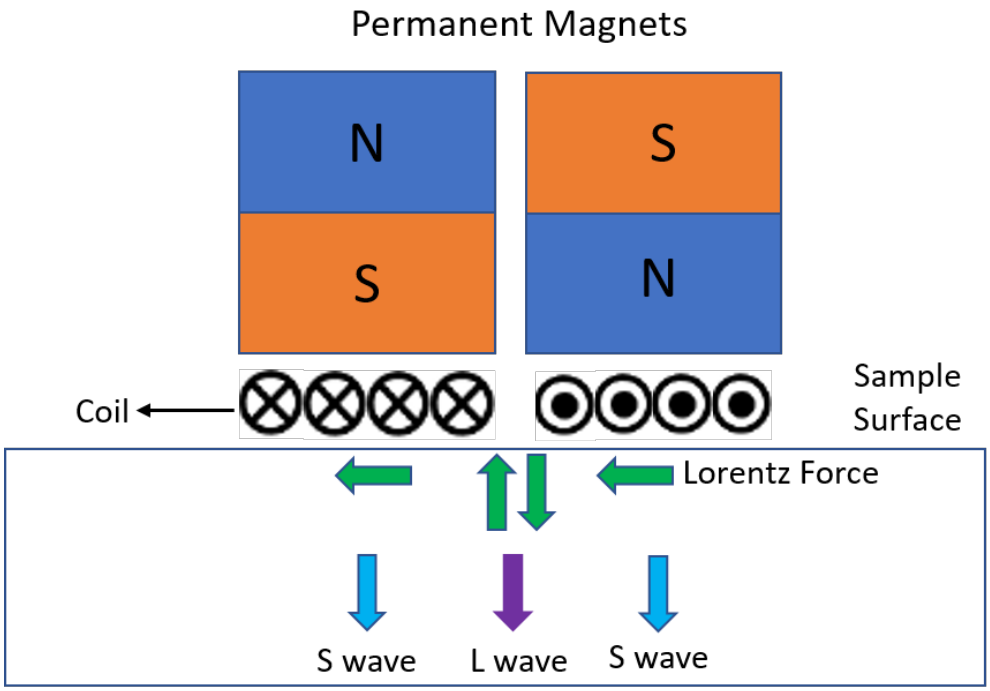

Figure 6.3 Schematic diagram of a Bulk-wave EMAT

6.3.2 Meander line EMAT

The meander line EMAT shown in Figure 6.4 is capable of generating Rayleigh (surface waves having a particle motion that is counterclockwise with respect to the direction of travel), angled shear and longitudinal waves, i.e., traveling obliquely into the sample.

The drawback of this EMAT lies in the challenge of identifying the modes in received echoes. The combination of a normal biasing field and the EMAT coil results in Lorentz force parallel to the surface. These forces alternate in direction according to the meander-line coil. The generation frequency is determined by the period of the meander-line, which can be adjusted through man-

ufacturing the coil using a printed circuit technique. Consequently, it is possible to modify the generation frequency by altering the coil's periodicity.

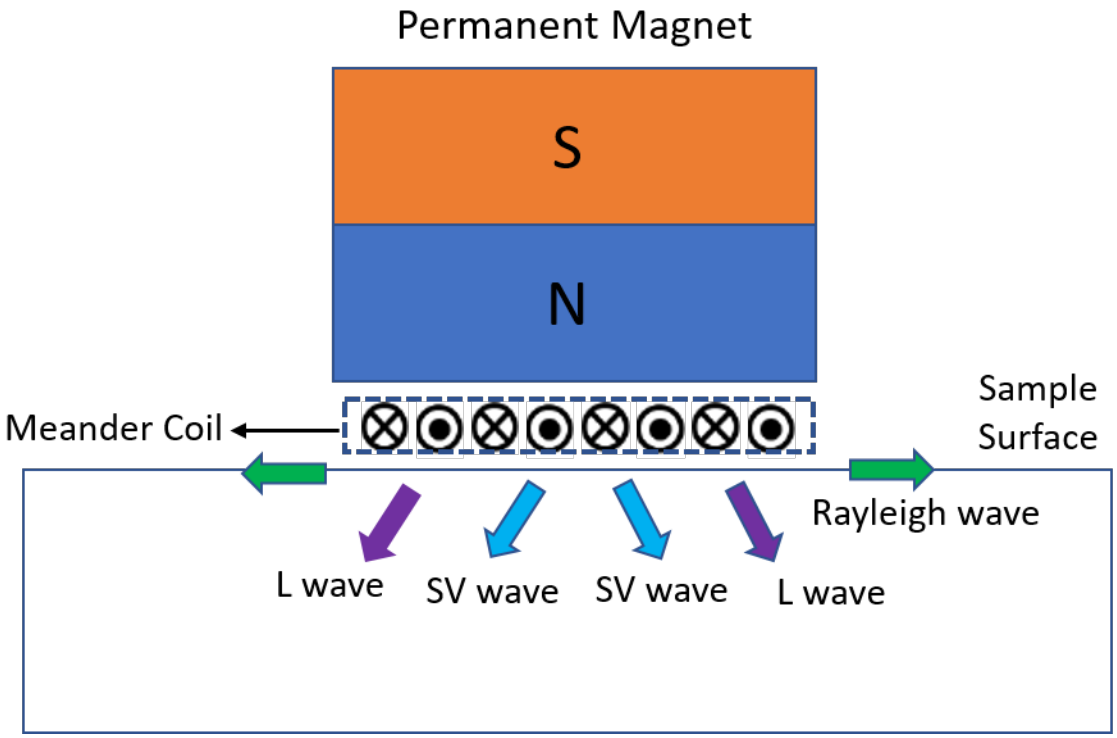

Figure 6.4 Schematic diagram of a Meander line EMAT

6.3.3 Periodic Permanent Magnet (PPM) EMAT

PPM-EMATs are devices designed to generate shear waves polarized parallel to the specimen's surface [56]. The EMAT configuration is commonly utilized for measurements involving Shear Horizontal (SH) waves in a plate. These waves are particularly advantageous for nondestructive testing (NDT) purposes and are generally challenging to excite with traditional piezoelectric transducers [53]. The classical configuration of this EMAT type is depicted in Figure 6.5.

PPM EMATs typically feature a racetrack-shaped coil positioned in front of the PPM array, where the north and south poles alternate periodically, as shown in Figure 6.5. The Lorentz force in the tangential direction vary due to the alternating polarity of the permanent magnets within the array [57]. The optimal transfer efficiency is achieved when the device is driven by a current selected in accordance with the spacing of magnets. The periodically alternating polarity establishes the wavelength of the generated ultrasound. Therefore, to excite higher frequency SH waves, the width

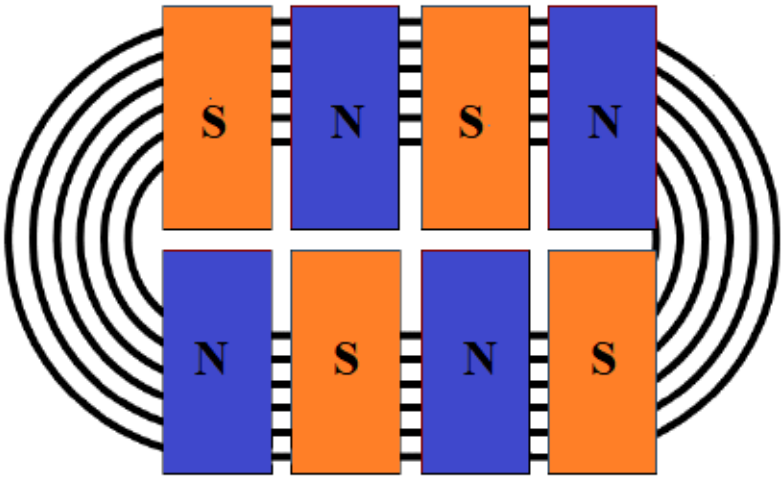

Figure 6.5 Schematic diagram of a PPM EMAT

of the magnets needs to be reduced, thereby decreasing the wavelength. However, it is essential to note that the efficiency significantly decreases with reduced magnet thickness, leading to a limitation on the operational frequency of this EMAT.

CHAPTER 7

LORENTZ FORCE EMAT

The Lorentz force transduction mechanism used in EMAT's, as discussed in previous chapter, converts electromagnetic waves into elastic waves. This chapter describes more details on the associated theory and modeling aspects of electromagnetic and acoustic phenomenon.

7.1 Theory

As discussed earlier, the current density in EMAT coil generates eddy currents in the conducting material. This current is opposite in direction (compared to current in EMAT coil) according to Faradays law given in (7.1). Eddy currents are loops of electric currents induced within a conductor due to the application of a time-varying magnetic field.

$$\nabla \times E = -\frac{\partial B}{\partial t} \tag{7.1}$$

Here E is the electric field (V/m) vector and B is the magnetic flux density (T) vector. Eddy currents are generated when there is a changing magnetic field (as can be deduced from (7.1)).

The eddy currents generated in the material are confined to a small region at the sample surface. The depth of this region is quantified by a parameter called skin depth (δ) and represented as given in (7.2).

$$\delta = \frac{1}{\sqrt{\pi f \sigma \mu}} \tag{7.2}$$

Here, f is the frequency of coil current, σ is the conductivity of the conductor (S/m) and μ is the permeability of the material.

$$\mu = \mu_0 \mu_r \tag{7.3}$$

where μ_0 is the permeability of free space ($\approx 4\pi \times 10^{-7}$ H/m) and μ_r is the relative permeability of the material.

When we have a charged particle (static or moving) in a magnetic field, it will experience a force known as the Lorentz force. In an EMAT, the Lorentz force generated is given in (7.4).

$$\begin{aligned} F &= qV \times B \\ &= J \times B \end{aligned} \tag{7.4}$$

Here q is the charge (C), V is the velocity vector $(\mathrm{m/s})$, B is the magnetic flux density vector (T) and J is the induced current density vector $(\mathrm{A/m^2})$.

In the following sections of this chapter, electromagnetic modeling, and elastic wave modeling details will be discussed.

7.2 Numerical model in COMSOL

The Finite Element Analysis (FEA) tool employed for the design and simulation of Electromagnetic Acoustic Transducers (EMATs) in this research is COMSOL. Renowned for its versatility, COMSOL serves as a robust FEA tool capable of modeling a diverse array of physical systems, encompassing domains such as electrical circuits, electromagnetics, fluid dynamics, heat transfer, and structural mechanics. This tool empowers engineers, scientists, and researchers to construct computer models mirroring real-world systems, enabling the simulation of their behavior under varied conditions.

The application of COMSOL proves instrumental in predicting real-world system performance, testing diverse designs and configurations, and optimizing overall system functionality. Its utility extends to gaining insights into the behavior of intricate physical systems, thereby facilitating informed engineering decisions.

The software tool is based on the concept of finite element analysis, which breaks down a complex system into smaller, simpler elements. Each element is then analyzed separately, taking into account the interactions between neighboring elements. This allows for a more detailed and accurate analysis of the system's behavior.

The subsequent subsections will delve deeper into the modeling intricacies of EMAT, elucidating the associated governing equations.

7.2.1 Electromagnetic modeling

The module used to simulate the electromagnetic phenomenon in this research work is the magnetic field (mf) interface, available within the AC/DC module. This is a specialized tool that allows users to model and simulate electromagnetic fields and their interactions with electric currents. It can be used to simulate a wide range of electromagnetic phenomena, such as magnetic fields, electric fields, and electromagnetic waves.

The magnetic field (mf) physics interface within the AC/DC module specifically focuses on the behavior of magnetic fields in various physical systems. It allows users to model the behavior of magnetic fields generated by electric currents or magnetic materials, and to analyze how these fields interact with other physical phenomena such as heat transfer or structural mechanics. The dependent variable in mf interface is the magnetic vector potential. One of the main advantages of the magnetic field interface in COMSOL is its ability to simulate both steady-state and time-varying magnetic fields. This can be useful for predicting the behavior of electromagnetic systems under various conditions, such as changes in electric currents or magnetic materials.

As discussed earlier, in an EMAT, we have the coil carrying an AC current which generates a time-varying magnetic field inducing eddy currents in a conducting material. Also, there is a permanent magnet which provides the static magnetic field. To obtain the Lorentz force (7.4), we will need both the eddy current density and magnetic flux density.

The governing equations for eddy current simulation in COMSOL can be described by Maxwell's equations given below:

1) (7.5) is also the Faraday's law of electromagnetic induction, which relates a changing magnetic field to an induced electric field. Here E is the electric field vector $(\mathrm{V/m})$ and B is the magnetic flux density vector (T).

$$\nabla \times E = -\frac{\partial B}{\partial t} \tag{7.5}$$

2) (7.6) is from Ampere's law, which relates the magnetic field to conduction current density and rate of change of electric displacement. Here H is the applied magnetic field strength vector $(\mathrm{A/m})$,

J is the conduction current density vector ($\mathrm{A/m^2}$) and the term $\frac{\partial \mathbf{D}}{\partial t}$ is negligible for frequencies lesser than 100 MHz (i.e., quasi-static approximation).

$$\nabla \times H = J + \frac{\partial D}{\partial t} \tag{7.6}$$

3) (7.7) states that the magnetic flux through any closed surface is zero, indicating that magnetic monopoles do not exist.

$$\nabla \cdot B = 0 \tag{7.7}$$

4) (7.8) relates the electric flux through a closed surface to the electric charge enclosed within the surface. Here ρ is the electric charge density vector in ($\mathrm{C/m^2}$)

$$\nabla \cdot D = \rho \tag{7.8}$$

The constitutive relations are given in (7.9), (7.10) and (7.11)

$$J = \sigma E \tag{7.9}$$

where σ is the conductivity of the conductor ($\mathrm{S/m}$)

$$D = \epsilon_0 \epsilon_r E \tag{7.10}$$

where ϵ_0 is the permittivity of free space (8.854×10^{-12} $\mathrm{F/m}$) and ϵ_r is the relative permittivity of the conductor.

$$B = \mu_0 \mu_r H \tag{7.11}$$

where μ_0 is the permeability of free space ($\approx 4\pi \times 10^{-7}$ $\mathrm{H/m}$) and μ_r is the relative permeability of the conductor.

The dependent variable in magnetic field physics interface in COMSOL (i.e., the magnetic vector potential which is a vector field) is linked to magnetic flux density as given in (7.12). The units of magnetic vector potential is Tm or Wb/m. Also, electric field can be written in terms of magnetic vector potential as given in (7.13).

$$\nabla \times A = B \tag{7.12}$$

$$E = -\frac{\partial A}{\partial t} \tag{7.13}$$

The permanent magnet is modeled using the Maxwell's equations and constitutive relations described earlier (7.5 - 7.13). The magnetization model describes the direction of static magnetic field. The constitutive relation used in COMSOL to specify magnetization (M) is given in (7.14).

$$B = \mu_0 \ (H + M) \tag{7.14}$$

From the results obtained using Maxwell's equations and constitutive relations (7.5 - 7.14), the electromagnetic FEM in COMSOL helps to calculate the Lorentz force given in (7.4). This concludes the electromagnetic modeling of EMAT in COMSOL. The next step is to describe the elastic wave modeling.

7.2.2 Elastic wave and Multiphysics modeling

To model the interaction between electromagnetic field and elastic waves, equations for elastic wave propagation needs to be considered. The solid mechanics interface within the structural mechanics module is utilized for simulating the acoustic phenomenon. The meshing in non-conducting sample is set to ensure a minimum of 10 elements per elastic wave wavelength (in all COMSOL models discussed in the thesis), and utilized free triangular meshing. A Courant-Friedrichs-Lewy (CFL) number of 0.1 will be used for simulating EMAT models in COMSOL.

The equations for elastic wave modeling in COMSOL can be written as follows:

1) Equation of Motion (Newton's second law):

$$\rho \frac{\partial^2 U}{\partial t^2} = \nabla \cdot \sigma + F \tag{7.15}$$

2) Stress-Strain Relationship (Constitutive Equation):

$$\sigma = \mathbf{C} : \varepsilon \tag{7.16}$$

In (7.15) and (7.16),:

U is the displacement vector,

t is time,

ρ is density of the sample,

$\boldsymbol{\sigma}$ is the stress tensor,

F is force vector acting on the structure,

∇ is the nabla operator (vector differential operator),

$\mathbf{C}$ is the fourth-order elasticity tensor, and

$\boldsymbol{\varepsilon}$ is the strain tensor.

Combining the electromagnetic and elastic models, the acoustic displacement vector for a continuous elastic isotropic medium can be computed using,

$$\mu\nabla\times\nabla\times U-(\lambda+2\mu)\nabla(\nabla\cdot U)+\rho\frac{\partial^2 U}{\partial t^2}=F \tag{7.17}$$

U is the displacement vector,

t is time,

μ, λ are Lame's constants,

ρ is density of the material,

F is force vector acting on the structure,

∇ is the nabla operator (vector differential operator),

7.3 Novel EMAT configurations for non-conductive samples

Conventional EMATs are primarily employed for generating elastic waves in conductive or ferromagnetic samples, as highlighted in [51]. However, the application of EMATs to non-conductive structures presents a challenge due to the inability to induce eddy currents, rendering the Lorentz force transduction mechanism ineffective. Additionally, if the material lacks ferromagnetic properties, the magnetostriction phenomenon is absent, resulting in the failure of the magnetostriction transduction mechanism.

The initial concept of applying EMATs to insulating samples was introduced in [58], where the proposed method involved directly bonding a current-carrying coil to the sample's surface. Subsequent research, as seen in [59] and [53], explored the application of a metal foil onto non-conductive samples for elastic wave generation using EMAT. In both cases, the induced configuration was utilized, with an adhesive layer beneath the metal foil serving as a couplant. Notably, these studies did not explore the direct application of current to the metal foil/strip and generation of longitudinal waves in through transmission mode for non-conductive sample inspection using EMAT.

This thesis addresses the gap by introducing novel EMAT configurations, specifically designed for non-conductive samples. Two approaches are proposed, (a) Direct excitation and (b) Non-contact induced excitation in an embedded metal patch, both relying on the Lorentz force transduction mechanism. The subsequent chapters will delve into a comprehensive investigation of these approaches, presenting numerical results that offer valuable insights into the design considerations for effective non-destructive evaluation of non-conductive materials.

CHAPTER 8

DIRECT EXCITATION

This chapter presents the outcomes derived from numerical simulations of EMATs applied to a non-conducting sample. The initial section introduces the direct excitation model, offering results that substantiate the propagation of an acoustic wave within the non-conducting sample. Subsequently, an exploration of acoustic velocity is presented for comparison. Moving forward, the subsequent sections delve into an examination of the impact of varying metal strip width and height on both Lorentz force and displacement, impact of skin effect in Aluminum strip with accompanying presentation of numerical findings and the chapter concludes with experimental validation.

8.1 EMAT model in COMSOL

The direct excitation model (two-dimensional) for an EMAT involves supplying current directly to the metal strip applied on a non-conducting sample. Figure 8.1 illustrates the schematic of the direct excitation model geometry in COMSOL, while Figure 8.2 provides a zoomed-in version to elucidate the metal strip and measurement point on the sample's back wall. The magnetic field interface within the AC/DC module is employed to simulate the electromagnetic phenomenon, and the structural mechanics module is utilized for simulating the acoustic phenomenon.

The model consists of a permanent magnet, a metal strip, a steel core, and the non-conducting sample (plastic). The permanent magnet generates the static magnetic field, and the metal strip produces a changing (dynamic) magnetic field. Perfectly matched layers, located at the left and right corners of the sample, are implemented to prevent reflections and eliminate high-frequency noise. The entire model is enclosed in air. The static magnetic field of the permanent magnet is specified in the x-direction.

A surface current density (A/m) is applied to the Aluminum strip in the z-direction, as depicted in Figure 8.3. Accordingly, following the right-hand rule, the Lorentz force generated should be in the y-direction. The resulting displacement and wave propagation (longitudinal wave) occur in the y-direction, along the thickness of the plastic (acrylic). Detailed model parameters are provided in Table 8.1.

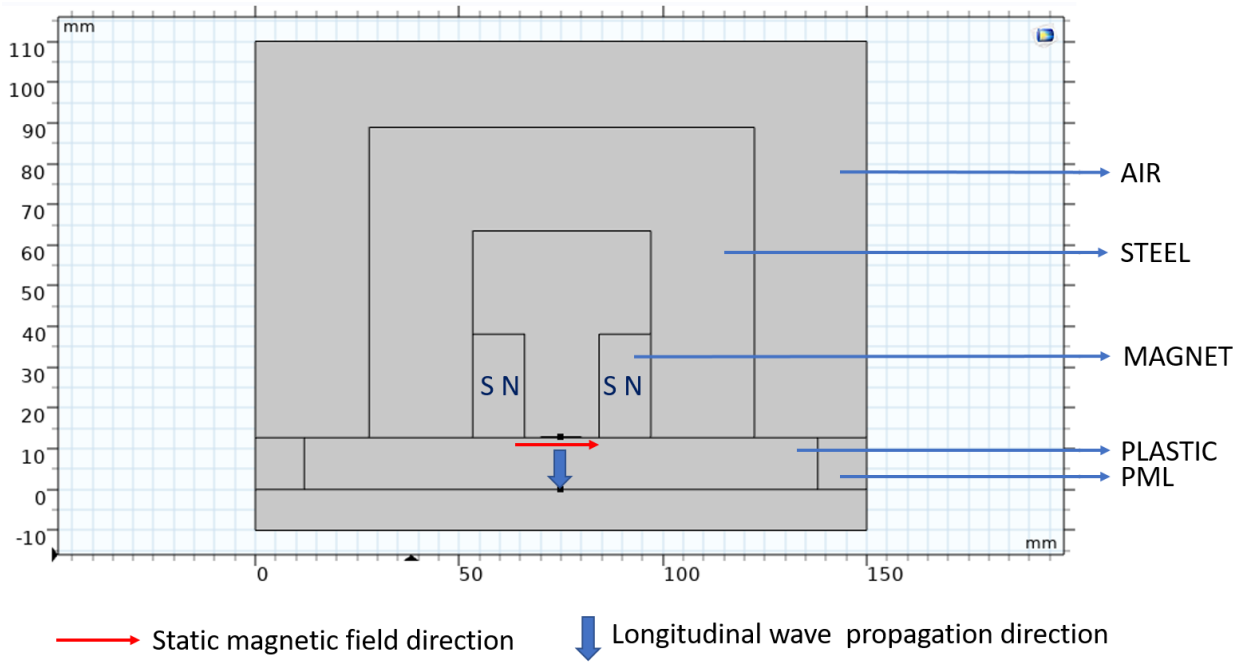

Figure 8.1 Direct Excitation model for an EMAT in COMSOL

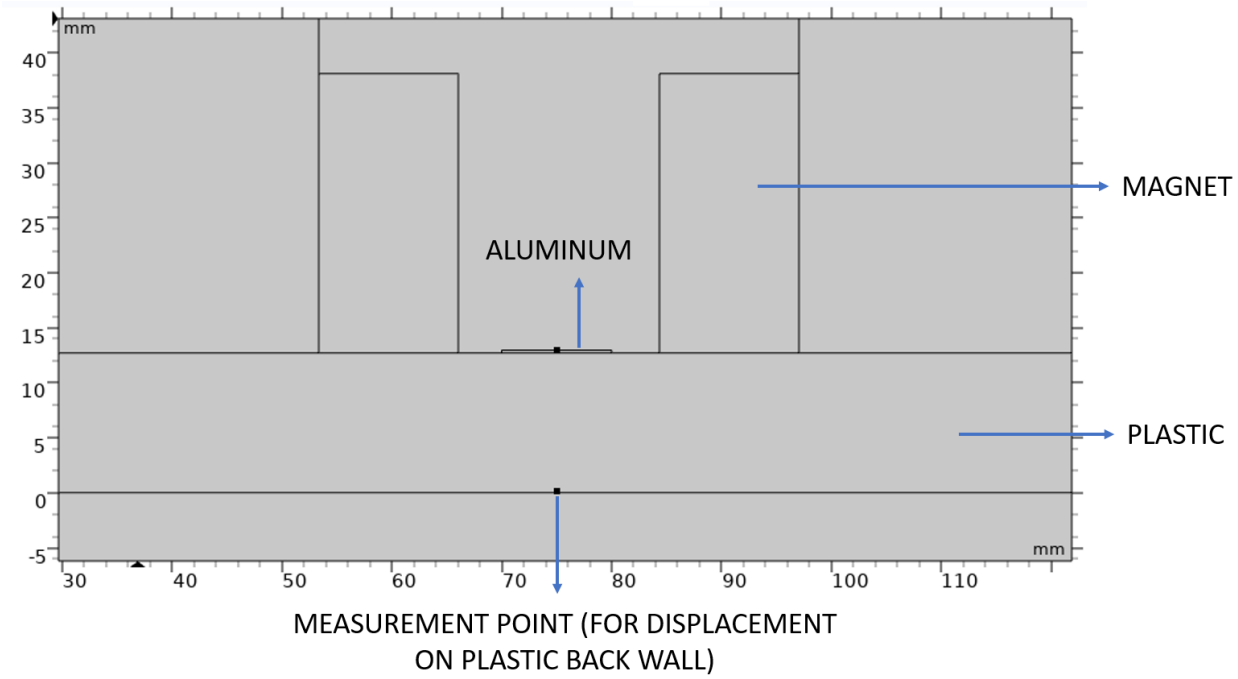

Figure 8.2 Zoomed version of the EMAT model shown in Figure 8.1

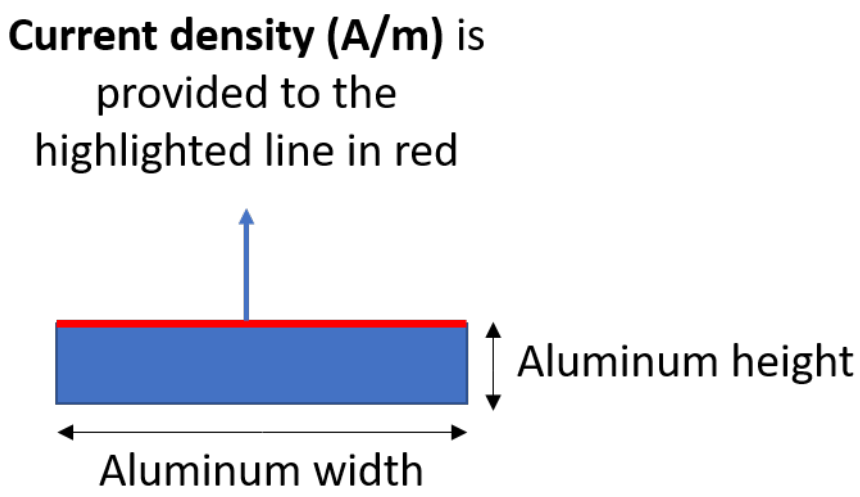

Figure 8.3 Representation of input current provided to the Aluminum strip

Table 8.1 Model parameters for Direct excitation EMAT

Parameter	Value
Plastic (Sample) Width	150 mm
Plastic (Sample) Height	12.7 mm
Magnet Width	12.7 mm
Magnet Height	25.4 mm
Longitudinal velocity in plastic	2077.45 m/s
Wavelength in plastic	4.15 mm
Aluminum strip Width	10 mm
Aluminum strip Height	0.254 mm
Conductivity of plastic	62.5 X 10-18 S/m
Poisson's ratio (Plastic)	0.35
Young's Modulus (Plastic)	3.2 G Pa
Density (Plastic)	1190 kg/m3
Frequency of coil current	500 kHz
Conductivity of Aluminum strip	36 MS/m

The coil current, as shown in Figure 8.4, is a Gaussian modulated pulse with a carrier frequency of 500 kHz as given in (8.1).

$$g(t) = A \cdot \exp\left(-\frac{(t-t_0)^2}{2\sigma^2}\right) \cdot \cos(2\pi f_c(t-t_0) + \phi) \tag{8.1}$$

where:

$g(t)$ is the Gaussian modulated pulse as a function of time, t,

A is the amplitude of the pulse,

t_0 is the center time of the pulse,

σ is the standard deviation of the Gaussian envelope,

f_c is the carrier frequency of the pulse,

ϕ is the phase of the pulse.

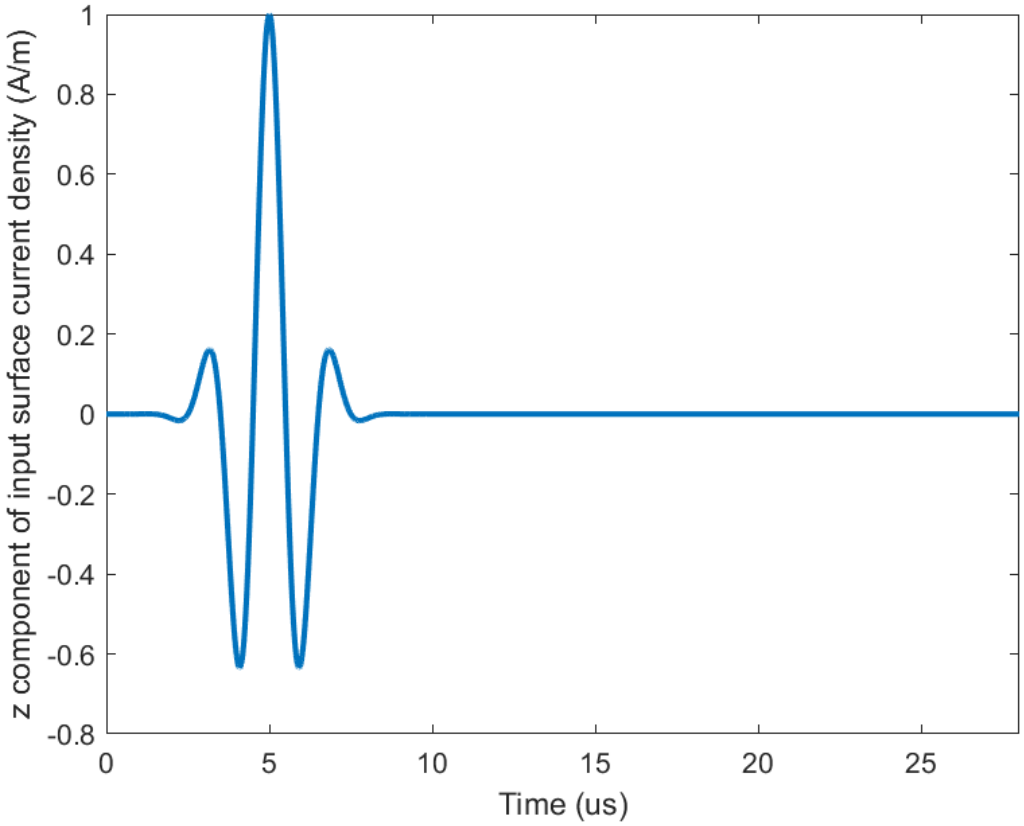

Figure 8.4 Input current density provided to Aluminum strip

Figure 8.5 depicts the current density at a measurement point on aluminum strip, specifically situated at center of the highlighted red line in Figure 8.3. Simultaneously, Figure 8.6 illustrates the y-component of the Lorentz force at this measurement point on aluminum strip. Notably, both the current density and Lorentz force exhibit analogous Gaussian-shaped temporal profiles. In accordance with equation (6.1), the Lorentz force is obtained by multiplying current density with magnetic flux density.

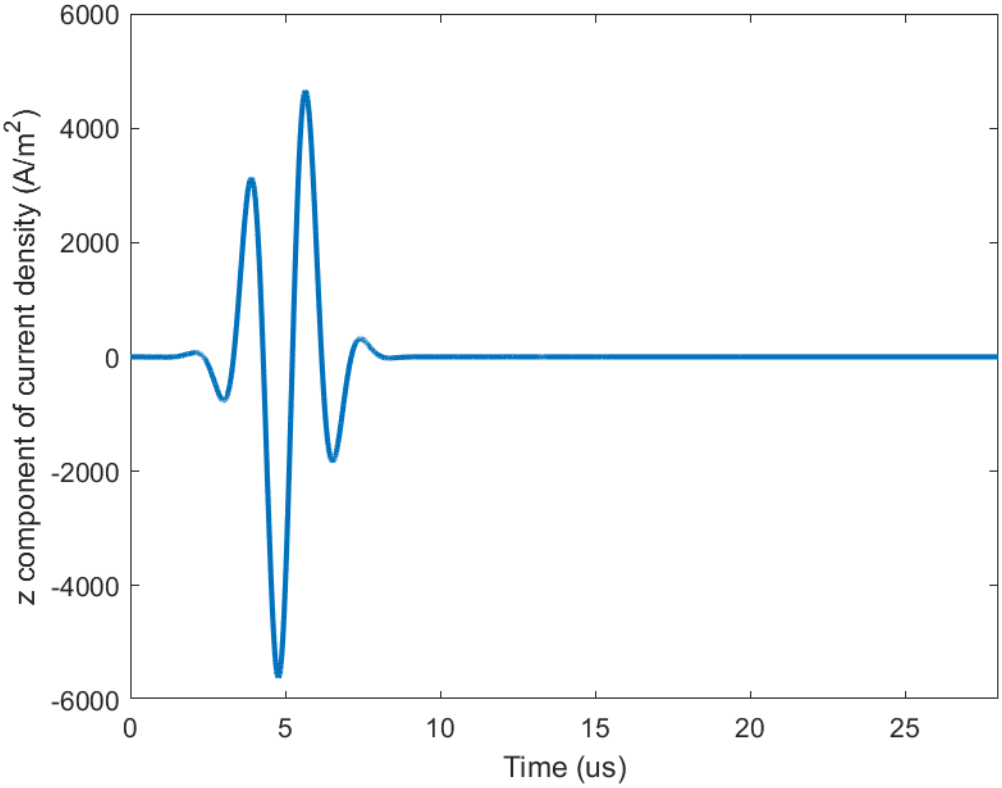

Figure 8.5 z-component of current density at measurement point in Aluminum strip

Figure 8.7, Figure 8.8, and Figure 8.9 present surface plots of current density and Lorentz force within the Aluminum strip at 5 µs. The selection of 5 µs is based on the expectation that the current density will peak at this time. The observed decrease in current density along the aluminum height is attributed to the skin effect of aluminum, as evident in Figure,8.7. The corresponding Lorentz force plots exhibit a similar trend, in accordance with equation (6.1). It is also noteworthy that there is a non-zero x-component of Lorentz force, attributed to the non-zero y-component of magnetic flux density.

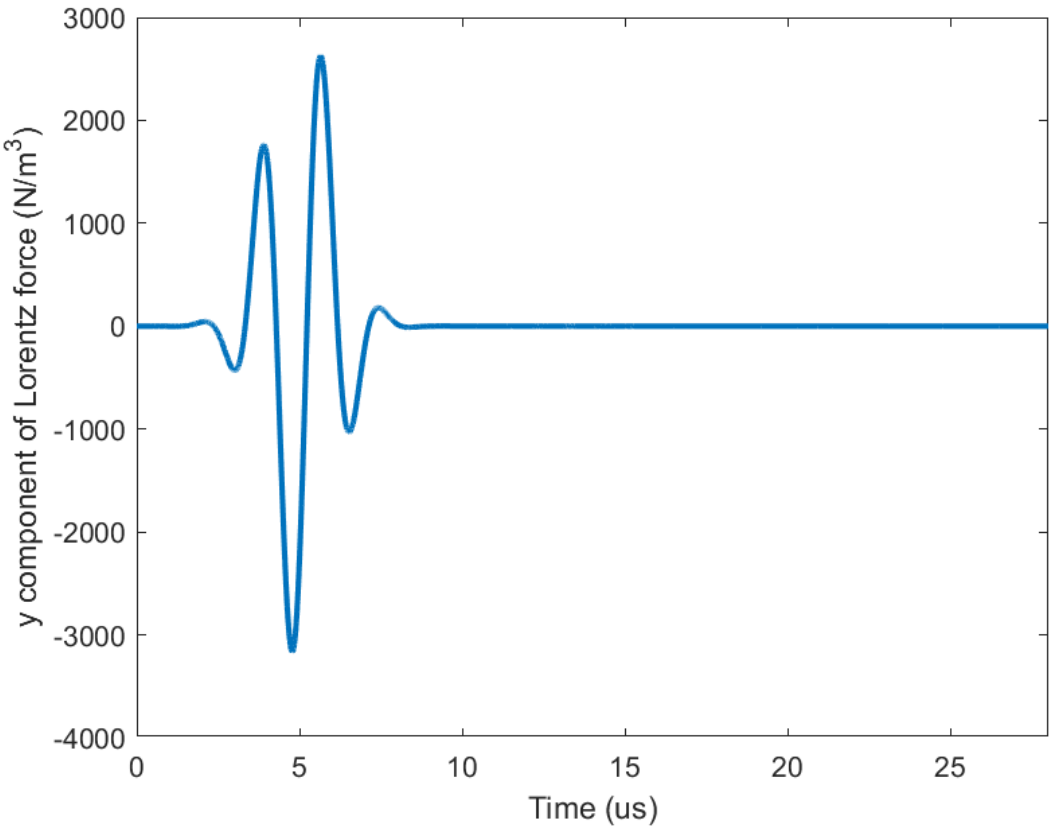

Figure 8.6 y-component of Lorentz force at measurement point in Aluminum strip

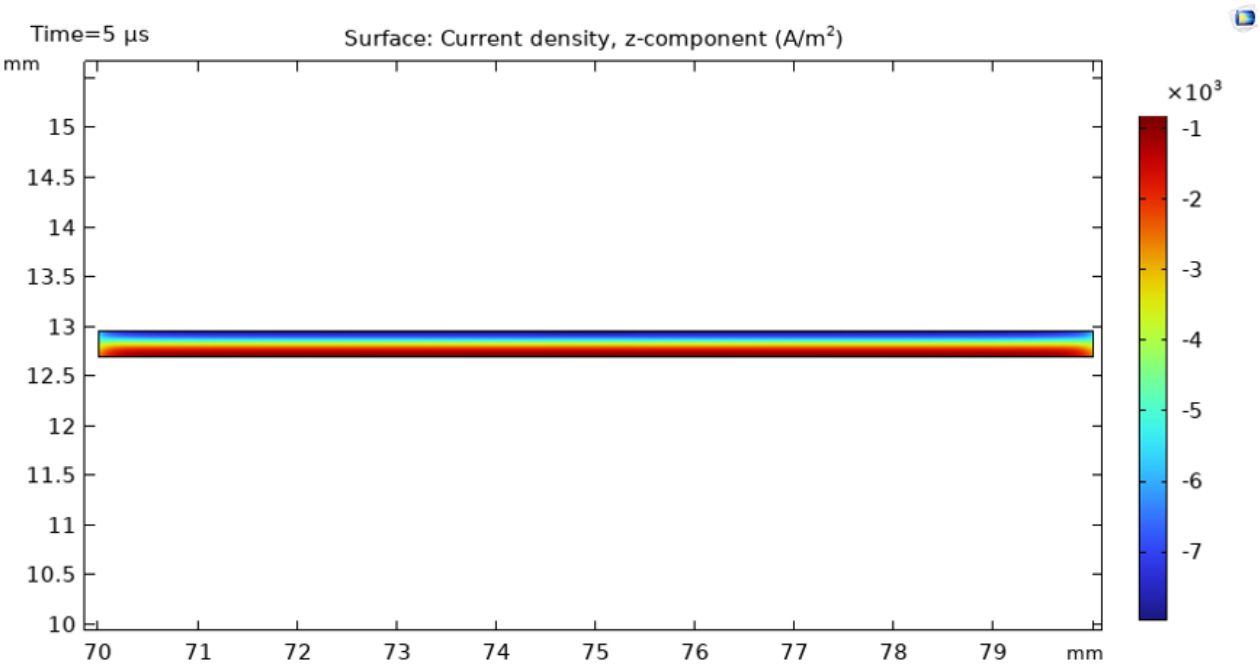

Figure 8.7 Surface plot of z-component of current density in Aluminum strip at 5 µs

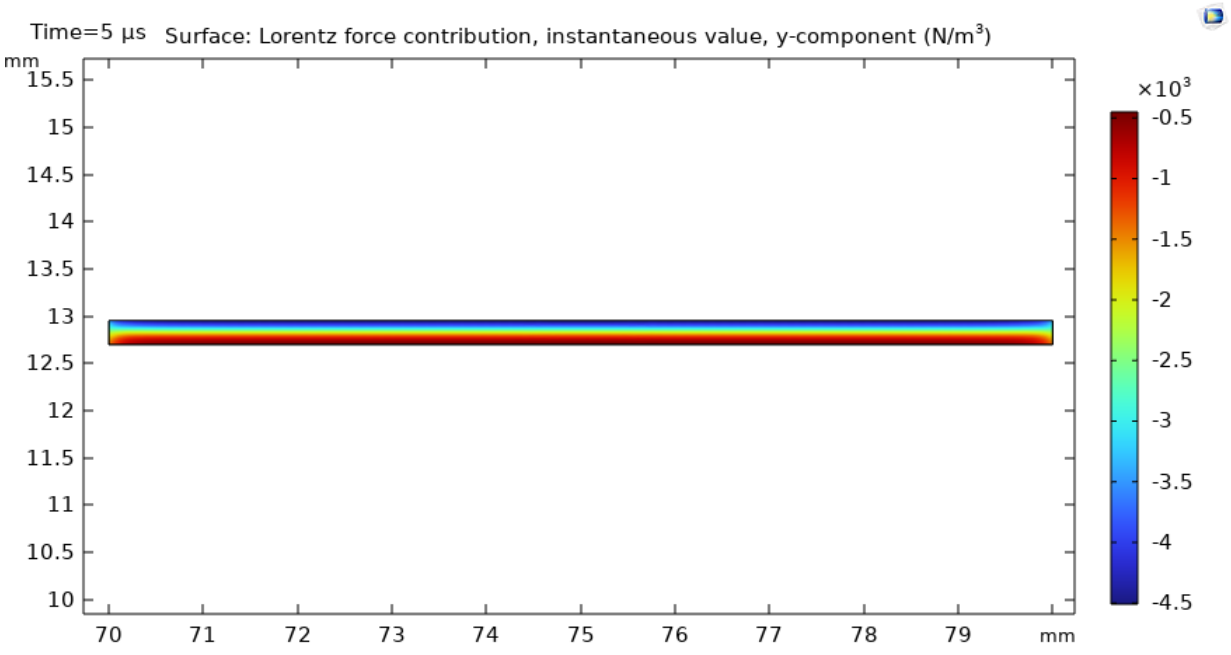

Figure 8.8 Surface plot of y-component of Lorentz force in Aluminum strip at 5 µs

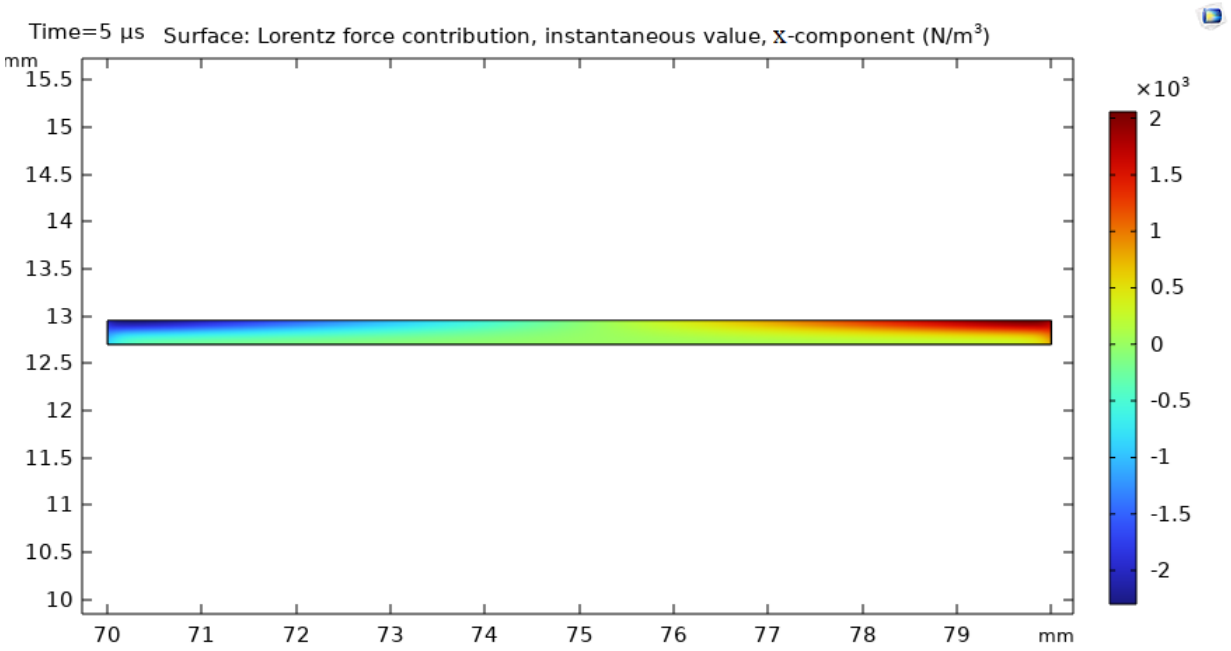

Figure 8.9 Surface plot of x-component of Lorentz force in Aluminum strip at 5 µs

Figure 8.10, Figure 8.11, and Figure 8.12 depict arrow surface plots of Lorentz force within the Aluminum strip at 5 µs. The arrow surface plots visually represent the skin effect, as previously discussed. Notably, the intriguing observation is the presence of the x-component of Lorentz force. This pattern in the x-component is a consequence of the variation in the y-component of magnetic

flux density. Such variations could give rise to coupled modes in the propagation of acoustic waves, adding complexity to the wave dynamics.

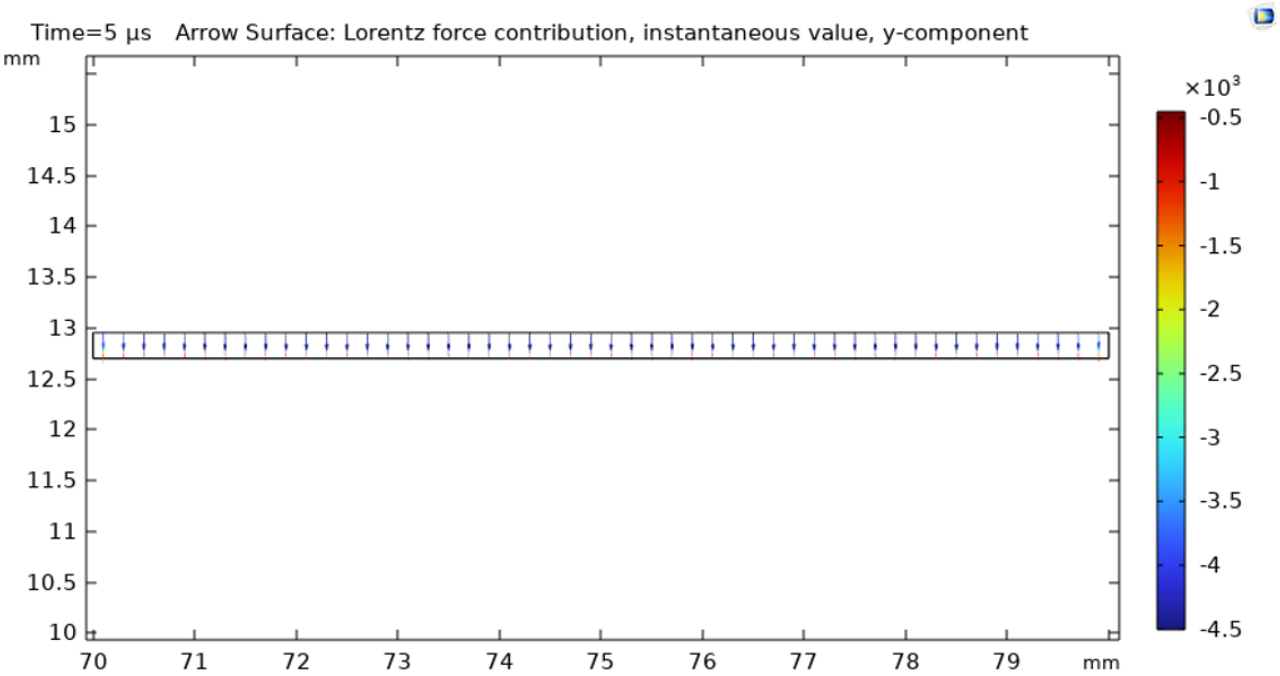

Figure 8.10 Arrow surface plot of y-component of Lorentz force (N/m^3) in Aluminum strip at 5 µs

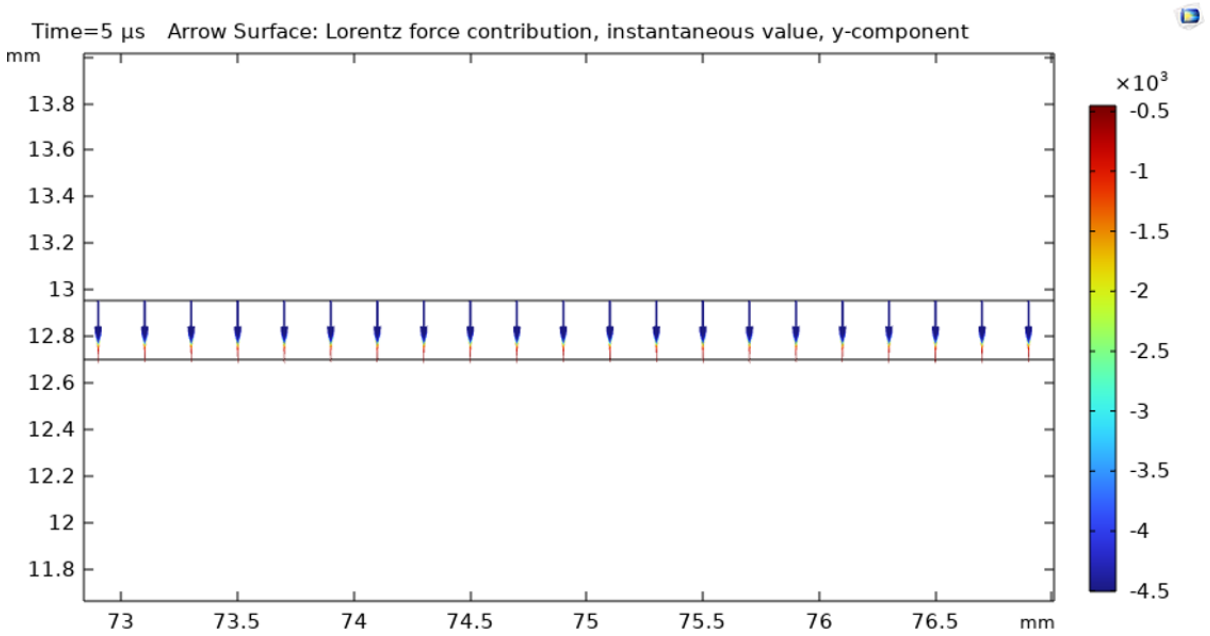

Figure 8.11 Zoomed version of Figure 8.10

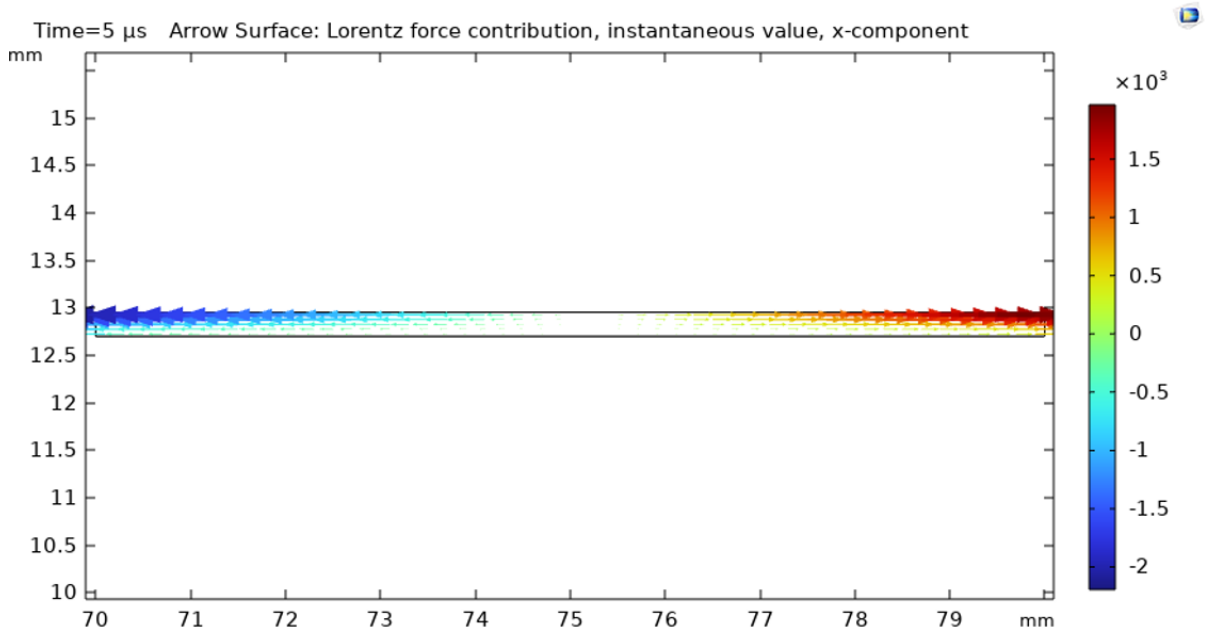

Figure 8.12 Arrow surface plot of x-component of Lorentz force (N/m^3) in Aluminum strip at 5 µs

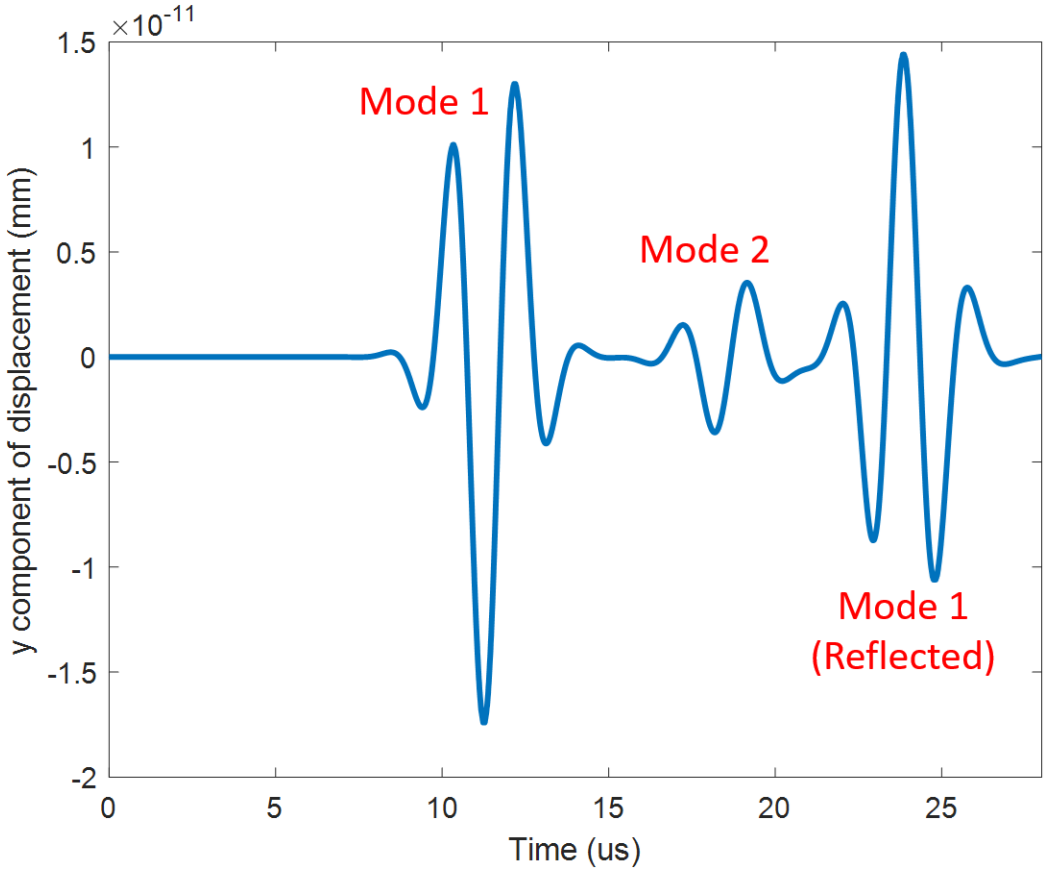

Figure 8.13 A-scan of displacement at measurement point on plastic back-wall

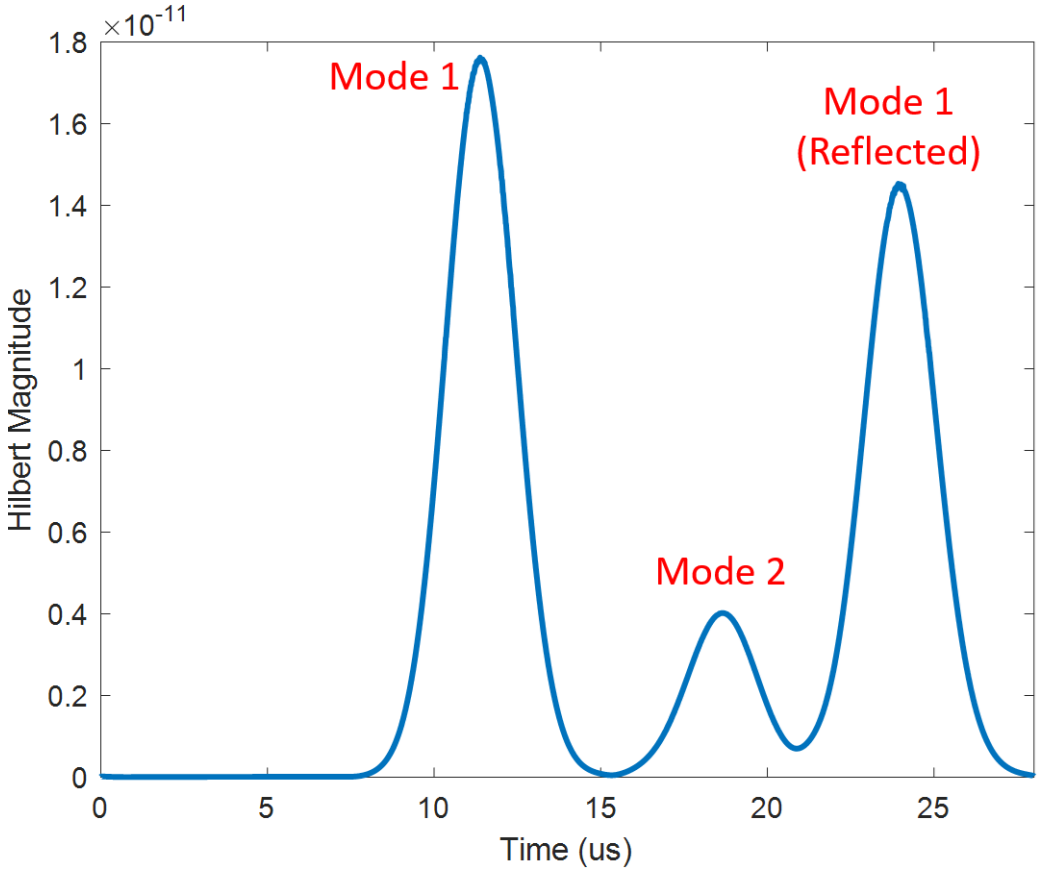

Figure 8.14 Hilbert magnitude of A-scan signal showed in Figure 8.13

Figure 8.13 shows the displacement at a measurement point on plastic back-wall (A-scan). Figure 8.14 shows the Hilbert magnitude plot for the A-scan of displacement. Few observations can be made from these plots:

1. The mode 1 (longitudinal wave) and the reflection of this wave can clearly be observed.
2. Mode 1 is expected to appear at 8.11 us from theoretical wave velocity calculation and can also be seen in the plot.
3. The interesting part to note here is the mode 2.

Wave velocity calculations

The longitudinal wave velocity for a solid sample can be calculated using (8.2),

$$V = \sqrt{\frac{E(1-v)}{\rho(1+v)(1-2v)}} \tag{8.2}$$

where:

V is the velocity of longitudinal wave,

E is the Young's modulus of the sample,

ρ is density of the sample,

v is the Poisson's ratio.

The theoretical value of longitudinal wave velocity for the non-conducting sample (acrylic plastic) using material properties (Table 8.1) can be calculated as 2077.45 m/s.

The Hilbert magnitude plot (Figure 8.14) is used to find the time at which mode 1, mode 2 and mode 3 peak. These values are given in Table 8.2. The wave velocities for mode 1 and mode 2 are calculated using the Hilbert magnitude data and sample thickness. These are presented in Table 8.3. The wave velocity of Mode 1 is comparable to the theoretical value of 2077.45 m/s. But, mode 2 has a velocity which is slightly greater than that of shear wave (half of longitudinal wave velocity) and much lesser than the longitudinal wave velocity. Hence, mode 2 can possibly be considered as a coupled mode.

Table 8.2 Time at which modes peak in Hilbert magnitude plot for Direct Excitation EMAT model

Mode	**Time (us)**
Mode 1	11.38
Mode 2	18.67
Mode 1 (reflected)	23.93

Table 8.3 Mode velocities for Direct excitation EMAT model

Mode	**Velocity (m/s)**
Mode 1	2023.9
Mode 2	1280.23

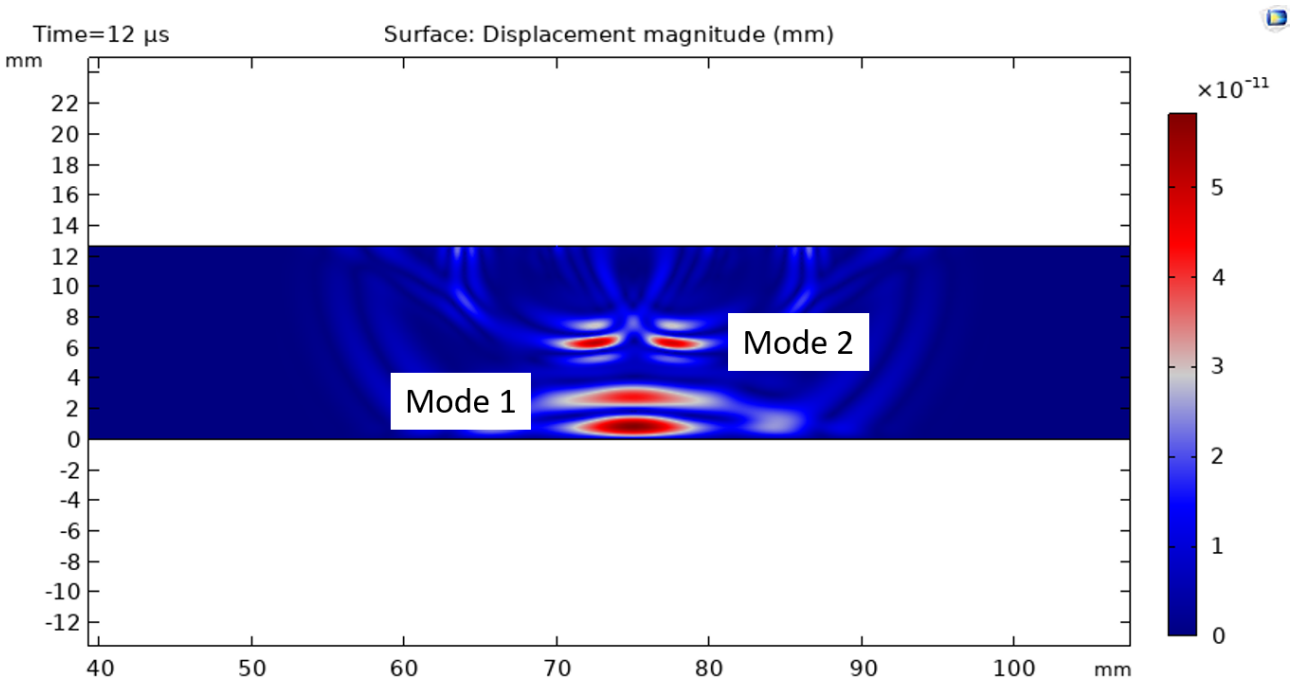

Figure 8.15 Surface plot of full-field displacement in plastic at 12 µs

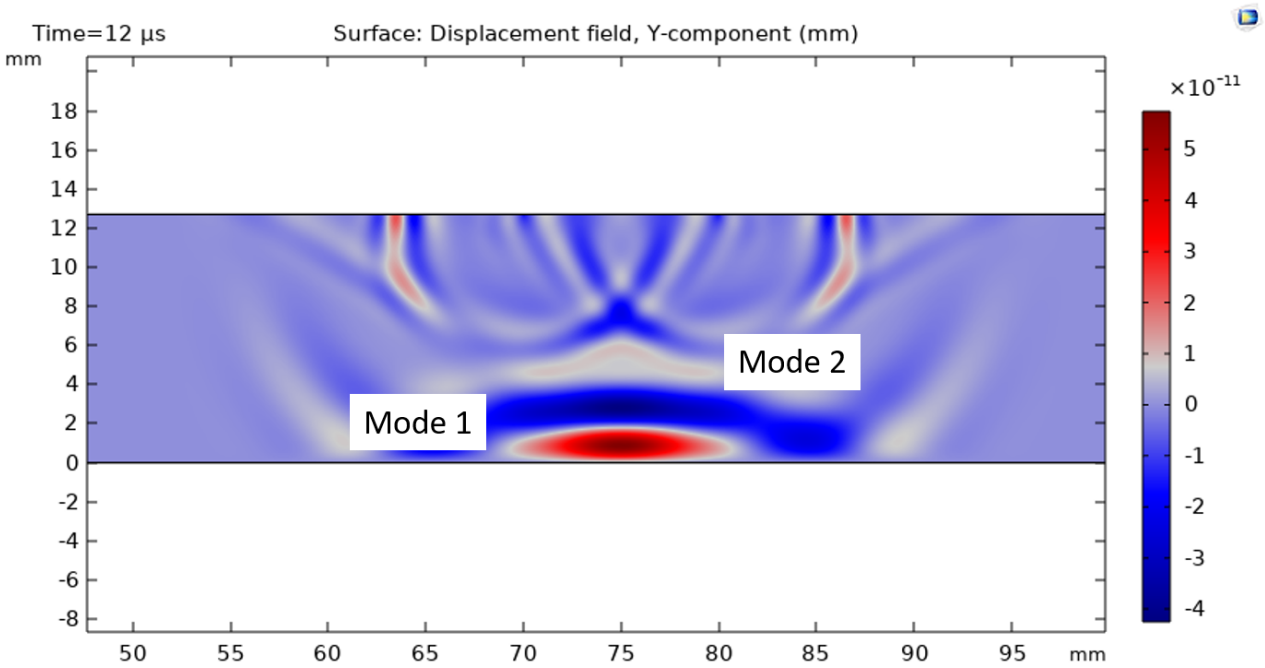

Figure 8.16 Surface plot of y-component of displacement in plastic at 12 µs

Figure 8.15, Figure 8.16 and Figure 8.17 shows the full-field displacement plots in the sample at 12 µs. 12 µs is chosen for a good representation of the wave modes. These plots validate the propagation of an acoustic wave in the non-conducting sample and provides a visual representation

of wave propagation in plastic. The mode 1 and mode 2 can be clearly observed in these plots.

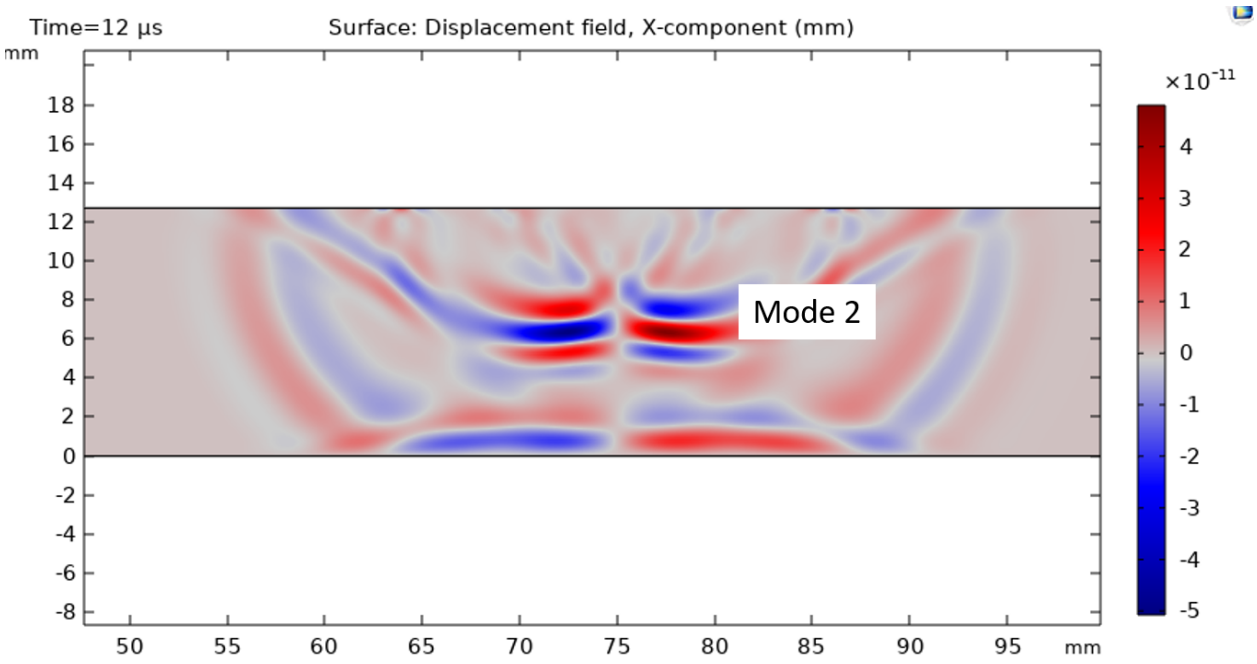

Figure 8.17 Surface plot of x-component of displacement in plastic at 12 µs

8.2 Effect of input current on Lorentz force and displacement in sample

This study aims to provide further validation for the EMAT direct excitation model by investigating the impact of two different input current magnitudes applied to the aluminum strip. Notably, all model parameters are maintained with precision throughout this investigation to ensure consistency.

Figure 8.18 and Figure 8.19 showcase the Lorentz force (in Aluminum strip at measurement point described earlier) and displacement A-scan (in plastic at measurement point on the back-wall) plots corresponding to input current magnitudes of 1A and 2A. It's essential to emphasize that the preceding results were presented for the current magnitude (peak) of 1A. This study serves as a validation step for the direct excitation model, confirming the expected doubling effect in both the Lorentz force within the aluminum strip and the resulting displacement in the plastic material with the increased input current magnitude.

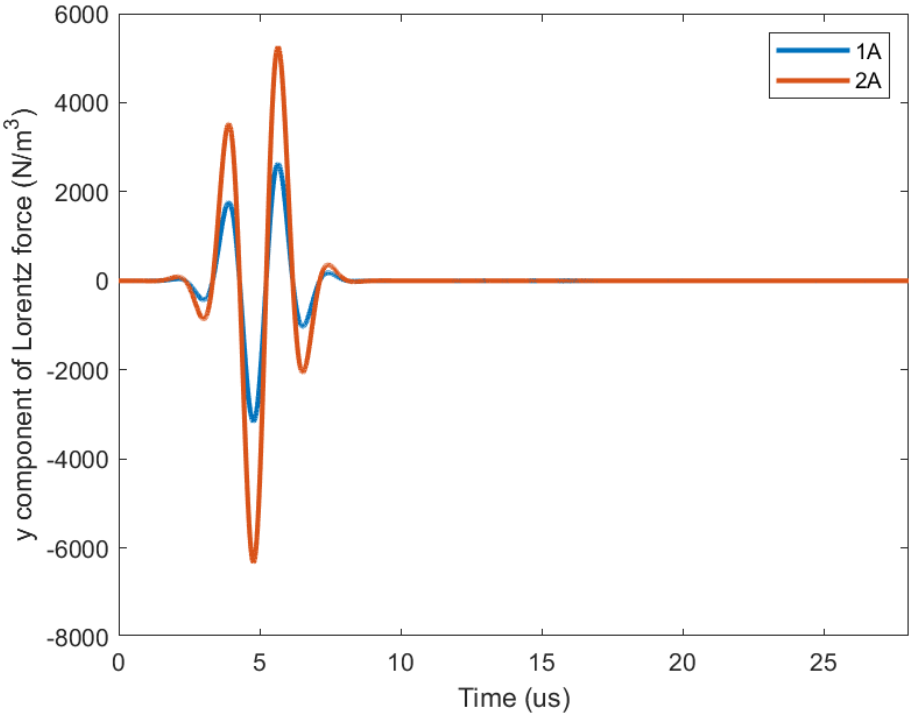

Figure 8.18 Comparison of Lorentz force at measurement point in Aluminum strip for varying coil current magnitudes

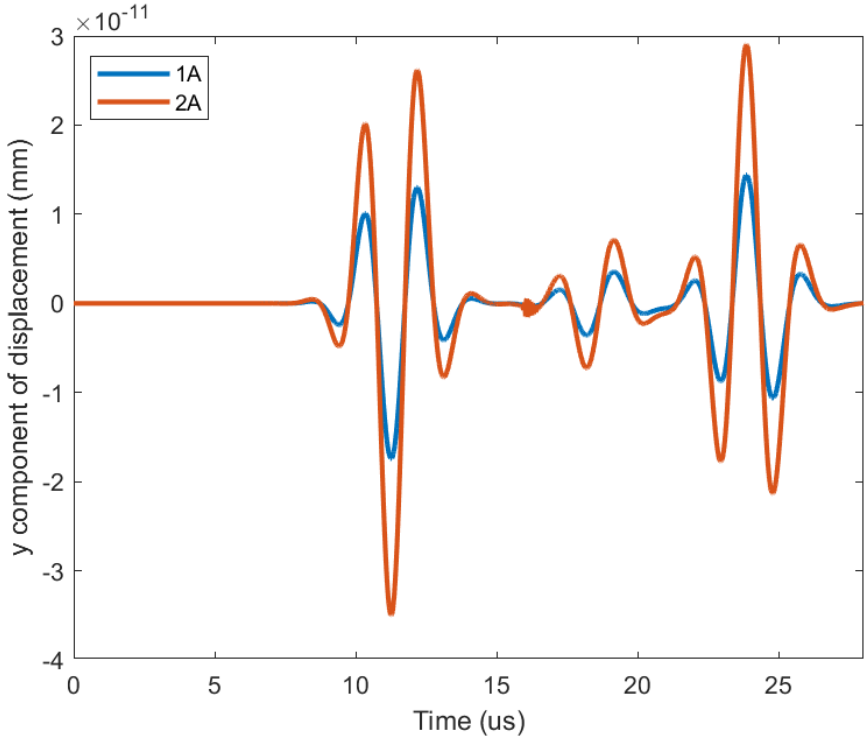

Figure 8.19 Comparison of A-scans of displacement at measurement point on plastic back-wall for varying coil current magnitudes

8.3 Effect of Aluminum strip geometry on displacement in sample

This section delves into an exploration of the influence of Aluminum strip width and height on the displacement within the sample (plastic). The objective is to study and analyze the effects of varying dimensions of the Aluminum strip on the observed acoustic modes within the EMAT model. This investigation contributes to an understanding of how geometric parameters impact the displacement characteristics, thereby providing valuable insights for optimizing EMAT design and performance.

8.3.1 Aluminum strip width variation

In this study, all model parameters remain constant, with the exception of the width of aluminum strip. The chosen widths for the aluminum strip in this study are 10mm and 5mm.

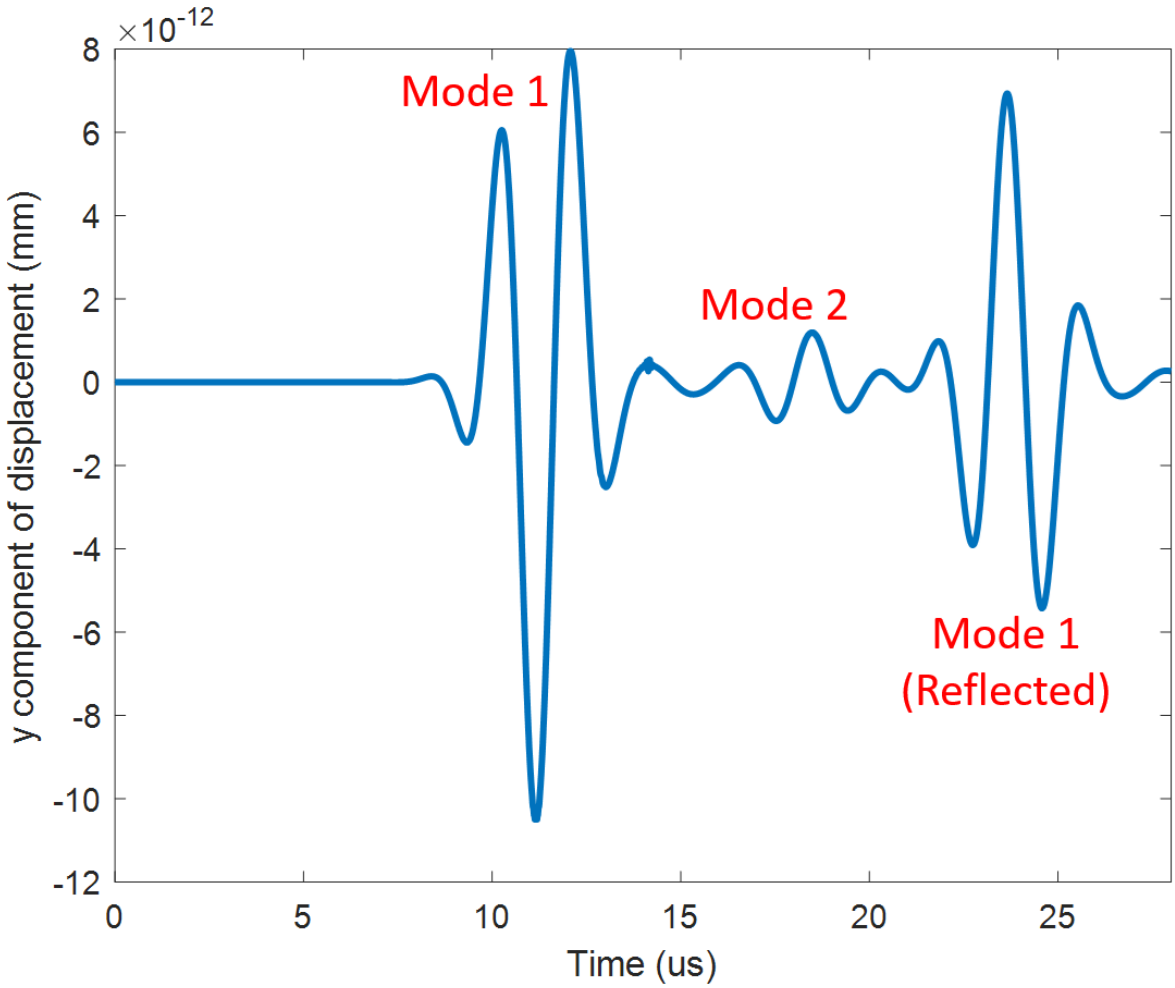

Figure 8.20 A-scan of displacement for Aluminum strip width = 5mm

Figure 8.20 illustrates the displacement A-scan at the plastic back-wall (measurement point) for an aluminum strip width of 5mm. Mode 1 is clearly observable, and it appears at the expected time of 8.11 us. Additionally, Mode 2 remains present.

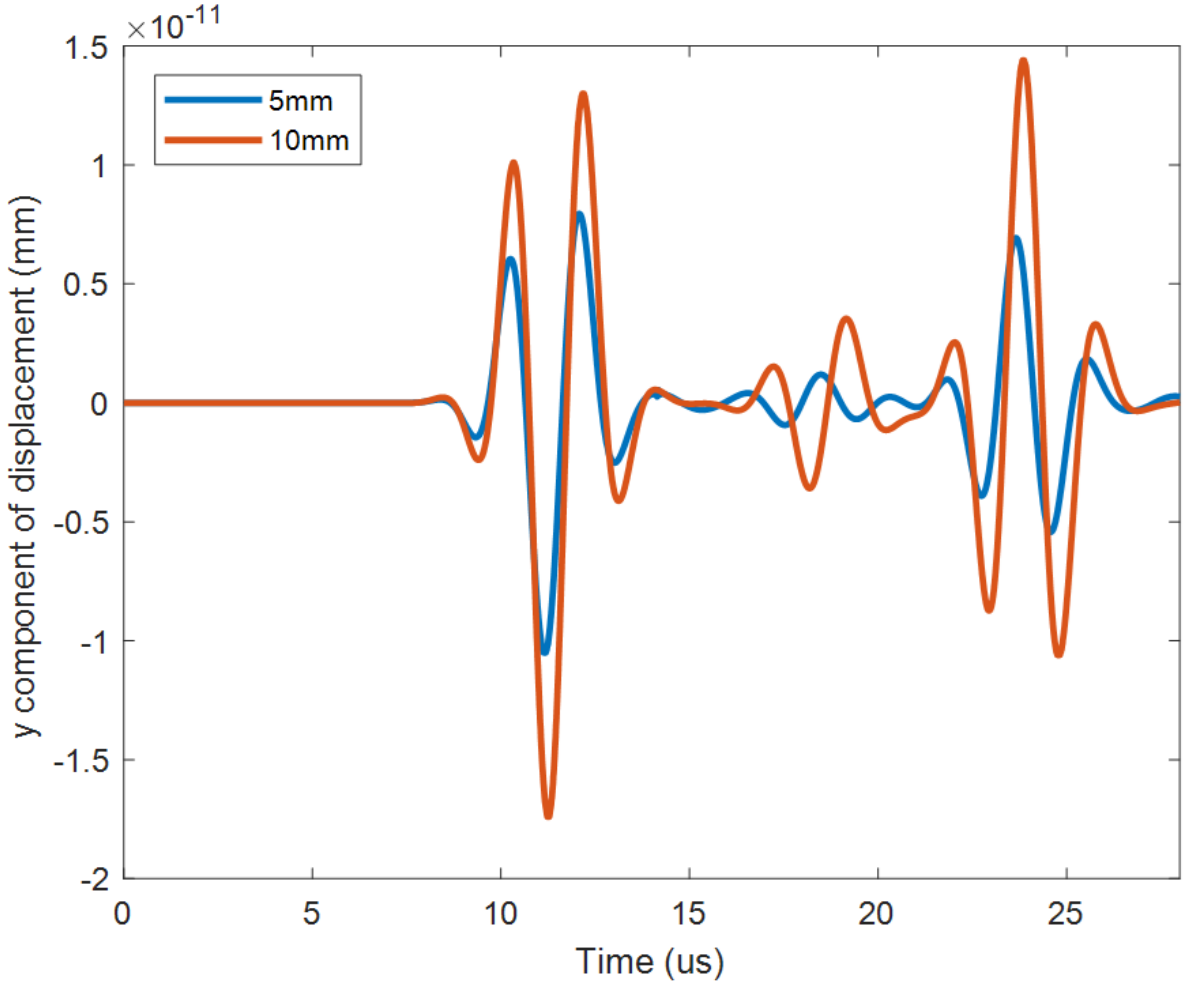

Figure 8.21 Comparison of displacement A-scans for varying Aluminum strip widths

Figure 8.21 provides a comparison of displacement A-scans for varying aluminum strip widths, specifically 10mm and 5mm. The observed increase in displacement amplitude for the 10mm aluminum width is attributed to the larger source width. Furthermore, maintaining a consistent input current leads to an increase in the effective line current for the 10mm Aluminum strip width, contributing to the amplified displacement amplitude. Acoustically, the larger source width narrows the beam spread, concentrating more acoustic energy at the center of the beam. This phenomenon is reflected in the displacement A-scan, clearly showcasing the increased displacement amplitude

for the 10mm aluminum strip width. This analysis offers valuable insights into the intricate interplay between geometric parameters (of Aluminum strip) and the electromagnetic and acoustic characteristics within the context of EMAT design.

Figure 8.22, Figure 8.23 and Figure 8.24 shows the full-field displacement plots in the sample at 12 µs for aluminum strip width of 5mm. These plots validate the propagation of an acoustic wave in the non-conducting sample, as in the previous case (aluminum strip width = 10mm). Also, the mode 1 and mode 2 can clearly be observed in these plots. The amplitude of displacements (in plastic) are reduced when compared to the previous set of results (Figure 8.15, Figure 8.16 and Figure 8.17, i.e., for Aluminum strip width = 10mm).

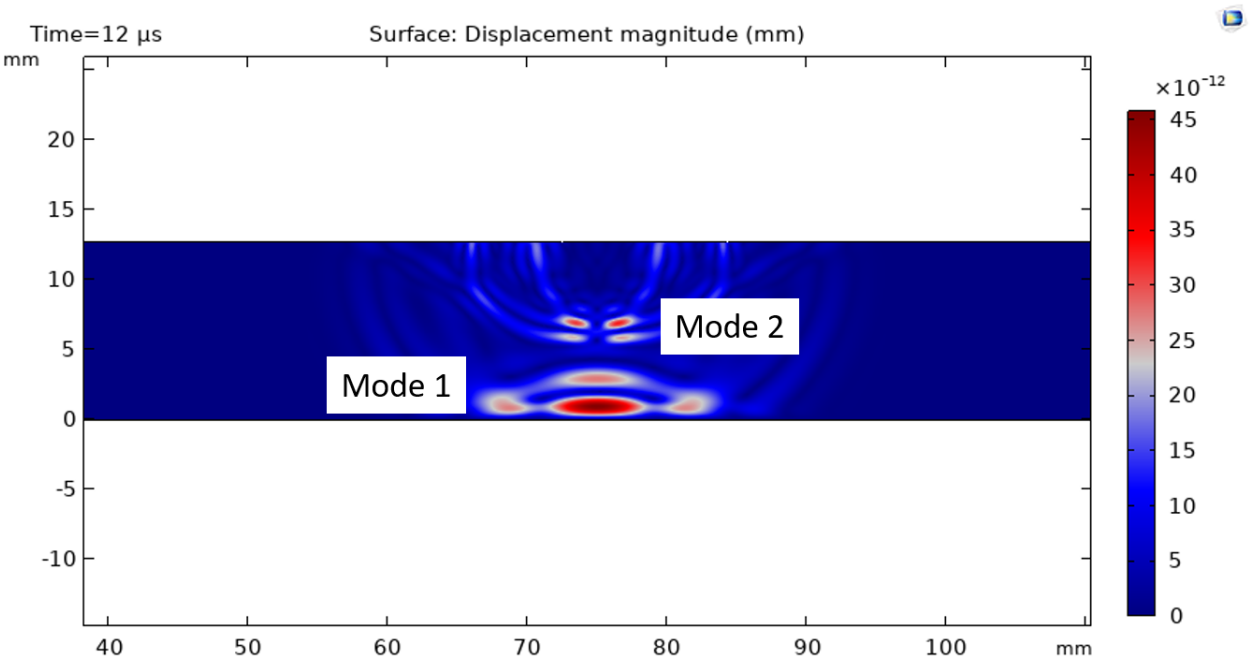

Figure 8.22 Surface plot of full-field displacement in plastic at 12 µs for Aluminum strip width = 5mm

Current density and Lorentz force plots are presented in Figure 8.25, Figure 8.26, Figure 8.27, Figure 8.28 and Figure 8.29 for aluminum strip width of 5mm. The presence of non-zero x-component of Lorentz force, attributed to the y-component of magnetic flux density, is still evident in these plots. The overall pattern remains similar when compared to the plots with an aluminum strip width of 10mm, as anticipated.

Units of Lorentz force in Figure 8.28 and Figure 8.29 are N/m^3. This concludes the study of

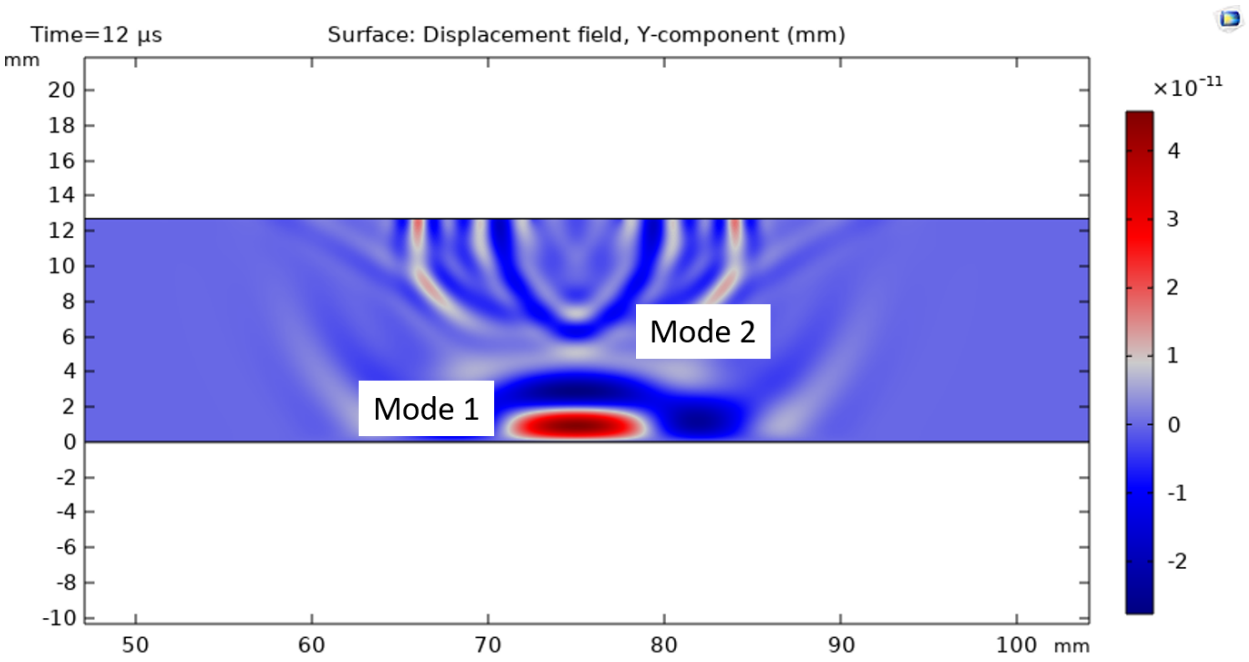

Figure 8.23 Surface plot of y-component of displacement in plastic at 12 µs for Aluminum strip width = 5mm

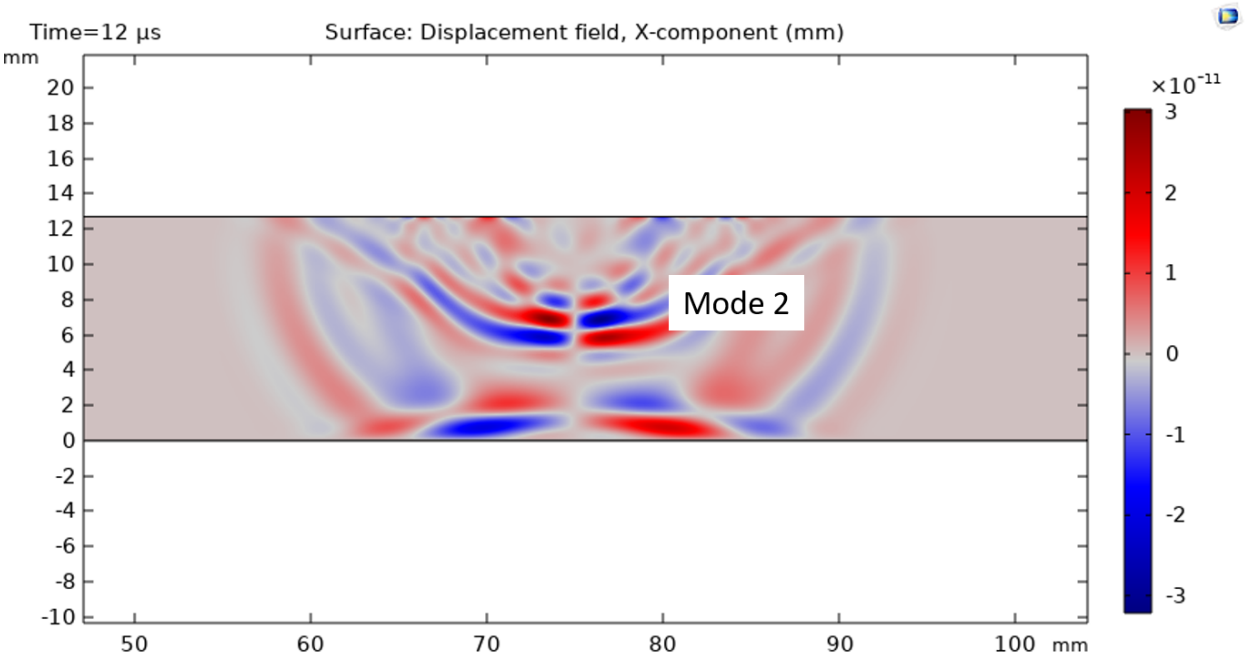

Figure 8.24 Surface plot of x-component of displacement in plastic at 12 µs for Aluminum strip width = 5mm

variation in aluminum strip width. The following subsection explores the impact of aluminum strip height on the displacement in plastic.

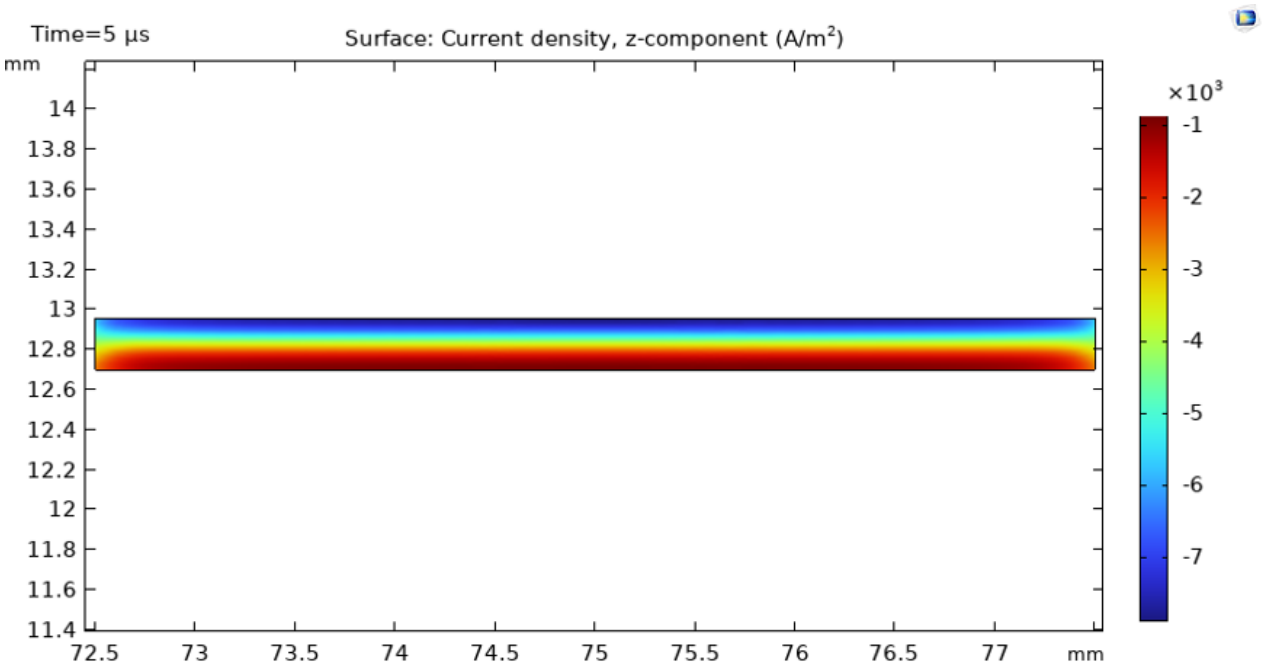

Figure 8.25 Surface plot of z-component of current density in Aluminum strip for strip width = 5mm

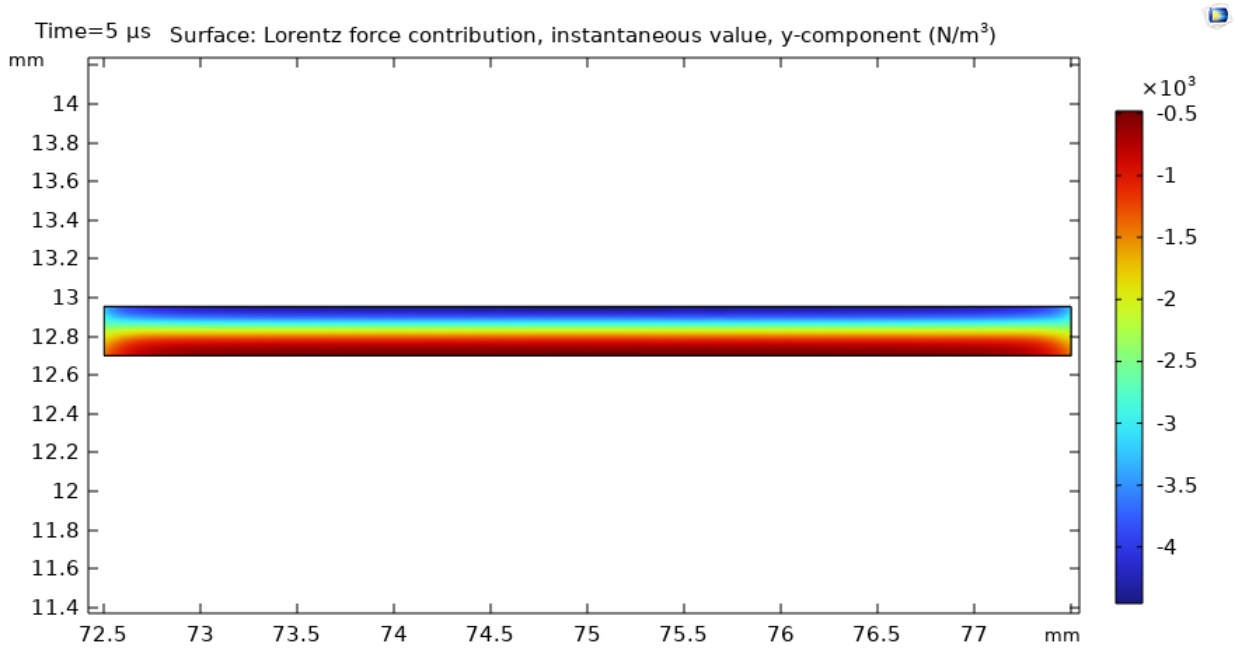

Figure 8.26 Surface plot of y-component of Lorentz force in Aluminum strip at 5 µs for strip width = 5mm

8.3.2 Aluminum strip height variation

In this investigation, the study maintains uniformity in all model parameters, except for the height of the aluminum strip. The objective is to assess the influence of varying aluminum strip

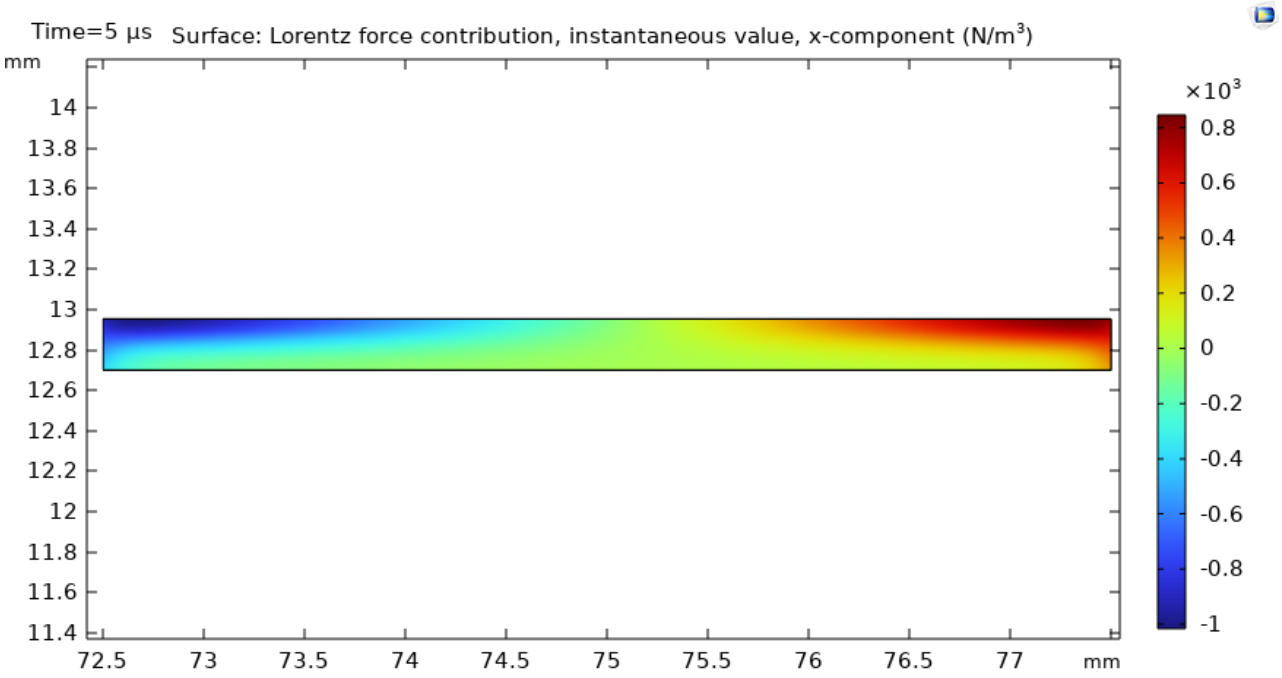

Figure 8.27 Surface plot of x-component of Lorentz force in Aluminum strip at 5 µs for strip width = 5mm

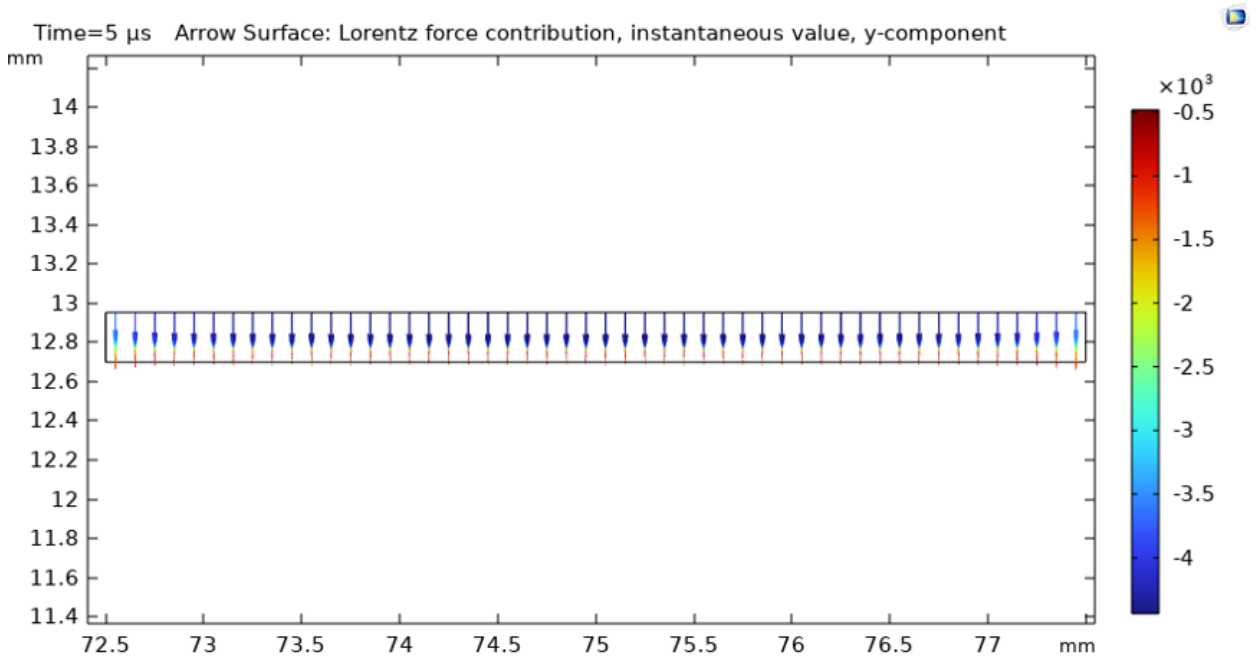

Figure 8.28 Arrow surface plot of y-component of Lorentz force in Aluminum strip at 5 µs for strip width = 5mm

heights on the displacement observed in the sample. The selected heights for the aluminum strip in this particular study are 0.25 mm and 0.1 mm.

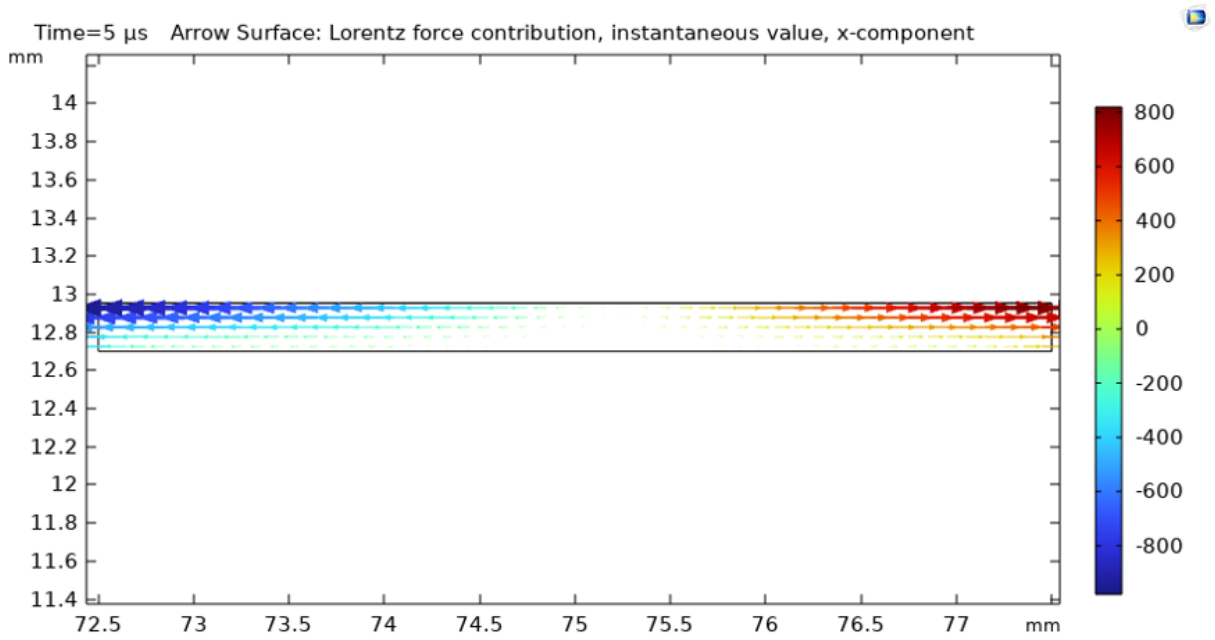

Figure 8.29 Arrow surface plot of x-component of Lorentz force in Aluminum strip at 5 µs for strip width = 5mm

Figure 8.30 represents the displacement A-scan at the plastic back-wall, precisely at the measurement point, for an aluminum strip height of 0.1mm. Notably, both modes are still present, as seen from the plot.

Figure 8.31 provides a comparative analysis of displacement A-scans for aluminum heights of 0.25 mm and 0.1 mm. Notably, the displacement amplitude for the 0.1mm aluminum strip height surpasses that of the 0.25mm aluminum strip height. This observed difference is attributed to the skin effect of the aluminum strip. It is essential to consider that the skin depth of the aluminum strip at 500 kHz is approximately 116 µm. As the aluminum height decreases, the Lorentz force increases, consequently resulting in an enhanced displacement at the sample back-wall.

Figure 8.32, Figure 8.33 and Figure 8.34 shows the full-field displacement plots in the sample at 12 µs. These plots validate the propagation of an acoustic wave in the non-conducting sample, as in the previous case (aluminum strip height = 0.25mm). Also, the mode 1 and mode 2 can clearly be observed in these plots. The amplitude of displacements are increased when compared to Figure 8.15, Figure 8.16 and Figure 8.17 (aluminum strip height = 0.25mm).

Current density and Lorentz force plots are presented in Figure 8.35, Figure 8.36 and Figure 8.37.

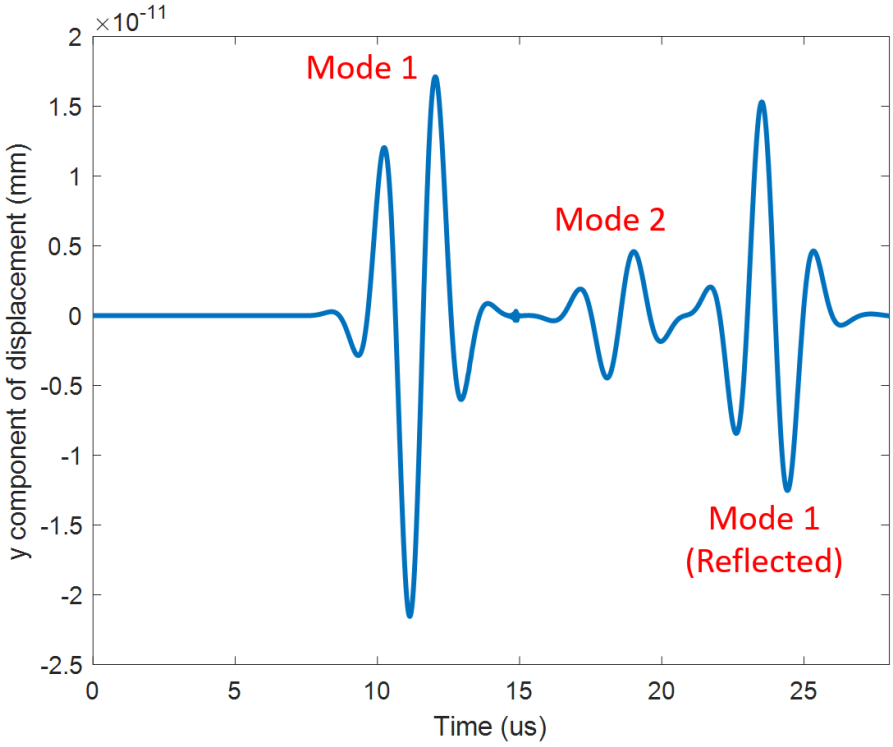

Figure 8.30 A-scan of displacement at measurement point on plastic back-wall for Aluminum strip height = 0.1mm

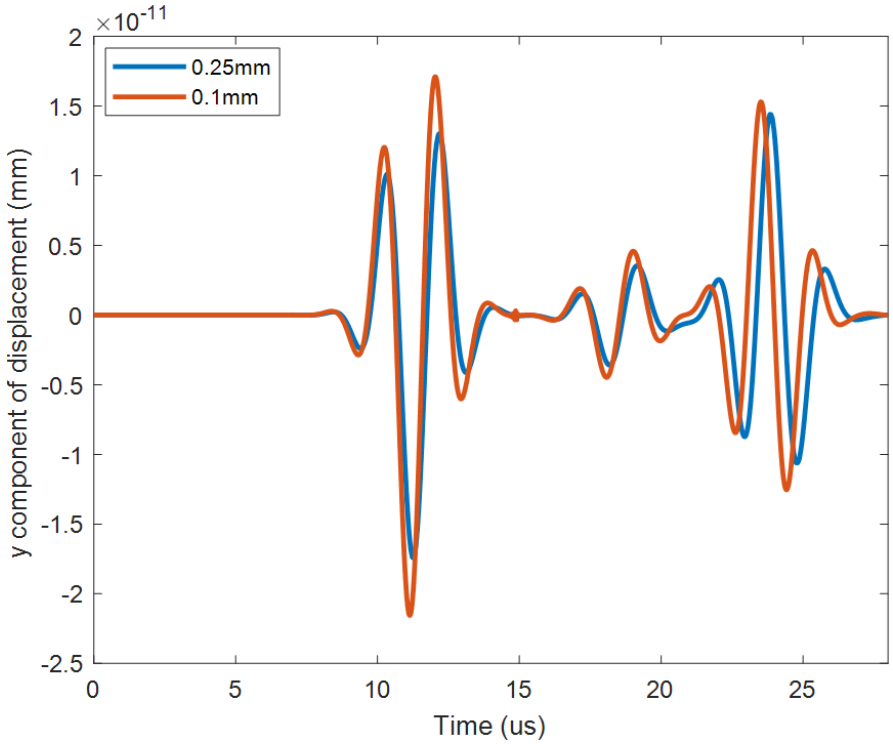

Figure 8.31 Comparison of displacement A-scans for varying Aluminum strip heights

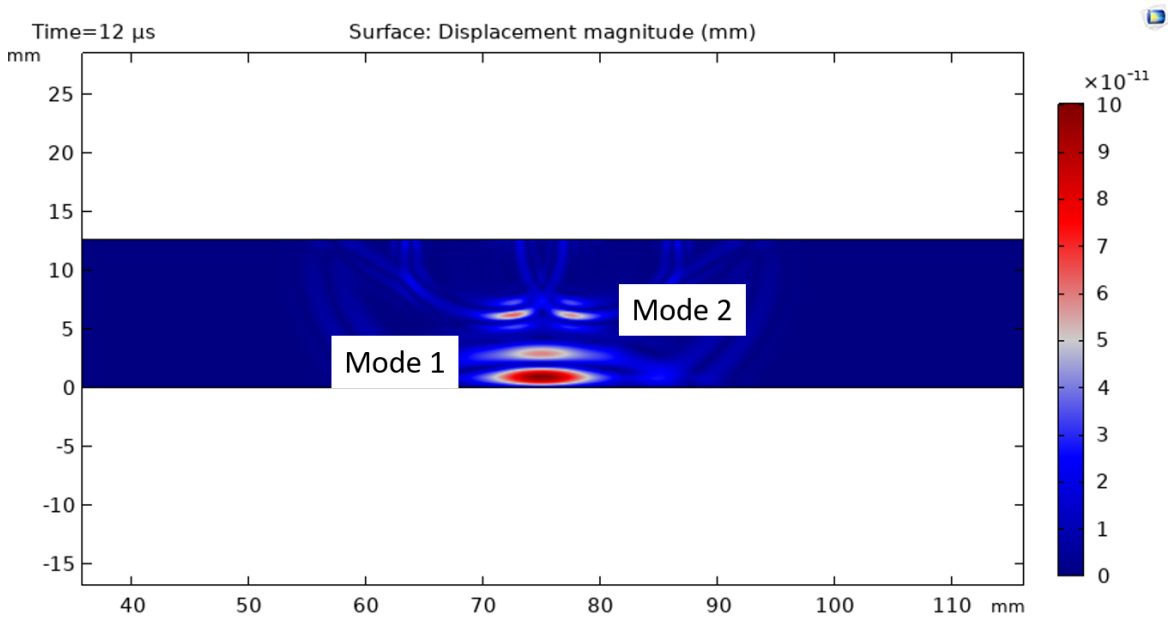

Figure 8.32 Surface plot of full-field displacement in plastic at 12 µs for Aluminum strip height = 0.1mm

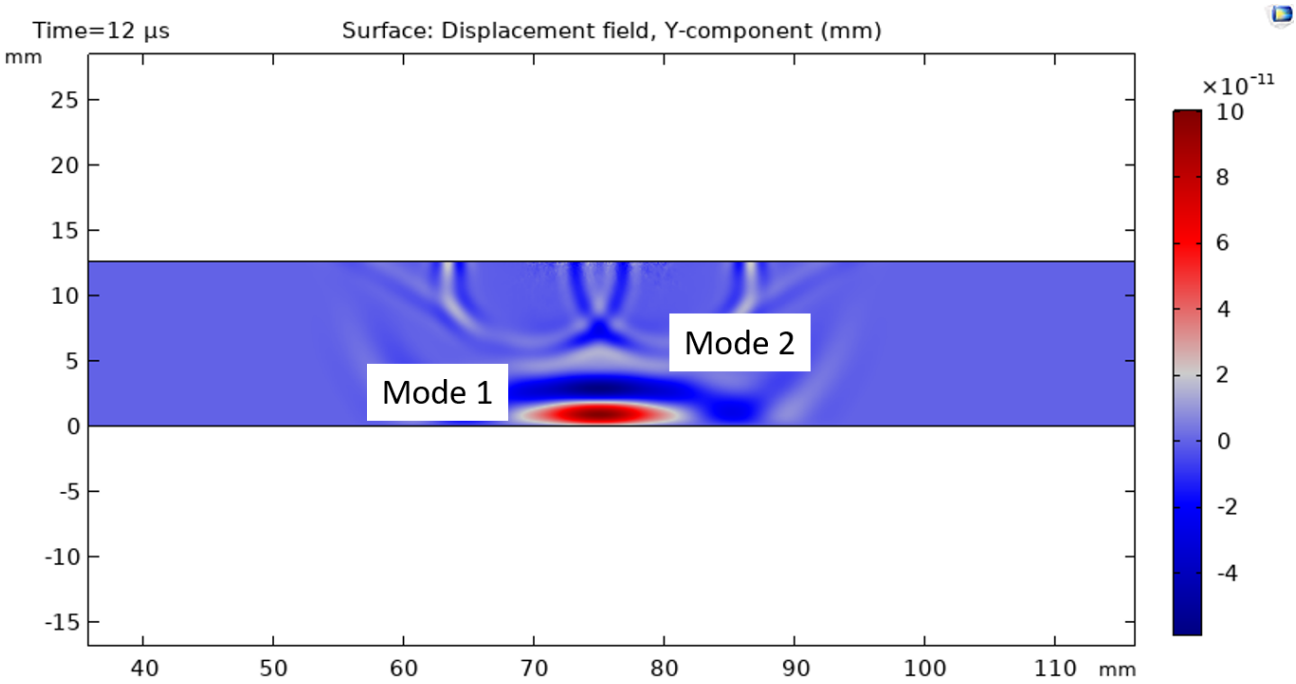

Figure 8.33 Surface plot of y-component of displacement in plastic at 12 µs for Aluminum strip height = 0.1mm

The pattern is similar when compared to plots with Aluminum strip width of 10mm, as expected.

Units of Lorentz force in Figure 8.36 and Figure 8.37 are N/m^3.

The interesting thing to observe is the variation of current density and Lorentz force inside

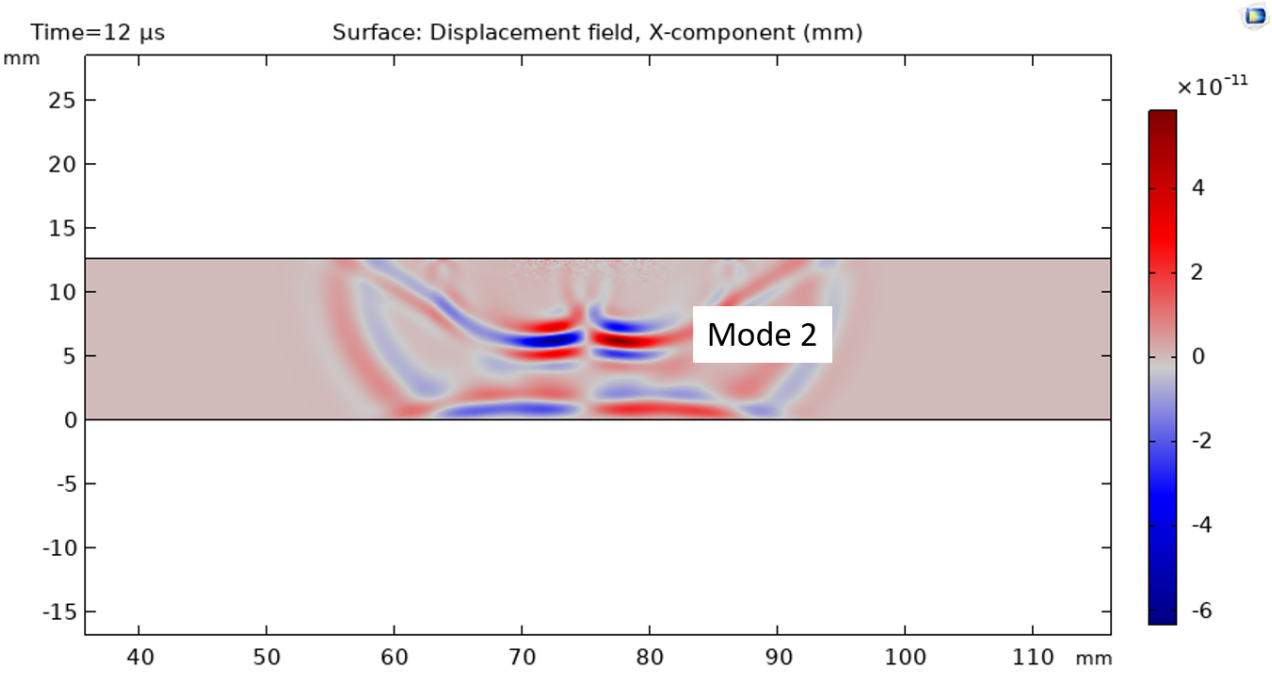

Figure 8.34 Surface plot of x-component of displacement in plastic at 12 µs for Aluminum strip height = 0.1mm

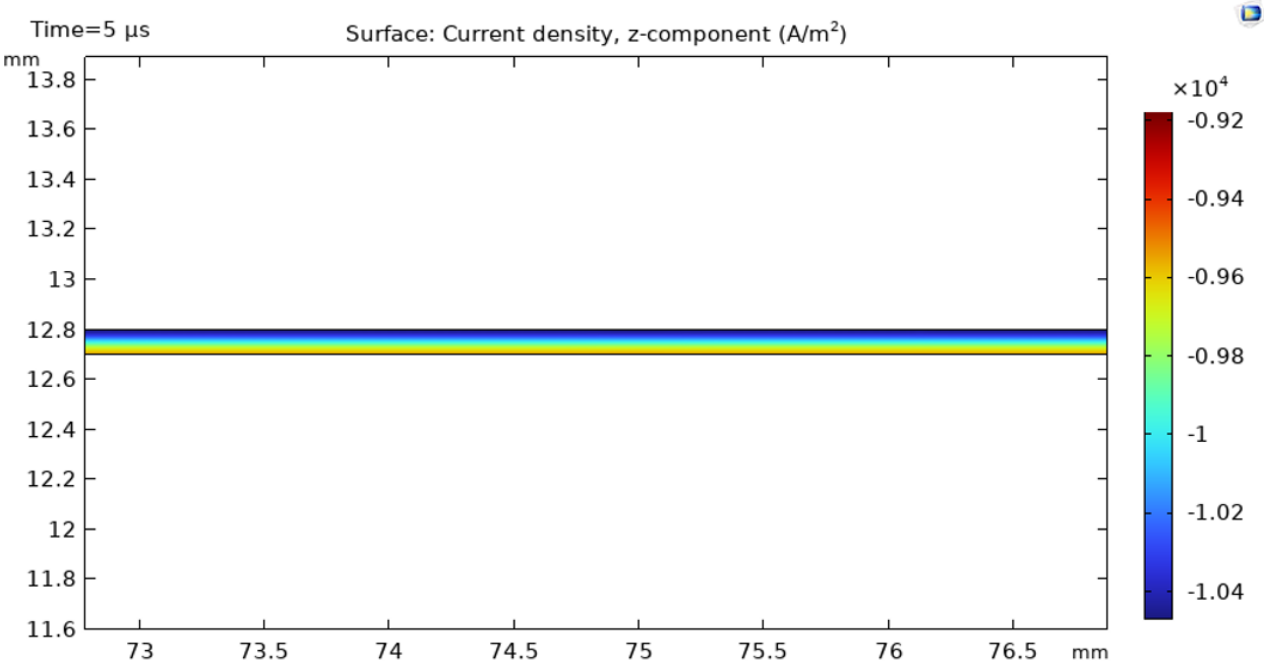

Figure 8.35 Surface plot of z-component of current density in Aluminum strip for strip height = 0.1mm

Aluminum strip. The variation is much lesser in the case where aluminum strip height is 0.1mm compared to when the aluminum strip height is 0.25mm (Figure 8.7, Figure 8.8, Figure 8.9, Fig-

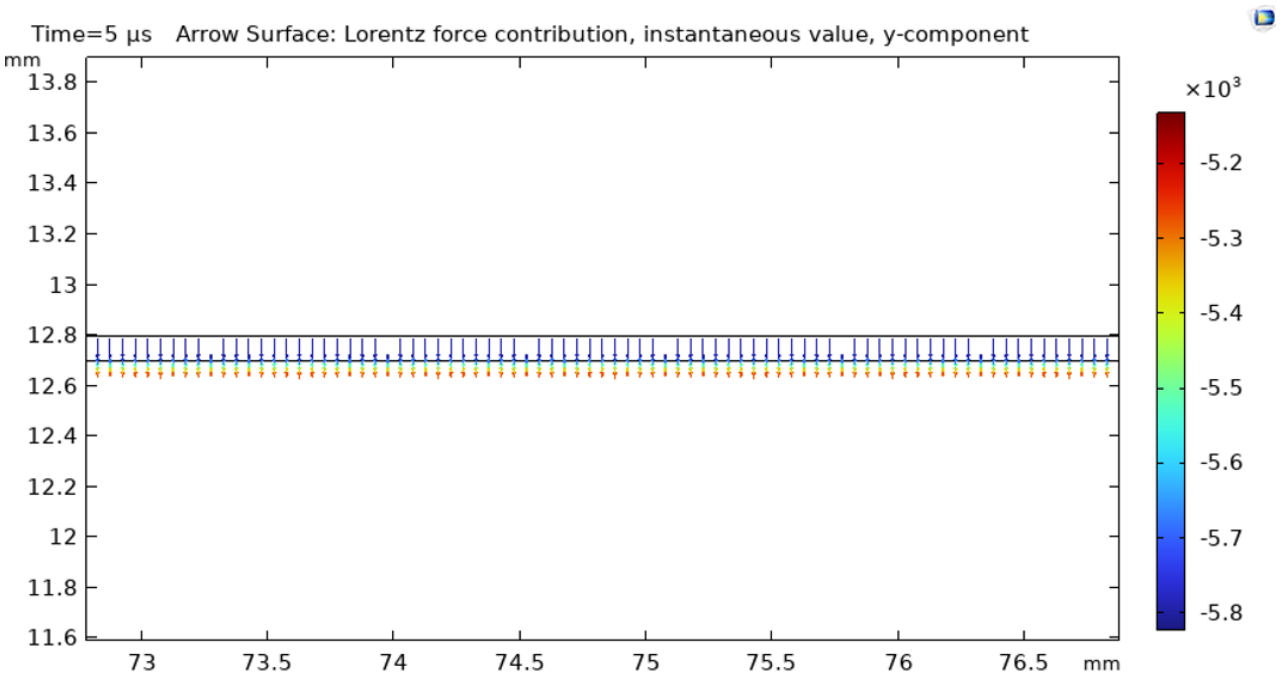

Figure 8.36 Arrow surface plot of y-component of Lorentz force in Aluminum strip at 5µs for strip height = 0.1mm

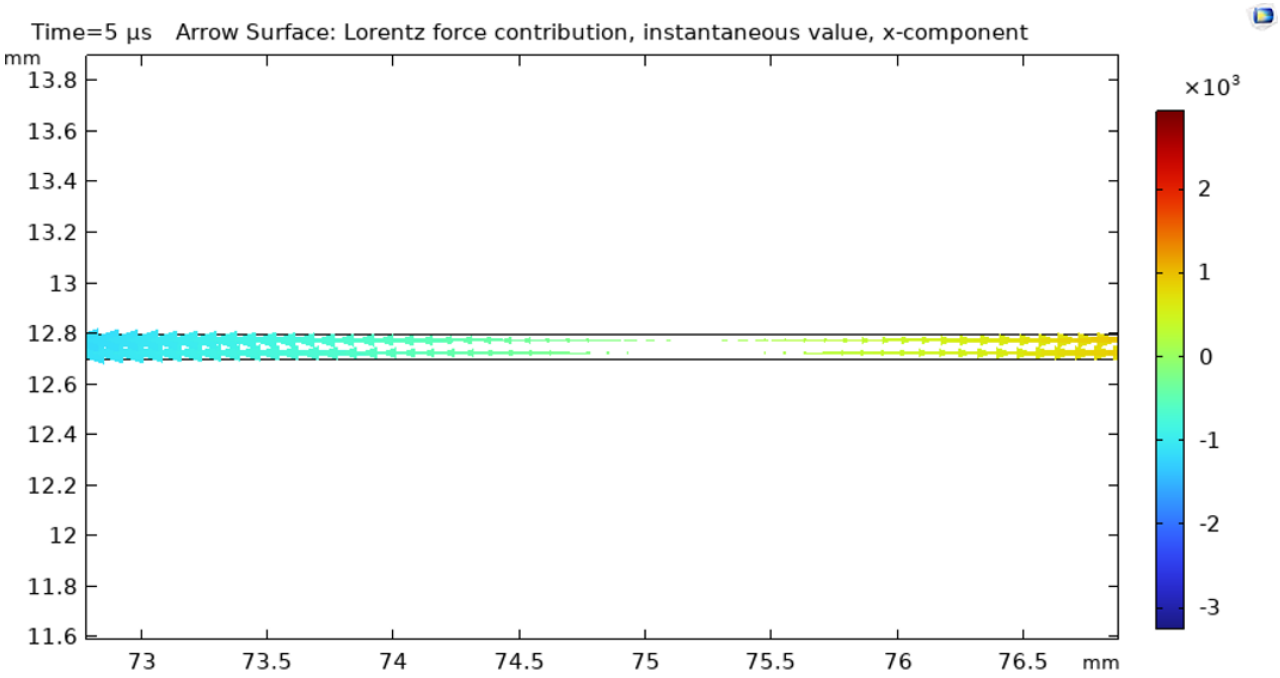

Figure 8.37 Arrow surface plot of x-component of Lorentz force in Aluminum strip at 5µs for strip height = 0.1mm

ure 8.10, Figure 8.11 and Figure 8.12). The decrease in Lorentz force variation is attributed to the skin effect. In the subsequent section, the numerical outcomes of a parametric study are presented

to delve deeper into comprehending the skin effect of aluminum on the displacement within the sample.

8.4 Impact of skin effect in Aluminum strip on displacement in sample

This section delves into the skin effect of the aluminum strip and its effect on the displacement within the plastic sample. Figure 8.38 offers a quantitative evaluation of displacement at the

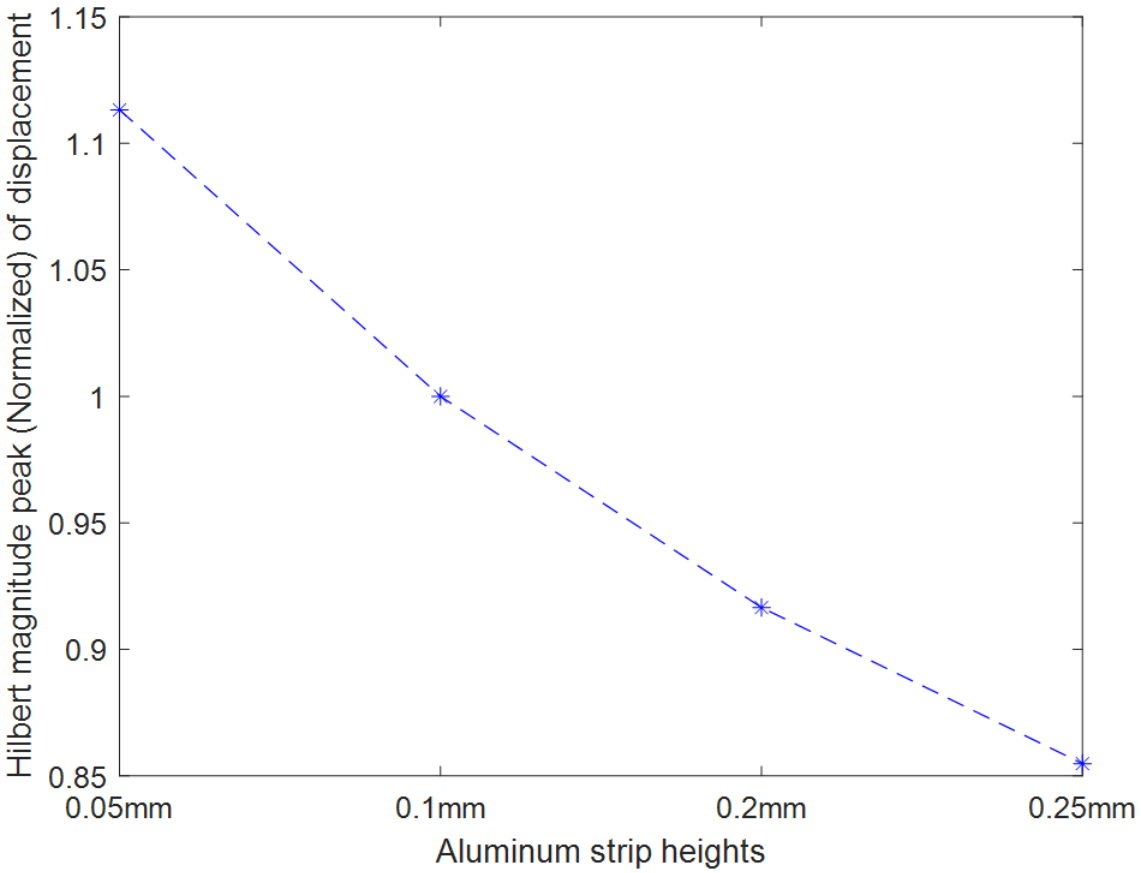

Figure 8.38 Comparison of Hilbert magnitude peaks of A-scans of displacement in plastic, for mode 1, and for different aluminum strip heights

plastic back-wall, shedding light on the influence of the skin effect in the aluminum strip. The skin depth of Aluminum at 500 kHz is calculated to be approximately 116 µm (as determined by equation (7.2)). The analysis encompasses four distinct aluminum strip heights (0.05mm, 0.1mm, 0.2mm, and 0.25mm). The Hilbert magnitudes of mode 1 (representing the longitudinal wave) are normalized relative to the Hilbert magnitude peak observed in the case of approximately 100% skin depth (i.e., aluminum strip height = 0.1mm).

The response exhibits an exponential trend, aligning with theoretical expectations. Additionally,

the findings highlight that optimal displacement in plastic occurs at half skin depth, a result of the heightened Lorentz force in the aluminum strip as the height decreases from 0.25mm to 0.05mm. In practical applications, setting the aluminum strip height to one skin depth, rather than half skin depth (i.e., 0.05mm), proves advantageous, facilitating a higher current input that can be provided to the aluminum strip. The following section is dedicated to the experimental validation of the induced EMAT configuration.

8.5 Experimental validation

This section focuses on the experimental validation of the EMAT model, providing a comparison between experimental and simulation results. The experimental validation in this chapter is

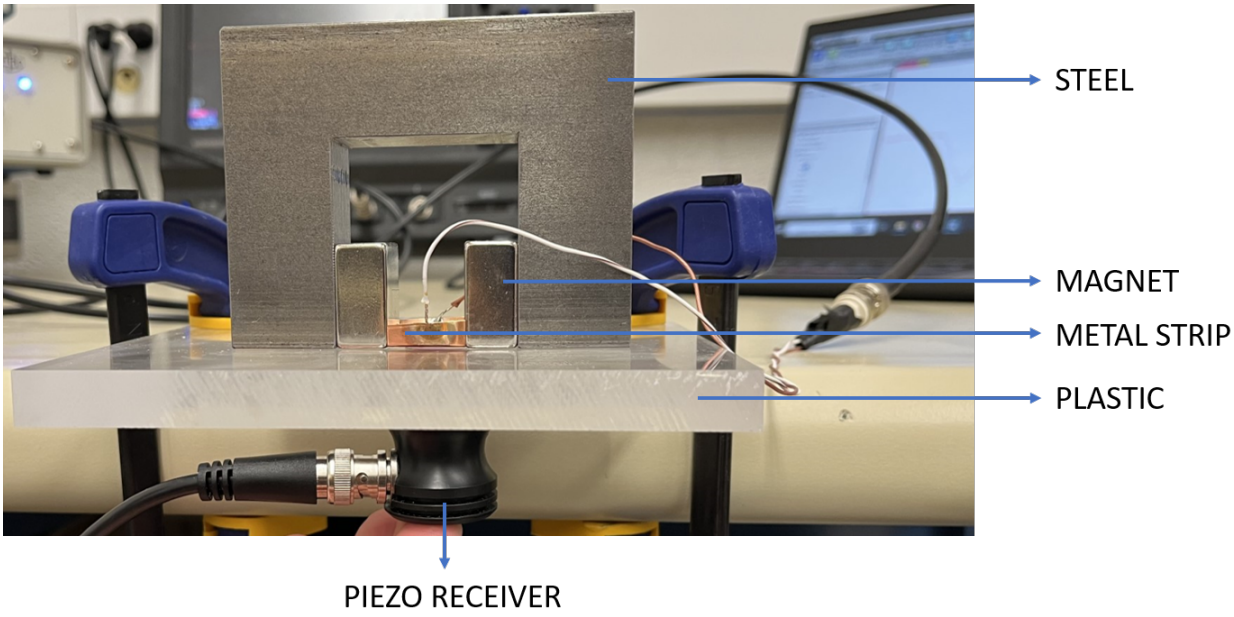

Figure 8.39 Experimental set-up for Direct Excitation EMAT

a collaborative effort with Zebadiah Miles, a PhD student at Michigan State University, and I acknowledge his valuable contribution to this work.

The experimental configuration includes a steel core, permanent magnet, metal strip (aluminum), and the sample (acrylic plastic), as depicted in Figure 8.39. This setup mirrors the simulation configuration. The magnet, yoke, and sample geometries adhere to the specifications outlined in Table 8.1. A 2-cycle tone-burst signal (at a frequency of 500 kHz) is generated using a function generator and subsequently amplified using a high-power RITEC GA-2500A Gated Am-

plifier. The output of the power amplifier is provided as input to the aluminum strip (EMAT coil). The resulting elastic waves were detected by a piezoelectric transducer (as shown in Figure 8.39), coupled to the sample with a liquid couplant. Conditioning and amplification of the received signals were performed using an ultrasonic pulser/receiver with +60 dB gain. Subsequently, the amplified signals were digitized through an 8-bit oscilloscope operating at a 1 GHz sampling rate.

The geometries of aluminum strips used in the experiments are provided in Figure 8.40.

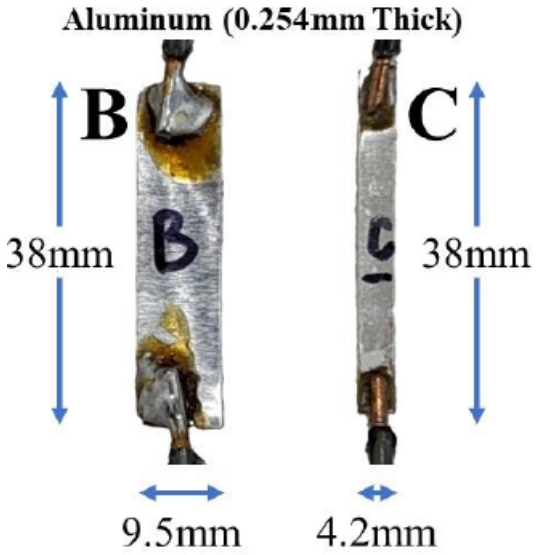

Figure 8.40 Aluminum strip geometry used for experiments

The simulation and experimental A-scan results for aluminum strip B are shown in Figure 8.41 and Figure 8.42. The simulation and experimental A-scan results for aluminum strip C are shown in Figure 8.43 and Figure 8.44. The simulation and experimental outcomes exhibit indications of a second mode (mode 2) alongside the mode 1 (longitudinal wave). However, the mode 2 wave is less distinct in experimental results, in comparison to the simulation results. Mode 2 can be seen occurring between mode 1 and the first reflection of mode 1 in both simulation and experimental results. Following the application of Hilbert transforms to the A-scan results (simulation and experiment), the velocity of mode 1 is calculated as 2707.88 m/s (experiment) and 2027.13 m/s (simulation). The difference between the experimental and simulation values for the longitudinal wave velocity (mode 1) arises from differences in material properties such as Young's modulus and Poisson's ratio for the acrylic samples used in experiments as compared to the simulation. The

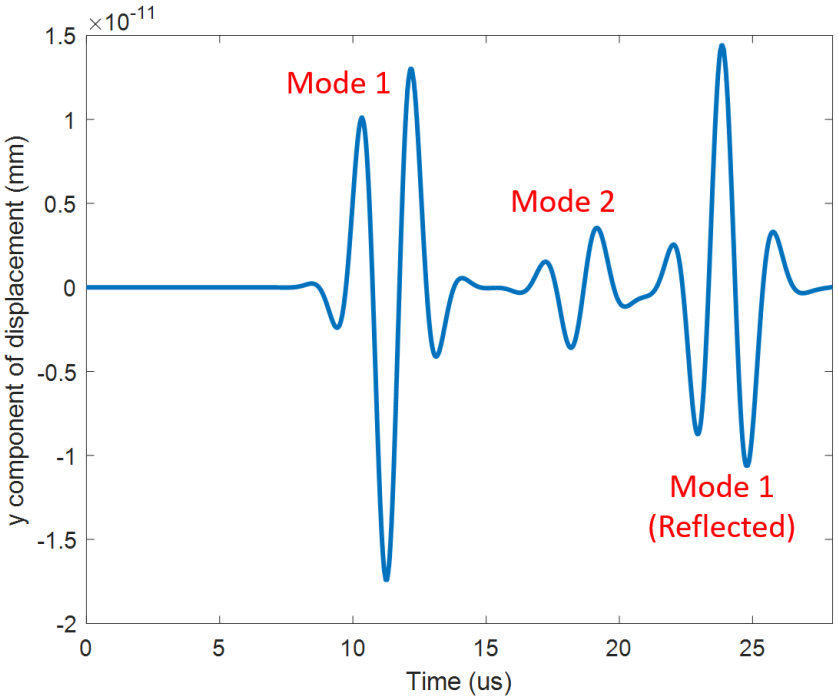

Figure 8.41 A-scan of displacement at measurement point on plastic back-wall - Simulation result for Aluminum strip B

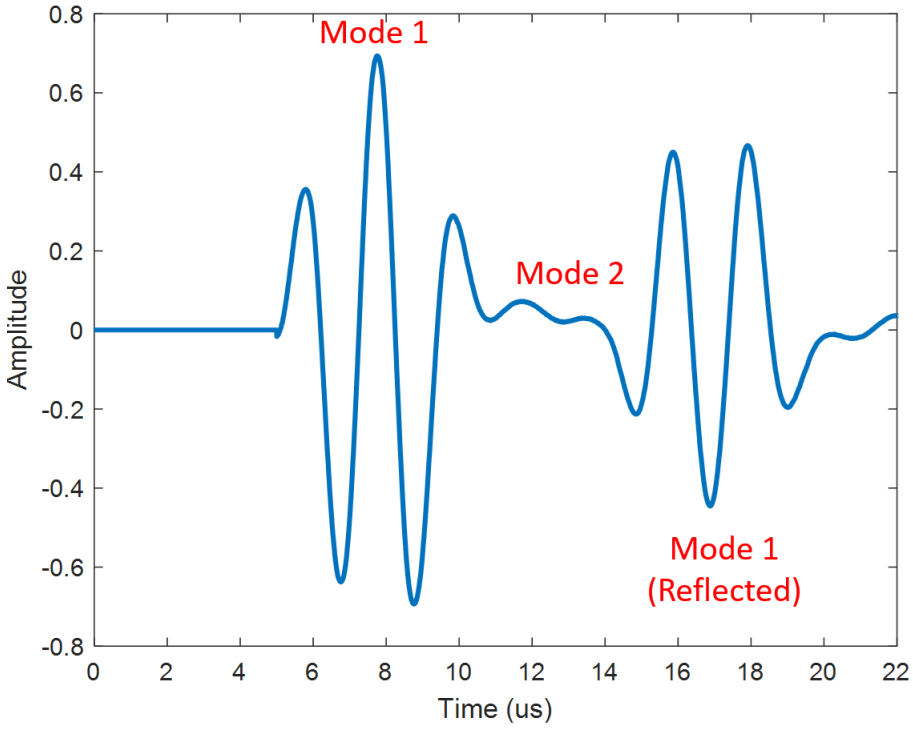

Figure 8.42 A-scan of displacement at measurement point on plastic back-wall - Experimental result for Aluminum strip B

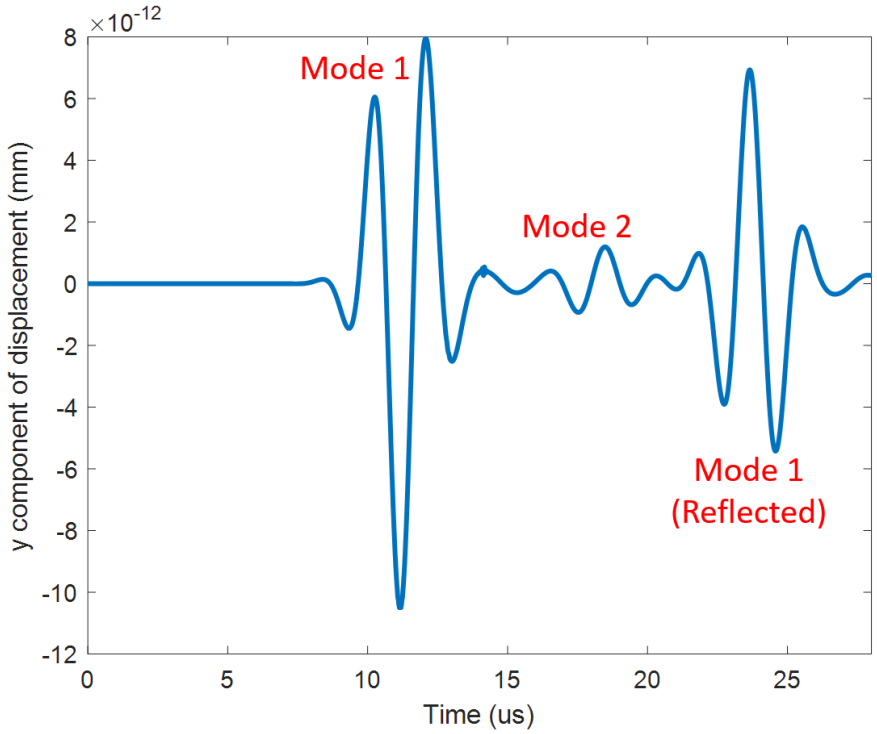

Figure 8.43 A-scan of displacement at measurement point on plastic back-wall - Simulation result for Aluminum strip C

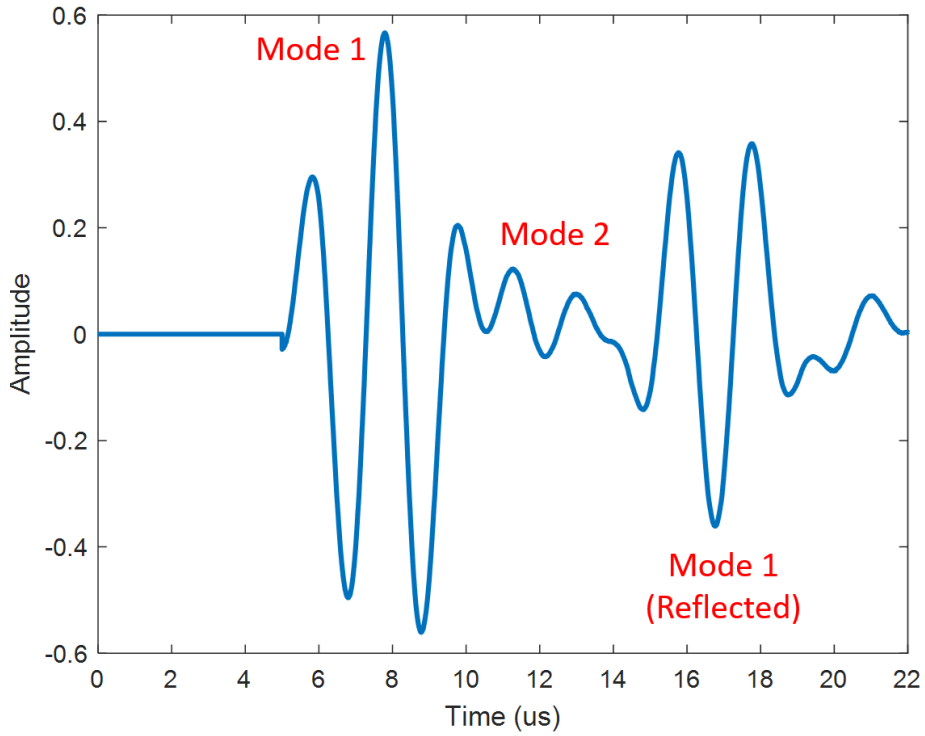

Figure 8.44 A-scan of displacement at measurement point on plastic back-wall - Experimental result for Aluminum strip C

experimentally obtained A-scan results validate the direct excitation EMAT model.

This concludes the discussion on direct excitation configuration of the EMAT for non-conductive materials. The direct excitation configuration's reliance on contact contradicts the fundamental non-contact nature of EMATs. To address this limitation, the proposed approach holds promise for an extension toward developing a non-contact-based approach. Further details on this potential solution will be elaborated upon in the following chapter.

CHAPTER 9

NON-CONTACT INDUCED EXCITATION: EMBEDDED EMAT

This chapter presents the findings obtained from extensive numerical simulations conducted on EMATs applied to a non-conductive sample using the non-contact induced excitation approach. The initial section introduces the induced excitation model specifically tailored for an embedded EMAT configuration, providing substantial results that validate the successful propagation of an acoustic wave within the non-conductive sample. It's crucial to note that this model serves as an extension of the previously discussed direct excitation model. Subsequently, the chapter includes a comparative analysis of acoustic velocity, enabling a comprehensive comparison with theoretically derived values. As the narrative progresses, the subsequent sections meticulously explore the impact of varying aluminum strip width and height on both Lorentz force and displacement, accompanied by the presentation of corresponding numerical results. Moreover, the chapter delves into a detailed examination of the implications of employing a line source in lieu of the aluminum strip, shedding light on the associated acoustic modes. The discussion also extends to the experimental validation, offering insights into the observed acoustic behavior and further contributing to the understanding of the induced excitation approach in EMATs applied to non-conductive samples.

9.1 EMAT model in COMSOL

The induced excitation model (two-dimensional) for the EMAT involves inducing current in the metal patch embedded inside the non-conducting sample. Figure 9.1 shows schematic of the non-contact induced excitation model geometry in COMSOL and Figure 9.2 shows the zoomed in version to illustrate the metal patch (copper patch) and measurement point on the sample back-wall. The magnetic field interface (in AC/DC module) is used to simulate the electromagnetic phenomenon and structural mechanics module is used to simulate the acoustic phenomenon.

The model comprises of a permanent magnet, aluminum strip, embedded copper patch, steel core and the non-conducting sample (plastic). The permanent magnet is used to generate the static magnetic field and the aluminum strip induces current in the copper patch to generate a changing (dynamic) magnetic field. The entire model is enclosed in air. The static magnetic field of the

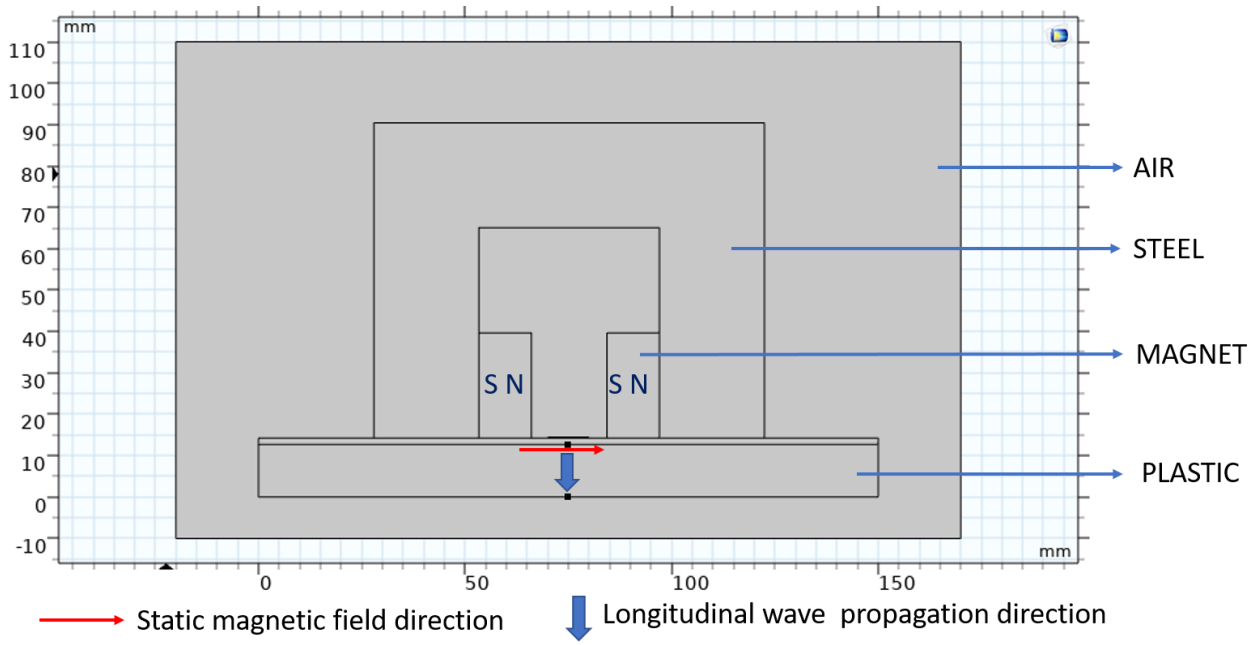

Figure 9.1 Induced Excitation model for an EMAT in COMSOL

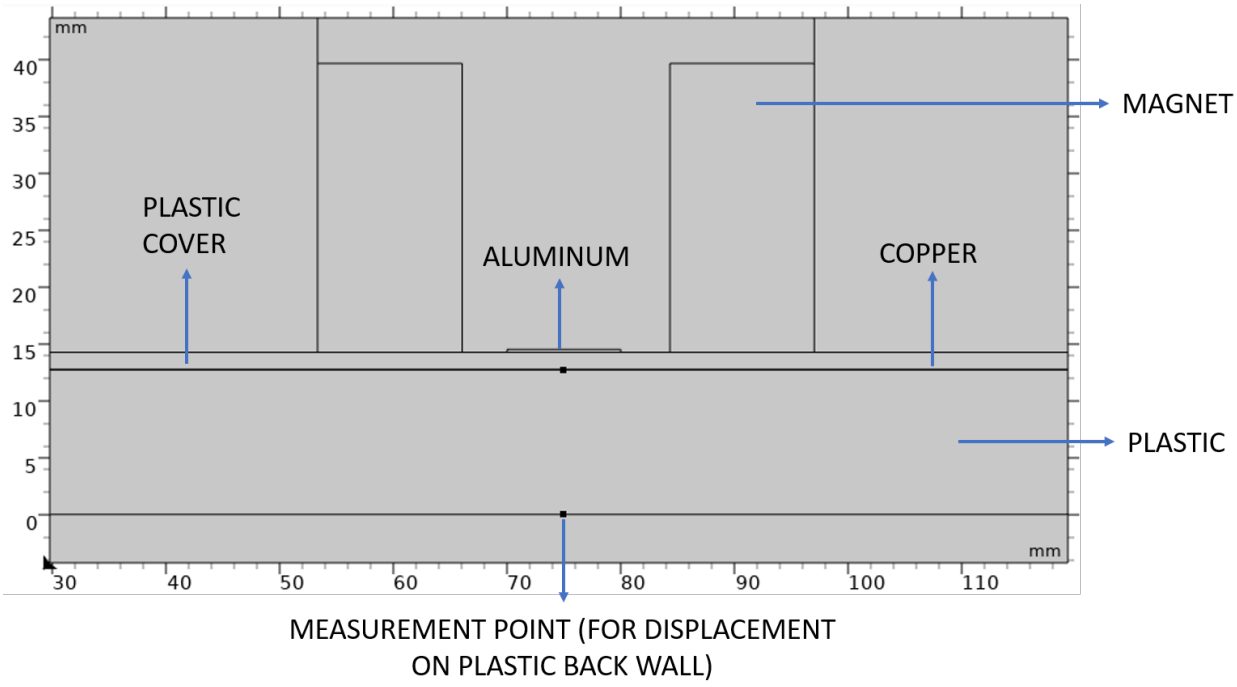

Figure 9.2 Zoomed version of Figure 9.1

permanent magnet is specified in x direction. A surface current density (A/m) is applied to the Aluminum strip as shown in Figure 8.3, in z direction. Hence according to right hand rule, the Lorentz force generated should be in the y-direction. And the displacement and wave propagation

(longitudinal wave) will also be in the y-direction, i.e., along the thickness of sample (plastic). The model parameters are given in Table 9.1.

Table 9.1 Model parameters for Induced excitation EMAT model

Parameter	**Value**
Plastic (Sample) Width	150 mm
Plastic (Sample) Height	12.7 mm
Magnet Width	12.7 mm
Magnet Height	25.4 mm
Longitudinal velocity in plastic	2077.45 m/s
Wavelength in plastic	4.15 mm
Aluminum strip Width	10 mm
Aluminum strip Height	0.254 mm
Conductivity of plastic	62.5 X 10-18 S/m
Poisson's ratio (Plastic)	0.35
Young's Modulus (Plastic)	3.2 G Pa
Density (Plastic)	1190 kg/m3
Frequency of coil current	500 kHz
Conductivity of Aluminum strip	36 MS/m
Copper patch Height	0.05 mm
Copper patch Width	150 mm
Conductivity of Copper	60 MS/m
Plastic cover Height	1.5 mm
Plastic cover Width	150 mm

The coil current, as shown in Figure 8.4, is a Gaussian modulated pulse with a carrier frequency of 500 kHz as given in (8.1).

Figure 9.3 and Figure 9.4 shows the arrow surface plots of Lorentz force in copper patch (y and x components) at 5 μs. The y component shows a uniform current density distribution, due to

application of a surface current density, as shown in Figure 8.3. The x component shows a pattern similar to the results obtained for direct excitation. As observed from the direct excitation model, this pattern of Lorentz force led to a coupled acoustic mode in the sample.

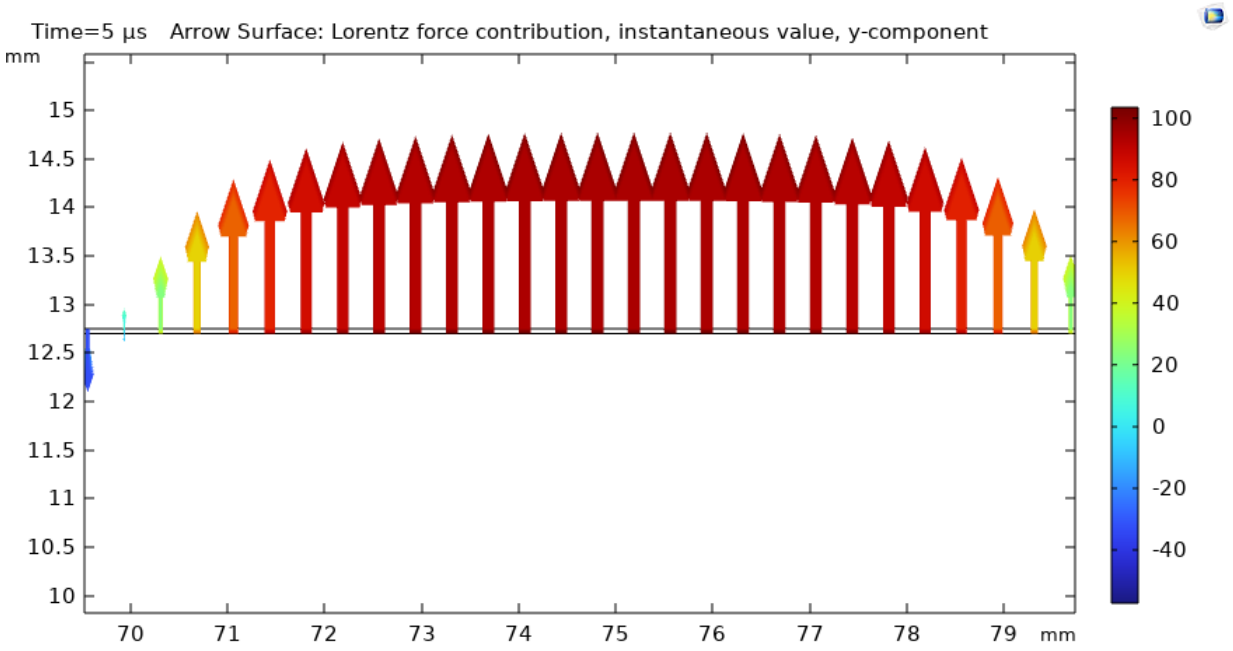

Figure 9.3 Arrow surface plot of y-component of Lorentz force in Copper patch at 5µs

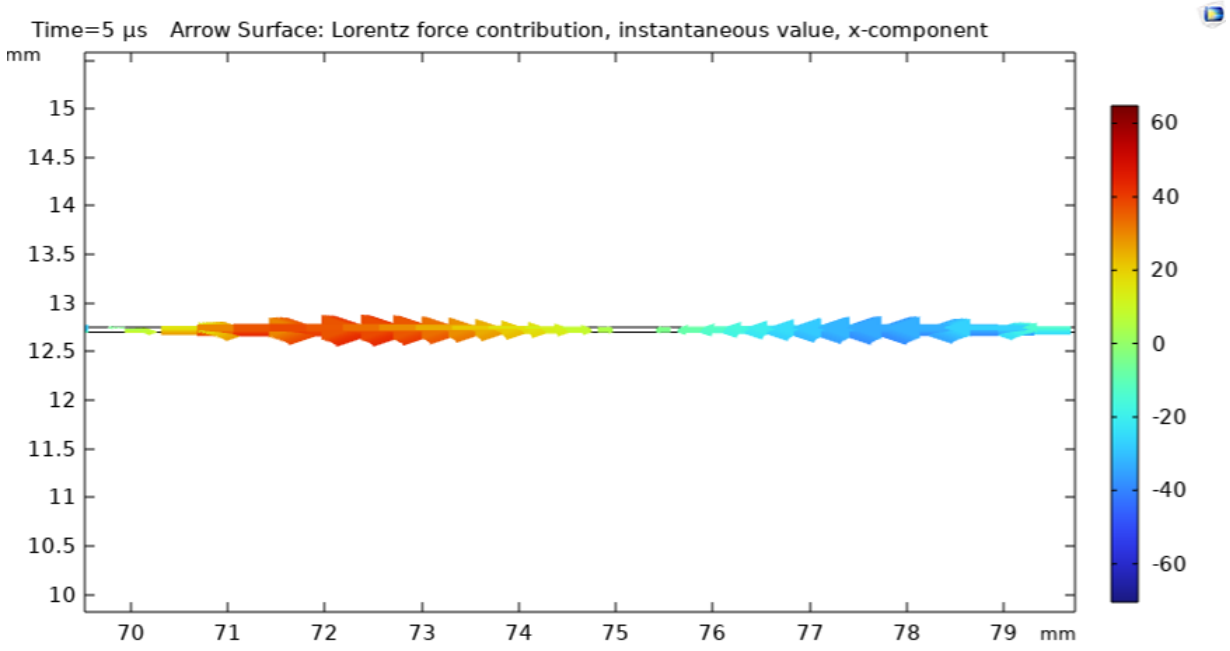

Figure 9.4 Arrow surface plot of x-component of Lorentz force in Copper patch at 5µs

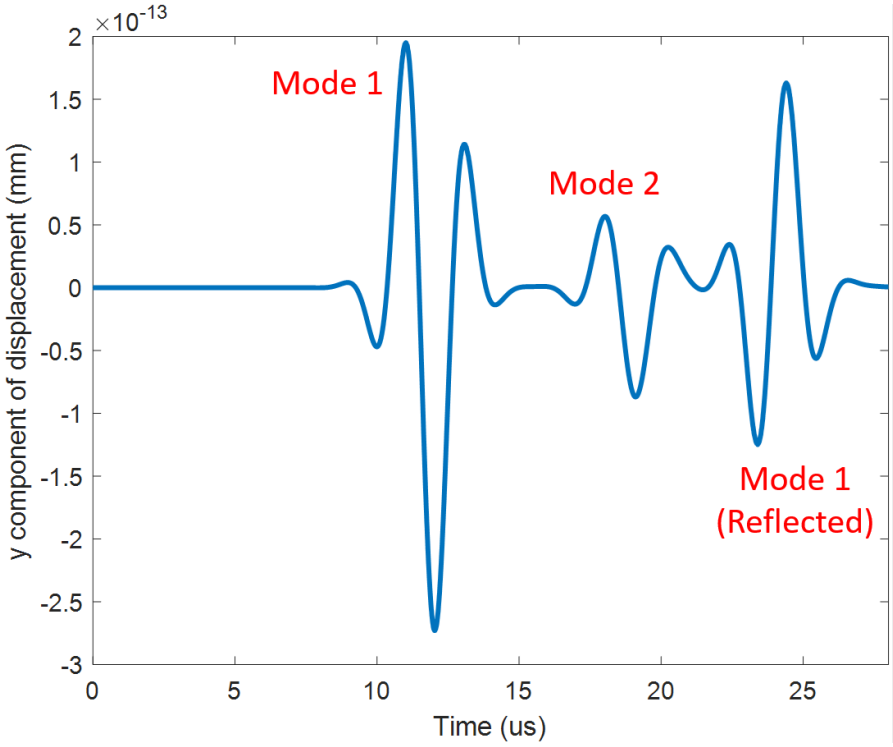

Figure 9.5 A-scan of displacement at measurement point on plastic back-wall for Induced excitation EMAT

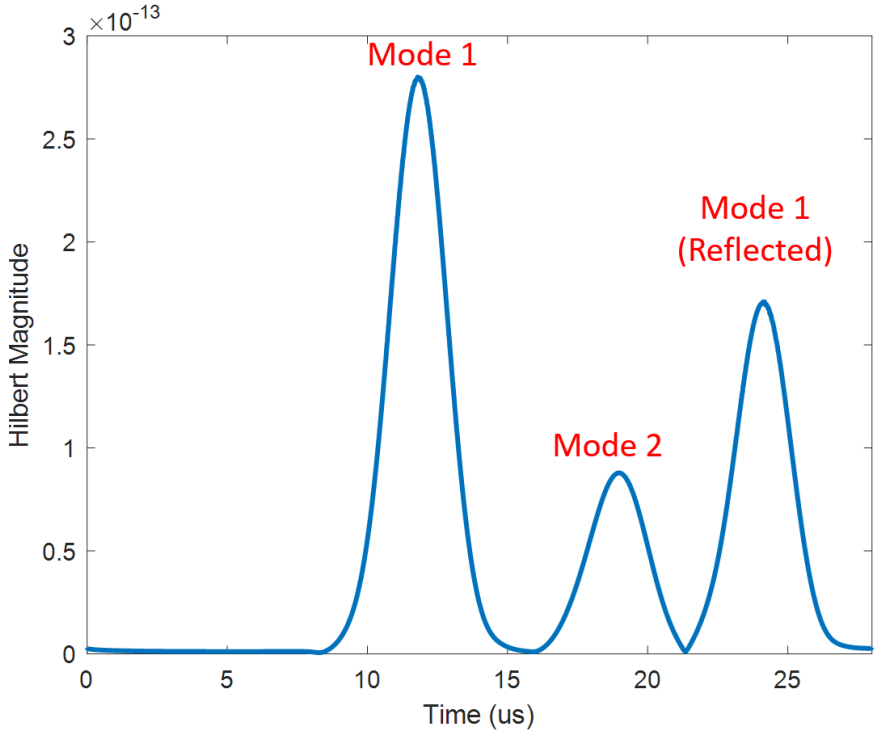

Figure 9.6 Hilbert magnitude of A-scan signal showed in Figure 9.5

Figure 9.5 shows the A-scan of displacement at the measurement point on plastic back-wall. Figure 9.6 shows the Hilbert magnitude plot for the displacement A-scan. Few observations can be made from these plots:

1. The mode 1 (longitudinal wave) and the reflection of this wave can clearly be observed (similar to the results obtained for direct excitation model).

2. Mode 1 is expected to appear at 8.11 us from theoretical wave velocity calculation and can also be seen in the plot.

3. Mode 2 can also be distinctly observed, similar to the direct excitation model results.

Wave velocity calculations

The longitudinal wave velocity for the acrylic sample can be calculated using (8.2). The theoretical value of longitudinal wave velocity for the non-conducting sample using material properties (Table 9.1) can be calculated as 2077.45 m/s.

The Hilbert magnitude plot (Figure 8.14) is used to find the time at which mode 1, mode 2 and mode 3 peak. These values are given in Table 9.2. The wave velocities for mode 1 and mode 2 are calculated using the Hilbert magnitude data and sample thickness. These are presented in Table 9.3. The wave velocity of Mode 1 is comparable to the theoretical value of 2077.45 m/s. But, mode 2 has a velocity which is a slightly greater than that of shear wave (half of longitudinal wave velocity) and much lesser than the longitudinal wave velocity. Hence, mode 2 can be considered as a coupled mode.

Table 9.2 Time at which modes peak in Hilbert magnitude plot for Induced Excitation EMAT

Mode	**Time (us)**
Mode 1	11.79
Mode 2	18.99
Mode 1 (reflected)	24.17

Table 9.3 Mode velocities for Induced Excitation EMAT

Mode	Velocity (m/s)
Mode 1	2051.69
Mode 2	1297.23

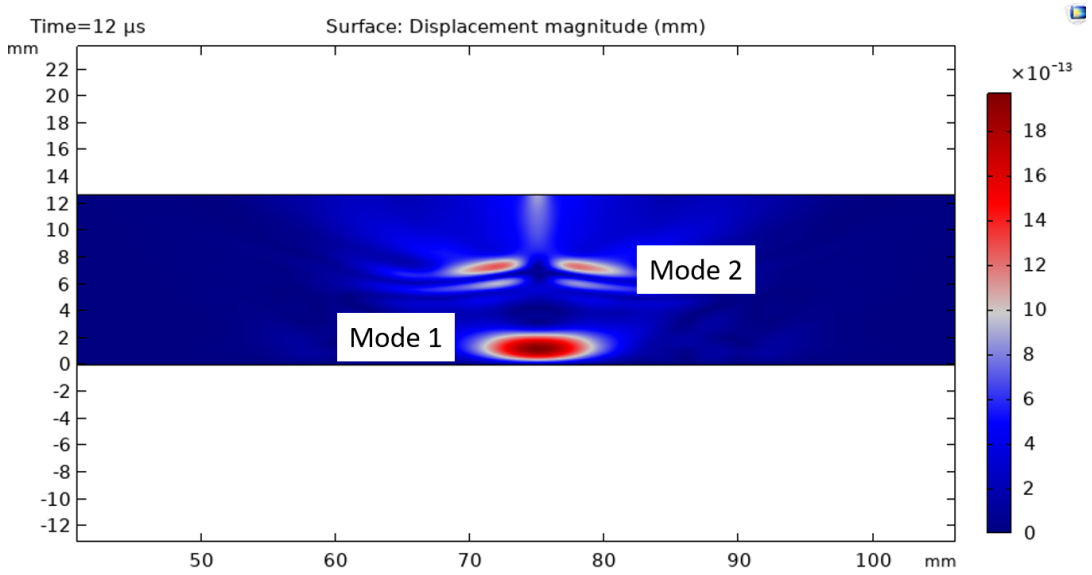

Figure 9.7 Surface plot of full-field displacement in plastic at 12 µs for Induced excitation EMAT

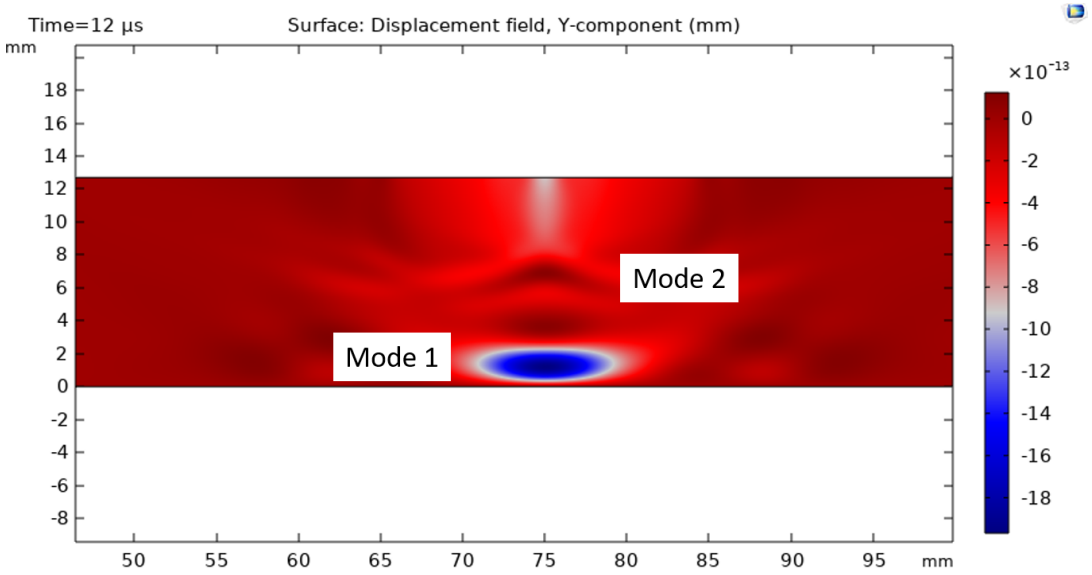

Figure 9.8 Surface plot of y-component of displacement in plastic at 12 µs for Induced excitation EMAT

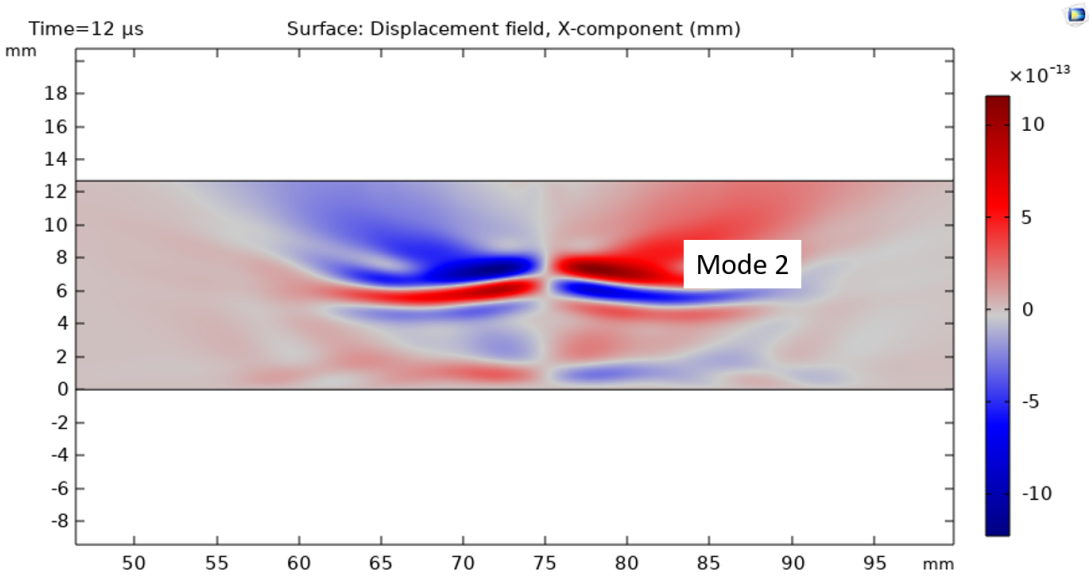

Figure 9.9 Surface plot of x-component of displacement in plastic at 12 µs for Induced excitation EMAT

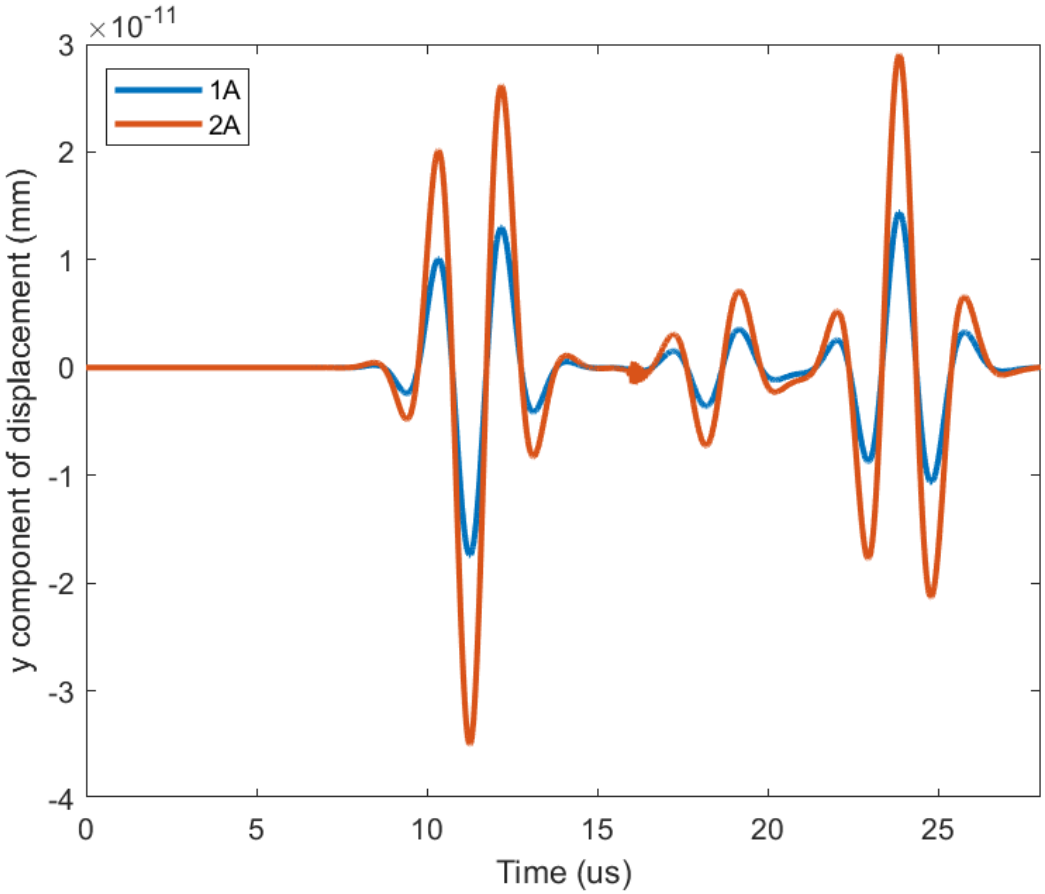

Figure 9.10 Comparison of A-scans of displacement at measurement point on plastic back-wall for varying coil current magnitudes (Induced Excitation EMAT)

Figure 9.7, Figure 9.8 and Figure 9.9 shows the full-field displacement plots in the sample at 12 µs. These plots validate the propagation of an acoustic wave in the non-conducting sample. The mode 1 and mode 2 can be clearly observed in these plots and the results are similar to that obtained for direct excitation configuration.

Figure 9.10 shows the displacement A-scan plots for input current magnitudes of 1A and 2A. The results presented so far for the induced configuration are for the current magnitude (peak) of 1A. This additional investigation serves to validate the induced excitation model, revealing that displacement in plastic has doubled, as anticipated, with the increase in input current magnitude. Additionally, it is important to note that all model parameters are maintained precisely the same for this study.

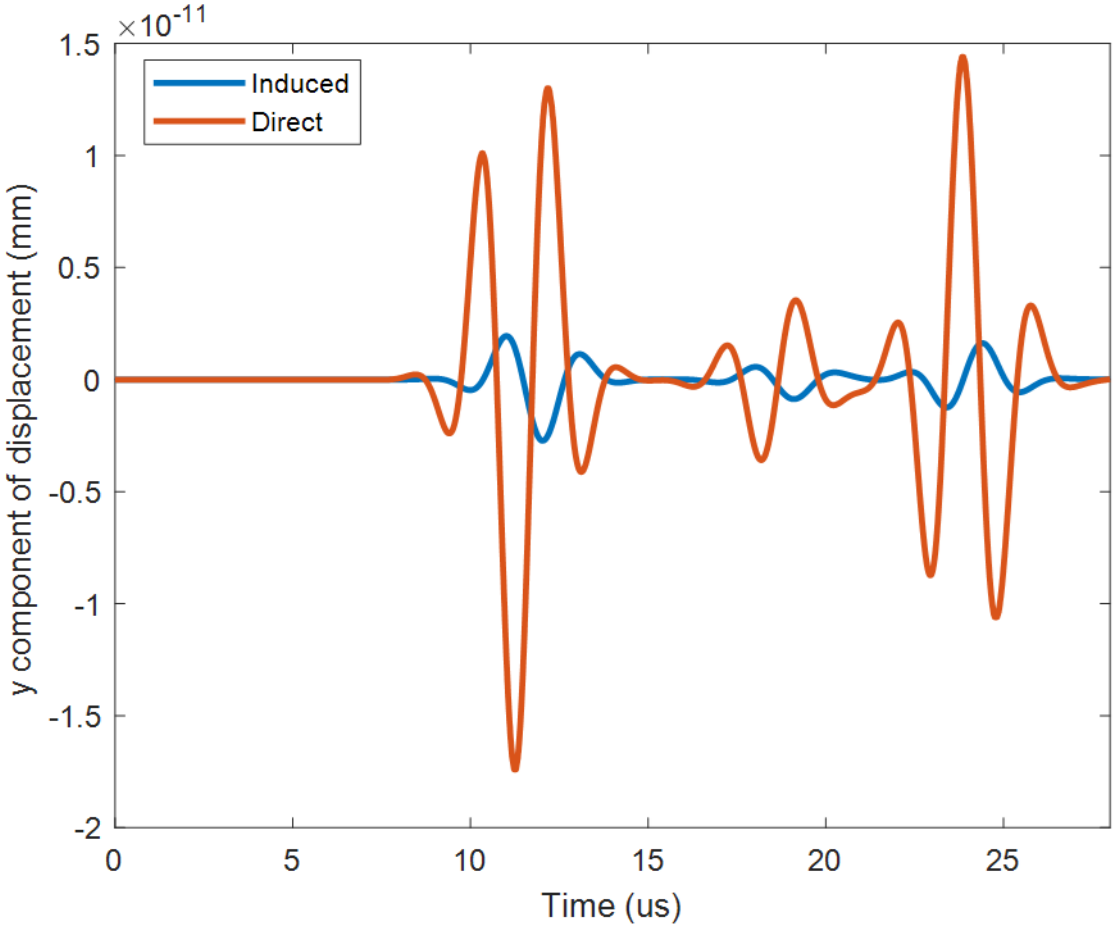

Figure 9.11 Comparison of A-scans of displacement at measurement point on plastic back-wall for direct excitation and induced excitation EMAT's

Figure 9.11 depicts the displacement A-scan plots for both direct and induced configurations, utilizing the model parameters described in Table 8.1 and Table 9.1, respectively. The aluminum strip width is set at 10mm. **It is important to note that the data for induced displacement is multiplied by 10**. This adjustment is made to enhance clarity for observation on the same plot. The reduction in displacement amplitude for the induced configuration can be attributed to lift-off between the aluminum strip and copper patch. Additionally, an intriguing observation is the phase shift between the direct and induced displacement A-scans. This is attributed to the phase difference between the applied current to the aluminum strip and induced eddy current in the copper patch.

9.2 Effect of Aluminum strip geometry on displacement in sample

This section delves into an exploration of the influence of Aluminum strip width and height on the displacement within the sample (plastic). The objective is to study and analyze the effects of varying dimensions of the Aluminum strip on the observed acoustic modes within the EMAT model. This investigation contributes to an understanding of how geometric parameters impact the displacement characteristics, thereby providing valuable insights for optimizing EMAT design and performance.

9.2.1 Aluminum strip width variation

In this study, all model parameters remain constant, with the exception of the width of aluminum strip. The chosen widths for the aluminum strip in this study are 10mm and 5mm.

Figure 9.12 illustrates the displacement A-scan at the plastic back-wall (measurement point) for an aluminum strip width of 5mm. Mode 1 is clearly observable, and it appears at the expected time of 8.11 us. The two modes can still be observed in this plot, similar to the direct excitation and induced excitation with 10mm aluminum strip width results.

Figure 9.13 provides a comparison of displacement A-scans for varying aluminum strip widths, specifically 10mm and 5mm. The observed increase in displacement amplitude for the 10mm aluminum width is attributed to the larger source width. Furthermore, maintaining a consistent input current leads to an increase in the effective line current for the 10mm Aluminum strip width, contributing to the amplified displacement amplitude. Acoustically, the larger source width narrows

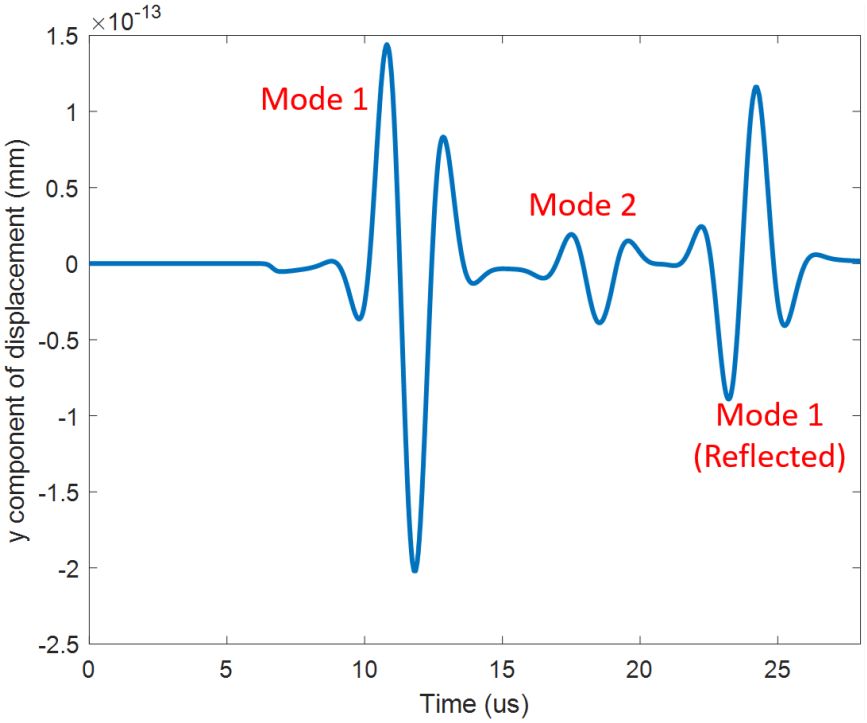

Figure 9.12 A-scan of displacement at measurement point on plastic back-wall for Aluminum strip width = 5mm

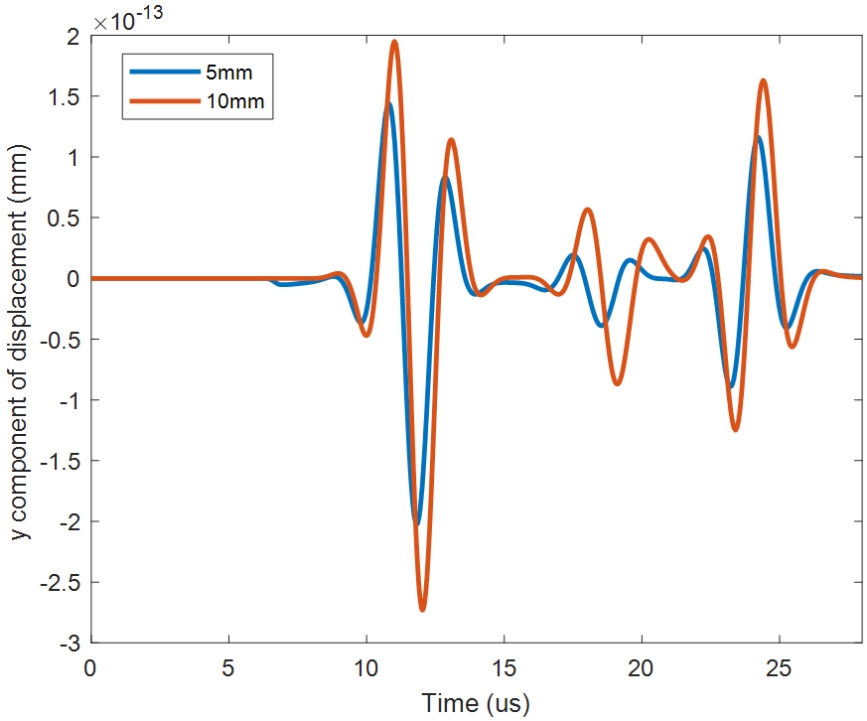

Figure 9.13 Comparison of A-scans of displacement at measurement point on plastic back wall for varying Aluminum strip widths (Induced Excitation EMAT)

the beam spread, concentrating more acoustic energy at the center of the beam. This phenomenon is reflected in the displacement A-scan, clearly showcasing the increased displacement amplitude for the 10mm aluminum strip width. This analysis offers valuable insights into the intricate interplay between geometric parameters (of Aluminum strip) and the electromagnetic and acoustic characteristics within the context of EMAT design. The results are in-line with the direct excitation configuration, as expected.

9.2.2 Aluminum strip height variation

In this study, all model parameters remain constant, with the exception of the height of aluminum strip. The chosen heights for the aluminum strip in this study are 0.25 mm and 0.1 mm. Figure 9.14

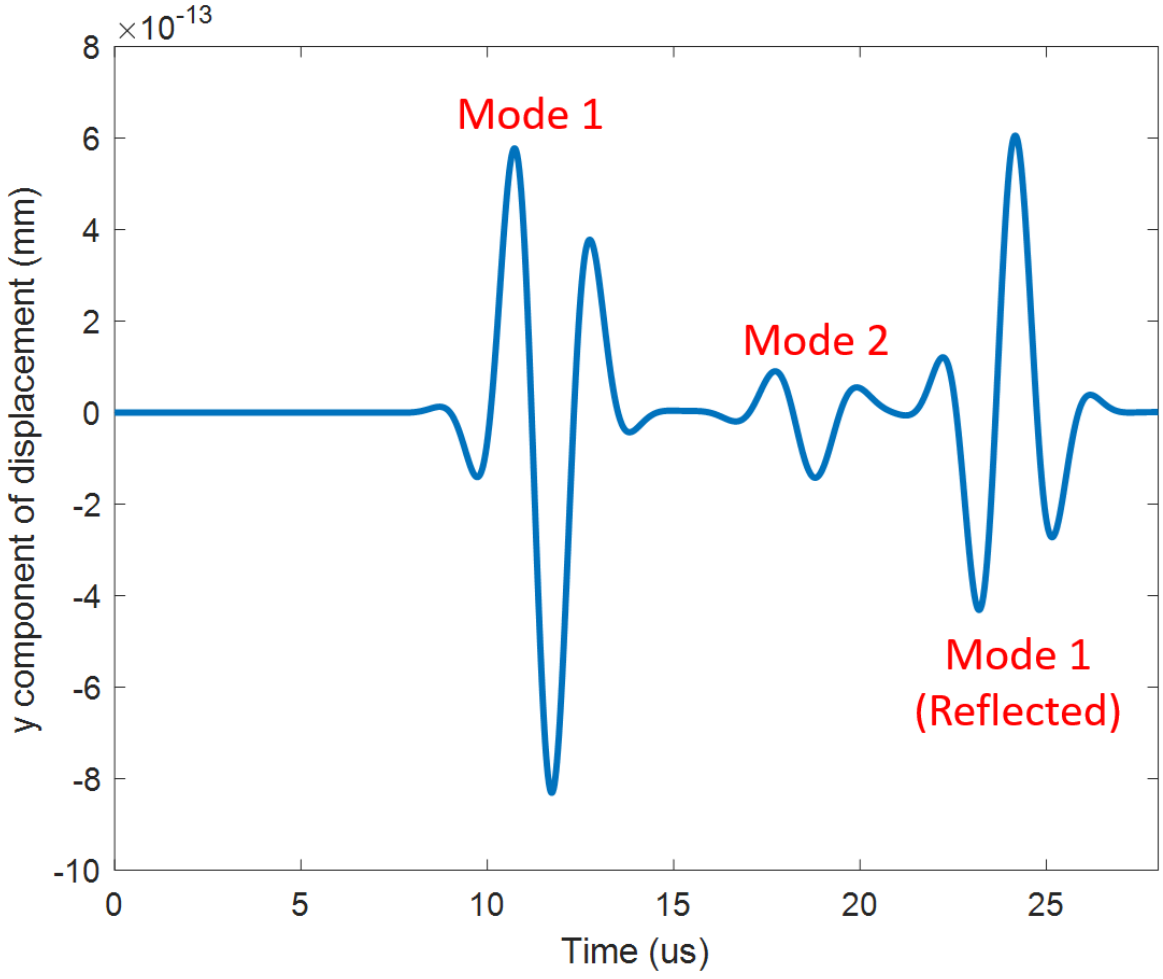

Figure 9.14 A-scan of displacement at measurement point on plastic back-wall for 0.1mm Aluminum strip height (Induced Excitation EMAT)

shows the displacement A-scan at plastic back-wall (at the measurement point) for aluminum strip height of 0.1mm. The two modes can still be observed in this plot, similar to the direct excitation results and induced excitation with aluminum strip heights of 0.25mm.

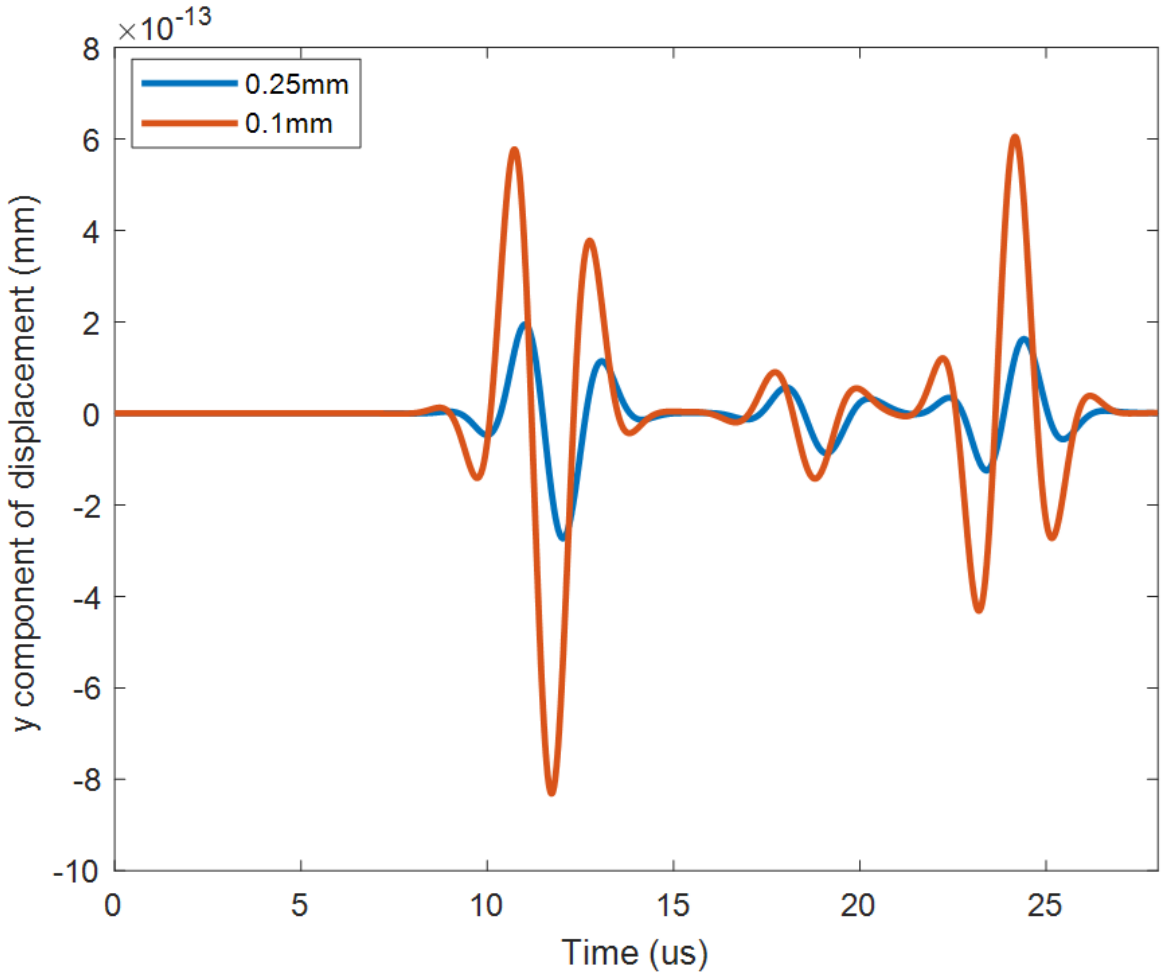

Figure 9.15 Comparison of A-scans of displacement at measurement point on plastic back wall for varying Aluminum strip heights (Induced Excitation EMAT)

Figure 9.15 provides a comparative analysis of displacement A-scans for aluminum heights of 0.25 mm and 0.1 mm. The displacement amplitude for the 0.1mm aluminum strip height surpasses that of the 0.25mm aluminum strip height, attributed to the lift-off between Aluminum strip and copper patch. A lower lift-off results in a higher Lorentz force in copper patch, consequently leading to an increased displacement in plastic.

9.3 Effect of line source on acoustic modes in sample

This section investigates the impact of a line source (modeled as a point source in 2D) on the acoustic modes. The objective of these simulations is to observe the potential emergence of a second mode in the absence of the aluminum strip. In the induced configuration model, the aluminum strip is substituted with the point source (2D), as depicted in Figure9.16.

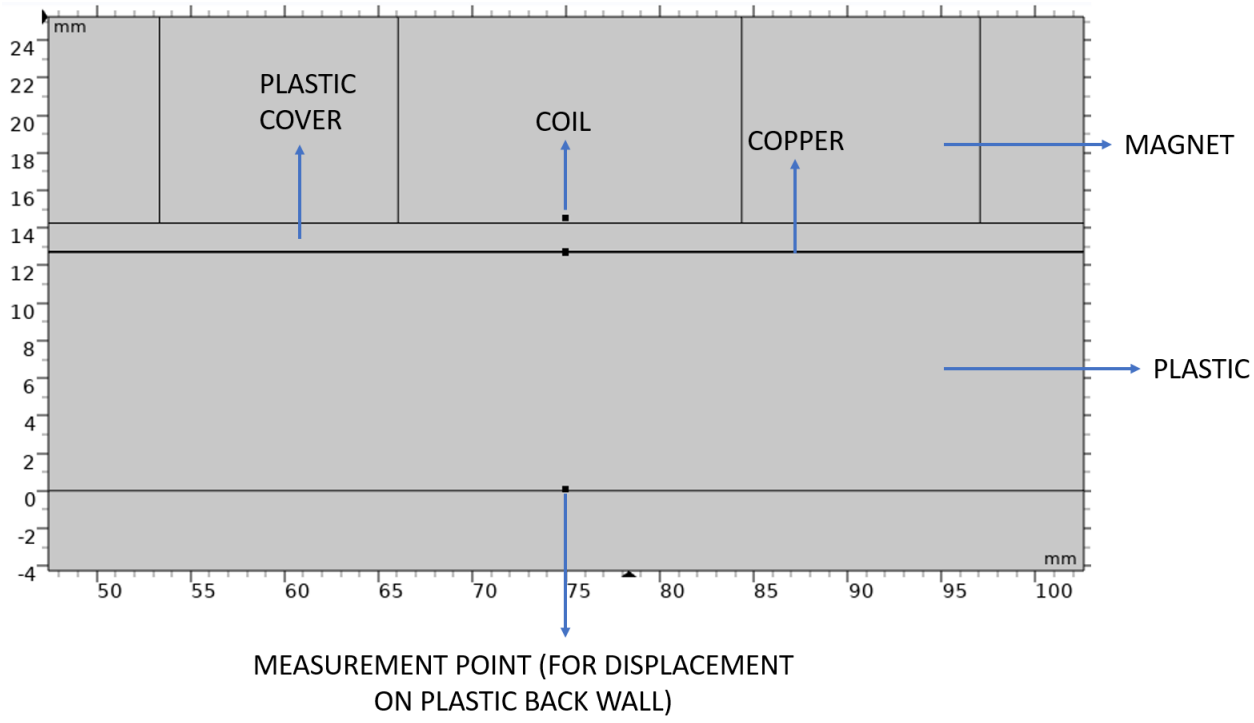

Figure 9.16 Induced excitation EMAT model with point source (in 2D) - No aluminum

Figure 9.17 and Figure 9.18 shows the arrow surface plots of Lorentz force in copper patch (x and y components) at 5 µs. The x component shows a pattern similar to the results obtained for direct excitation and induced excitation with aluminum strip. But, the interesting thing to note here is that y component of Lorentz force is much higher than the x component of Lorentz force. Figure 9.19 displays the A-scan of displacement at the plastic back-wall, revealing the presence of two distinct acoustic modes in the displacement plot. This simulation provides confirmation of the existence of the second mode, even in the absence of the aluminum strip. But, the peak of mode 2 is seen to be much lesser than peak of mode 1.

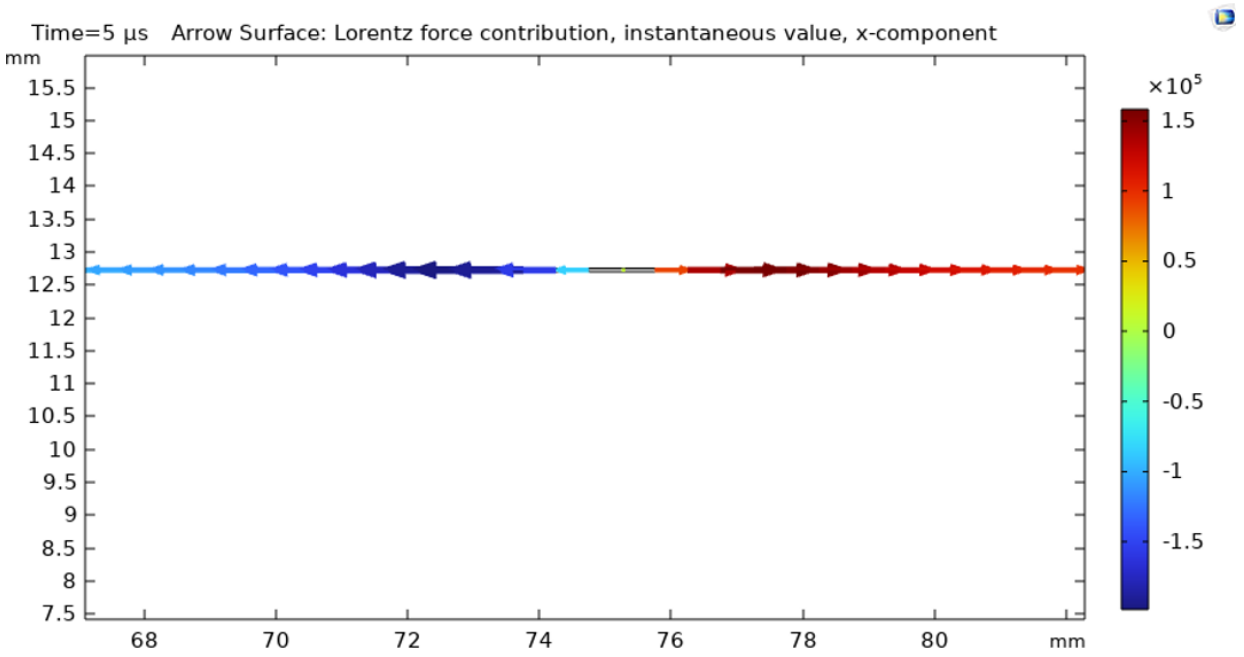

Figure 9.17 Arrow surface plot of x-component of Lorentz force in Copper patch at 5 µs for Induced Excitation EMAT model shown in Figure 9.16

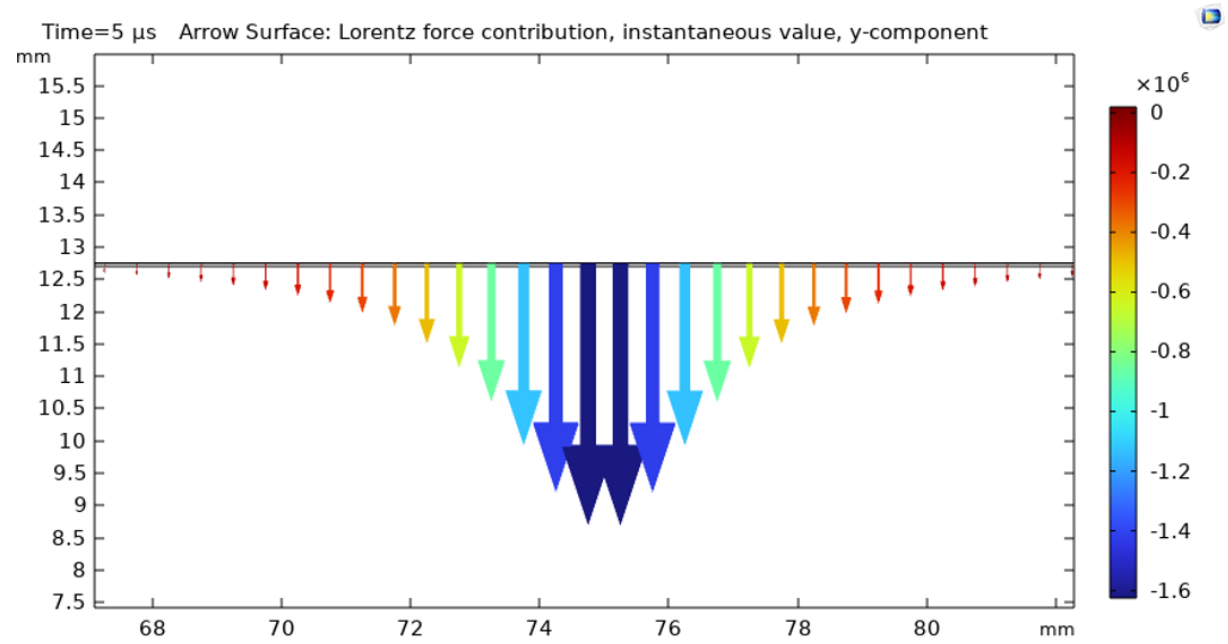

Figure 9.18 Arrow surface plot of y-component of Lorentz force in Copper patch at 5 µs for Induced Excitation EMAT model shown in Figure 9.16

Figure 9.20 presents a comparative analysis of induced configurations with aluminum strip widths of 5mm, 10mm, and a point source. All other parameters in the model are kept constant. The plots specifically illustrate the ratio of mode 2 Hilbert magnitude (HM) peak to mode 1

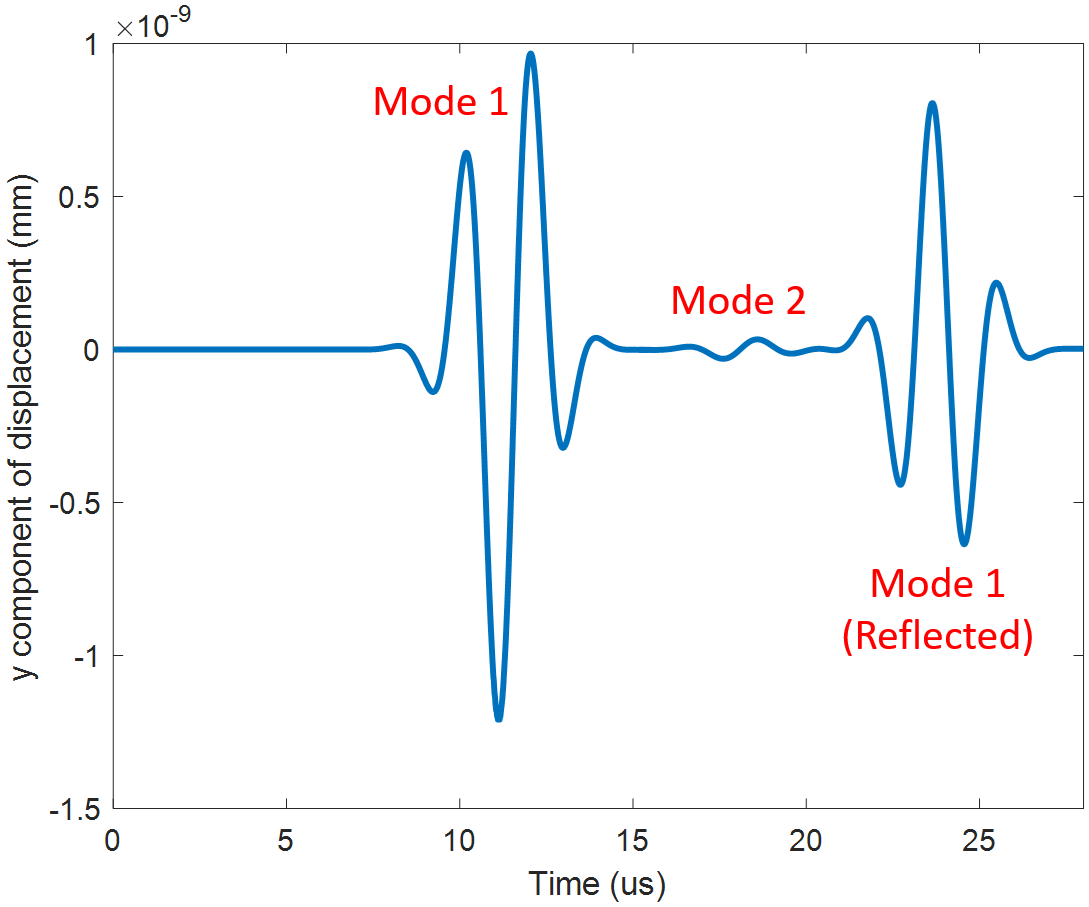

Figure 9.19 A-scan of displacement at measurement point on plastic back-wall for Induced Excitation EMAT model shown in Figure 9.16

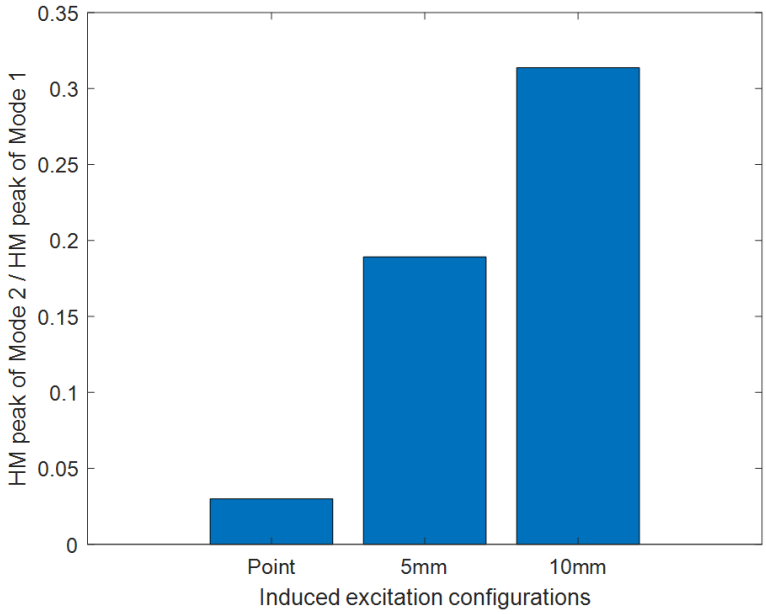

Figure 9.20 Quantitative comparison of Induced Excitation EMAT's

HM peak for the three induced excitation configurations. This study aims to observe the trend in amplitude reduction for mode 2 in comparison with mode 1, as the source width decreases, providing valuable insights into the acoustic behavior under varying source widths. The outcomes indicate that a decrease in source width leads to a reduction in the HM peak for mode 2, when compared with mode 1. This reduction is associated with the decrease in x-component of Lorentz force relative to the y-component of Lorentz force in the Aluminum strip.

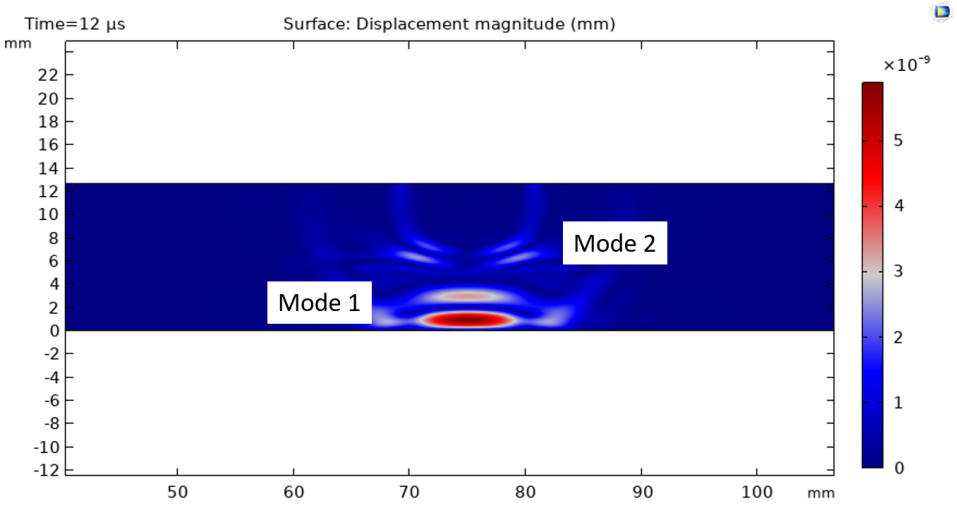

Figure 9.21 Surface plot of full-field displacement in plastic at 12 µs for EMAT model shown in Figure 9.16

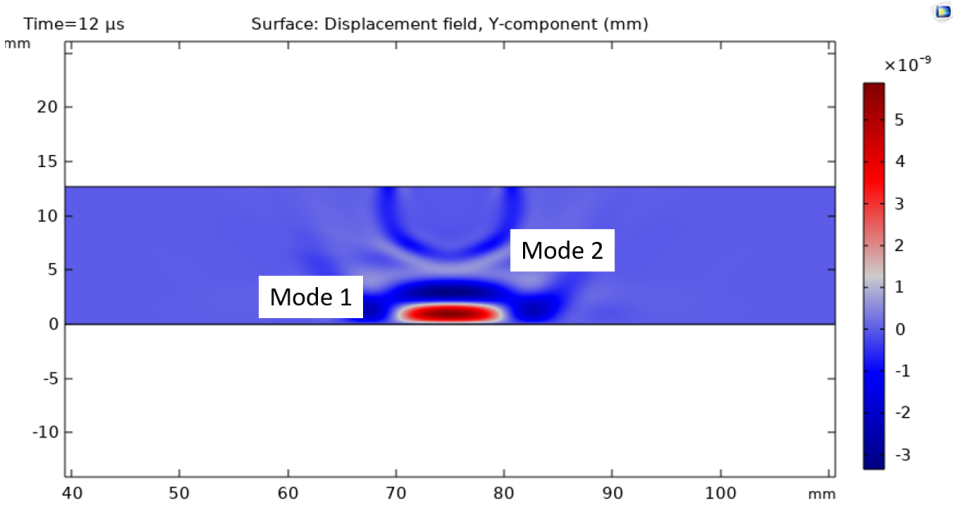

Figure 9.22 Surface plot of y-component of displacement in plastic at 12 µs for EMAT model shown in Figure 9.16

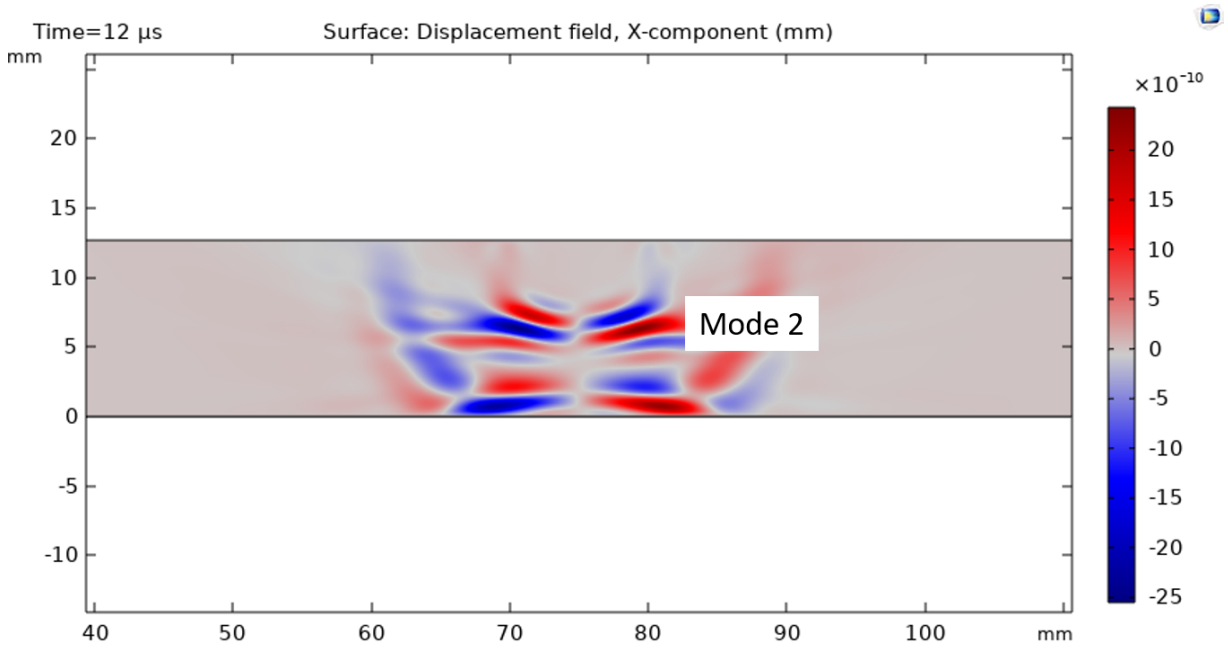

Figure 9.23 Surface plot of x-component of displacement in plastic at 12 µs for EMAT model shown in Figure 9.16

Figure 9.21, Figure 9.22 and Figure 9.23 shows the full-field displacement plots in the sample at 12 µs. These plots provide a visual representation and validate the propagation of an acoustic wave in the non-conducting sample. The mode 1 and mode 2 can clearly be observed in these plots.

9.4 Effect of plastic cover height on displacement in sample

In this section, the impact of plastic cover height on the induced excitation configuration EMAT is explored. The plastic presents as a lift-off for the source (Aluminum strip), and the copper patch is embedded within the sample (plastic), characterizing it as an embedded EMAT. The investigation involves a comparison of displacements at the sample back-wall, considering variations in plastic cover heights. Additionally, a scenario where aluminum is positioned at a specific height above the plastic cover is examined. The primary goal is to validate the induced excitation model further and ensure consistency in the generation of acoustic wave modes.

In the first study, all model parameters (Figure 9.1) remain constant, with the exception of the plastic cover height. Figure 9.24 presents a comparative analysis of displacement A-scans for plastic cover heights of 0.5 mm and 1.5 mm. The displacement amplitude for the 0.5 mm plastic cover height exceeds that of the 1.5 mm plastic cover height, attributed to the lift-off between

Aluminum strip and copper patch. A lower lift-off results in a higher Lorentz force in copper patch, consequently leading to an increased displacement in the sample. Therefore, having a thin layer of plastic above the copper patch is certainly desirable for this application.

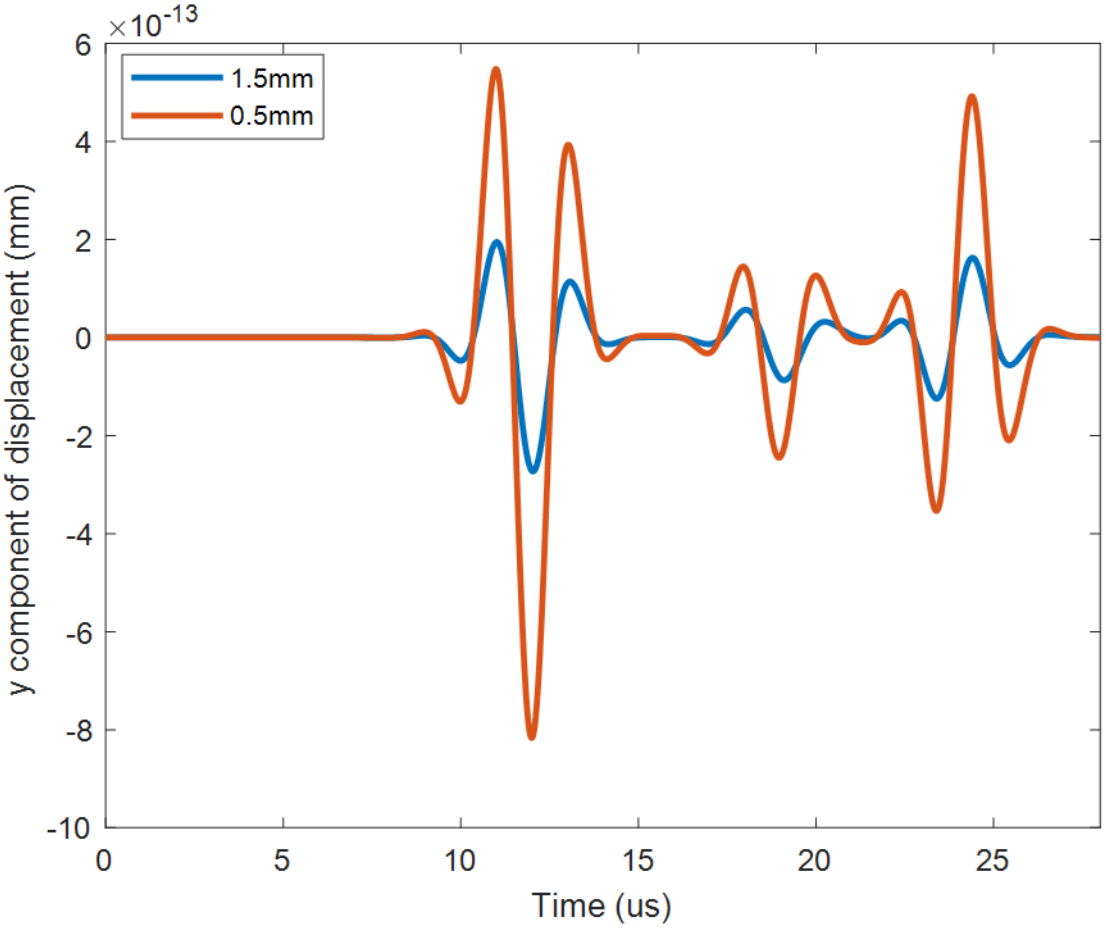

Figure 9.24 Comparison of displacement A-scans at measurement point on plastic back-wall for varying plastic cover heights (Induced Excitation EMAT)

In the second study, the objective is to verify the acoustic modes in plastic with variation in aluminum strip placement above the plastic cover. Figure 9.25 provides a comparative analysis of displacement A-scans for plastic cover heights of 0.5 mm, where a) The aluminum strip is placed on the plastic cover and b) The aluminum strip is placed 0.5mm above the plastic cover. The displacement amplitude for the case where aluminum strip is positioned on the plastic cover shows a slightly higher displacement amplitude. This is attributed to the lift-off between aluminum strip and the copper patch. A lower lift-off results in a higher Lorentz force in the copper patch, consequently leading to an increased displacement in the sample. Hence, positioning the aluminum

strip in close proximity to the plastic cover is certainly desirable for this application.

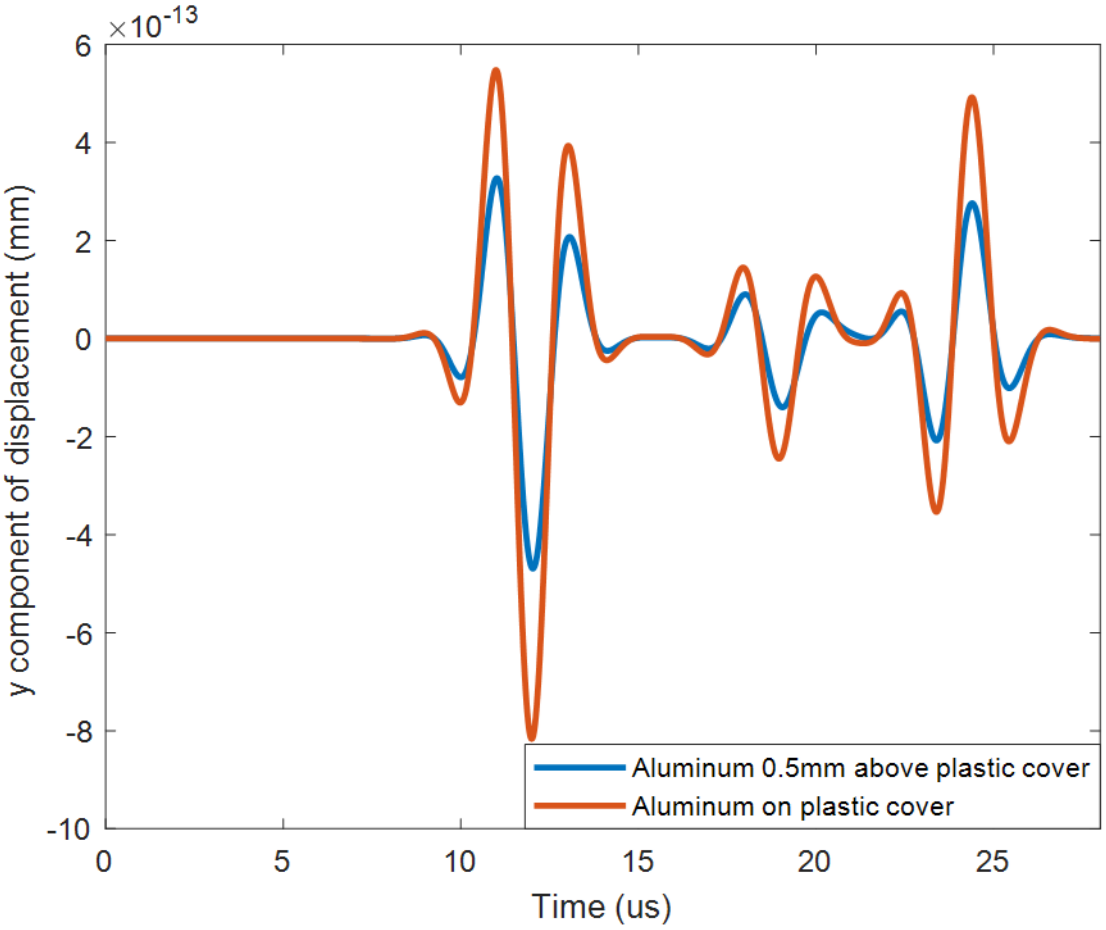

Figure 9.25 Comparison of displacement A-scans at measurement point on plastic back-wall for varying aluminum strip placements (Induced Excitation EMAT)

9.5 A Comparative Analysis: Gaussian vs. Uniform Distribution of Lorentz force in space

In this investigation, the input is applied to aluminum strip as outlined in Figure 9.26. Gaussian weights are assigned to the currents provided to the designated points in Case 1, representing a Gaussian distribution in space (along the x, i.e., direction of aluminum width). Conversely, in Case 2 (Uniform distribution in space), all points illustrated in Figure 9.26 receive equal weights. All other parameters in the model remain consistent with the details provided in Table 9.1. The aluminum strip width is 10mm. In Case 1, the simulation is designed to generate a Gaussian distribution in the Lorentz force. The objective of this study is to validate the model for different spatial Lorentz force distributions.

Figure 9.27 and Figure 9.28 shows the arrow surface plots of Lorentz force in copper patch

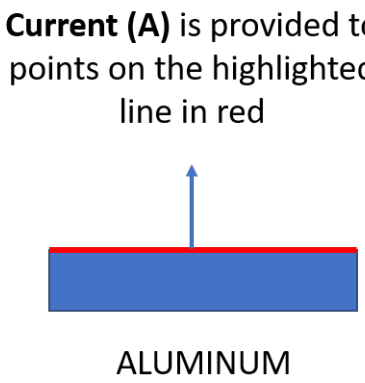

Figure 9.26 Representation of input current provided to Aluminum strip

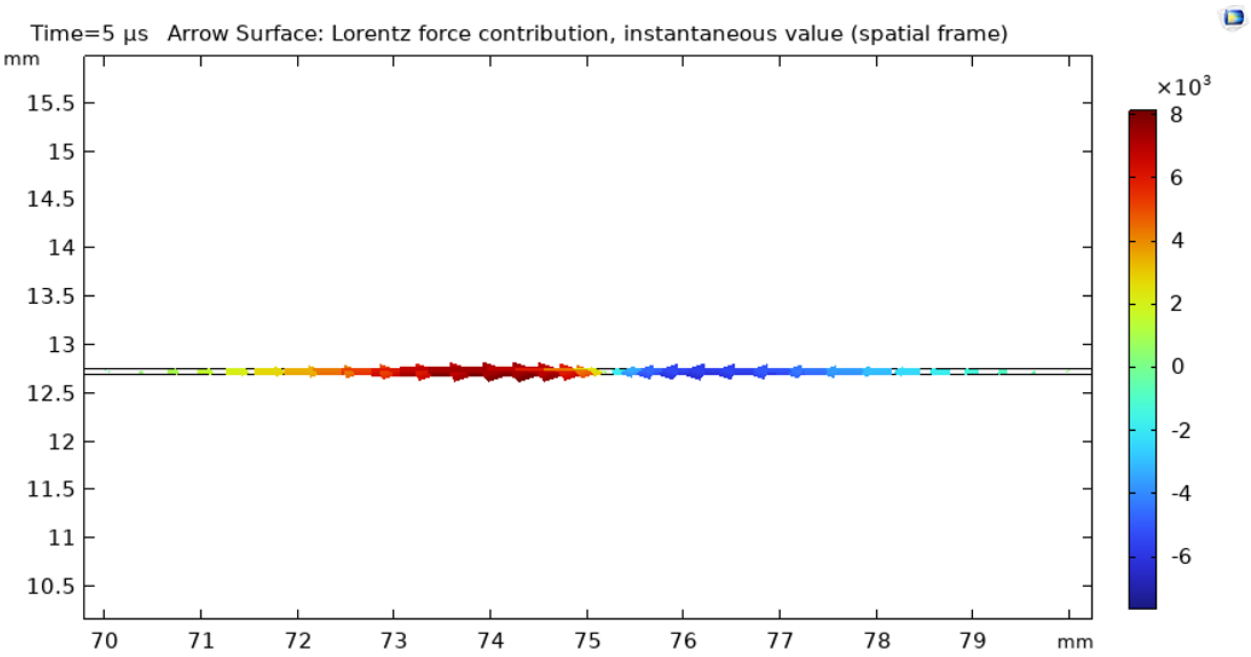

Figure 9.27 Arrow surface plot of x-component of Lorentz force (Case 1) in Copper patch at 5 µs

(x and y components) at 5 µs for case 1. The x component shows a pattern similar to the results obtained for direct excitation and induced excitation with aluminum strip. The y-component exhibits a Gaussian distribution in space (along the x-axis) due to the spatial pattern in which the input current is applied to the aluminum strip.

Figure 9.29 and Figure 9.30 shows the arrow surface plots of Lorentz force in copper patch (x and y components) at 5 µs for case 2. The x component shows a pattern similar to the results obtained for direct excitation and induced excitation with aluminum strip. The y component shows a uniform distribution in space, as discussed earlier.

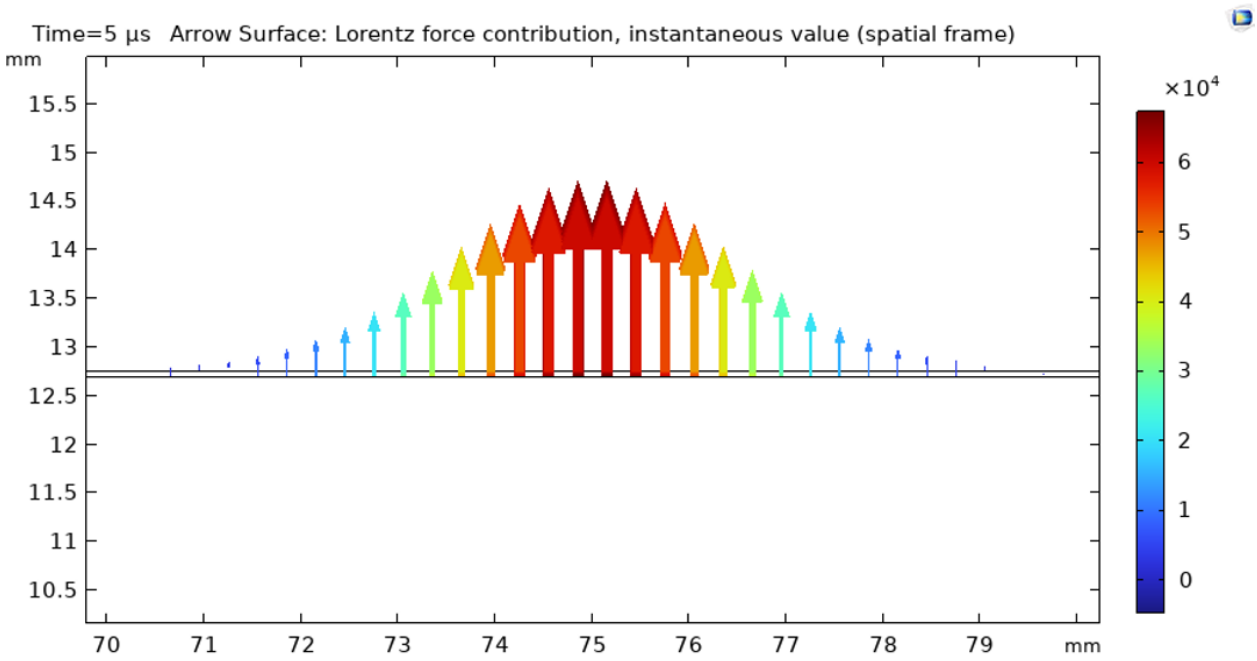

Figure 9.28 Arrow surface plot of y-component of Lorentz force (Case 1) in Copper patch at 5 µs

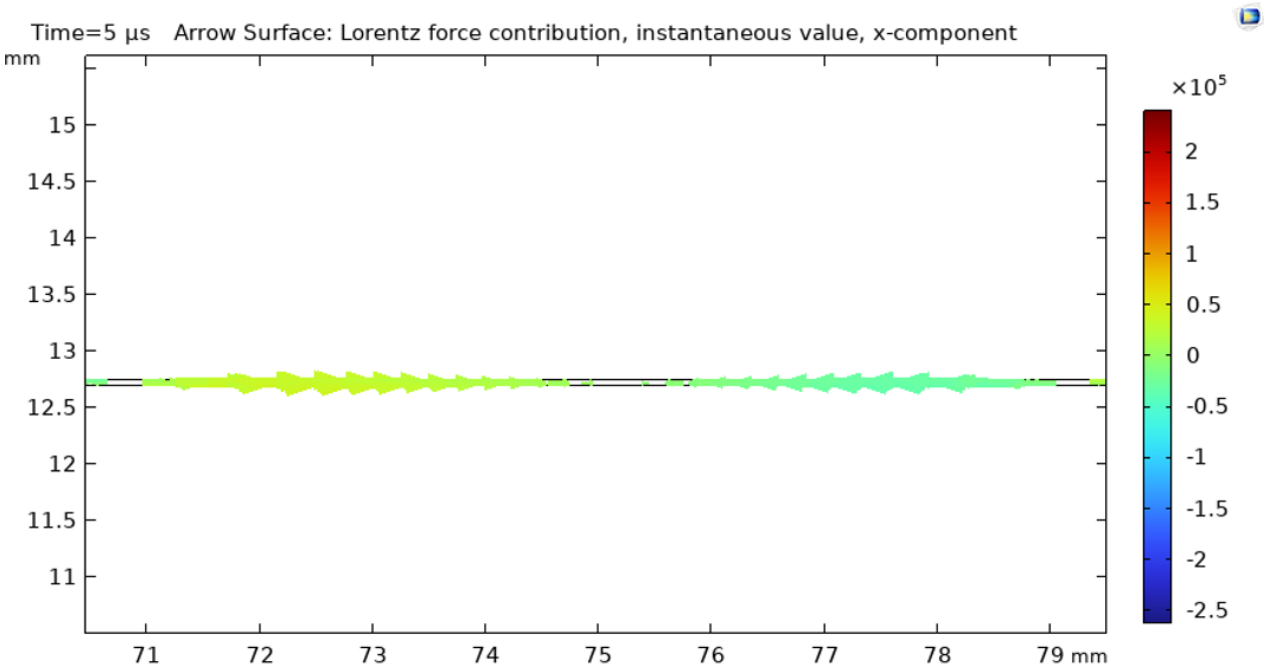

Figure 9.29 Arrow surface plot of x-component of Lorentz force (Case 2) in Copper patch at 5 µs

Figure 9.31 presents a comparative analysis depicting displacement (mode 1) at the plastic back-wall for Gaussian (Case 1) and uniform distributions (Case 2) in space. As expected, the displacement amplitude is higher for the uniform distribution. Mode 2 is evident in the displacement surface plots within the sample (plastic).

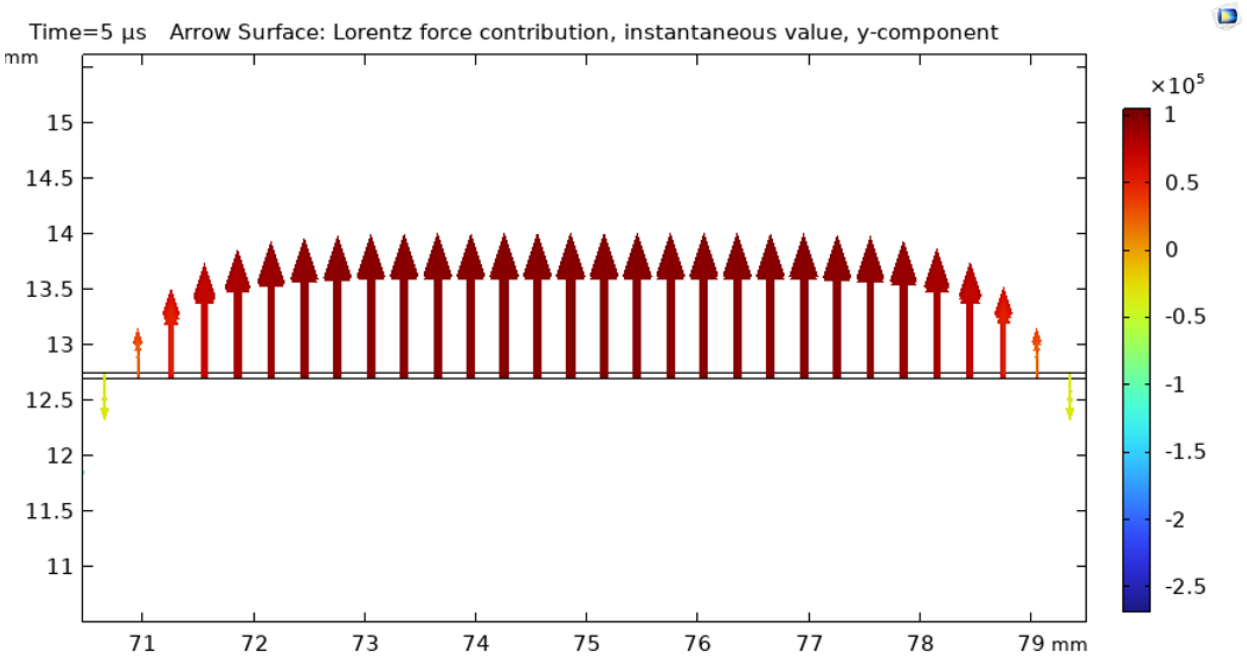

Figure 9.30 Arrow surface plot of y-component of Lorentz force (Case 2) in Copper patch at 5 µs

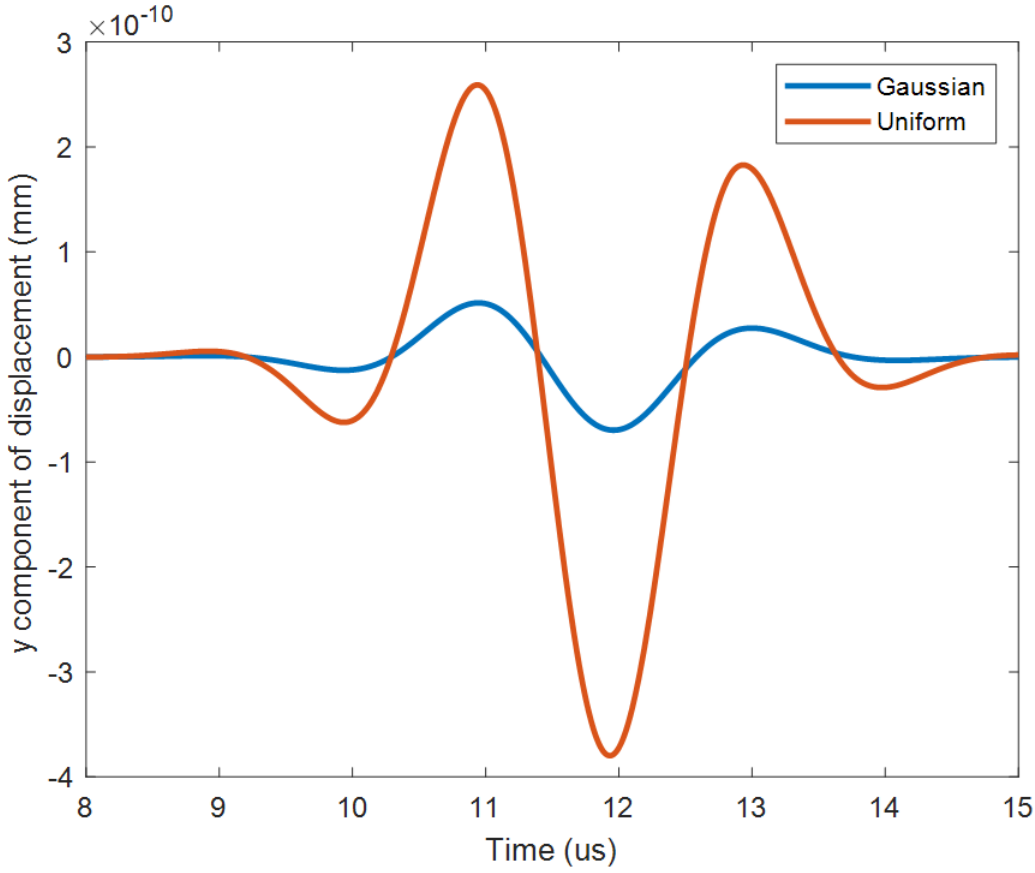

Figure 9.31 Displacement A-scans (Mode 1) at measurement point on plastic back-wall

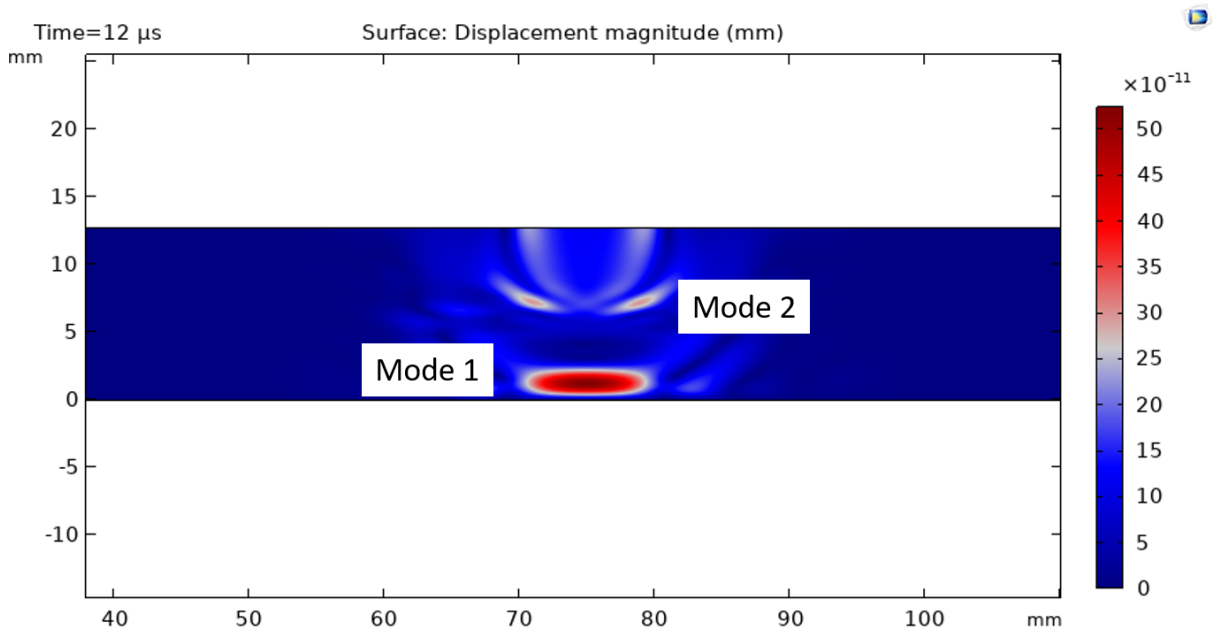

Figure 9.32 Surface plot of full-field displacement in plastic at 12 µs - Case 1

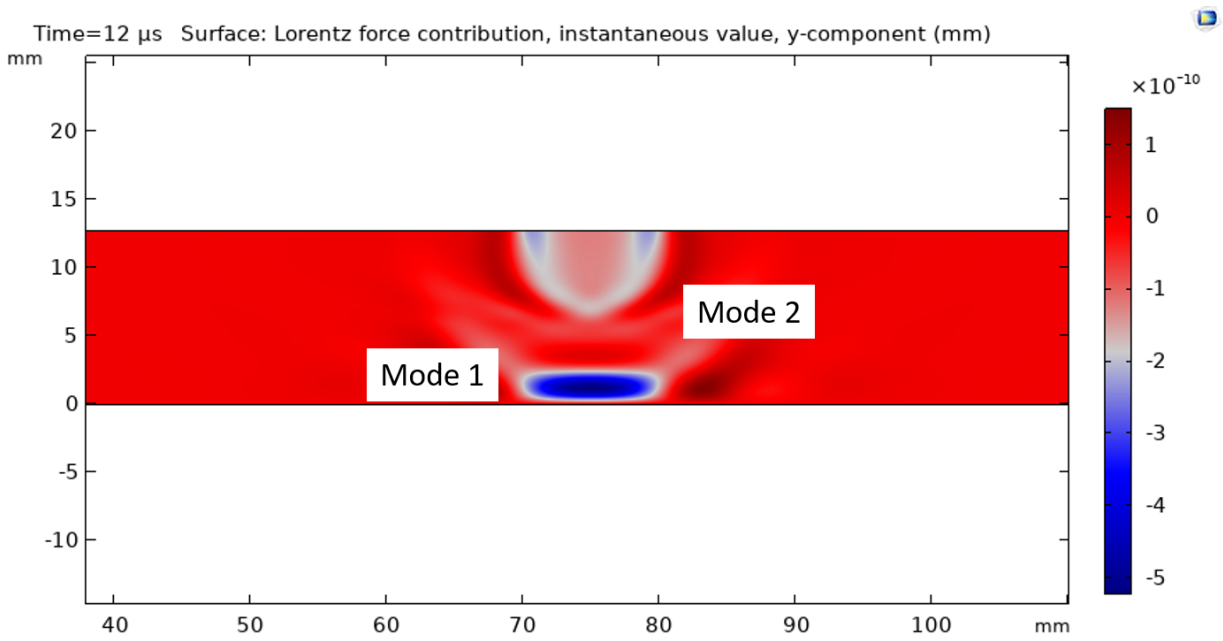

Figure 9.33 Surface plot of y-component of displacement in plastic at 12 µs - Case 1

Figure 9.32, Figure 9.33 and Figure 9.34 presents the full-field displacement plots in the sample at 12 µs for case 1 (i.e., Gaussian distribution of Lorentz force in space). These plots provides a visual representation and validate the propagation of an acoustic wave in the non-conducting sample. The mode 1 and mode 2 can be clearly observed in these plots.

Figure 9.35, Figure 9.36 and Figure 9.37 presents the full-field displacement plots in the sample

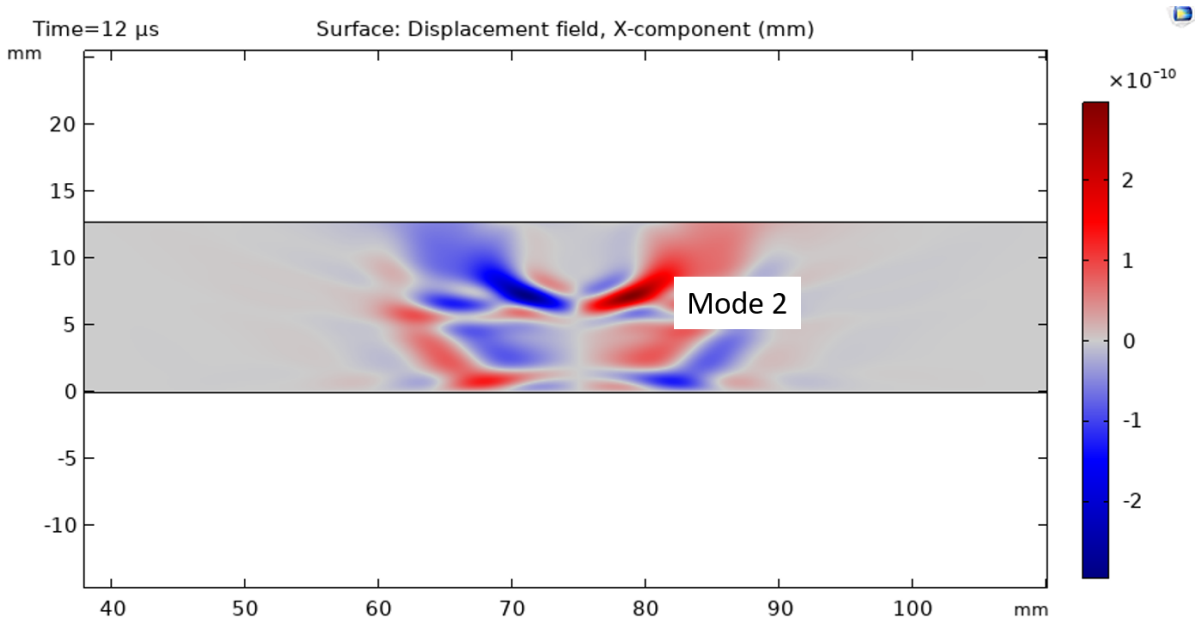

Figure 9.34 Surface plot of x-component of displacement in plastic at 12 µs - Case 1

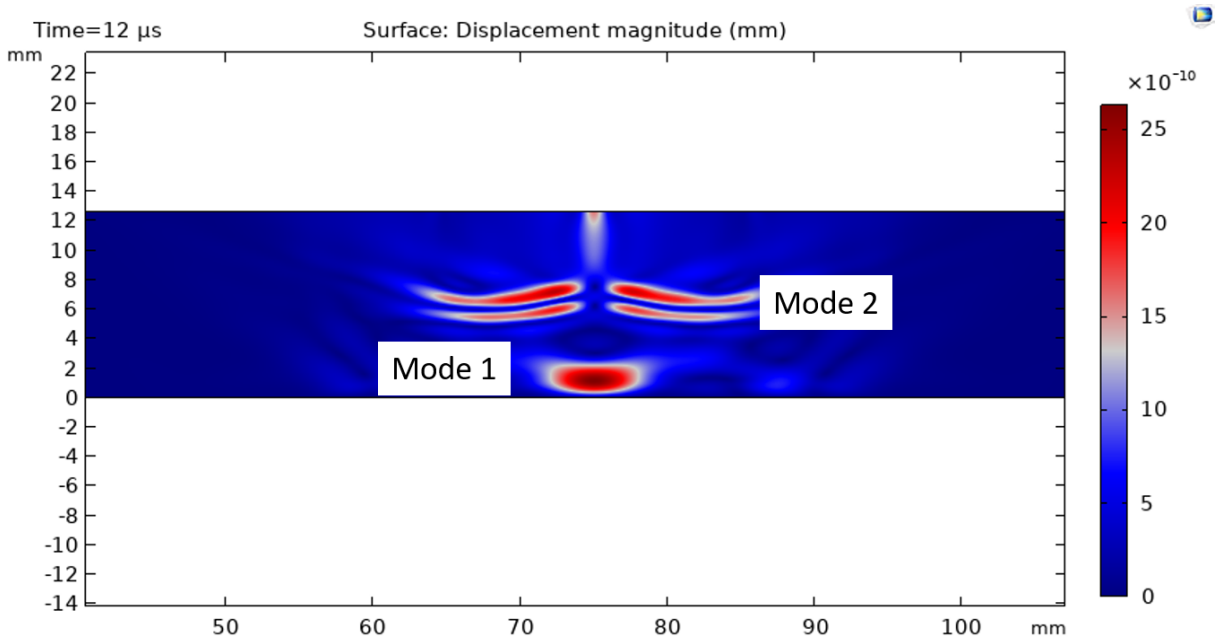

Figure 9.35 Surface plot of full-field displacement in plastic at 12 µs - Case 2

at 12 µs for case 2 (i.e., uniform distribution of Lorentz force in space). These plots provides a visual representation and validate the propagation of an acoustic wave in the non-conducting sample. It can be observed that the displacement amplitudes are much higher for case 2 when compared to case 1. The mode 1 and mode 2 can be clearly observed in these plots. The following section is dedicated to experimental validation of the induced EMAT configuration.

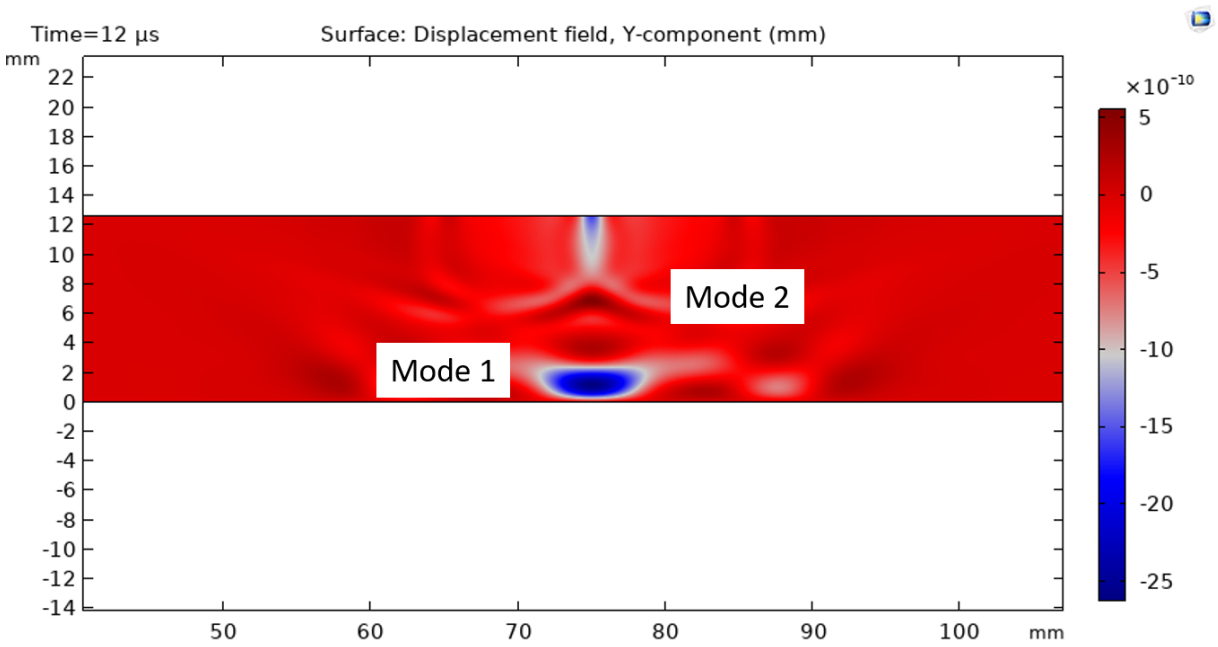

Figure 9.36 Surface plot of y-component of displacement in plastic at 12 µs - Case 2

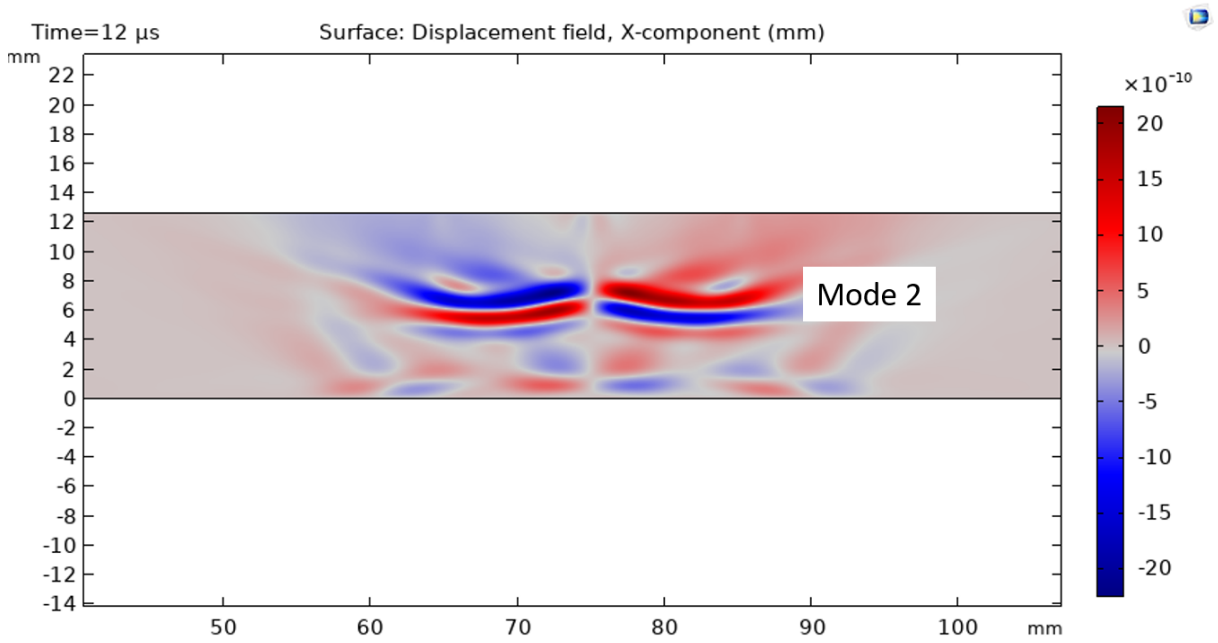

Figure 9.37 Surface plot of x-component of displacement in plastic at 12 µs - Case 2

9.6 Experimental validation

This section focuses on the experimental validation of the induced EMAT model, providing a comparison between experimental and simulation results. The experimental validation in this chapter is a collaborative effort with Zebadiah Miles, a PhD student at Michigan State University,

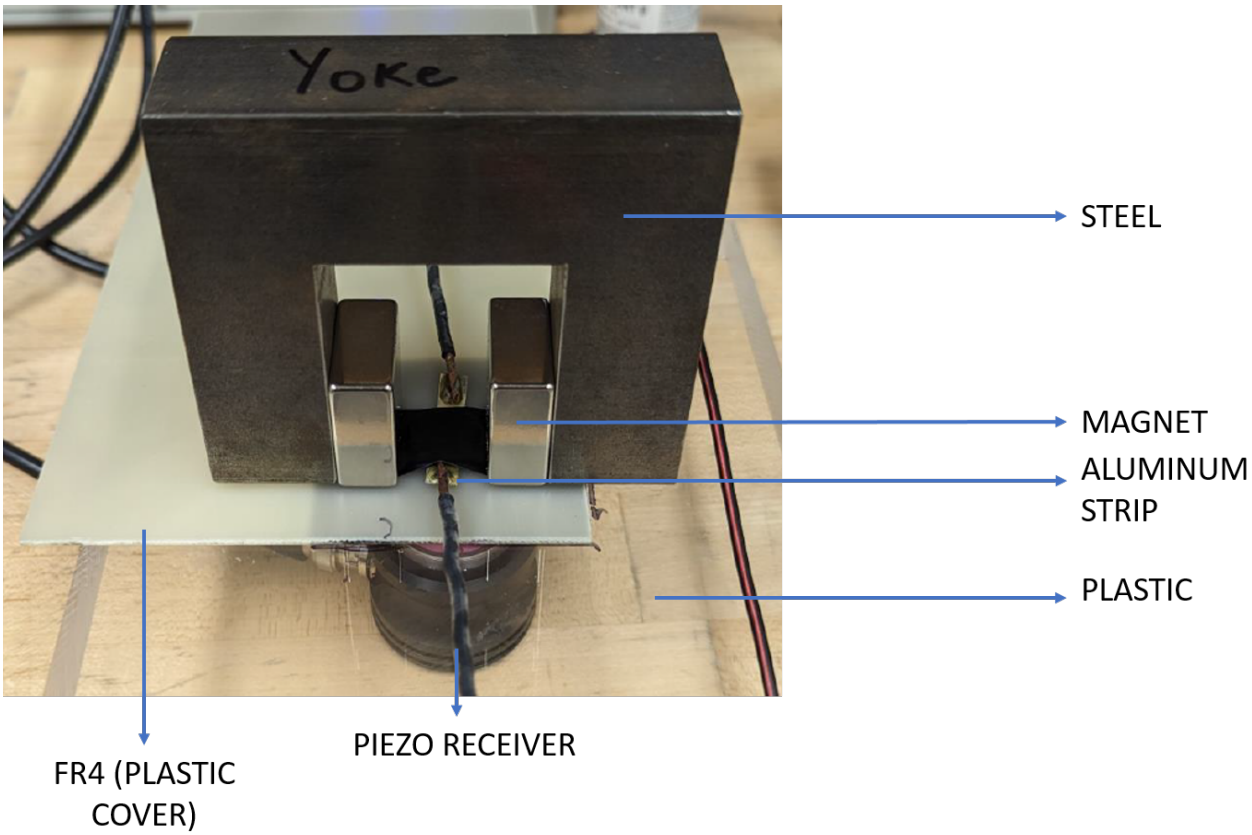

Figure 9.38 Experimental set-up for Induced Excitation EMAT

and I acknowledge his valuable contribution to this work.

The experimental set-up consists of the steel core, permanent magnet, metal strip (aluminum), copper patch, FR4 (plastic cover) and the sample (acrylic plastic) as shown in Figure 9.38. This setup mirrors the simulation configuration. The magnet, yoke, and sample geometries adhere to the specifications outlined in Table 9.1. The copper patch is available underneath the FR4 material (a single sided copper clad PCB) and located on the acrylic plastic. The copper patch is coupled to the sample using a liquid couplant. 3D printed structures can avoid this use of the liquid couplant. A 2-cycle tone-burst signal (at a frequency of 500 kHz) is generated using a function generator and subsequently amplified using a high-power RITEC GA-2500A Gated Amplifier. The output of the power amplifier is provided as input to the aluminum strip (EMAT coil). The resulting elastic waves were detected by a piezoelectric transducer (as shown in Figure 9.38), coupled to the sample with a liquid couplant. Conditioning and amplification of the received signals were performed using

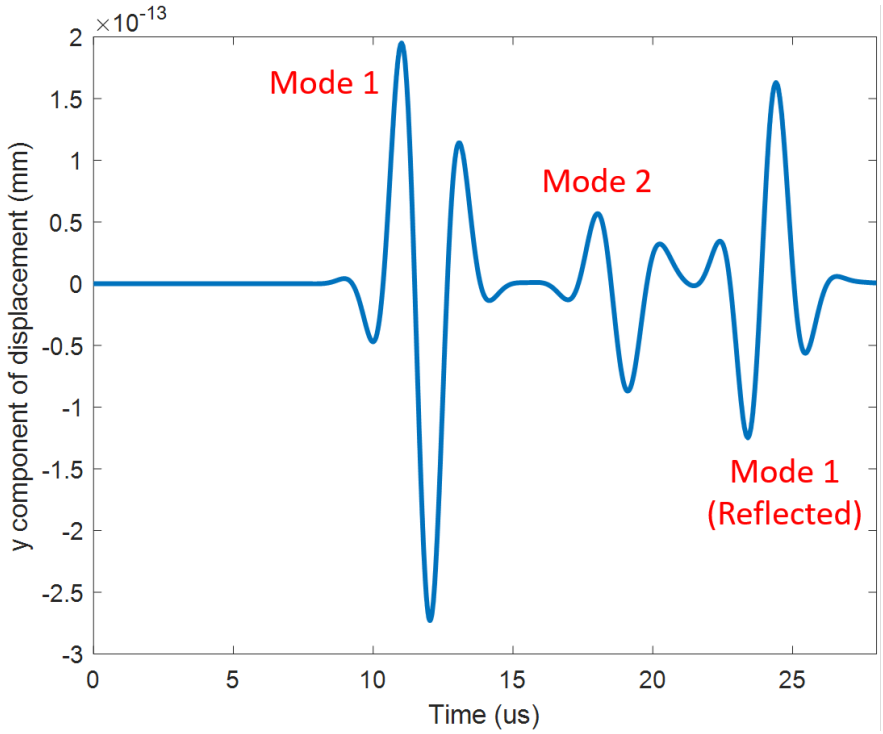

Figure 9.39 A-scan of displacement at measurement point on plastic back-wall - Simulation result for Aluminum strip B (Induced Excitation EMAT)

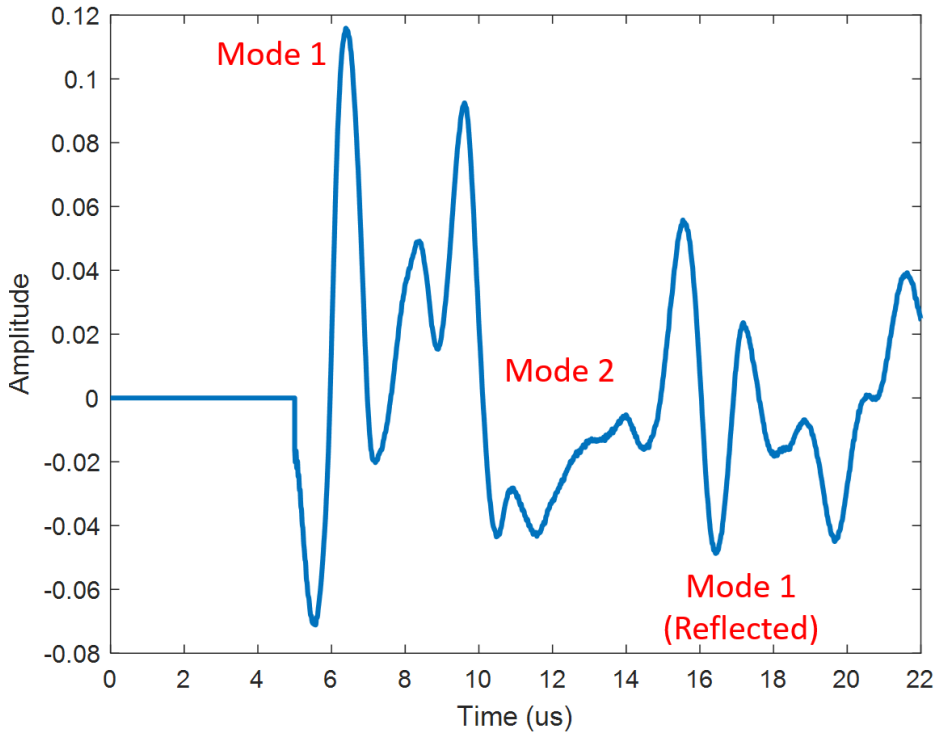

Figure 9.40 A-scan of displacement at measurement point on plastic back-wall - Experimental result for Aluminum strip B (Induced Excitation EMAT)

an ultrasonic pulser/receiver with +60 dB gain. Subsequently, the amplified signals were digitized through an 8-bit oscilloscope operating at a 1 GHz sampling rate. The geometries of aluminum strips used in the experiments are provided in Figure 8.40.

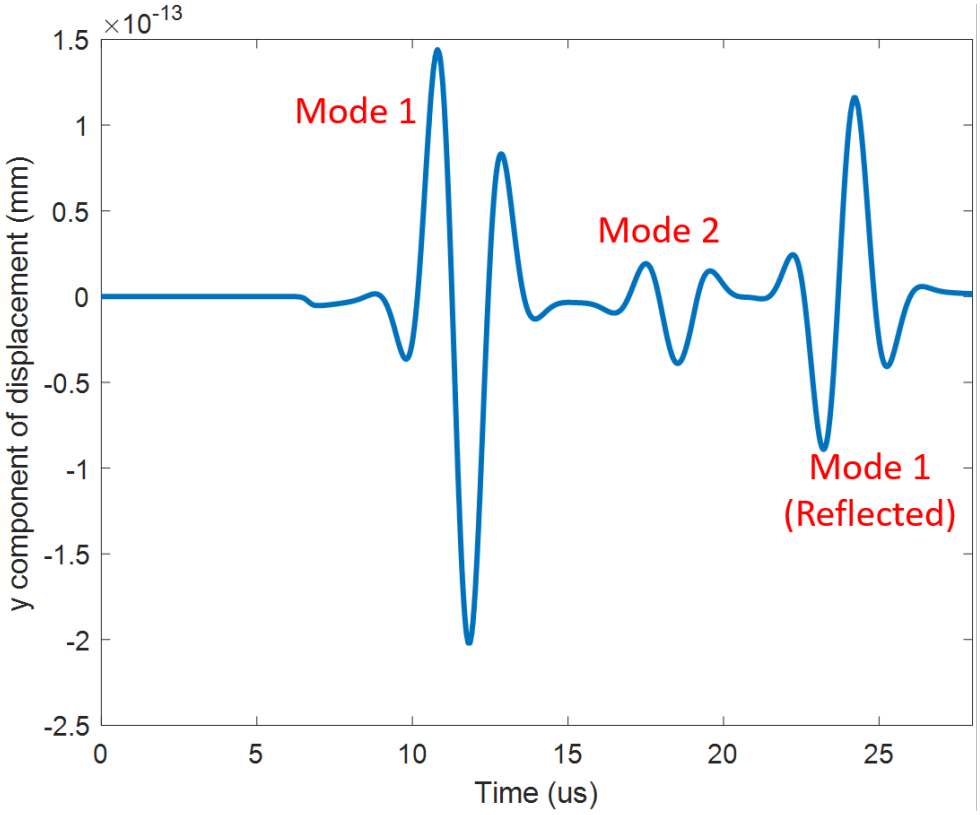

Figure 9.41 A-scan of displacement at measurement point on plastic back-wall - Simulation result for Aluminum strip C (Induced Excitation EMAT)

The simulation and experimental A-scan results for aluminum strip B are shown in Figure 9.39 and Figure 9.40. The simulation and experimental A-scan results for aluminum strip C are shown in Figure 9.41 and Figure 9.42. The simulation and experimental outcomes exhibit indications of a second mode (mode 2) alongside the mode 1 (longitudinal wave). However, the mode 2 wave is more noisy in experimental results when compared with simulation results. Mode 2 can be seen occurring between mode 1 and the first reflection of mode 1 in both simulation and experimental results. Following the application of Hilbert transforms to the A-scan results (simulation and experiment), the velocity of mode 1 is calculated as 2582.35 m/s (experiment) and 2051.69 m/s (simulation). The difference between the experimental and simulation values for the longitudinal

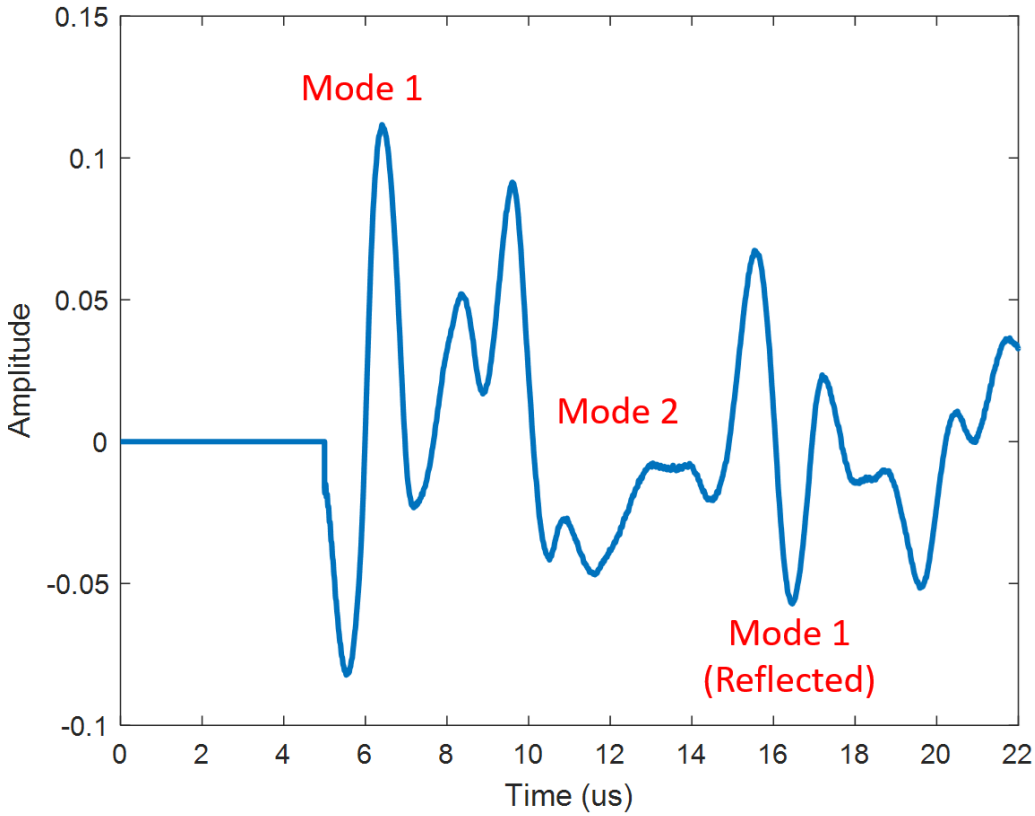

Figure 9.42 A-scan of displacement at measurement point on plastic back-wall - Experimental result for Aluminum strip C (Induced Excitation EMAT)

wave velocity (mode 1) arises from differences in material properties such as Young's modulus and Poisson's ratio for the acrylic samples used in experiments as compared to the simulation. The experimentally obtained A-scan results validate the non-contact induced excitation EMAT model. This concludes the discussion on induced excitation configuration of the EMAT for non-conductive materials. The following chapter will extensively explore the application of non-contact induced excitation EMAT, also called the Embedded EMAT.

CHAPTER 10

DAMAGE DETECTION IN SAMPLE

The preceding chapter offered detailed descriptions of the EMAT models and elucidated the influence of metal strip and metal patch geometries on the displacement in plastic. This chapter delves into the application of embedded EMAT for detecting defects within the sample under test. The study focuses on two distinct types of defects: a) Vertical slot/crack and b) Horizontal crack.

10.1 Vertical slot defect

Figure 10.1 illustrates the model used for simulating the vertical slot type of defect. Notably, this model is identical to the one employed for induced excitation, as depicted in Figure 9.1. The model parameters remain consistent and are detailed in Table 9.1. The defect width considered for this study is 1mm and defect height is chosen as 4mm and the defect geometry representation is shown in Figure 10.2.

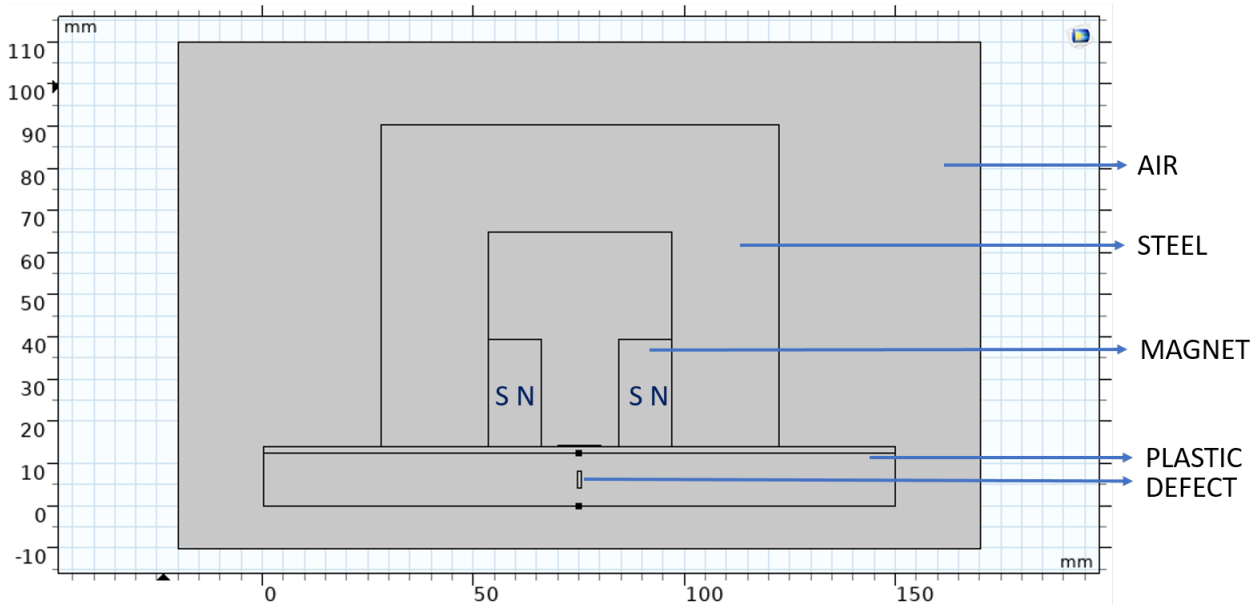

Figure 10.1 Embedded EMAT model with defect in COMSOL

Figure 10.3 presents the A-scans of displacement both with and without a defect in plastic at the measurement point. The ends of the defect function as diffraction sources. The amplitude of mode 1 is diminished due to energy absorption, scattering and reflection by the defect. Meanwhile, mode 2 generates a Rayleigh wave along the vertical flats, leading to diffraction and a subsequent

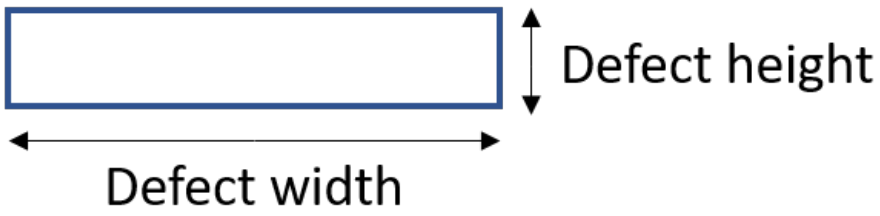

Figure 10.2 Defect geometry representation

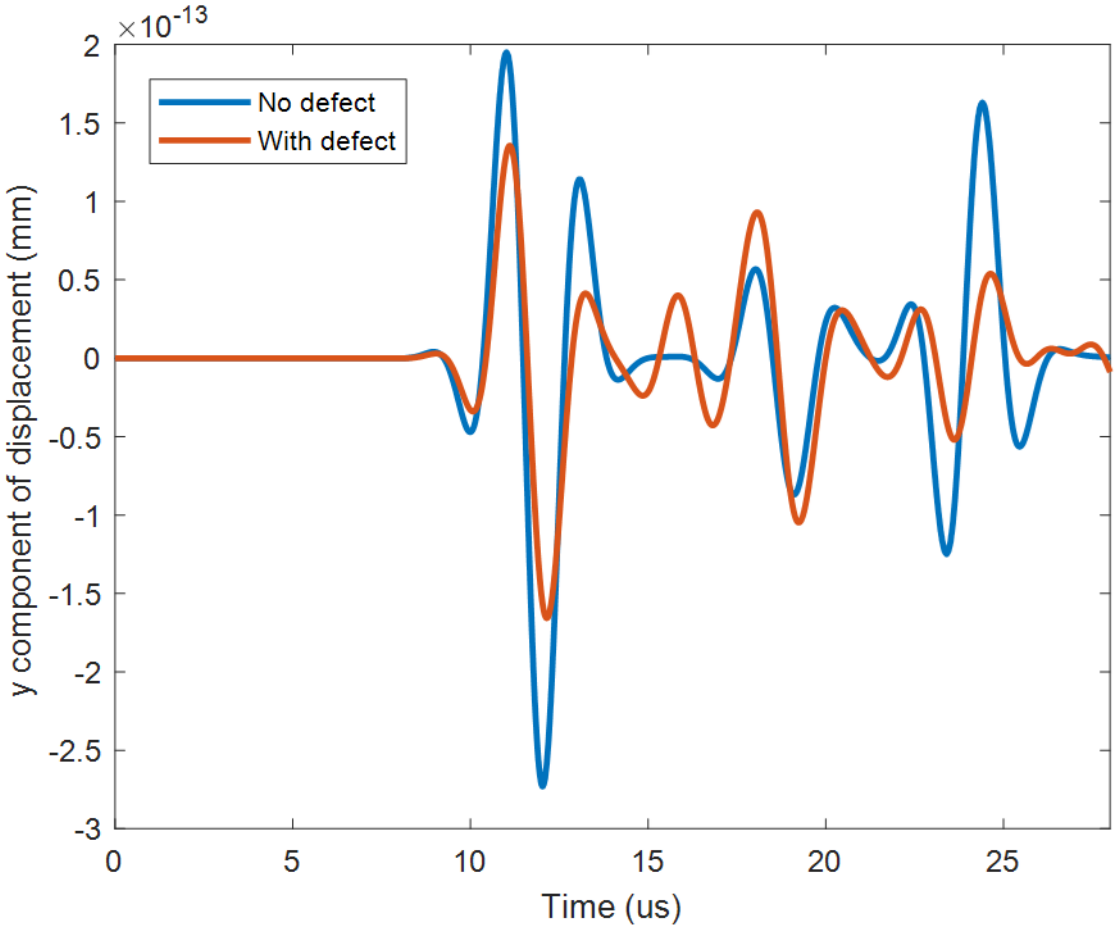

Figure 10.3 A-scan of displacement at measurement point on plastic back wall (No defect and With vertical slot defect)

increase in amplitude, as observed. The full-field displacement plots depicted in Figure 10.4 and Figure 10.5 provide additional visual insights into the wave propagation, scattering and reflection occurring within the sample in the presence and absence of a vertical slot defect.

Figure 10.6 and Figure 10.7 displays the A-scans of displacement with variations in defect width and defect height. For the study on defect width variation, defect height is kept constant at 4mm

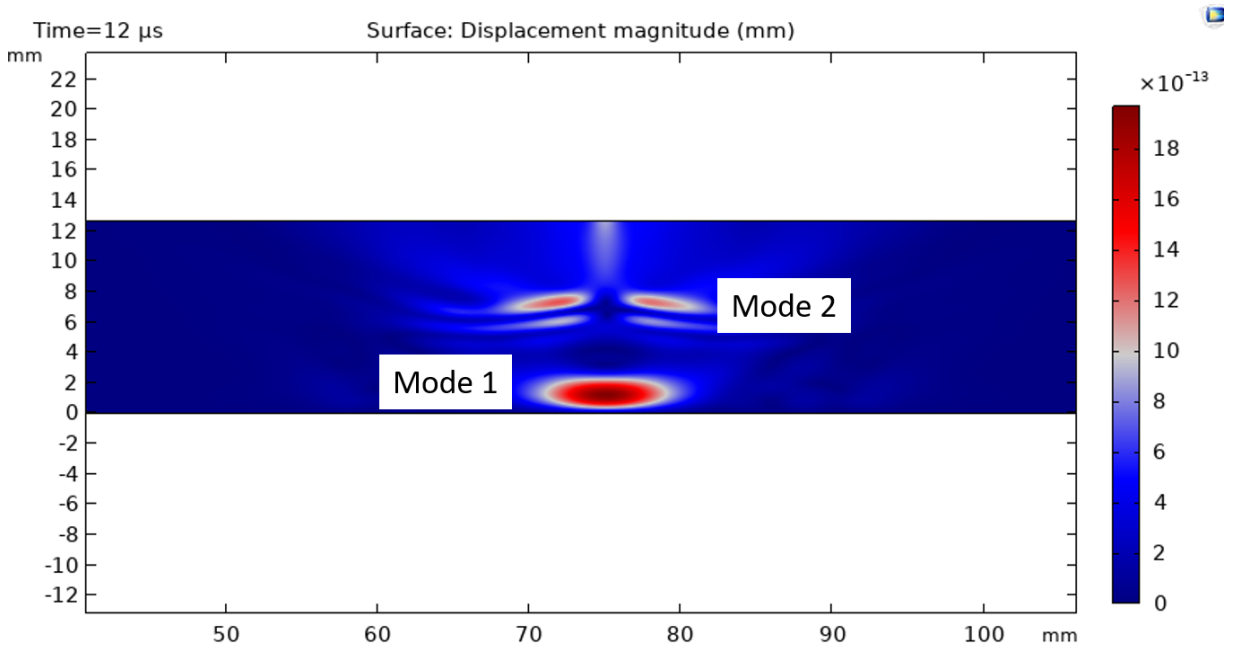

Figure 10.4 Surface plot of full-field displacement in plastic at 12 µs - No defect

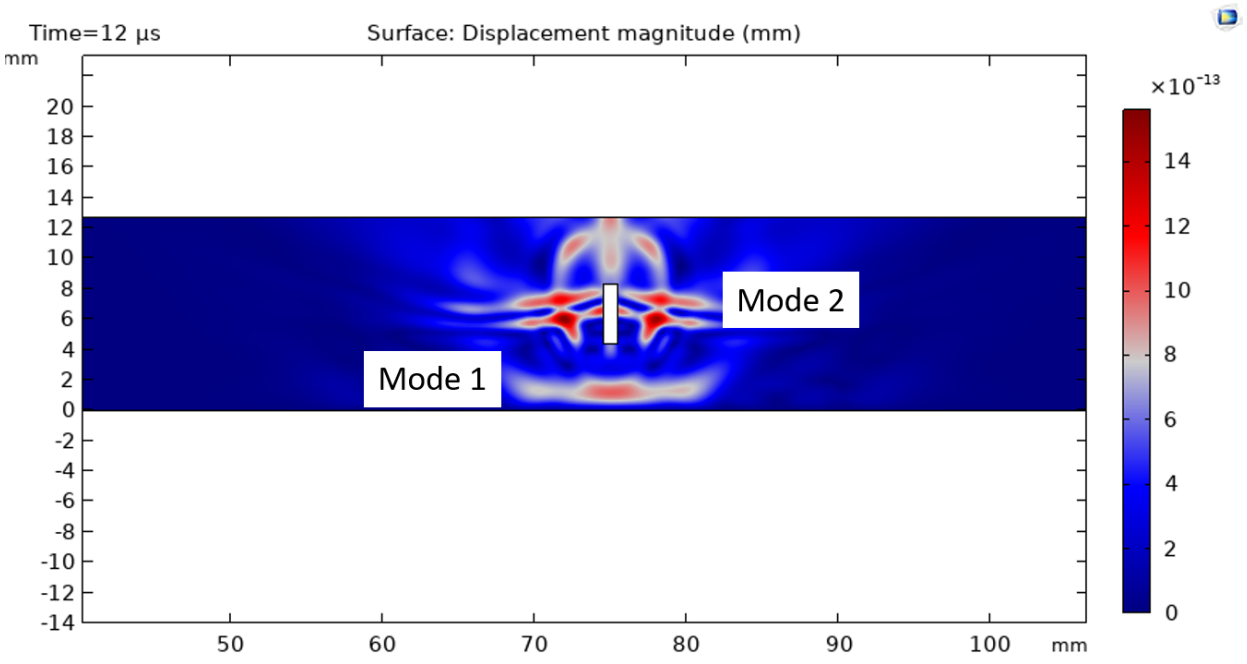

Figure 10.5 Surface plot of full-field displacement in plastic at 12 µs - With defect

and for study on defect height variation, defect width is held constant at 1 mm. As anticipated, the amplitude of mode 1 decreases with increase in defect width. Conversely, mode 2 exhibits greater sensitivity to changes in defect height.

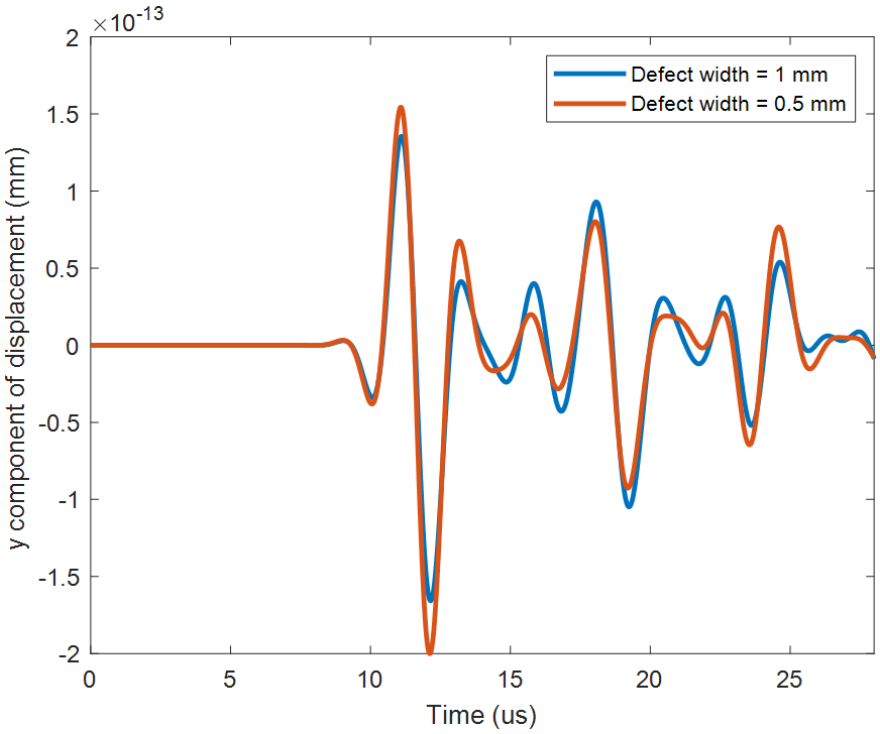

Figure 10.6 A-scan of displacement at measurement point on plastic back-wall for varying defect widths (Defect height = 4mm)

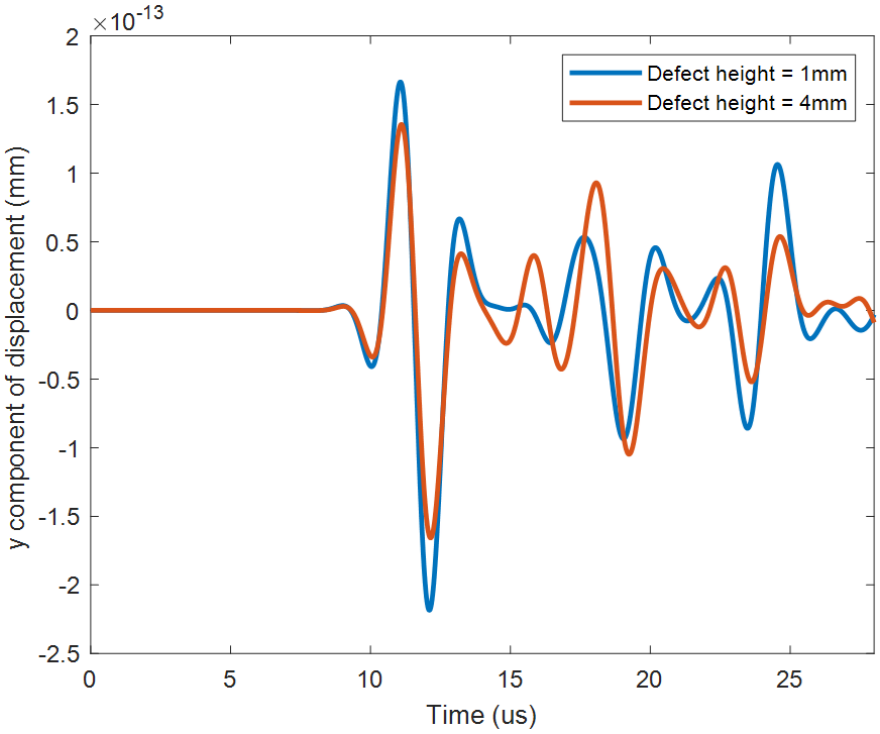

Figure 10.7 A-scan of displacement at measurement point on plastic back-wall for varying defect heights (Defect width = 1mm)

10.2 Horizontal crack defect

The model utilized for this investigation remains consistent with the one described for the vertical slot defect (Figure 10.1). The sole distinction lies in the rotation of the vertical slot to generate a horizontal crack defect. The defect width chosen for this study is 4mm, and the defect height is set at 1mm.

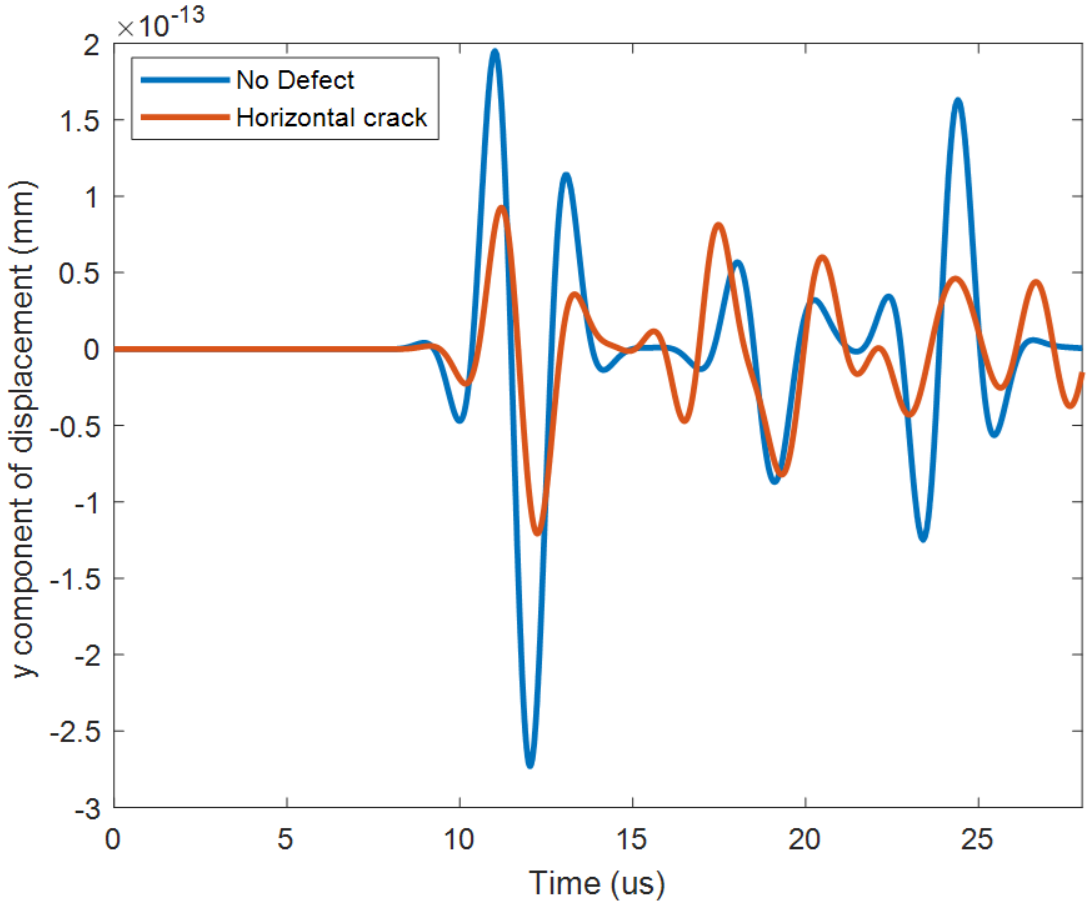

Figure 10.8 A-scans of displacement at measurement point on plastic back-wall (No defect and with Horizontal crack defect)

Figure 10.8 presents the A-scans of displacement both with and without a defect in plastic at the measurement point. The ends of the defect function as diffraction sources, as discussed earlier. The amplitude of mode 1 is diminished considerably due to energy absorption, scattering and reflection by the defect, when compared to vertical slot defect.

Mode 1 is highly sensitive to horizontal crack defect, when compared to the vertical slot defect. Meanwhile, mode 2 generates a Rayleigh wave along the vertical flats, leading to diffraction and a

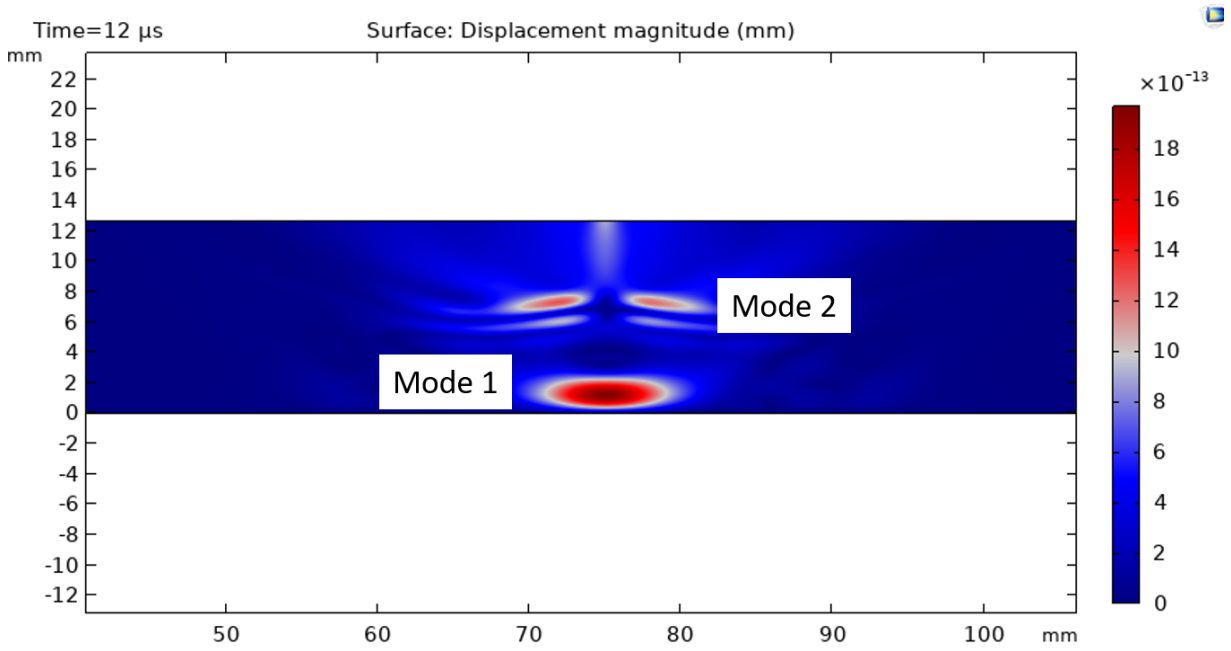

Figure 10.9 Surface plot of full-field displacement in plastic at 12 µs - No defect

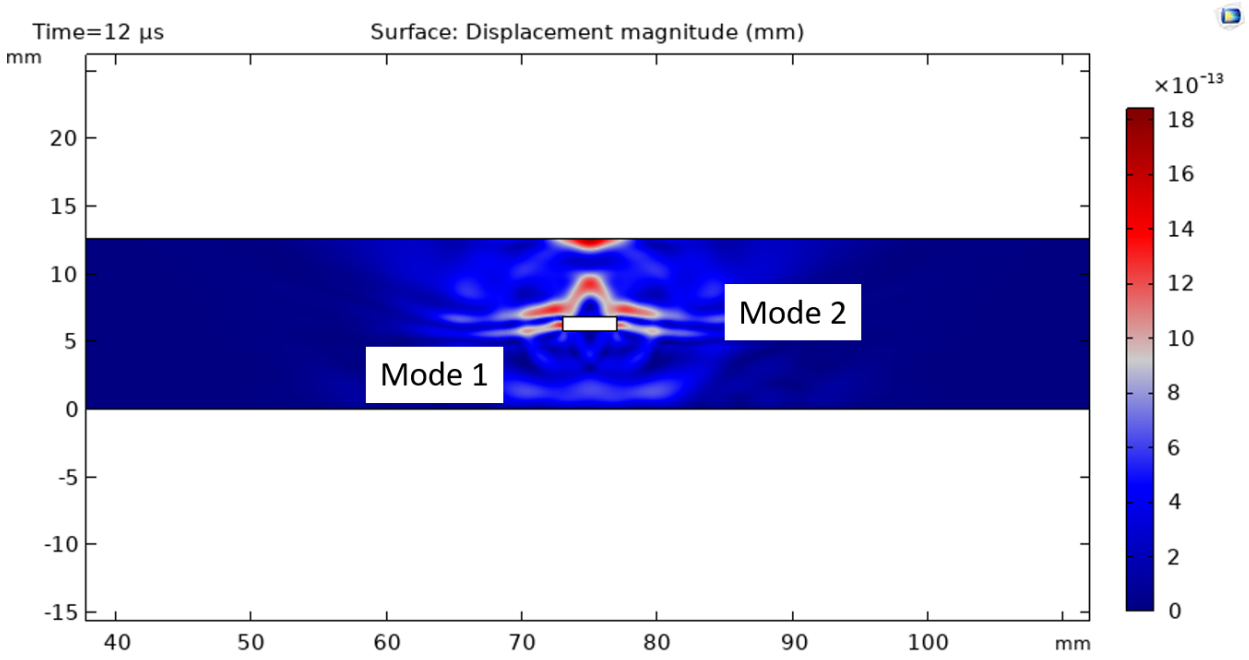

Figure 10.10 Surface plot of full-field displacement in plastic at 12 µs - With defect

subsequent increase in amplitude, as observed and discussed earlier. The full-field displacement plots depicted in Figure 10.9 and Figure 10.10 provide additional visual insights into the wave propagation, scattering and reflection occurring within the sample in the presence and absence of the horizontal crack defect.

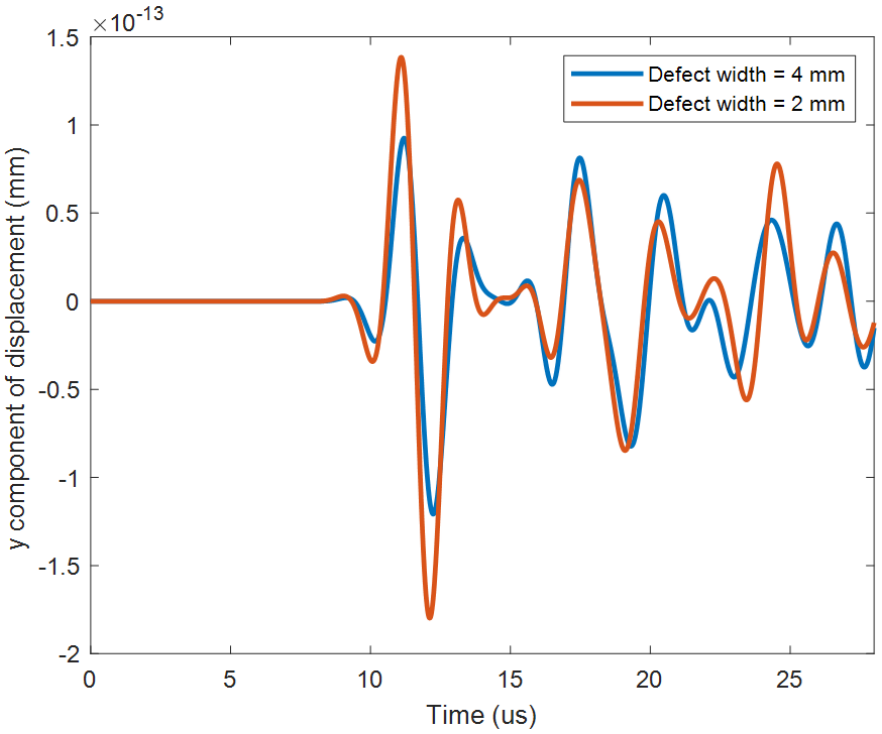

Figure 10.11 A-scans of displacement at measurement point on plastic back-wall for varying defect widths (Defect height = 1mm)

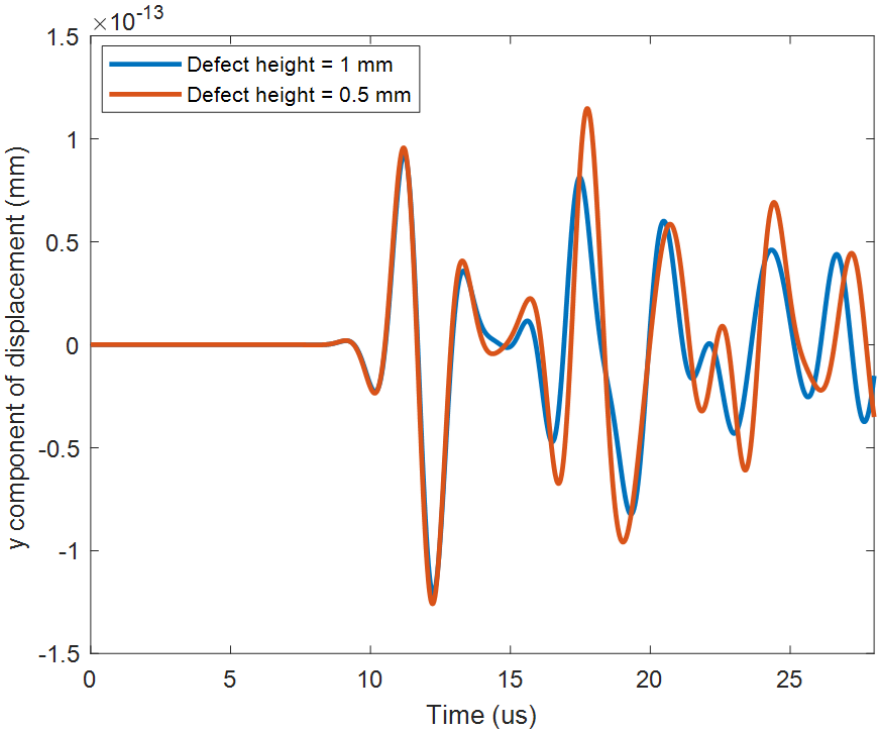

Figure 10.12 A-scans of displacement at measurement point on plastic back-wall for varying defect heights (Defect width = 4mm)

Figure 10.11 presents the A-scans of displacement with variations in defect width, maintaining a constant defect height of 1mm. Figure 10.12 presents the A-scans of displacement with variations in defect height, maintaining a constant defect width of 4mm. As expected, the amplitude of mode 1 diminishes for a wider defect. Conversely, mode 2 exhibits greater sensitivity to changes in defect height (Figure 10.12).

10.3 A-scans on sample back-wall

This section presents A-scan results for various points on the plastic back-wall, considering the horizontal crack and vertical slot defect types. Details regarding defect locations, aluminum strip positions, and other parameters are provided in Table 10.1.

Table 10.1 Model parameters with defect dimensions

Parameter	**Value**
Horizontal crack width	4 mm
Horizontal crack height	1 mm
Vertical slot width	2 mm
Vertical slot height	4 mm
Horizontal crack defect location (x-coordinate)	73 to 77 mm
Vertical slot defect location (x-coordinate)	74 to 76 mm
Aluminum strip location (x-coordinate)	70 to 80 mm
Magnet location on left (x-coordinate)	53.35 to 66.05 mm
Magnet location on right (x-coordinate)	84.35 to 97.05 mm
Magnet width	12.7 mm
Magnet height	25.4 mm
Aluminum strip width	10 mm
Aluminum strip height	0.254 mm

Figure 10.13 presents the outcomes of this investigation for the horizontal crack defect. Displacement A-scans on the plastic back-wall (for with and without defect) are acquired at intervals of 0.25 mm, ranging from 30 mm to 120 mm. Subsequently, Hilbert magnitudes are extracted from the displacement A-scans. The earlier discussions emphasized that mode 1 is particularly sensitive to horizontal dimension (width) of the defect. Therefore, the Hilbert magnitudes of mode 1 are the focus of consideration in this study for the horizontal crack-type defect.

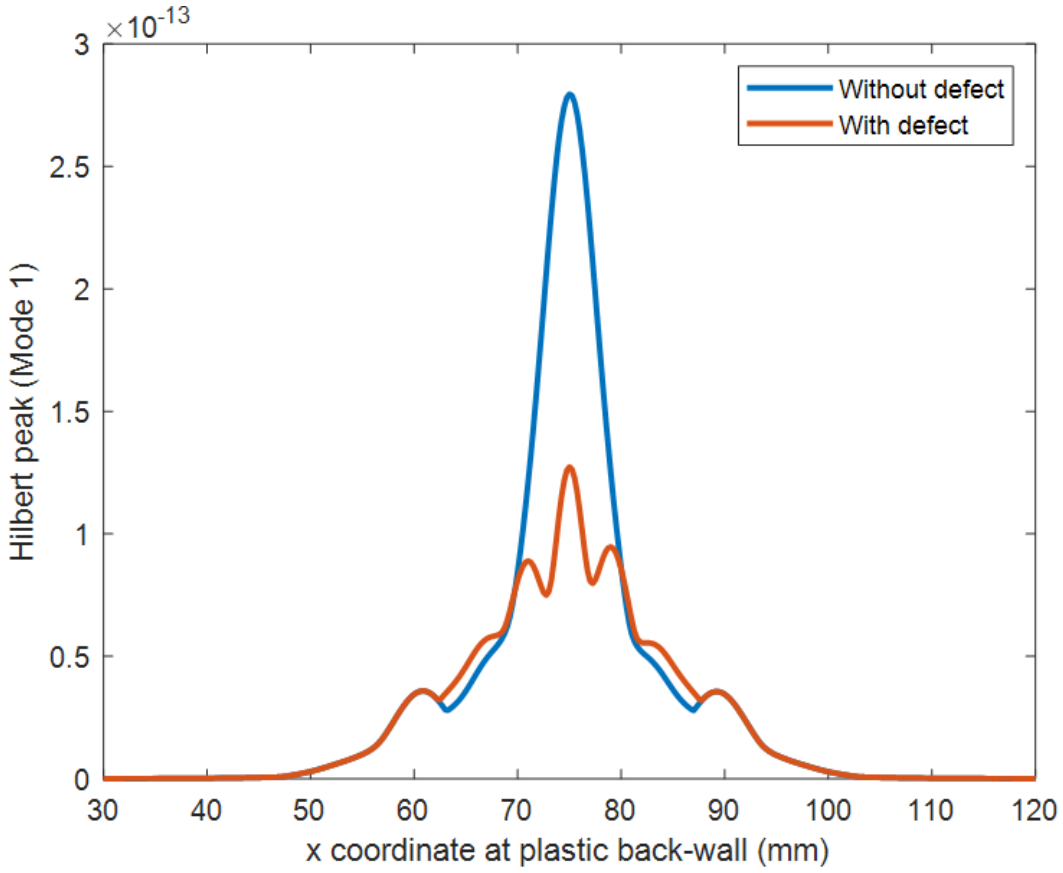

Figure 10.13 A-scan results for a Horizontal crack defect

Key observations from the results in Figure 10.13 are:

1. The beam profile in the absence of a defect exhibits a Gaussian shape, spanning from 70 to 80 mm, coinciding with the location of the source (Aluminum strip).

2. The signal amplitude is diminished in the presence of a defect when compared to the scenario without any defect.

3. The beam profile in the presence of a defect exhibits multiple peaks, particularly in the region of the defect and source. The dominant one here is between 73 to 77 mm, which coincides with the location of defect.

4. A prominent peak is observed at the center-line of both the source and the defect, precisely at 75 mm. Additionally, peaks are evident at the edges of the defect, specifically at 73 mm and 77 mm.

5. The next set of dominant peaks are occurring at 70 mm and 80 mm, which coincide with the location of aluminum strip (source).

6. From all the above observations, it can be concluded the embedded EMAT is able to detect the horizontal crack type defect (located between 73 to 77 mm as indicated in Table 10.1).

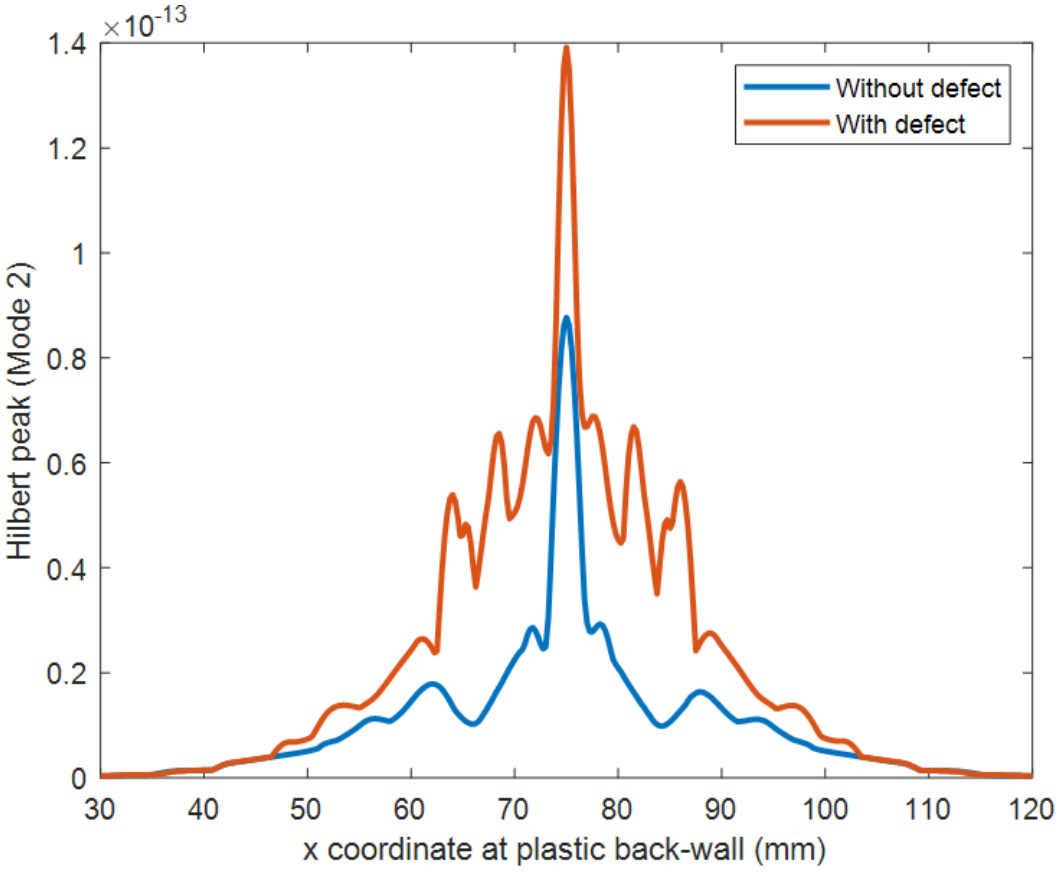

Figure 10.14 A-scan results for a Vertical slot defect

Figure 10.14 presents the outcomes of a similar investigation for the vertical slot type defect. Displacement A-scans on the plastic back-wall (for with and without defect) are again acquired at intervals of 0.25 mm, ranging from 30 mm to 120 mm. Subsequently, Hilbert magnitudes are extracted from the displacement A-scans. The earlier discussions emphasized that mode 2 is more sensitive to vertical dimensions (height) of the defects. Therefore, the Hilbert magnitudes of mode 2 are the focus of consideration in this study for the vertical slot type defect. The dominant peak for the signal with defect is at the center-line of the defect, i.e., at 75mm. It can observed that the beam profile (for the signal with defect) coincides with the defect location.

Conclusively, the findings from the damage detection study indicate that mode 1 is more sensitive to the horizontal dimension (width) of the defect, while mode 2 demonstrates greater sensitivity to the vertical dimension (height) of the defect. Given the availability of both mode 1 and a coupled mode (mode 2), the embedded EMAT emerges as a valuable tool for advanced nondestructive evaluation in structural health monitoring.

CHAPTER 11

CONCLUSIONS AND FUTURE WORK

The numerical model for an Electromagnetic Acoustic Transducer (EMAT) tailored for inspecting non-conductive samples is developed using COMSOL. Two distinct approaches, namely direct excitation and non-contact induced excitation, are systematically explored. The simulation results affirm the propagation of an elastic wave within the non-conductive sample for both approaches. The numerical findings reveal the presence of two modes in the displacement A-scans: the longitudinal mode and a coupled mode.

An in-depth analysis of the influence of aluminum strip geometry on both the Lorentz force in aluminum strip and displacement in plastic is conducted, yielding pertinent numerical results. Notably, a reduction in height of the aluminum strip corresponds to an increased displacement at the back-wall of plastic, while an increase in the aluminum strip width is correlated with an enhanced displacement at the plastic back-wall. The influence of skin effect (in copper patch and aluminum strip) on displacement in plastic is also explored and presented as part of this research work.

The limitation of the direct excitation configuration, rooted in its reliance on contact and contradicting the non-contact nature of EMATs, is addressed through the extension of the proposed approach to a novel non-contact induced excitation configuration – the embedded EMAT.

Moreover, the simulations involving defects in the embedded EMAT highlight the robustness of this non-contact NDE technique for efficient damage detection. Furthermore, the embedded EMAT technique demonstrates potential for detecting not only horizontal defects but also vertical slot-type defects. This capability is attributed to the coupled mode, as evident in the numerical simulation results. In conclusion, the outcomes from the damage detection study emphasize that mode 1 exhibits higher sensitivity to the horizontal dimension of the defect, while mode 2 displays greater sensitivity to the vertical dimension of the defect.

As part of future work, delving into the application of 3D printing techniques for the fabrication of embedded EMATs emerges as a promising avenue. Such an exploration extends beyond conventional manufacturing approaches, offering opportunities to optimize the performance and efficiency

of embedded EMATs through innovative design considerations. Additionally, the investigation of coil and magnet configurations, specifically tailored for flux focusing to enhance the x-component of magnetic flux density within copper, holds substantial potential. This line of inquiry aims to further enhance the efficacy of EMAT systems, contributing to advancements in non-destructive evaluation techniques for damage detection and structural health monitoring.

BIBLIOGRAPHY

[1] S. Xie, Y. Li, W. Cai, H.-E. Chen, Z. Chen, T. Takagi, T. Uchimoto, and Y. Yoshida, "A numerical method for simulation of nonlinear eddy current testing signals based on transient ar formulation," *Materials Transactions*, vol. 54, no. 6, pp. 964–968, 2013.

[2] Y.-L. Lee, M. E. Barkey, and H.-T. Kang, *Metal fatigue analysis handbook: practical problem-solving techniques for computer-aided engineering*. Elsevier, 2011.

[3] B. Wisner, K. Mazur, and A. Kontsos, "The use of nondestructive evaluation methods in fatigue: A review," *Fatigue & Fracture of Engineering Materials & Structures*, vol. 43, no. 5, pp. 859–878, 2020.

[4] V. Terent'ev, "Stages in fatigue failure of metallic materials," *Metally (Moscow)*, pp. 14–20, 1996.

[5] Y. Bai, *Marine structural design*. Elsevier, 2003.

[6] L. Cartz, "Nondestructive testing," 1995.

[7] B. D. Cullity and C. D. Graham, *Introduction to magnetic materials*. John Wiley & Sons, 2011.

[8] A. W. Mello, A. Nicolas, R. A. Lebensohn, and M. D. Sangid, "Effect of microstructure on strain localization in a 7050 aluminum alloy: comparison of experiments and modeling for various textures," *Materials Science and Engineering: A*, vol. 661, pp. 187–197, 2016.

[9] J. Vasco-Olmo, F. Díaz, A. García-Collado, and R. Dorado-Vicente, "Experimental evaluation of crack shielding during fatigue crack growth using digital image correlation," *Fatigue & Fracture of Engineering Materials & Structures*, vol. 38, no. 2, pp. 223–237, 2015.

[10] A. Iziumova and O. Plekhov, "Calculation of the energy j-integral in plastic zone ahead of a crack tip by infrared scanning," *Fatigue & Fracture of Engineering Materials & Structures*, vol. 37, no. 12, pp. 1330–1337, 2014.

[11] B. Wisner, M. Cabal, P. Vanniamparambil, J. Hochhalter, W. Leser, and A. Kontsos, "In situ microscopic investigation to validate acoustic emission monitoring," *Experimental Mechanics*, vol. 55, no. 9, pp. 1705–1715, 2015.

[12] I. Sevostianov, A. Zagrai, W. A. Kruse, and H. C. Hardee, "Connection between strength reduction, electric resistance and electro-mechanical impedance in materials with fatigue damage," *International Journal of Fracture*, vol. 164, no. 1, pp. 159–166, 2010.

[13] Y. Y. Lim and C. K. Soh, "Fatigue life estimation of a 1d aluminum beam under mode-i loading using the electromechanical impedance technique," *Smart Materials and Structures*, vol. 20, no. 12, p. 125001, 2011.

[14] L. Bodelot, E. Charkaluk, L. Sabatier, and P. Dufrénoy, "Experimental study of heterogeneities in strain and temperature fields at the microstructural level of polycrystalline metals through fully-coupled full-field measurements by digital image correlation and infrared thermography," *Mechanics of Materials*, vol. 43, no. 11, pp. 654–670, 2011.

[15] N. Castaneda, B. Wisner, J. Cuadra, S. Amini, and A. Kontsos, "Investigation of the z-binder role in progressive damage of 3d woven composites," *Composites Part A: Applied Science and Manufacturing*, vol. 98, pp. 76–89, 2017.

[16] P. Dobroň, J. Bohlen, F. Chmelík, P. Lukáč, D. Letzig, and K. U. Kainer, "Acoustic emission during stress relaxation of pure magnesium and az magnesium alloys," *Materials Science and Engineering: A*, vol. 462, no. 1-2, pp. 307–310, 2007.

[17] F. Di Gioacchino and J. Q. Da Fonseca, "Plastic strain mapping with sub-micron resolution using digital image correlation," *Experimental Mechanics*, vol. 53, no. 5, pp. 743–754, 2013.

[18] A. Kontsos, T. Loutas, V. Kostopoulos, K. Hazeli, B. Anasori, and M. W. Barsoum, "Nanocrystalline mg–max composites: Mechanical behavior characterization via acoustic emission monitoring," *Acta Materialia*, vol. 59, no. 14, pp. 5716–5727, 2011.

[19] D. Jiles and D. Utrata, "Effects of tensile plastic deformation on the magnetic properties of aisi 4140 steel," *Journal of Nondestructive Evaluation*, vol. 6, no. 3, pp. 129–134, 1987.

[20] M. Devine, D. Kaminski, L. Sipahi, and D. Jiles, "Detection of fatigue in structural steels by magnetic property measurements," *Journal of Materials Engineering and Performance*, vol. 1, no. 2, pp. 249–253, 1992.

[21] S. Zhang, X. Shi, L. Udpa, and Y. Deng, "Micromagnetic measurement for characterization of ferromagnetic materials' microstructural properties," *AIP Advances*, vol. 8, no. 5, p. 056614, 2018.

[22] J. Błachnio, J. Dutkiewicz, and A. Salamon, "The effect of cyclic deformation in a 13% cr ferritic steel on structure and barkhausen noise level," *Materials Science and Engineering: A*, vol. 323, no. 1-2, pp. 83–90, 2002.

[23] Z. Li, B. B. Shenoy, L. Udpa, S. Udpa, and Y. Deng, "Magnetic barkhausen noise technique for early-stage fatigue prediction in martensitic stainless-steel samples," *Journal of Nondestructive Evaluation, Diagnostics and Prognostics of Engineering Systems*, vol. 4, no. 4, p. 041004, 2021.

[24] D. Jiles, "Review of magnetic methods for nondestructive evaluation," *NDT international*, vol. 21, no. 5, pp. 311–319, 1988.

[25] S. C. Chan, R. Grimberg, J. A. Hejase, Z. Zeng, P. Lekeakatakunju, L. Udpa, and S. S. Udpa, "Nonlinear eddy current technique for characterizing case hardening profiles," *IEEE transactions on magnetics*, vol. 46, no. 6, pp. 1821–1824, 2010.

[26] G. Dobmann, "Physical basics and industrial applications of 3ma–micromagnetic multiparameter microstructure and stress analysis," *Fraunhofer IZFP, Saarbrcken, Germany*, pp. 1–17, 2007.

[27] G. Dobmann, C. Boller, H.-G. Herrmann, and I. Altpeter, "Micromagnetic and electromagnetic ndt for lifetime management by monitoring ageing of structural materials," *International Journal of Microstructure and Materials Properties*, vol. 9, no. 3-5, pp. 348–359, 2014.

[28] B. B. Shenoy, Z. Li, L. Udpa, S. Udpa, Y. Deng, and T. Seuaciuc-Osorio, "Fatigue detection and estimation in martensitic stainless-steel using magnetic nondestructive evaluation technique," in *Quantitative Nondestructive Evaluation*, vol. 85529, p. V001T14A001, American Society of Mechanical Engineers, 2021.

[29] B. Basti Shenoy, Z. Li, L. Udpa, S. Udpa, Y. Deng, and T. Seuaciuc-Osorio, "Magnetic barkhausen noise technique for fatigue detection and classification in martensitic stainless-steel," *Journal of Nondestructive Evaluation, Diagnostics and Prognostics of Engineering Systems*, vol. 5, no. 4, p. 041010, 2022.

[30] L. Piotrowski, B. Augustyniak, M. Chmielewski, and Z. Kowalewski, "Multiparameter analysis of the barkhausen noise signal and its application for the assessment of plastic deformation level in 13hmf grade steel," *Measurement Science and Technology*, vol. 21, no. 11, p. 115702, 2010.

[31] A. Sorsa, K. Leiviskä, S. Santa-aho, M. Vippola, and T. Lepistö, "An efficient procedure for identifying the prediction model between residual stress and barkhausen noise," *Journal of Nondestructive Evaluation*, vol. 32, no. 4, pp. 341–349, 2013.

[32] M. Lindgren and T. Lepisto, "Barkhausen noise evaluation of fatigue in high strength steel," *International Journal of Materials and Product Technology*, vol. 26, no. 1-2, pp. 140–151, 2006.

[33] R. Ranjan, D. Jiles, and P. Rastogi, "Magnetic properties of decarburized steels: an investigation of the effects of grain size and carbon content," *IEEE transactions on magnetics*, vol. 23, no. 3, pp. 1869–1876, 1987.

[34] L. B. Sipahi, D. C. Jiles, and D. Chandler, "Comprehensive analysis of barkhausen emission spectra using pulse height analysis, frequency spectrum, and pulse wave form analysis," *Journal of applied physics*, vol. 73, no. 10, pp. 5623–5625, 1993.

[35] J. A. Perez-Benitez, J. Capó-Sánchez, J. Anglada-Rivera, and L. Padovese, "A model for the influence of microstructural defects on magnetic barkhausen noise in plain steels," *Journal of magnetism and magnetic materials*, vol. 288, pp. 433–442, 2005.

[36] R. Xie, D. Chen, M. Pan, W. Tian, X. Wu, W. Zhou, and Y. Tang, "Fatigue crack length sizing using a novel flexible eddy current sensor array," *Sensors*, vol. 15, no. 12, pp. 32138–32151, 2015.

[37] C. Accettura, D. Amorim, A. S. Antipov, A. Baris, A. Bertarelli, N. Biancacci, S. Calatroni, F. Carra, F. Caspers, E. García-Tabarés Valdivieso, *et al.*, "Resistivity characterization of molybdenum-coated graphite-based substrates for high-luminosity lhc collimators," *Coatings*, vol. 10, no. 4, p. 361, 2020.

[38] O. BRUCHWALD, W. FRACKOWIAK, S. ZWOCH, W. REIMCHE, and H. J. MAIER, "In-situ monitoring of the microstructure evolution using eddy current technology," in *19th World Conference on Non-destructive Testing*, 2016.

[39] L. Fricke, M. Skalecki, S. Barton, H. Klümper-Westkamp, H.-W. Zoch, and D. Zaremba, "In-situ characterization by eddy current testing of graded microstructural evolution in the core and peripheral zone during material conversion during case hardening," *HTM Journal of Heat Treatment and Materials*, vol. 74, no. 6, pp. 345–356, 2019.

[40] B. B. Shenoy, Z. Li, L. Udpa, S. Udpa, Y. Deng, V. Rathod, and T. Seuaciuc-Osorio, "Nonlinear eddy current technique for fatigue detection and classification in martensitic stainless-steel samples," *Research in Nondestructive Evaluation*, pp. 1–15, 2021.

[41] P. Wang, L. Zhu, Q. Zhu, X. Ji, H. Wang, G. Tian, and E. Yao, "An application of back propagation neural network for the steel stress detection based on barkhausen noise theory," *Ndt & E International*, vol. 55, pp. 9–14, 2013.

[42] D. S. Jardeleza, C. J. G. Aliac, and E. A. Maravillas, "Predictive modeling of compressive strength composition values for structural studies using k-medoids clustering and quantile regression forests," in *2019 IEEE 11th International Conference on Humanoid, Nanotechnology, Information Technology, Communication and Control, Environment, and Management (HNICEM)*, pp. 1–5, IEEE.

[43] D. S. Weile and E. Michielssen, "Genetic algorithm optimization applied to electromagnetics: A review," *IEEE Transactions on Antennas and Propagation*, vol. 45, no. 3, pp. 343–353, 1997.

[44] M. Augustyniak and Z. Usarek, "Finite element method applied in electromagnetic ndte: A review," *Journal of Nondestructive Evaluation*, vol. 35, pp. 1–15, 2016.

[45] N. K. Mutlib, S. B. Baharom, A. El-Shafie, and M. Z. Nuawi, "Ultrasonic health monitoring in structural engineering: buildings and bridges," *Structural Control and Health Monitoring*, vol. 23, no. 3, pp. 409–422, 2016.

[46] G. Alers, "A history of emats," in *AIP Conference Proceedings*, vol. 975, pp. 801–808, American Institute of Physics, 2008.

[47] H. Miao and F. Li, "Shear horizontal wave transducers for structural health monitoring and nondestructive testing: A review," *Ultrasonics*, vol. 114, p. 106355, 2021.

[48] R. B. Thompson *et al.*, "Physical principles of measurements with emat transducers," *Physical acoustics*, vol. 19, pp. 157–200, 1990.

[49] S. Thomas, H. Muazu, T. A. Zarma, and A. Galadima, "Finite element analysis of emat using comsol multiphysics," in *2017 13th International Conference on Electronics, Computer and Computation (ICECCO)*, pp. 1–5, IEEE, 2017.

[50] F. Karimi, *Numerical model of magnetostriction and Lorentz force mechanisms in electromagnetic acoustic transducers*. University of Toronto (Canada), 2020.

[51] M. Mićić, L. Brajović, L. Lazarević, and Z. Popović, "Inspection of rcf rail defects–review of ndt methods," *Mechanical Systems and Signal Processing*, vol. 182, p. 109568, 2023.

[52] E. C. Ashigwuike, O. J. Ushie, R. Mackay, and W. Balachandran, "A study of the transduction mechanisms of electromagnetic acoustic transducers (emats) on pipe steel materials," *Sensors and Actuators A: Physical*, vol. 229, pp. 154–165, 2015.

[53] S. Amato, *Inspection of composite aerospace structures using capacitive imaging and guided waves*. PhD thesis, University of Warwick, 2021.

[54] D. Jiles, *Introduction to magnetism and magnetic materials*. CRC press, 2015.

[55] R. B. Thompson, "A model for the electromagnetic generation of ultrasonic guided waves in ferromagnetic metal polycrystals," *IEEE Transactions on Sonics and Ultrasonics*, vol. 25, no. 1, pp. 7–15, 1978.

[56] C. Vasile and R. Thompson, "Excitation of horizontally polarized shear elastic waves by electromagnetic transducers with periodic permanent magnets," *Journal of Applied Physics*, vol. 50, no. 4, pp. 2583–2588, 1979.

[57] Y. Ohtsuka, M. Higashi, and M. Nishikawa, "Fundamental experiment for inspection of cooling pipes in operation by using ultrasonic technique," *Fusion engineering and design*, vol. 81, no. 8-14, pp. 1583–1587, 2006.

[58] R. B. Thompson, "A model for the electromagnetic generation and detection of rayleigh and lamb waves," *IEEE Transactions on Sonics and Ultrasonics*, vol. 20, no. 4, pp. 340–346, 1973.

[59] D. K. Hsu, K.-H. Im, and I.-Y. Yang, "Applications of electromagnetic acoustic transducers in the nde of non-conducting composite materials," *KSME International Journal*, vol. 13, pp. 403–413, 1999.